

Cover Page



Universiteit Leiden



The handle <http://hdl.handle.net/1887/42923> holds various files of this Leiden University dissertation

Author: Krause-Feldmeier, A.

Title: The assembly history of the milky way nuclear star cluster

Issue Date: 2016-09-13

The Assembly History of the Milky Way Nuclear Star Cluster

Anja Krause née Feldmeier

The Assembly History of the Milky Way Nuclear Star Cluster

Proefschrift

ter verkrijging van
de graad van Doctor aan de Universiteit Leiden,
op gezag van Rector Magnificus prof.mr. C. J. J. M. Stolker,
volgens besluit van het College voor Promoties
te verdedigen op dinsdag 13 september 2016
klokke 15.00 uur

door

Anja Krause née Feldmeier

geboren te Landau a. d. Isar, Duitsland
in 1985

Promotiecommissie

Promotor:	Prof. dr. P. T. de Zeeuw	
Co-promotores:	Dr. N. Neumayer	(MPIA Heidelberg)
	Dr. G. van de Ven	(MPIA Heidelberg)
Overige leden:	Prof. dr. H. J. A. Röttgering	
	Prof. dr. A. Helmi	(Rijksuniversiteit Groningen)
	Prof. dr. P. van der Werf	
	Prof. dr. K. H. Kuijken	
	Dr. R. M. McDermid	(Macquarie University, Sydney)

Cover design by C. Krause (Word Cloud using <http://www.wordle.net/>)

The research was funded by the European Southern Observatory (ESO) and carried out at the ESO headquarters in Garching, Germany.

Contents

1	Introduction	1
1.1	Nuclear star clusters	2
1.1.1	Properties	3
1.1.2	Formation	4
1.2	The Milky Way nuclear star cluster	5
1.3	Supermassive black holes	6
1.4	Stellar populations	6
1.5	Dynamical models	7
1.6	This thesis	8
1.7	Conclusions and outlook	9
2	Large scale kinematics and dynamical modelling	13
2.1	Introduction	14
2.2	Observations	16
2.3	Data reduction and analysis	17
2.3.1	Data reduction	17
2.3.2	Deriving stellar kinematics	20
2.3.3	Line strength measurements	26
2.4	Stellar kinematics and population results	26
2.4.1	Kinematic structure and substructure of the nuclear star cluster	26
2.4.2	Specific angular momentum λ_R	30
2.4.3	Radial profiles	31
2.4.4	Distribution of young stars	37
2.5	Dynamical modelling	38
2.5.1	Surface brightness profile	38
2.5.2	Axisymmetric Jeans models	40
2.5.3	Mass profile	42
2.6	Discussion	43
2.6.1	Clues to the formation of the Milky Way nuclear star cluster	43
2.6.2	Underestimation of the black hole mass	44
2.6.3	Mass profile of the cluster	45
2.6.4	Anisotropy	47
2.6.5	Extreme velocities for individual stars	47
2.7	Conclusions	47
2.8	Appendix: Persistence removal	49
2.9	Appendix: H ₂ gas emission kinematics	51

3	Triaxial orbit-based modelling	53
3.1	Introduction	54
3.2	Description of the data	55
3.2.1	Kinematic data	55
3.2.2	Imaging data and surface brightness distribution	57
3.3	Dynamical models of the Milky Way nuclear star cluster	58
3.3.1	Schwarzschild’s method	58
3.3.2	Constraining the input parameters	61
3.3.3	Modelling results	61
3.4	Discussion	66
3.4.1	Difference of the resulting black hole mass	66
3.4.2	Triaxial cluster shape	70
3.4.3	Caveats and considerations	71
3.5	Summary and outlook	72
4	KMOS view of the Galactic centre I. Young stars are centrally concentrated	75
4.1	Introduction	76
4.2	Observations and data reduction	77
4.2.1	Spectroscopic observations	77
4.2.2	Data reduction	79
4.3	Data analysis	80
4.3.1	Photometry	80
4.3.2	Completeness	81
4.3.3	Spectral identification of late- and early-type stars	84
4.3.4	Deriving stellar kinematics	84
4.4	Results	85
4.4.1	O/B type stars	86
4.4.2	Emission line sources	91
4.4.3	Featureless spectra	97
4.4.4	Spatial distribution of early-type stars	99
4.4.5	Kinematics of early-type stars	102
4.4.6	O/B star orbits	103
4.5	Discussion	106
4.5.1	Detection of 19 new O/B stars	106
4.5.2	O/B star mass estimates	106
4.5.3	Total mass of young stars	107
4.5.4	Disc membership	108
4.5.5	Origin of the early-type stars	108
4.5.6	Early-type stars beyond the central 0.5 pc	110
4.6	Summary	110
4.7	Appendix: Spectral classification of emission-line stars	111
4.8	Appendix: O/B star tables	113

5	KMOS view of the Galactic centre II. Metallicity distribution of late-type stars	121
5.1	Introduction	122
5.2	Data set	123
5.2.1	Observations and data reduction	123
5.2.2	Spectral resolution	124
5.2.3	Data selection	124
5.2.4	Spectral indices	125
5.3	Full spectral fitting	127
5.3.1	Fitting method and assumptions	127
5.3.2	Error estimation	128
5.4	Results	132
5.4.1	Effective temperatures	134
5.4.2	Metallicities	134
5.4.3	Surface gravities	135
5.4.4	Radial velocities	135
5.4.5	Long-period variable stars	136
5.4.6	Spatial distribution and kinematics of metal-poor stars	137
5.4.7	Influence of radial velocity shift	138
5.4.8	Influence of spectral resolution	139
5.5	Discussion	141
5.5.1	Detection of stars with low metallicity $[M/H] \lesssim -0.5$ dex	141
5.5.2	Note of caution on the measurement of high metallicities	142
5.5.3	Metallicity distribution	143
5.5.4	Contamination from foreground or background sources	143
5.5.5	Luminosity classes and implications for stellar ages	144
5.5.6	Clues to the formation of the Milky Way nuclear star cluster	145
5.6	Conclusions	146
5.7	Appendix: The $T_{\text{eff}} - EW_{\text{CO}}$ relation for giants	147
	Bibliography	149
	Bibliography	149
	Samenvatting	157
	Summary	167
	Publications	175
	Curriculum Vitae	177
	Acknowledgements	179

1

Introduction

On a clear, moonless night one can see a diffuse glowing band across the sky, even without a telescope. This band consists of billions of stars, and is called the Milky Way. In addition to this band there are several smaller diffuse nebulae distributed all over the sky. Many of these nebulae are dense gravitationally bound accumulations of stars, gas, dust, and invisible mass, called dark matter. These structures are called galaxies. Our own solar system is located within the Milky Way, which is one such galaxy.

Galaxy sizes range over four orders of magnitude, from a few tens of parsecs in dwarf galaxies to nearly 100,000 parsecs in giant galaxies. Their masses extend over ten orders of magnitude, from about 10^3 to $10^{13} M_{\odot}$. The shape of a galaxy can be elliptical, lenticular, irregular, or disc-like, see Fig. 1.1. High-resolution images show that galaxies can have distinct structures, such as shells, bars, or a cluster of stars in the nucleus. Some galaxies have extraordinary bright nuclei, which can only originate from an accreting supermassive black hole.

These observations lead to several questions: How do galaxies form? Why is there such a huge variety in size and shape? What is at the centre of the galaxy, at the bottom of the gravitational potential well? Do all galaxies contain a supermassive black hole? How did the supermassive black holes and bright star clusters in galactic nuclei form? In order to address the last of these questions, we study the assembly history of the closest galactic nucleus. We investigate the stellar populations and kinematics of the Milky Way's nuclear star cluster in order to find out how it was assembled.

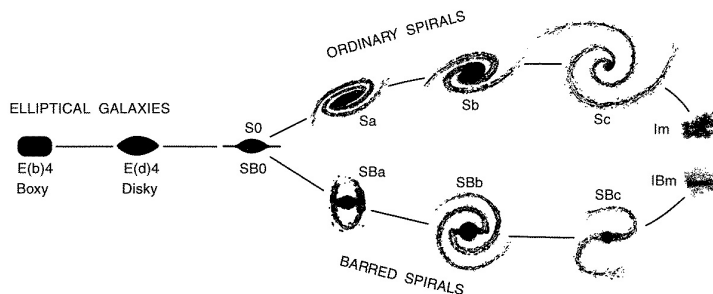


Figure 1.1: Morphological galaxy classification based on Hubble (1926). Galaxies can be divided in ellipticals (E), lenticulars (S0, SB0), spirals (S and SB), and irregulars (Im and IBm, image from Kormendy & Bender 1996).

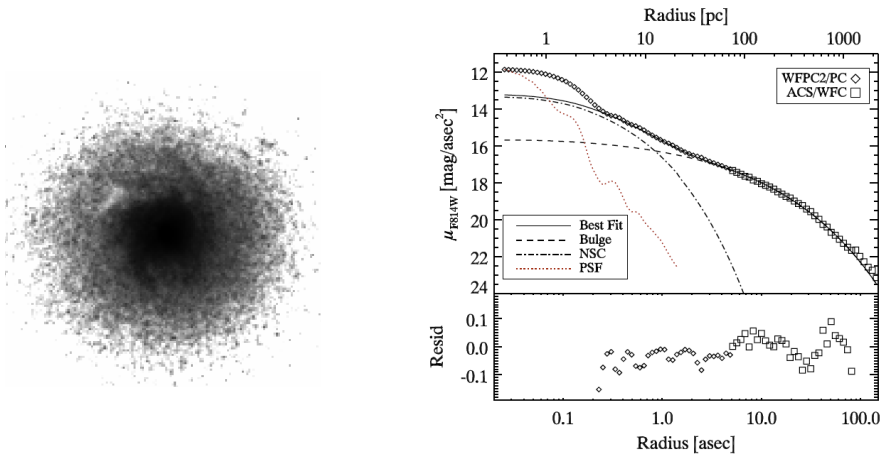


Figure 1.2: Left: *Hubble Space Telescope* WFPC2 image of the central $15'' \times 15''$ of NGC 404 (downloaded from the Hubble legacy archive). Right: Surface brightness profile of NGC 404 (upper panel). Diamond and square symbols denote the data, the dashed line is a fit to the outer (bulge) component, the dot-dashed line is a fit to the inner nuclear star cluster component. The combined best fit is shown as solid line. The lower panel shows the fit residuals (image from Seth et al. 2010).

In this chapter we summarise the main properties and formation scenarios of nuclear star clusters in Section 1.1, and give an overview on the Milky Way nuclear star cluster in Section 1.2. The Milky Way harbours a supermassive black hole in the centre, and we introduce these objects in Section 1.3. In this thesis we study stellar populations, and construct dynamical models for the nuclear star cluster. The applied concepts and methods are briefly summarised in Section 1.4 and Section 1.5. We give an overview on the content of this thesis in Section 1.6. We conclude and close with an outlook in Section 1.7.

1.1 Nuclear star clusters

In the 1990s, nuclear star clusters were discovered in large numbers (e.g. Phillips et al. 1996; Carollo et al. 1998; Matthews et al. 1999). Only the *Hubble Space Telescope* and large 8–10 m telescopes with adaptive optics reach the required angular resolution to resolve the centres of galaxies and the compact sources therein. Galaxies with a nuclear star cluster have a surface brightness profile that exhibits a sharp rise at the centre. Fig. 1.2 shows the image and surface brightness profile of a galaxy with a nuclear star cluster. The surface brightness profile can only be fitted by including a separate component for the nuclear star cluster (dot-dashed line).

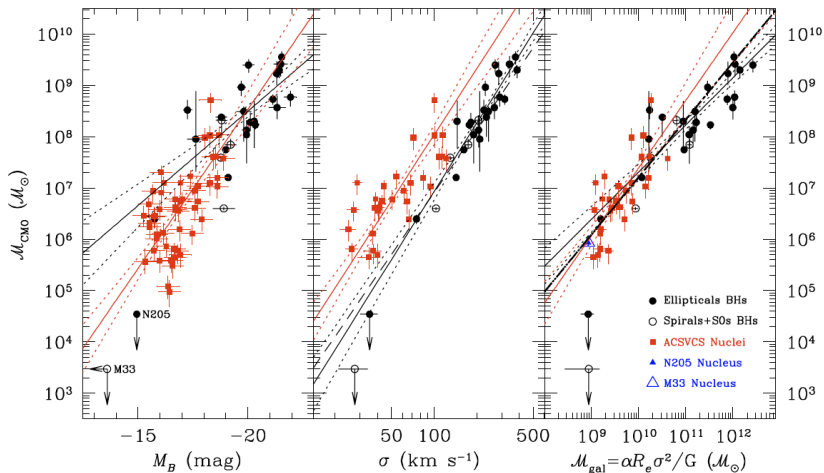


Figure 1.3: Scaling relations of the nuclear star cluster mass (red symbols) and supermassive black hole mass (black symbols) with different galaxy properties, such as B -band magnitude M_B (left panel), velocity dispersion σ (middle panel), and galaxy mass M_{gal} (right panel, image from Ferrarese et al. 2006).

1.1.1 Properties

The effective radii¹ of nuclear star clusters are in the range of 1–10 pc. This means their size is similar to the size of Galactic globular clusters. However, nuclear star clusters are more luminous (by ~ 4 mag) and more massive than globular clusters (by ~ 2 orders of magnitude). Typical masses of nuclear star clusters range over $10^6 - 10^8 M_\odot$. The surface mass density of nuclear star clusters is $\sim 10^3 - 10^5 M_\odot \cdot \text{pc}^{-2}$, which makes them the densest stellar systems in the Universe (Böker et al. 2004; Walcher et al. 2005; Côté et al. 2006; Misgeld & Hilker 2011; Georgiev & Böker 2014).

Nuclear star clusters are very common in low- to intermediate-mass galaxies, regardless of the host galaxies' morphological type. However, nuclear star clusters are absent in massive, bright galaxies (B -band magnitude $M_B \lesssim -20$ mag). The fraction of galaxies with an unambiguous nuclear star cluster detection is ≈ 70 per cent in spheroidal galaxies (Hubble types E and S0), ≈ 50 per cent in early-type spirals (Hubble types Sa-Sc), and ≈ 75 per cent in late-type spirals (Hubble types Scd-Sm). However, these numbers are only lower limits, as bright bulges or dust lanes can prevent the detection of a nuclear star cluster (Carollo et al. 1998; Böker et al. 2002; Côté et al. 2006; Turner et al. 2012; den Brok et al. 2014; Georgiev & Böker 2014).

Some properties of nuclear star clusters correlate with large-scale properties of their host galaxies. These correlations are physically interesting since nuclear star clusters are several orders of magnitude smaller than their host galaxy. The correlations indicate a strong

¹The effective radius indicates the region within half of the total light of a stellar system is emitted.

connection in the evolution of the central component and the galaxy. Finding these correlations makes it worthwhile to study the central regions of galaxies, in order to understand how galaxies themselves formed and evolved. Several studies found different types of correlations, for example between the mass of the nuclear star cluster and the host galaxy's luminosity, velocity dispersion, or mass (Carollo et al. 1998; Böker et al. 2004; Ferrarese et al. 2006; den Brok et al. 2014; Georgiev et al. 2016). We show such correlations in Fig. 1.3. Similar scaling relations are found for the mass of a supermassive black hole and the luminosity, mass, or velocity dispersion of the host galaxy (Kormendy & Richstone 1995; Häring & Rix 2004; Gültekin et al. 2009). This suggests that nuclear star clusters are the low-mass counterparts of supermassive black holes, which are mainly detected in more massive, brighter galaxies (Wehner & Harris 2006; Côté et al. 2006; Ferrarese et al. 2006). However, more recent studies have shown that nuclear star cluster scaling relations differ from supermassive black hole scaling relations (Balcells et al. 2007; Leigh et al. 2012; Scott & Graham 2013). There are also some galaxies, including the Milky Way, which host both a nuclear star cluster and a central supermassive black hole within it (Filippenko & Ho 2003; Seth et al. 2008a; Graham & Spitler 2009).

The star formation history of nuclear star clusters is complex, as they consist of multiple stellar populations. The dominating stellar populations in nuclear star clusters are rather old ($10^8 - 10^{10}$ yr), however, the youngest population can be $\lesssim 10^6$ yr old (Walcher et al. 2006; Rossa et al. 2006; Seth et al. 2006; Carson et al. 2015). Koleva et al. (2011) and Lyubenova et al. (2013) found that some galactic nuclei are more metal-enriched and younger than their host galaxies.

1.1.2 Formation

The process that leads to the formation of nuclear star clusters remains an open question. The formation scenario can be divided in two main categories:

- Gas falls to the centre, and stars are formed in-situ, i.e., in the central parsecs of the galaxy (e.g. Loose et al. 1982; Milosavljević 2004; Schinnerer et al. 2008; Pflamm-Altenburg & Kroupa 2009; Aharon & Perets 2015).
- Dense star clusters, which formed elsewhere in the galaxy, migrate towards the centre of the galaxy (e.g. Tremaine et al. 1975; Capuzzo-Dolcetta & Mocchi 2008; Gnedin et al. 2014; Antonini et al. 2012; Antonini 2013; Perets & Mastrobuono-Battisti 2014).

The first scenario, dissipational gas infall and in-situ star formation, is supported by a number of observations. For example, some nuclear star clusters co-rotate with their host galaxies (Seth et al. 2008b), which indicates accretion from the galactic disc. Moreover, some nuclear star clusters contain molecular gas, or show signs of recent star formation (Schinnerer et al. 2003; Walcher et al. 2006). Stellar winds from recently formed stars and supernovae may reduce the gas supply, leading to episodic star formation (Schinnerer et al. 2008).

For the second scenario, the dissipationless infall of star clusters, Tremaine et al. (1975) suggested that massive globular clusters migrate to the galactic centre due to dynamical fric-

tion. Simulations show that about ten consecutive infalls of globular clusters can recover several properties of nuclear star clusters, for example their size, velocity dispersion, density distribution, and the scaling relations (Capuzzo-Dolcetta & Miocchi 2008; Antonini et al. 2012; Antonini 2013). The accretion of young massive star clusters, which formed near the galactic centres, could also explain the presence of young stars and the rotation of nuclear star clusters (Agarwal & Milosavljević 2011; Hartmann et al. 2011). A combination of the two different formation scenarios is also possible (Neumayer et al. 2011; Hartmann et al. 2011; Leigh et al. 2012), and the relative importance of the two processes may depend on the galaxy mass or morphology. Turner et al. (2012) suggested that star cluster infall is most important for low-mass galaxies, whereas gas accretion is dominant in high-mass galaxies.

1.2 The Milky Way nuclear star cluster

The Milky Way nuclear star cluster offers a unique opportunity to study the structure and dynamics of a nuclear star cluster in much more detail than possible in other galaxies. The Milky Way nuclear star cluster was discovered by Becklin & Neugebauer (1968) in the near-infrared. They detected a $5'$ large source, elongated along the Galactic plane, in the Galactic centre, and suggested that the radiation originates from a cluster of cool (~ 4000 K) stars. Later observations resolved several discrete sources, which could be identified as stars (Becklin et al. 1978).

There are two important obstacles when observing the Milky Way nuclear star cluster. One of them is the high stellar density. Since the cluster is extremely crowded, it is difficult to resolve single stars. This problem can be addressed by using adaptive optics. However, the correction works only for rather small fields (Clénet et al. 2001; Genzel et al. 2003; Eisenhauer et al. 2005). The other problem is high interstellar extinction. Since the cluster is located in the centre of the Galaxy and the Solar system lies within the Galactic disc, the line-of-sight goes through the Milky Way's spiral arms and the central molecular zone, which are rich in molecular gas. This causes high extinction and reddening, making it effectively impossible to observe the Galactic centre in the optical and ultraviolet. The extinction decreases with wavelength (e.g. Schödel et al. 2010), and the Galactic centre becomes accessible in the near-infrared, at wavelengths $\lambda \gtrsim 1.2 \mu\text{m}$.

Our distance to the Milky Way nuclear star cluster is approximately 8 kpc (Malkin 2012). The cluster's size is rather typical for nuclear star clusters, with an effective radius of $r_{\text{eff}} = (4.2 \pm 0.4)$ pc and a total mass of approximately $(2.5 \pm 0.4) \times 10^7 M_{\odot}$ (Schödel et al. 2014a). The Milky Way nuclear star cluster is not spherically symmetric but point-symmetric in projection, and flattened along the Galactic plane, with a ratio $q = 0.71 \pm 0.02$ between minor and major axis (Schödel et al. 2014a). The flattening is consistent with observations of other nuclear star clusters in edge-on galaxies (Seth et al. 2006). Figure 1.4 illustrates the Galactic centre. The nuclear star cluster is embedded in the nuclear stellar disc, which has a radius of 230 ± 20 pc, and a scale height of 45 ± 5 pc (Launhardt et al. 2002). These components form the nuclear bulge (panel a). The nuclear star cluster is shown in panel b). In the very centre

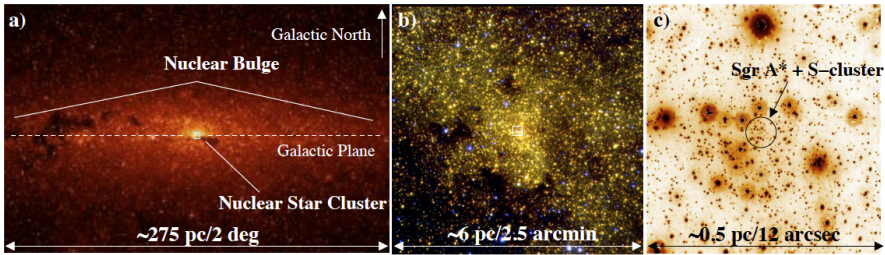


Figure 1.4: a) *Spitzer* 4.5 μm image of the central 275 pc of the Milky Way. (b) ISAAC near-infrared image of the central 6 pc \times 6 pc of the nuclear star cluster. (c) The central 0.5 pc \times 0.5 pc of the Milky Way observed with NACO in the near-infrared. All images are centred on the supermassive black hole Sgr A* (image from Schödel et al. 2014b).

of the Milky Way nuclear star cluster lies the radio source Sgr A*, which is surrounded by the so-called S-stars, a star cluster with a size of $1''$.

1.3 Supermassive black holes

Supermassive black holes are located in the centres of most galaxies, especially in massive galaxies. Also the Milky Way contains a supermassive black hole at its centre. It is associated with the radio source Sgr A*. The S-stars in the central arcsec of the Galaxy around Sgr A* have been monitored over more than a decade. From the measurements of the stellar orbits of the S-stars, the mass of the supermassive black hole was derived to $(4.1 \pm 0.6) \times 10^6 M_{\odot}$ (Ghez et al. 2008), $(4.3 \pm 0.39) \times 10^6 M_{\odot}$ (Gillessen et al. 2009b), and $(4.02 \pm 0.20) \times 10^6 M_{\odot}$ (Boehle et al. 2016).

Supermassive black holes can be detected and weighted through their gravitational influence on the surrounding stars and gas, also in other galaxies. The masses of supermassive black holes range from $M_{\bullet} \gtrsim 10^4 M_{\odot}$ (e.g. in RGG 188, Baldassare et al. 2015) to several $10^9 M_{\odot}$ (e.g. in M87, Gebhardt et al. 2011). There is no consensus on the processes that formed supermassive black holes and let them grow. It was suggested that black holes either formed as the end-product of stellar evolution, or directly from a collapsing gas cloud in the early Universe (e.g. Volonteri 2010; Greene 2012, and references therein). The black hole seeds must then have grown rapidly to explain the detection of supermassive black holes at high redshift, only about 10^9 yr after the Big Bang (Barth et al. 2003).

1.4 Stellar populations

The concept of stellar populations is used to describe subgroups of stars with distinct properties in a stellar system. Each subgroup or stellar population has a characteristic age, metallicity, spatial distribution, and distinct kinematic properties, bearing witness to their different

formation history and evolution. Understanding the stellar populations in a stellar system helps to derive the assembly history of the stellar system itself.

A key tool to study stellar populations is spectroscopy. The absorption lines in stellar spectra carry information on the physical structure and chemical composition of the stellar atmosphere. We measure the absorption line strength and equivalent width of stellar spectra in the near-infrared to discern hot and cool stars, and use full spectral fitting to measure the effective temperature T_{eff} , metallicity $[M/H]$, and radial velocity v_z of stars. We use synthetic spectra and stellar libraries of stars for which these properties are known in order to calibrate our measurements.

1.5 Dynamical models

Dynamical models are a useful tool to infer the mass distribution of a stellar system. In a dynamical model, the observed light distribution and kinematics of the visible stars can be reconstructed. Since the stellar kinematics is influenced by the entire gravity of the system, the dynamical model reveals the total mass distribution of the stellar system, including the mass of invisible components such as black holes and dark matter. We use dynamical models to measure the mass distribution of the Milky Way nuclear star cluster and the mass of the central supermassive black hole. We apply axisymmetric Jeans models and triaxial orbit-based Schwarzschild models. Both types of model assume that the stellar system is in dynamical equilibrium. This means that the modelled stellar system has neither formed recently, nor has it been perturbed recently (Schwarzschild 1979).

Jeans models are based on the Jeans (1922) equations, which are derived from the collisionless Boltzmann equation. We solve the Jeans equations using the surface brightness and stellar root-mean-square velocity $V_{\text{rms}} = \sqrt{V^2 + \sigma^2}$ as constraints, where V is the velocity and σ is the velocity dispersion of stars in the system. The solutions provide constraints on the black hole mass M_{\bullet} , dynamical mass-to-light ratio Y , and velocity anisotropy $\beta = 1 - \sigma_z^2 / \sigma_R^2$. We use the Jeans Anisotropic Models by Cappellari (2008).

Schwarzschild (1979) models require a representative library of orbits in the modelled stellar system. The orbits are integrated in the gravitational potential. Then, a combination of orbit weights is fitted that reproduces the observed density distribution and kinematics of the stellar system. One can include all higher order kinematic moments of the line-of-sight velocity distribution to the fit, i.e. the velocity V , velocity dispersion σ , and the Gauss-Hermite moments h_3, h_4 , etc. (Rix et al. 1997). Schwarzschild models have the advantages that they make no assumptions on the velocity anisotropy, and they allow to study the orbital structure of the stellar system (van de Ven et al. 2008). We use the triaxial orbit-based modelling code by van den Bosch et al. (2008).

1.6 This thesis

In this Ph.D. thesis we study the assembly history of the Milky Way nuclear star cluster. We combine spatially extended spectroscopic and photometric data with state-of-the-art dynamical modelling codes and spectral fitting methods.

In **Chapter 2** (based on Feldmeier et al. 2014) we study the kinematics and mass distribution of the Milky Way nuclear star cluster. We use the near-infrared long-slit spectrograph ISAAC at the *Very Large Telescope* (VLT) to map the central $\sim 60 \text{ pc}^2$ of the Milky Way nuclear star cluster. In addition we observe six smaller fields out to 19 pc along the Galactic plane. The data extend out to the radius of influence of the central supermassive black hole. We measure radial velocities and CO absorption line strengths on 1375 spectra from individual stars. We derive line-of-sight velocity and velocity dispersion maps of the unresolved integrated light spectra. The velocity map reveals rotation of the nuclear star cluster, and additional complex structures. In particular, we discover a misalignment of the kinematic position angle by 9° with respect to the Galactic plane, and indications for a rotating substructure perpendicular to the Galactic plane at a radius $\sim 0.8 \text{ pc}$. These structures may be the signatures of distinct accretion events. In addition to the kinematic maps we use *Spitzer* and NACO photometry and run anisotropic axisymmetric Jeans models. We derive the mass distribution of the nuclear star cluster and measure the black hole mass. The resulting black hole mass is 50 per cent lower than measured via resolved orbits of individual stars.

In **Chapter 3** (based on Feldmeier-Krause et al. submitted b) we study the mass distribution and orbital structure of the Milky Way nuclear star cluster. We construct triaxial orbit-based Schwarzschild models of the Milky Way nuclear star cluster, and apply them to the spectroscopic maps and photometric *Spitzer* data from Chapter 2. We use these models to constrain the triaxial shape of the nuclear star cluster, the dynamical mass-to-light ratio Y , and supermassive black hole mass M_\bullet . We obtain a black hole mass of $M_\bullet = (3.0_{-1.3}^{+1.1}) \times 10^6 M_\odot$, in agreement with the black hole mass measurement via resolved stellar orbits. Our best-fitting model recovers complex kinematic substructures in the velocity map. We find tangential anisotropy in the central $r = 2 \text{ pc}$, but isotropy at larger radii.

Chapter 4 (based on Feldmeier-Krause et al. 2015) presents a study of the young stellar population in the central 4 pc^2 of the Milky Way nuclear star cluster. Our near-infrared KMOS (VLT) data contain spectra of 114 hot, young stars that formed only 3–8 Myr ago. We classify the young stars as O/B-type stars, Wolf-Rayet stars, and bow-shock sources. The young stars are very centrally concentrated, in contrast to the cool red giant population, which is distributed over the entire radial range of the data. The strong concentration of hot, young stars indicates that their formation happened in situ, as we would expect more young stars at larger radii for the migration scenario.

In **Chapter 5** (based on Feldmeier-Krause et al. submitted a) we analyse the metallicity distribution of late-type stars in the Milky Way nuclear star cluster. The data were obtained with KMOS (VLT) and cover the central 4 pc^2 of the cluster. The stars have a higher average Na I equivalent width than comparable stars in spectral libraries. We apply full spectral fitting on the spectra of more than 700 stars. Using a library of synthetic spectra, we fit the

stellar effective temperatures T_{eff} , metallicities $[M/H]$, surface gravities $\log(g)$, and radial velocities v_z . Most of the stars in our data set are cool red giants with $T_{\text{eff}} = 3\,000 - 5\,000$ K. We find a smooth metallicity distribution, ranging from $[M/H] < -1$ dex to $\gtrsim +0.3$ dex. Only approximately five per cent of the stars are metal-poor ($[M/H] \leq -0.5$ dex), most stars have super-solar metallicities. The metal-poor stars might originate from infalling globular clusters. However, the cluster is dominated by metal-rich stars, for which the globular cluster infall scenario can be ruled out.

1.7 Conclusions and outlook

Detailed studies of nuclear star clusters can provide insight into the physical processes that formed and shaped the centres of galaxies. We study the stellar kinematics and stellar populations of the nearest nuclear star cluster at the heart of the Milky Way, and use it as a benchmark to understand the formation and evolution of nuclei in other galaxies.

We found indications for two different formation mechanisms of nuclear star clusters. Velocity maps of old red giant stars reveal complex structures. This indicates that star clusters were accreted by the nuclear star cluster. The detection of metal-poor stars is another indication for the cluster infall scenario, in particular the migration and merger of a globular cluster. Metal-poor stars are also observed in the Galactic disc and bulge, and may have formed within the Galaxy. Based on the low fraction of metal-poor stars, globular cluster infall cannot be the major formation process for the Milky Way nuclear star cluster. Most stars have solar or super-solar metallicities, which are inconsistent with a globular cluster origin. These stars must have formed from enriched material. They either formed directly in the Galactic nucleus, or somewhere inside the Milky Way with later migration to the nucleus. The young stars, though, formed directly within the central parsec of the Milky Way. They are very centrally concentrated, which is inconsistent with a migration scenario.

Our stellar population study was limited to only 4 pc^2 . Although this is already a significantly larger area compared to previous studies, it is only a small region of the nuclear star cluster. The cluster's effective radius is 4.2 pc , and the nuclear stellar disc becomes only dominant at 30 pc . It is interesting to study the stellar populations over a larger area of the nuclear star cluster, and search for possible gradients of age or metallicity. As we showed, there are only few metal-poor stars in the centre of the Milky Way nuclear star cluster, but it could be that there are more metal-poor stars further out. If globular clusters migrated to the centre of the Milky Way, they would have lost stars on their way to the centre. These stars could be located at the outer regions of the nuclear star cluster. There might also be isolated young stars at larger radii, which have not been detected yet. These stars would trace recent accretion events. A gradient of the stellar populations also implies that the mass-to-light ratio, which we assumed to be constant, is spatially varying. This would change our results of the cluster's stellar mass distribution.

In order to analyse if there is a gradient in the stellar populations, we observed a larger area of the Milky Way nuclear star cluster. In particular, we observed eight further fields

with KMOS, out to and beyond the effective radius. From these data we will extract spectra of about 7 000 stars. To analyse the spectra, we will benefit from spectral libraries in the K -band that will be available in the near future. They will allow us to compare the spectra with different abundances and metallicities. We will implement different abundance ratios and stellar age in the spectral fitting. The spectroscopic data will be complemented with the HAWK-I photometric data of a large observing programme (P. I. Schödel). In order to verify our metallicity measurements and to measure element abundances of cool stars, we will propose observations at higher spectral resolution, e.g. with the instruments X-SHOOTER or CRIRES at the VLT. It is also interesting to obtain higher resolution spectra of the newly discovered young stars, in order to determine their spectral type and age. In this thesis we assumed that their age is consistent with the already known young stars, but this assumption should be tested.

There is also room for improvement in the kinematic studies of the nuclear star cluster. The rotation curve of the inner Galaxy and the central Galactic potential are still largely unconstrained. Our kinematic map extends only to the effective radius. We observed a larger region of 140 pc^2 along the Galactic plane with the spectrograph FLAMINGOS-2 (Gemini South Telescope). This is more than twice the area we observed with ISAAC. We will extract spectra from a further $\sim 3\,000$ stars and measure their radial velocities and stellar parameters. We will also measure the kinematics of the integrated light from underlying faint stars, towards the outer edge of the nuclear star cluster. Our measurement of the central Galactic potential will be useful to compute the deceleration of hypervelocity stars (Kenyon et al. 2008), and the dynamical friction timescale of infalling star clusters (Antonini et al. 2012).

These two data sets can be combined and used for dynamical modelling. The kinematics of individual stars can be studied in discrete dynamical models, which do not require binning (Chanamé et al. 2008; Watkins et al. 2013). It is also possible to include proper motion measurements. In the future, it will be interesting to include the knowledge of the stellar ages and metallicities to dynamical models, and model the different populations separately. Such models are under development. Further, we neglected the neutral gas disc in the orbit-based models. By adding an additional gas disc component, the dynamical mass-to-light ratio would decrease. We also ignored figure rotation, which causes chaotic orbits and influences the orbital structure. Modelling figure rotation is computationally expensive, but will be possible in the future with more powerful computers.

The future will open new horizons for observations of galactic nuclei. New observing facilities are presently planned and built. For example, the *James Webb Space Telescope* (*JWST*) will be launched in 2018. At wavelengths from 0.6 to $28 \mu\text{m}$ it will reach high spatial resolution ($0''.023$ to $1''.01$). The small field of view of the *JWST* spectrographs is unpractical to observe the Milky Way nuclear star cluster, but *JWST* will be very useful to study nuclei of other galaxies. Its high sensitivity and spatial resolution are needed to detect and image distant nuclear star clusters. Further, the low- to medium- resolution integral field spectrographs MIRI and NIRSpec will allow us to observe stellar populations in galactic nuclei, and due to the high spatial resolution, also stellar population gradients.

In addition, a new generation of ground-based telescopes is currently being constructed: Extremely large telescopes with mirror diameters $d > 20$ m. The *Giant Magellan Telescope* (GMT, $d = 24.5$ m) and the *European Extremely Large Telescope* (E-ELT, $d = 39.3$ m) are built in Chile, the *Thirty Meter Telescope* (TMT, $d = 30$ m) possibly in Hawai‘i. All three facilities allow observations of the Galactic centre, and together cover the northern and southern hemisphere. Due to their high sensitivity, it will be possible to observe fainter stars in the Galactic centre, including A- and F-type dwarfs. The spatial resolution reached by extremely large telescopes with adaptive optics will be better than what can be achieved with the *Hubble Space Telescope* and *JWST*. In combination with high-spectral resolution instruments, it will be possible to search for supermassive black holes in other nuclear star clusters. Such measurements are useful to study the aforementioned scaling relations.

New telescopes and models will help to achieve a better understanding of the formation and evolution of galactic nuclei, and their host galaxies. We are looking into a bright future for the research of galactic nuclei.

2

Large scale kinematics and dynamical modelling of the Milky Way nuclear star cluster

Within the central 10 pc of our Galaxy lies a dense cluster of stars. This nuclear star cluster forms a distinct component of the Galaxy, and similar nuclear star clusters are found in most nearby spiral and elliptical galaxies. Studying the structure and kinematics of nuclear star clusters reveals the history of mass accretion and growth of galaxy nuclei and central massive black holes. Because the Milky Way nuclear star cluster is at a distance of only 8 kpc, we can spatially resolve the cluster on sub-parsec scales. This makes the Milky Way nuclear star cluster a reference object for understanding the formation of all nuclear star clusters.

We have used the near-infrared long-slit spectrograph ISAAC (VLT) in a drift-scan to construct an integral-field spectroscopic map of the central $\sim 9.5 \times 8$ pc of our Galaxy, and six smaller fields out to 19 pc along the Galactic plane. We use this spectroscopic data set to extract stellar kinematics both of individual stars and from the unresolved integrated light spectrum. We present a velocity and dispersion map from the integrated light spectra and model these kinematics using KINEMETRY and axisymmetric Jeans models. We also measure radial velocities and CO bandhead strengths of 1 375 spectra from individual stars.

We find kinematic complexity in the nuclear star cluster's radial velocity map including a misalignment of the kinematic position angle by 9° counterclockwise relative to the Galactic plane, and indications for a rotating substructure perpendicular to the Galactic plane at a radius of $20''$ or ~ 0.8 pc. We determine the mass of the nuclear star cluster within $r = 4.2$ pc to $(1.4_{-0.7}^{+0.6}) \times 10^7 M_\odot$. We also show that our kinematic data results in a significant underestimation of the supermassive black hole (SMBH) mass.

The kinematic substructure and position angle misalignment may hint at distinct accretion events. This indicates that the Milky Way nuclear star cluster grew at least partly by the mergers of massive star clusters. Compared to other nuclear star clusters, the Milky Way nuclear star cluster is on the compact side of the $r_{\text{eff}} - M_{\text{NSC}}$ relation. The underestimation of the SMBH mass might be caused by the kinematic misalignment and a stellar population gradient. But it is also possible that there is a bias in SMBH mass measurements obtained with integrated light, and this might affect SMBH mass determinations of other galaxies.

A. Feldmeier, N. Neumayer, A. Seth, R. Schödel, N. Lützgendorf, P. T. de Zeeuw,
M. Kissler-Patig, S. Nishiyama, C. J. Walcher

Astronomy & Astrophysics, Volume 570, id.A2, 20 pp, 10/2014

2.1 Introduction

The Milky Way nuclear star cluster lies within the central 10 pc of our Galaxy and is composed of a dense population of stars. The cluster forms a distinct component, with a half-light radius or effective radius r_{eff} of $\sim 110\text{--}127''$ (4.2–5 pc, Schödel et al. 2014a; Fritz et al. 2016), and a mass of $(2\text{--}3) \times 10^7 M_{\odot}$ (Launhardt et al. 2002; Schödel et al. 2014a). However, the formation and growth of the nuclear star cluster and the supermassive black hole (SMBH) in the centre are not understood. The stars in the cluster provide a record of the nuclear accretion history and formation processes.

The nuclear star cluster in the Galactic centre is not a unique object, as such clusters are common in other galaxies as well. They have been detected in ~ 75 per cent of spiral galaxies (Carollo et al. 1998; Böker et al. 2002), and spheroidal galaxies (Côté et al. 2006). These are lower limits, as the presence of bulges and dust lanes can obscure the nuclear cluster and prevent detection (Carollo et al. 2002; Seth et al. 2006). Galaxies with higher mass than $\sim 10^{10} M_{\odot}$ usually only host a SMBH, while nuclear star clusters are preferentially detected in galaxies with lower mass (Ferrarese et al. 2006; Wehner & Harris 2006; Böker 2010; Scott & Graham 2013). But there are also cases where both nuclear star cluster and SMBH coexist in the same galactic nucleus (Seth et al. 2008a). The most convincing case is our own Galaxy. Precise measurements of stellar orbits around the central radio source Sagittarius A* (Sgr A*) provide the most direct evidence for the presence of a SMBH at the centre of our Galaxy. Ghez et al. (2008) and Gillessen et al. (2009b) observed a full Keplerian orbit of one of the innermost stars and measured the mass of the black hole as $\sim 4 \times 10^6 M_{\odot}$. Also other nuclear clusters show evidence for a central massive black hole from dynamical modelling or the presence of an AGN (e.g. Filippenko & Ho 2003; Graham & Spitler 2009; Seth et al. 2010; Neumayer & Walcher 2012).

With a distance of only ~ 8 kpc (Ghez et al. 2008; Gillessen et al. 2009b) it is possible to resolve single stars in the Milky Way nuclear star cluster spectroscopically and infer their age. The stellar populations of the central 1 pc ($\sim 26''$) of the Milky Way can be studied only in the near-infrared (e.g by Pfuhl et al. 2011; Do et al. 2013a), as high extinction makes the Galactic centre impenetrable for observations in the visible bands. The stars are predominantly cool and old (> 5 Gyr old, e.g. Blum et al. 2003; Pfuhl et al. 2011), but in the central ~ 0.5 pc there exists an additional stellar component in the form of hot, young stars (4 – 8 Myr e.g. Paumard et al. 2006; Lu et al. 2009; Bartko et al. 2009), and stars of intermediate age (~ 100 Myr, e.g. Krabbe et al. 1995; Pfuhl et al. 2011). So far, multiple stellar populations have been found in all other nuclear star clusters as well (e.g. Walcher et al. 2006; Rossa et al. 2006; Seth et al. 2006; Siegel et al. 2007; Seth et al. 2010; Lauer et al. 2012), with an underlying old population (> 1 Gyr) and a generation of younger stars (< 100 Myr). This suggests a complex star formation history.

There are two prevalent formation scenarios for nuclear star clusters: 1) Stars form in dense clusters elsewhere in the galaxy and then migrate to the galaxy's centre. Tremaine et al. (1975) suggested the formation of the M31 nucleus by the infall of globular clusters due to dynamical friction. The clusters would merge to become the observed nuclear star cluster.

Capuzzo-Dolcetta & Mocchi (2008), Antonini (2013), Gnedin et al. (2014), and Antonini (2014) studied the infall of massive clusters in central regions of galaxies and found that the expected density and velocity-dispersion profiles of the merged nuclear star cluster matches the observations. 2) Nuclear star clusters form in-situ by gas infall from the disc followed by star formation (Milosavljević 2004; Pflamm-Altenburg & Kroupa 2009). This theory is supported by the discovery of rotation in the nuclear star clusters of the Milky Way (Trippe et al. 2008; Schödel et al. 2009) and NGC 4244 (Seth et al. 2008b). A combination of both formation scenarios is also possible (Hartmann et al. 2011; Neumayer et al. 2011; Turner et al. 2012; De Lorenzi et al. 2013).

At the Galactic centre the presence of young stars indicates star formation within the past few Myr, as well as the presence of molecular gas within a few pc of Sgr A*. This demonstrates that the necessary material for star formation can be found within the nuclear star cluster. The ring of clumpy gas and dust is called circumnuclear disc or circumnuclear ring and extends to a Galactocentric radius of ~ 7 pc ($3'$, e.g. Yusef-Zadeh et al. 2001; Christopher et al. 2005; Lee et al. 2008; Liu et al. 2012). Oka et al. (2011) suggested that the circumnuclear disc was formed from an infalling disrupted giant molecular cloud, and may eventually fragment and trigger star formation. Yusef-Zadeh et al. (2008) detected methanol masers, which could hint to an early stage of star formation.

There are several kinematic studies of the stars in the central parsec of the Milky Way nuclear star cluster. For example Trippe et al. (2008) and Schödel et al. (2009) studied both radial velocities and proper motions but not beyond a distance of 1 pc from the Galactic centre. They found that the velocity dispersions of the stars are consistent with an isotropic, rotating cluster. However, the larger-scale kinematics are not so extensively studied. Lindqvist et al. (1992b) collected a sample of 134 OH/IR stars at a distance of 5–100 pc (~ 2 – $40'$) from the Galactic centre, but only 15 of their targets are within 8 pc from the Galactic centre, and therefore likely cluster members. McGinn et al. (1989) obtained integrated light spectra of selected fields with a $20''$ (0.78 pc) aperture at $2.3 \mu\text{m}$ out to ~ 4 pc ($1.7'$) distance along the Galactic plane and ~ 1.5 pc ($0.6'$) perpendicular to it. They found decreasing velocity dispersion and increasing velocities with Galactocentric distance, and a flattening of the rotation curve between 2 pc and 3 pc (~ 50 – $80''$). But McGinn et al. (1989) had large scattering in their data.

Hence the Milky Way nuclear star cluster kinematics are known in detail at small scales, but the large scale kinematics beyond 1 pc remain uncertain. For example, the rotation is not yet well determined, although a rotation law can provide insights on the processes that play a role in the formation of the nuclear star cluster. Calculations of the Galactic potential beyond 1 pc used $\lesssim 200$ stars to trace the kinematics, but the stars were spread over a large area of several tens of pc^2 . Therefore there is large uncertainty in these measurements.

In order to overcome this lack of knowledge we have obtained a new spectroscopic data set of the Milky Way nuclear star cluster on a large scale, covering the central ~ 9.5 pc \times 8 pc ($4' \times 3.5'$). The purpose of this work is two-fold: (i) to perform the first detailed kinematic analysis of the Milky Way nuclear star cluster on large scales in integrated light; (ii) to construct a dynamical model, in which we derive the cluster mass and constrain the central

Galactic potential. As by-product we also extract an H₂ gas kinematic map and almost 1 400 spectra of bright stars. We compute the velocities and CO indices of these stars, from which we can identify young star candidates.

This paper is organised as follows: The observations are summarised in Section 2.2, and in Section 2.3 we describe the data reduction and analysis. Our results for the stellar kinematics and stellar populations are presented in Section 2.4. In Section 2.5 we fit a surface brightness profile and present the results of dynamical Jeans models. We discuss our results in Section 2.6. Our conclusions are provided in Section 2.7. The H₂ gas emission line results are shown in Appendix 2.9. Throughout this paper we assume a Galactocentric distance R_0 of 8.0 kpc (Malkin 2012), i.e. 1'' corresponds to ~ 0.039 pc.

2.2 Observations

We used the near-infrared long-slit spectrograph ISAAC (Infrared Spectrometer And Array Camera, Moorwood et al. 1998) in a drift-scan technique to observe the central ~ 9.5 pc \times 8 pc ($4' \times 3'.5$) of our Galaxy. To complement our data set we also observed six fields out to a distance of ~ 19 pc ($8'$) along the Galactic plane, a region where the nuclear stellar disc becomes important.

Observations were performed on VLT-UT3 (Melipal) in the nights of July 3 and 4, 2012. We used the ISAAC short wavelength medium resolution spectroscopic mode. In this mode the spectral coverage is only $0.122 \mu\text{m}$. The central wavelength of our observations is $2.35 \mu\text{m}$, and the resulting spectral range is $\sim 2.289\text{--}2.411 \mu\text{m}$. The ISAAC slit has a length of $120''$, and we chose a slit width of $0'.6$ to obtain a spectral resolution of $R = 4\,400$, corresponding to $\Delta V \approx 68 \text{ km}\cdot\text{s}^{-1}$. The spatial pixel scale is $0'.148\text{-pixel}^{-1}$, the spectral pixel size is $1.2 \times 10^{-4} \mu\text{m}\cdot\text{pixel}^{-1}$. The drift scan worked as follows: To cover the Galactic nuclear star cluster to the effective radius, we scanned the slit across the Galactic centre while integrating. During every 120 s exposure, the slit moved perpendicular to the slit length over $2''$. The scan direction was along the Galactic plane applying a position angle of $31^\circ 40'$ east of north (J2000.0 coordinates, Reid & Brunthaler 2004). During the first night we scanned the central $\sim 120'' \times 240''$. In the second night we scanned a smaller region north-west of the centre, which partly overlaps with the observations of the first night, covering $\sim 120'' \times 120''$. Additionally we observed six smaller regions with $\sim 120'' \times 16''$ each along the Galactic plane. They are at distances from the centre of $4'$, $6'$, and $8'$, respectively. The scanned regions are illustrated in Fig. 2.1.

For sky observations we made offsets to a dark cloud that is located about $30'$ east of the Galactic Centre ($\alpha \approx 267^\circ 00'$, $\delta \approx -28^\circ 99'$, diameter approximately $11'$, Dutra & Bica 2001). The sky was also observed in a drift scan with the same scanning velocity. After a sequence of 8 – 10 object frames we made sky offsets and followed an object – sky – object sequence. We obtained five spectroscopic sky exposures in each sky offset, in order to remove stars in the sky field and compute a Mastersky frame. Moreover, we observed four B dwarfs as telluric

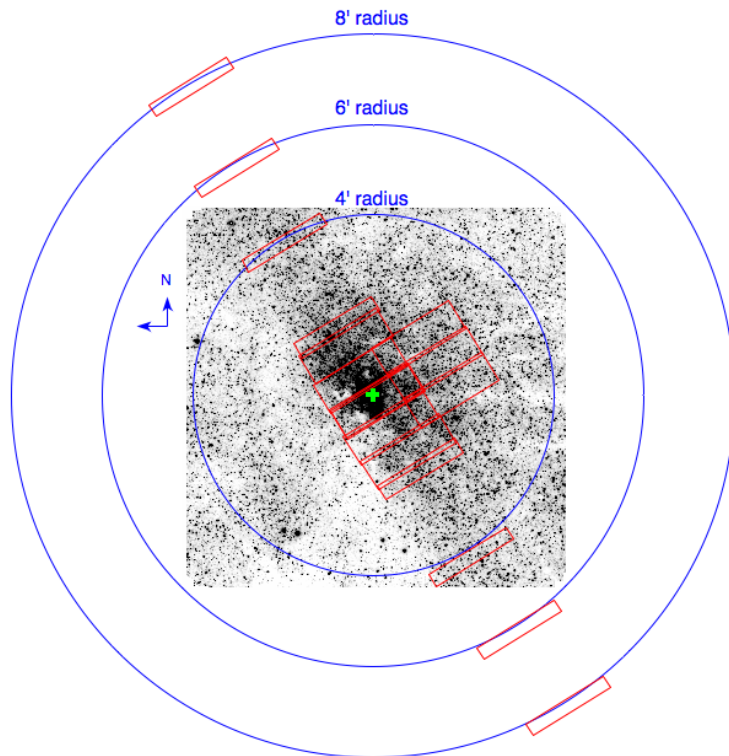


Figure 2.1: Positions of the regions scanned with ISAAC (red rectangles). The underlying image is from IRSF/SIRIUS in K_S band (Nishiyama et al. 2006). The circles denote a distance of $4'$, $6'$, and $8'$ from the position of Sgr A*, respectively, and the green cross is the position of Sgr A*. The outer fields are not exactly symmetric due to the drift towards the south-west during the acquisition.

standards in both nights using a standard nodding technique. For wavelength calibrations we obtained Xenon and Argon arc lamp calibration frames.

2.3 Data reduction and analysis

2.3.1 Data reduction

The data reduction of the spectra included the following steps: First we used the ISAAC pipeline ISAACP (Amico et al. 2002) to remove electrical ghosts from all frames with the recipe GHOST, and with the recipe SP_FLAT we obtained master flats. We further combined the dark files to master darks and subtracted them using IRAF (Imaging Reduction and Analysis

Facility¹), and removed bad pixels. For cosmic ray removal we used the LAPLACIAN COSMIC RAY IDENTIFICATION L.A.COSMIC written by van Dokkum (2001). Flat fielding as well as distortion correction and wavelength calibrations were performed with IRAF. The spectra contain thermal background, which is partly due to the sky and partly to the detector. We made a robust two-dimensional polynomial fit to each two-dimensional spectral frame along the dispersion axis and subtracted the polynomial fit from the spectra.

Unfortunately, the spectra suffer from persistence. This means that bright stars, especially those which were saturated in the images taken before the spectra, were burnt in the detector and remain visible for some time as bright spots in the spectra taken afterwards. Our approach to remove the persistence from the spectra is described in Appendix 2.8. After subtracting the persistence from object and sky spectra we combined the sky frames to master sky frames and performed sky subtraction with an IDL routine written by Davies (2007).

We reduced the telluric spectra using the double sky subtraction technique, which is the standard for nodding, to ensure optimal sky subtraction. A telluric correction was performed for every single row of the two-dimensional spectral frames separately with the IRAF task TELLURIC. We scaled the intensity of the telluric spectra with the difference in air mass and searched for an optimum scale factor, but omitted a shift option for the telluric correction. The next step was to shift the reduced spectra to the local standard of rest using the IRAF recipes RVCORRECT and DOPCOR.

To determine the astrometry of our spectra, we created images from spectra taken subsequently before a sky offset. We summed the flux of every spectrum along the dispersion axis and reconstructed images, where every exposure extends over 15 columns of the ISAAC pixel scale of $0''.148\text{-pixel}^{-1}$. This means we have a spatial resolution of $2''.22$ in the drift direction (Galactic east-west) and a spatial resolution of $0''.148\text{-pixel}^{-1}$ along the slit (Galactic north-south direction). Every red box in Fig. 2.1 corresponds to one reconstructed image. The image was blurred with a Gaussian point spread function (PSF) with the full width half maximum (FWHM) of the seeing during the observations. This makes the stars less rectangular. The images were cross correlated with the ISAAC acquisition images that were matched to the 2MASS point source catalogue (Skrutskie et al. 2006) and also blurred. While the wavelength range of the acquisition images covers the entire *K*-band, the spectra contain a much narrower wavelength range. Still, we could identify enough stars to perform a meaningful cross correlation. Thus we obtained the astrometry for every spectrum.

We compared the reconstructed image in the new coordinate system with stars from star catalogues (2MASS point source catalogue by Skrutskie et al. 2006, and the star catalogue constructed by Nishiyama et al. 2006). Thereby we found a systematic distortion along the slit direction by up to 6 pixels. We measured the positions of bright stars along the slit and computed the offset from the expected position as in the star catalogue. This deviation was modelled by a second order polynomial, and the data was resampled along the slit direction. After applying the distortion correction to all spectra, the mean offset of the position of bright

¹IRAF is distributed by the National Optical Astronomy Observatory, which is operated by the Association of Universities for Research in Astronomy (AURA) under cooperative agreement with the National Science Foundation.

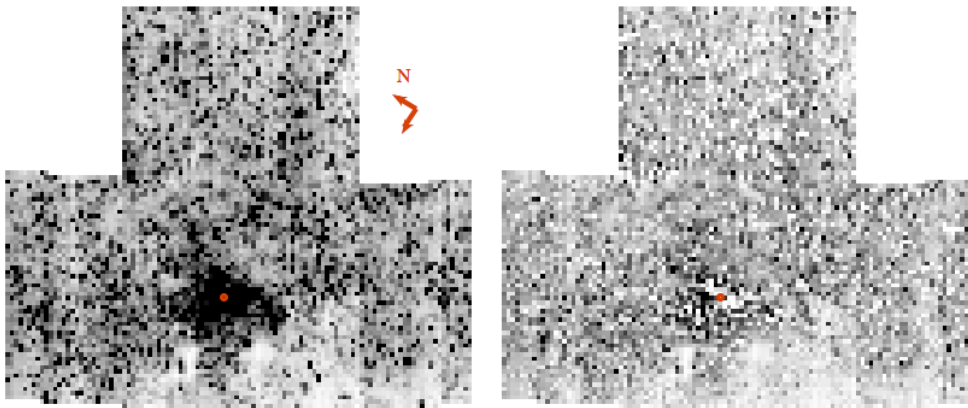


Figure 2.2: Reconstructed data cube from all central exposures, covering $\sim 240'' \times 210''$, flux summed over $2.29 - 2.365 \mu\text{m}$. The left panel uses all available data, i.e. the full data cube. The right panel is the data cube after removing foreground and background stars based on their colour, and stars brighter than $K_S = 11.5$ mag, i.e. the cleaned data cube. It contains only light from faint member stars. The red point denotes Sgr A*. The maps are oriented with the Galactic plane horizontally and Galactic North up and Galactic East left. The arrows indicate the orientation in the equatorial system. Both images are in the same linear flux scaling.

stars along the slit to the position of the star catalogue was reduced from 0.9 to 0.2 pixels, and we reran the cross correlation.

We could identify single bright stars in the unbinned data using the aforementioned catalogues. We selected all stars brighter than $K_S = 11.5$ mag within our observations and extracted their spectra. These stars are much brighter than the sun and thus mostly RGB and AGB stars. For comparison, a solar mass star has a K -band magnitude of $20 - 21$ mag at a distance of 8 kpc with an extinction of $A_{K_S} = 2 - 3$ mag. The position of the star along the slit and its FWHM were fitted with a Gaussian function. We extracted the spectrum within two times the FWHM². The median signal-to-noise ratio (S/N) for these spectra is 25, which is high enough to fit the kinematics.

To examine also the contribution of the fainter stars we constructed a single data cube by combining the spectra of the central field in the form of a “T”, which is roughly $240'' \times 210''$ (see Figs. 2.1 and 2.2). We determined a relative flux calibration factor for every sequence of subsequently taken spectra before putting the data set of the central field together. To calibrate the relative flux we used an IRSF/SIRIUS image in K_S -band (Nishiyama et al. 2006), and the reconstructed images with the flux between 2.29 and $2.365 \mu\text{m}$ summed up. We estimate the uncertainty for the relative flux calibration to be about 10 per cent.

To bin the data to one data cube, we summed up 15 ISAAC pixel rows along the slit, multiplied with the respective flux calibration factor, and obtained a final pixel size of $2''.22 \times 2''.22$. The cube extends over $\sim 240''$ along the Galactic plane and $\sim 210''$ in perpendicular

²These spectra are publicly available at the CDS.

direction. We used our ISAAC data to produce two separate data cubes: 1) A data cube with the full integrated light in each $2''.22 \times 2''.22$ pixel³. 2) A data cube with the brightest stars, foreground, and background stars removed. We will refer to these products as “full data cube” and “cleaned data cube”. The full data cube, integrated in wavelength direction, is shown on the left panel in Fig. 2.2. For the very centre we have multiple exposures, which were combined by taking the arithmetic mean. We also constructed a noise cube, containing the uncertainty of the persistence removal and sky subtraction.

To produce the cleaned data cube, we cut out stars from the unbinned data before setting up the $\sim 240'' \times 210''$ data cube. By cutting out the brightest stars ($K_S \leq 11.5$ mag, i.e. $K_{\text{cut}} = 11.5$ mag), we obtained light just from the underlying fainter population, reducing the effects of shot noise caused by single stars in our data cube. In addition to removing the brightest stars, we also used colour information to remove the fainter foreground and background stars. For this purpose we applied colour cuts and assumed that all stars with $H-K_S < 1.5$ mag or $H-K_S > 3.5$ mag are foreground or background stars, respectively. Our exclusion criterion is more inclusive than the one applied by Schödel et al. (2010), who excluded all stars with $H-K_S < 1.8$ mag or $H-K_S > 2.8$ mag. We removed foreground and background stars brighter than magnitude $K_S = 14$ mag. For stars fainter than $K_S = 14$ mag we cannot reliably determine their position along the slit and might misidentify a cluster member star. After fitting the position and FWHM of a star which we want to cut out, we set the pixel counts within one FWHM on either side of the position of the star to zero. The integrated light of the cleaned data cube is shown in Fig. 2.2 (right panel). Some of the pixels are empty and hence contain no information at all.

2.3.2 Deriving stellar kinematics

To derive stellar kinematics we fitted the line-of-sight-velocity distribution (LOSVD) of the CO absorption lines ($2.2902 - 2.365 \mu\text{m}$). These lines are most prominent in cool late-type stars with several Gyr age. Moreover, the CO lines are an excellent tracer of the stellar kinematics in the highly extinction affected Galactic centre region because the CO lines lie within the near-infrared K -band, where extinction is low enough to allow for sensitive observations. To obtain the LOSVD, we used the IDL routine `pPXF` (Cappellari & Emsellem 2004). It recovers the Gauss-Hermite parameters ($V, \sigma, h_3, h_4, \dots$) of the LOSVD by convolving template spectra with the parameterised LOSVD and finding the best fit to the observed spectrum in pixel space. We fitted only the first two moments of the LOSVD, the first moment corresponds to the velocity, the second moment to the velocity dispersion. As template spectra we used the high-resolution ($R \geq 45\,000$) spectra of Wallace & Hinkle (1996), which contain supergiant, giant, and dwarf star spectra in the spectral types from G to M. Those spectra were convolved with a Gaussian to obtain the same spectral resolution as our data set. The program `pPXF` finds an optimal template, which is a linear combination of the template spectra. The optimal template convolved with the LOSVD recovers the shape of the integrated light spectrum. Errors were calculated from Monte Carlo simulations. We added random

³This data cube is publicly available at the CDS.

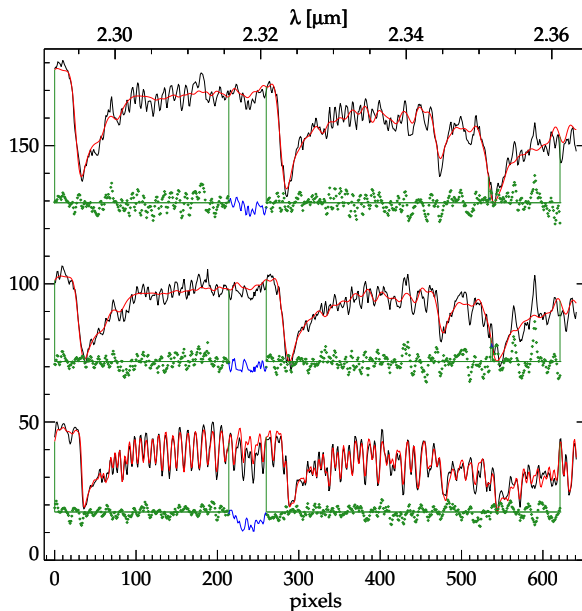


Figure 2.3: Example of CO absorption line spectra (black) of a Voronoi bin of the full data cube (upper spectrum), a Voronoi bin of the cleaned data cube (middle spectrum) and of a single star (lower spectrum). The red lines are the pPXF-fits to the data. The blue regions are not fitted, as there is a strong telluric absorption line in this wavelength region. Green dots are the residuals of the fits. The fluxes of the spectra are scaled for this plot.

noise to the spectra in each pixel and calculated the LOSVD in 100 runs. The fits were performed in the wavelength range of $2.2902 - 2.365 \mu\text{m}$, which contains four CO absorption lines, ^{12}CO (2-0), ^{12}CO (3-1), ^{13}CO (2-0), and ^{12}CO (4-2).

We used the two data cubes to obtain a velocity and velocity dispersion map of the integrated light. By applying adaptive spatial binning (Cappellari & Copin 2003) to our data we make sure that the integrated spectrum of every bin has approximately the same signal-to-noise ratio (S/N). Therefore we calculated the S/N for every single pixel of the data cubes with pPXF before the binning. We then summed the spectra of all pixels in a Voronoi bin to one integrated light spectrum per bin and fitted the LOSVD. Figure 2.3 shows three example spectra, and the respective fits. The upper spectrum is an integrated light spectrum from the full data cube, the middle spectrum is from the cleaned data cube, and the lower spectrum is from a single bright star. Figure 2.4 shows the velocity and velocity dispersion maps for a binning of at least $\text{S/N} = 60$ for the full data cube. One can see the rotation of the nuclear star cluster around Sgr A*, and an increase of the velocity dispersion up to $\sim 200 \text{ km}\cdot\text{s}^{-1}$. The bright supergiant star IRS 7 with apparent magnitude $K_S \approx 7.0 \text{ mag}$ (Schödel et al. 2013) dominates its bin, and the bin has therefore only low velocity dispersion. Figure 2.5 shows the kinematic maps for the data cube where single stars are cut out. It appears smoother and

less affected by shot noise. Some pixels contain no information at all after the bright stars and foreground stars were cut out, and those pixels are displayed in white.

To quantify the amount of shot noise in the cleaned data cube we produced two additional cleaned data cubes for which we vary the magnitude of the stars we cut out from $K_{\text{cut}} = 11.5$ mag to $K_{\text{cut}} = 11$ mag and $K_{\text{cut}} = 12$ mag. On these data cubes we applied the same Voronoi binning as on the cleaned data cube. The number of stars per bin in the data cube with $K_{\text{cut}} = 11$ mag increased by 1.85 on average, and decreased in the data cube with $K_{\text{cut}} = 12$ mag by 2.3 on average. We find that a variation of the magnitude cut by 0.5 mag has no strong influence on our results. In 75 per cent of all Voronoi bins the difference of the velocity measurements by varying K_{cut} by 0.5 mag is less than the velocity uncertainties. For only 5 per cent of all Voronoi bins the difference is more than two times the velocity uncertainties. The difference of the velocity measurements has a standard deviation of $8.2 \text{ km}\cdot\text{s}^{-1}$. There is also no systematic trend in the velocity dispersions obtained from the different cleaned data cubes. The difference of the velocity dispersions in the same bin from the different cleaned data cubes has a mean value of $0.7 \text{ km}\cdot\text{s}^{-1}$. We conclude that on average our measurements are robust and not severely influenced by shot noise.

We further estimated the shot noise in the velocity map obtained from the full data cube by a comparison of the total flux in each Voronoi bin with the flux given by a K -band luminosity function (KLF). Therefore we used the surface brightness profile from Section 2.5.1 scaled to the K -band. We calculated the total flux for each Voronoi bin by multiplying the surface brightness at a given bin with the respective area covered by the bin. The KLF tells us how many stars of a given magnitude are present in the nuclear star cluster. We used the KLF of Zoccali et al. (2003, their Table 3), which was measured in the Galactic bulge. However, Genzel et al. (2003) showed that the KLF of the central $9''$ of the Milky Way nuclear star cluster is very similar to the KLF measured by Zoccali et al. (2003). For a rough estimation of the number of stars we can therefore assume that a normalised KLF does not vary strongly over the entire field. We computed the integrated flux of the normalised KLF. Therefore we considered the KLF only for stars brighter than $K_S = 17$ mag, since this is the approximate magnitude limit for red clump stars, and fainter stars have rather weak CO absorption features. A comparison with the total flux of the Voronoi bins tells us that in each bin we expect at the least 740 stars and 5 500 stars on average. When we assume that the brightest star in a Voronoi bin has a magnitude of $K_S = 7.27$ mag, the fraction of light it would contribute to a Voronoi bin is 12 per cent on average, and 51 per cent in the worst case. The high light fraction of single stars indicates that shot noise can have a severe effect on results obtained from the full data cube.

According to the KLF, the stars fainter than $K_S = 11.5$ mag contribute 36 per cent of the total flux of the nuclear star cluster. So, in the Voronoi bins of the cleaned data cube the total flux is decreased to 36 per cent. We compared the remaining flux of a Voronoi bin of the cleaned data cube with the flux of a star with $K = 11.52$ mag. We found that a single star of $K_S = 11.52$ mag contributes at maximum 1.9 per cent of the remaining light of the Voronoi bin. This is significantly decreased compared to the maximum light fraction of 51 per cent of the full data cube. Even if all the light of the cleaned data cube would come from the brightest

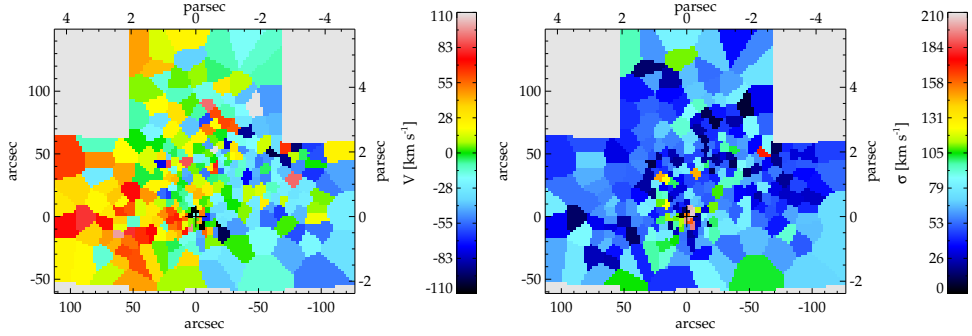


Figure 2.4: CO absorption line map of velocity, and velocity dispersion (left, and right, respectively) obtained by using the full data cube. Both, velocity and velocity dispersion are in units of $\text{km}\cdot\text{s}^{-1}$. The coordinates are centred on Sgr A* and along the Galactic plane with a position angle of $31^\circ:40$. The plus sign marks the position of Sgr A*. The velocity is in the local standard of rest, Galactic North is up, Galactic East is left.

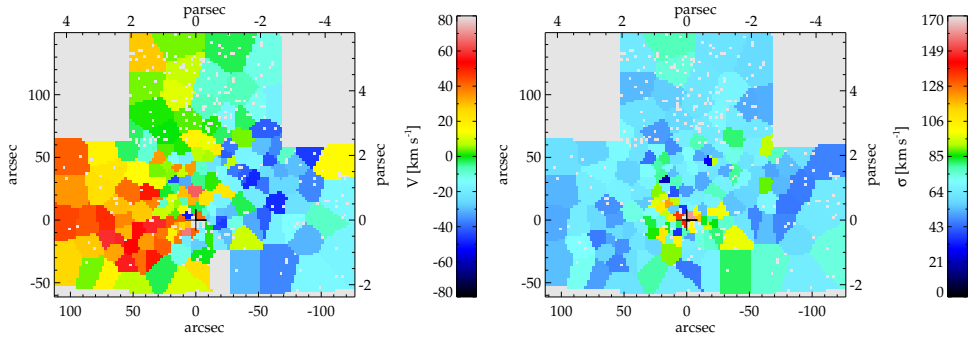


Figure 2.5: Same as Fig. 2.4, but for the cleaned data cube. White pixels mark regions where there was no signal left after cutting out stars.

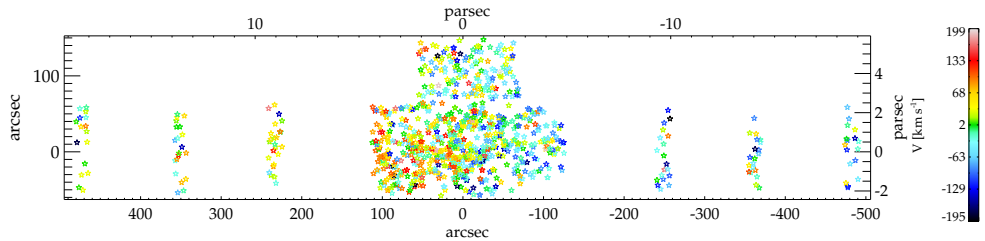


Figure 2.6: Velocity map of 1094 bright stars ($K_S \leq 11.5$ mag) with CO absorption lines in the colour interval $1.5 \text{ mag} \leq H - K_S \leq 3.5$ mag. We plot only stars with $S/N > 12$ and $|V| < 200 \text{ km}\cdot\text{s}^{-1}$.

stars with $K_S = 11.52$ mag, there would be on average 400 of these stars in each bin, and at the least 53 stars. This shows that the influence of a single star is significantly decreased in the cleaned data cube, and shot noise is no longer an issue.

We also fitted the LOSVD for each spectrum of the single bright stars with $K_S \leq 11.5$ mag. From these 1 375 spectra we found that $\sim 1\,200$ are from stars in the colour range $1.5 \text{ mag} \leq H - K_S \leq 3.5$ mag, suggesting their membership to the nuclear star cluster. Some of the spectra are from the same star, since we had overlapping exposures. The result for ten of these stars is shown in Table 2.1, the full Table is publicly available together with the spectra at the CDS. Figure 2.6 displays the velocity map of stars in the colour interval $1.5 \text{ mag} \leq H - K_S \leq 3.5$ mag. The mean velocity of our data set is consistent with zero, and the standard deviation is $74 \text{ km}\cdot\text{s}^{-1}$. The most extreme radial velocities we obtain are $-340.3 \pm 59.5 \text{ km}\cdot\text{s}^{-1}$ on the blue side, and $291.9 \pm 1.5 \text{ km}\cdot\text{s}^{-1}$ on the red side. We also see rotation in the same sense as the Galactic rotation.

To ensure the accuracy of our wavelength calibration and velocity determination, we compared our derived velocities to previous stellar velocity measurements. The cleanest comparison is for the bright supergiant IRS 7, where we find a velocity of $-116 \pm 1 \text{ km}\cdot\text{s}^{-1}$, in excellent agreement with the value from Reid et al. (2007, $-114 \pm 3 \text{ km}\cdot\text{s}^{-1}$). For other stars our low spatial resolution along the galactic plane creates possible issues with contamination in our data. Comparing stellar velocities derived from SiO masers by Deguchi et al. (2004), we find that four stars have $\Delta V \leq 6 \text{ km}\cdot\text{s}^{-1}$ (stars with names 3-6, 3-16, 3-5.2 and 16-49 in Deguchi et al. 2004). Two other stars have a $30 \text{ km}\cdot\text{s}^{-1}$ and $60 \text{ km}\cdot\text{s}^{-1}$ offset in velocity (stars with names 3-885 and 3-57 in Deguchi et al. 2004). These larger offsets could result from intrinsic changes in the velocities in pulsing AGB stellar atmospheres (Habing & Olofsson 2004), but for star 3-885 a misidentification is also possible. Overall, it appears that our absolute velocities are accurate to within approximately $5 \text{ km}\cdot\text{s}^{-1}$.

The large field of view results in the radial direction not being constant over the entire field and the proper motion of the sun with respect to the Galactic centre has to be taken into account. We tested the amplitude of this so-called perspective rotation using Equation 6 of van de Ven et al. (2006). Assuming that the sun moves with $v_x = 220 \text{ km}\cdot\text{s}^{-1}$ in the Galactic plane (Chaisson & McMillan 1993) at a distance of 8 kpc from the centre, and with $v_y = 7 \text{ km}\cdot\text{s}^{-1}$ towards the Galactic North, we find that this effect is negligible perpendicular to the Galactic plane. Along the Galactic plane the perspective rotation is $\lesssim 0.13 \text{ km}\cdot\text{s}^{-1}$ for the central field. For the outermost fields at $8'$ distance from the centre, it is $0.5 \text{ km}\cdot\text{s}^{-1}$. This is less than the usual velocity uncertainty we obtain. Nevertheless, we corrected the velocities of the six outer fields shown in Fig. 2.6 for perspective rotation.

Table 2.1: Table of stars with coordinates RA and Dec, K_S - and H -band magnitude according to the source catalogue, measured line-of-sight velocity V , CO index CO_{mag} and signal-to-noise ratio S/N. We only reproduce 13 lines of this table here. A full table with the spectra is available in electronic form at the CDS.

ID	RA [$^{\circ}$]	Dec [$^{\circ}$]	K_S [mag]	H [mag]	source catalogue	V [$\text{km} \cdot \text{s}^{-1}$]	CO_{mag}	S/N
1	266.44606	-28.99290	11.24	13.50	SIRIUS	86.7 ± 1.6	0.31	21.1
2	266.44566	-28.99287	9.73	11.28	2MASS	80.9 ± 1.5	0.45	18.9
3	266.44671	-28.99027	11.02	14.12	SIRIUS	26.3 ± 3.6	0.40	18.7
4	266.44510	-28.99095	10.54	12.13	2MASS	-55.5 ± 0.2	0.48	22.4
5	266.44680	-28.98703	10.82	12.28	2MASS	34.9 ± 2.5	0.39	22.9
6	266.44453	-28.98938	11.48	14.13	SIRIUS	-4.9 ± 1.2	0.26	22.9
7	266.44371	-28.99045	10.32	11.91	2MASS	77.4 ± 1.8	0.40	17.9
8	266.44243	-28.99068	11.33	13.71	SIRIUS	63.3 ± 0.3	0.39	21.9
9	266.44301	-28.98553	10.44	13.40	SIRIUS	93.0 ± 1.0	0.30	16.2
10	266.44122	-28.98636	9.34	11.21	2MASS	-38.9 ± 0.7	0.51	20.2
high velocity stars								
521	266.41859	-29.00958	8.66	11.06	SIRIUS	-340.3 ± 59.5^a	0.07	16.7
1042	266.37746	-28.99331	11.41	13.35	SIRIUS	291.9 ± 1.5	0.20	22.2
1056	266.39317	-29.01596	10.14	11.87	2MASS	-265.6 ± 0.5	0.11	45.2

Notes. (a) The high uncertainty is caused by the limited wavelength range. In this spectrum there is no continuum on the blue side of the CO absorption line. However, this star is known as IRS 9 and its velocity was measured by Zhu et al. (2008) to $-347.8 \text{ km} \cdot \text{s}^{-1}$.

2.3.3 Line strength measurements

With our data set we can give a rough age estimation of bright stars. We use the fact that CO absorption lines are prominent in old stars, but not in young, hot stars. To quantify the depth of the CO line, we used the CO index CO_{mag} in a colour-like way as defined by Kleinmann & Hall (1986)

$$CO_{\text{mag}} = -2.5 \log \frac{F_a}{F_c}, \quad (2.1)$$

where F_a is the mean flux at the first CO absorption line (2.2931 – 2.2983 μm), and F_c is the mean flux at the continuum (2.2885 – 2.2925 μm), corrected for radial velocity shifts. This is not the same continuum wavelength region as defined in Kleinmann & Hall (1986), which is at shorter wavelengths. As we are very limited in our spectral range, we had to modify the CO index definition. To calibrate our CO_{mag} with a temperature, we used the IRTF Spectral Library (Rayner et al. 2009). The metallicities of both the stars in the library and in the Milky Way nuclear star cluster are near-solar (Cunha et al. 2007; Pfuhl et al. 2011). We computed CO_{mag} for giants and supergiants, with the spectral class ranging from F0 to M6. Lang (1992) lists the temperature of stars depending on the spectral class and type. The relation between effective temperature T_{eff} and CO_{mag} is shown in Fig. 2.7. We found that for stars with a temperature $T_{\text{eff}} > 4800$ K, the CO_{mag} is less than 0.09. Using Padova isochrones for solar metallicity stars with $M_K \leq -3$ mag (which corresponds to $K_S \leq 11.5$ mag in the Galactic centre), we found that stars hotter than 4800 K are younger than approximately 300 Myr. Therefore we conclude that stars with $CO_{\text{mag}} < 0.09$ are younger than 300 Myr. Also for higher values of CO_{mag} , the CO index correlates roughly with the age of the stars.

2.4 Stellar kinematics and population results

2.4.1 Kinematic structure and substructure of the nuclear star cluster

In this section we show that the overall rotation of the Milky Way nuclear star cluster is misaligned by $\sim 9^\circ \pm 3^\circ$ counterclockwise from the major axis of the galaxy at radii from 1 to 4 pc. Furthermore, we find evidence for one cold rotating substructure within the central parsec.

We modelled the stellar kinematics of the velocity maps using `KINOMETRY`, which was developed by Krajnović et al. (2006). `KINOMETRY` assumes that the velocity profile along an ellipse around the centre can be expressed by a simple cosine law. The IDL routine written by Krajnović et al. (2006) divides the velocity map into individual elliptical rings, which are described by harmonic terms. The best fitting ellipse depends on two parameters, the kinematic position angle PA_{kin} , and kinematic axial ratio $q_{\text{kin}} (= 1 - \varepsilon_{\text{kin}})$. By default q_{kin} is constrained to the interval $[0.1, 1]$, while we let PA_{kin} unconstrained.

The result of the kinematic analysis of the velocity map from the cleaned data cube (Fig. 2.5) is listed in Table 2.2, and the left panel of Fig. 2.8 shows the kinometry model velocity map. The Voronoi bin with the highest uncertainty was excluded from the model. From

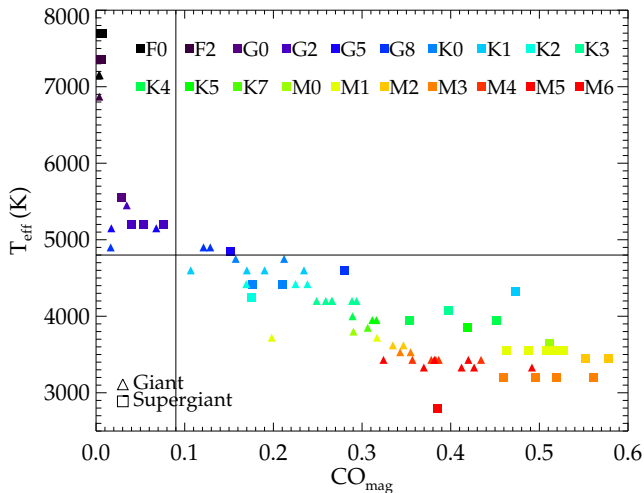


Figure 2.7: Relationship between effective temperature T_{eff} in K and the CO index CO_{mag} for giant (triangle symbol) and supergiant (square symbol) stars of the IRTF Spectral Library (Rayner et al. 2009). Different colours denote a different spectral type. The black horizontal line marks 4800 K, the black vertical line marks $CO_{\text{mag}} = 0.09$

the axial ratio one can distinguish three families of ellipses. The three innermost ellipses form the first family, the next seven ellipses the second family, and the outermost five ellipses the third family.

For the two outer families the kinematic position angle PA_{kin} is $4 - 15^\circ$ Galactic east of north, with a median value of 9° . However, the photometric position angle PA_{phot} was measured by Schödel et al. (2014a) using *Spitzer* data to $\sim 0^\circ$. This means that there is an offset between PA_{phot} and PA_{kin} . To test whether this offset could be caused by extinction from the 20-km-s $^{-1}$ -cloud (M-0.13-0.08, e.g. García-Marín et al. 2011) in the Galactic southwest, we flagged all bins in the lower right corner as bad pixels and repeated the analysis, but the position angle offset remained. We tested the effect of Voronoi binning by running kinemetry on a velocity map with $S/N = 80$. While the values of q_{kin} for the second family are by up to a factor two higher with this binning, the PA_{kin} fit is rather robust. We obtained a median value for PA_{kin} of 12.6 beyond a semi-major axis distance of $r \sim 40''$. We conclude that the effect of the binning can vary the value of the PA_{kin} , but the PA offset from the Galactic plane is robust to possible dust extinction and binning effects. Also our cleaning of bright stars and foreground stars may cause a bias in the PA_{kin} measurements. For comparison we ran the kinemetry on the velocity map of the full data cube (Fig. 2.4). In this case there is higher scattering in the kinematic parameters, caused by shot noise. However, beyond $35''$ semi-major axis distance the median PA_{kin} is at 6.1 , i.e. the PA offset is retained. This smaller value could come from the contribution of foreground stars, which are aligned along the Galactic

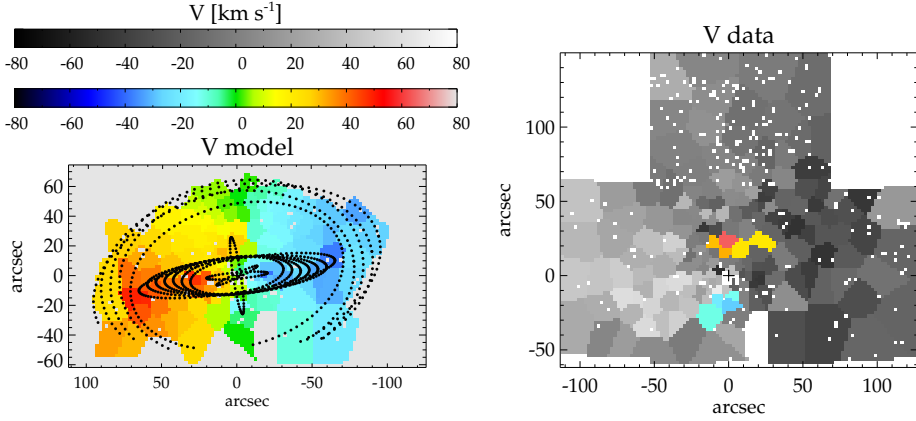


Figure 2.8: Left panel: Kinematic model velocity map of the cleaned data cube. Black dots denote the best fitting ellipses. The model goes only to $r \sim 100''$ along the Galactic plane and to $\sim 60''$ perpendicular to it. Right panel: The velocity map as in Fig. 2.5 shown in grayscale, the bins that show rotation perpendicular to the Galactic plane are overplotted in colour scale.

plane. It could also mean that bright stars are not as misaligned to the photometric major axis as fainter stars are. Young stars tend to be brighter, thus the integrated light likely samples an older population than the individual stars. Analysis of the resolved stars in the colour interval $1.5 \text{ mag} \leq H - K_S \leq 3.5 \text{ mag}$ and in the radial range of $50''$ to $100''$ shows an offset in the rotation from the Galactic plane by $2^\circ.7 \pm 3^\circ.8$. As previous studies focused on the brightest stars of the cluster, the PA offset of the old, faint population remained undetected.

In the innermost family there is one ellipse with a position angle of $-81^\circ.5$, i.e. PA_{kin} is almost perpendicular to the photometric position angle $\text{PA}_{\text{phot}} \approx 0^\circ$. This is caused by a substructure at $\sim 20''$ north and south of Sgr A*, that seems to rotate on an axis perpendicular to the Galactic major axis. This feature is highlighted in the right panel of Fig. 2.8. North of Sgr A* we find bins with velocities of 20 to 60 $\text{km}\cdot\text{s}^{-1}$, while in the Galactic south bins with negative velocities around -10 to $-30 \text{ km}\cdot\text{s}^{-1}$ are present. The feature expands over several Voronoi bins north and south of Sgr A*. It extends over $\sim 35''$ (1.4 pc) along the Galactic plane, and $\sim 30''$ (1.2 pc) perpendicular to it.

This substructure also causes the small axial ratio values of the second family of ellipses between $30''$ and $70''$ in our kinematic model. All semi-minor axis distances from Sgr A* are below $20''$, i.e. at smaller distances to Sgr A* than the perpendicular substructure. Only the third family of ellipses, which has semi-major axis values above $70''$, skips over this substructure and reaches higher values of q_{kin} .

To check if the perpendicular rotating substructure is real, we applied Voronoi binning with a higher S/N of 80 instead of 60, and obtained again this almost symmetric north-south structure. Also with a lower S/N of 50, the substructure appeared in both data cubes. We also checked the influence of the cleaning from bright stars on this feature using the cleaned

Table 2.2: Result of the kinematic analysis of the cleaned data cube velocity map. The columns denote the semi-major axis distance r in arcsec of the best fitting ellipses to Sgr A*, the kinematic position angle PA_{kin} in degrees, the kinematic axial ratio q_{kin} , and the rotation velocity V_{rot} in $\text{km}\cdot\text{s}^{-1}$. The position angle is defined such that 0° corresponds to rotation around the Galactic North-South direction.

r [arcsec]	PA_{kin} [$^\circ$]	q_{kin}	V_{rot} [$\text{km}\cdot\text{s}^{-1}$]
15.0	25.2 ± 1.4	0.10 ± 0.00	30.5 ± 1.4
20.5	4.9 ± 2.0	0.10 ± 0.00	43.9 ± 1.1
26.1	-81.5 ± 1.3	0.10 ± 0.00	24.1 ± 1.4
31.7	9.1 ± 1.3	0.37 ± 0.01	38.5 ± 1.1
37.3	6.7 ± 1.2	0.34 ± 0.01	31.5 ± 0.9
43.1	4.4 ± 1.0	0.29 ± 0.01	32.2 ± 0.7
48.9	4.8 ± 1.0	0.25 ± 0.01	35.5 ± 0.6
54.7	4.8 ± 1.1	0.22 ± 0.01	37.4 ± 0.5
60.7	5.9 ± 1.0	0.20 ± 0.01	40.8 ± 0.5
66.8	9.0 ± 1.5	0.17 ± 0.02	46.8 ± 0.5
73.0	14.5 ± 0.5	0.65 ± 0.01	37.1 ± 0.6
79.3	7.0 ± 1.0	0.72 ± 0.02	29.7 ± 0.7
85.7	10.5 ± 1.1	0.74 ± 0.01	27.5 ± 0.8
92.3	10.2 ± 1.3	0.66 ± 0.01	32.1 ± 0.9
99.0	15.6 ± 1.1	0.57 ± 0.01	35.8 ± 0.9

maps with $K_{\text{cut}} = 11$ mag and $K_{\text{cut}} = 12$ mag. The substructure remained also in these data cubes, independent of the applied binning. The fact that this feature persists independent on the applied magnitude cut, or binning, and that it extends over several bins, indicates that the observed kinematic structure is not caused by shot noise of individual stars.

We ran a Monte Carlo simulation to test if shot noise can mimic the observed substructure. We did this in 1 000 runs by adding random velocities to a smooth velocity map and running KINEMETRY on the simulated velocity maps. Then we tested if there are substructures in the simulated velocity maps. First, we constructed a smooth velocity map using KINEMETRY on the velocity map of the cleaned data cube. By constraining the PA_{kin} to the interval $[-25^\circ, 25^\circ]$ we obtained a velocity map without any substructures. To this smooth velocity map we added random velocities drawn from a normal distribution with a mean velocity of $0 \text{ km}\cdot\text{s}^{-1}$, and a standard deviation of $\sigma = 8.2 \text{ km}\cdot\text{s}^{-1}$. The value of $\sigma = 8.2 \text{ km}\cdot\text{s}^{-1}$ is a measure for the shot noise (see Section 2.3.2). On 1 000 simulated velocity maps we ran KINEMETRY models. Then we analysed if there are substructures in the simulated velocity maps. A substructure has to fulfil the following criteria: 1.) In the Kinemetry model there is an ellipse with a PA_{kin} that deviates by more than 45° from the median of the other PA_{kin} in this run; 2.) The velocity of this ellipse V_{rot} is greater than $8.2 \text{ km}\cdot\text{s}^{-1}$. Our Monte Carlo simulation reveals that in 1,000 simulated velocity maps only 9.1 per cent have such a substructure. Only 0.2 per cent have a substructure with $V_{\text{rot}} > 20 \text{ km}\cdot\text{s}^{-1}$, which is comparable to the value of $V_{\text{rot}} = 24.1 \text{ km}\cdot\text{s}^{-1}$ we find in the ISAAC data (see Table 2.2). We conclude that the feature is significant at 99.8 per cent and it is unlikely that a statistical fluctuation can mimic a kinematic substructure in our data.

We do not find a velocity substructure for the single bright stars as seen in the integrated light. In both the northern and the southern region, the median velocities are $\sim 3 \text{ km}\cdot\text{s}^{-1}$, i.e. consistent with zero. We note that the bright stars likely represent different stellar populations than the unresolved light. The bright stars are dominated by younger populations with supergiants and AGB stars, while the unresolved light is dominated by older populations, where supergiants and AGB stars are rare. Thus this substructure, if real, would likely have an older stellar population. We discuss this discovery in more detail in Section 2.6.1.

The rotation velocity obtained by the KINEMETRY model is at median values of $\sim 33 \text{ km}\cdot\text{s}^{-1}$ for all different tested data cubes and binnings. The exact shape of the curve however depends on the fitted ellipse axial ratios, which varies with the binning of the velocity map.

2.4.2 Specific angular momentum λ_R

Emsellem et al. (2007) introduced the specific angular momentum λ_R to classify early-type galaxies in slow and fast rotators. This is a more robust classification criterion than the relation V/σ_e . We calculated the quantity λ_R for the first time for a nuclear star cluster. λ_R is a dimensionless parameter that quantifies the observed projected stellar angular momentum per unit mass. To compute λ_R we used the two-dimensional spatial information from the kinematic maps, weighted by the luminosity. Slow rotators have values of $\lambda_R < 0.1$ within

their effective radius r_{eff} , while fast rotators have values above 0.1. We calculated λ_R using Equation 6 of Emsellem et al. (2007):

$$\lambda_R = \frac{\sum_{i=1}^{N_p} F_i R_i |V_i|}{\sum_{i=1}^{N_p} F_i R_i \sqrt{V_i^2 + \sigma_i^2}} \quad (2.2)$$

Here i runs over all pixels of the data cube, F_i is the flux in the i -th pixel, R_i is its distance to Sgr A*, V_i and σ_i are the velocity and velocity dispersion in the pixel. To compute λ_R we used the SIRIUS image and transformed it to the same pixel size and astrometry as the data cubes for luminosity weighting. We used the kinematic maps from the cleaned data cube, and summed within ellipses with ellipticity $\varepsilon = 0.29$. This is the photometric ellipticity found by Schödel et al. (2014a) in *Spitzer* mid-infrared data. The resulting λ_R profile is shown in Fig. 2.9, where r is the mean radius of the ellipses, and $r_{\text{eff}} = 4.2$ pc (110'', Schödel et al. 2014a). Assuming a smaller value for ε decreases λ_R and the slope of λ_R , but even with $\varepsilon = 0$, we obtain $\lambda_R > 0.2$ for all radii.

The specific angular momentum is used to classify galaxies as fast and slow rotators. Emsellem et al. (2011) found that fast rotators have $\lambda_R > k_{FS} \times \sqrt{\varepsilon}$, where k_{FS} is a scaling parameter. k_{FS} is 0.31 when using λ_{R_e} , i.e. λ_R at one effective radius r_{eff} . This means a value of $\lambda_{R_e} > 0.16$ would be expected for a fast rotator with an ellipticity of 0.29. For the Milky Way nuclear star cluster r_{eff} is ~ 4.2 pc (Schödel et al. 2014a). At our outermost ellipse radius of 3.5 pc we obtain $\lambda_R \approx 0.36$ with $\varepsilon = 0.29$. So the Milky Way nuclear star cluster has similar rotational support as fast rotating elliptical galaxies have. A comparison with Fig. 5 of Emsellem et al. (2007) shows that λ_{R_e} is below the value expected for an isotropic oblate rotator. This suggests that the Milky Way nuclear star cluster has anisotropic kinematics at large radii.

2.4.3 Radial profiles

In this section we study the kinematics of the nuclear star cluster by applying different binnings to the data cubes and compute profiles. We investigate the rotation curve and compare our findings to previous results.

When we plot the projected distance of each Voronoi bin from Sgr A* along the Galactic plane against the velocity of each bin, we obtain a position-velocity diagram, which is shown in Fig. 2.10 for both data cubes. From the data cube containing only faint member stars (red circle points), we deduce that the maximum rotation velocity is about $50 \text{ km}\cdot\text{s}^{-1}$. For the outer fields, the rotation is flatter. Only one of the six data points has a velocity higher than $36 \text{ km}\cdot\text{s}^{-1}$.

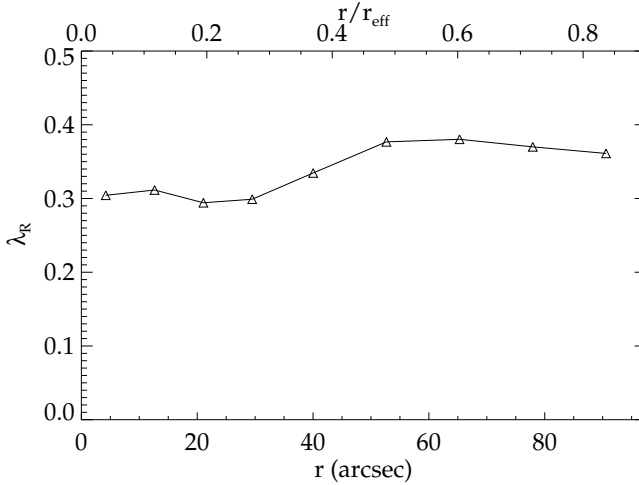


Figure 2.9: The specific angular momentum λ_R profile calculated in ellipses with ellipticity $\varepsilon = 0.29$ (Schödel et al. 2014a), and plotted against the mean radius of the ellipses. The upper x-axis of the plot displays the ratio of r/r_{eff} , where r_{eff} is the effective radius ($r_{\text{eff}} = 4.2$ pc, Schödel et al. 2014a).

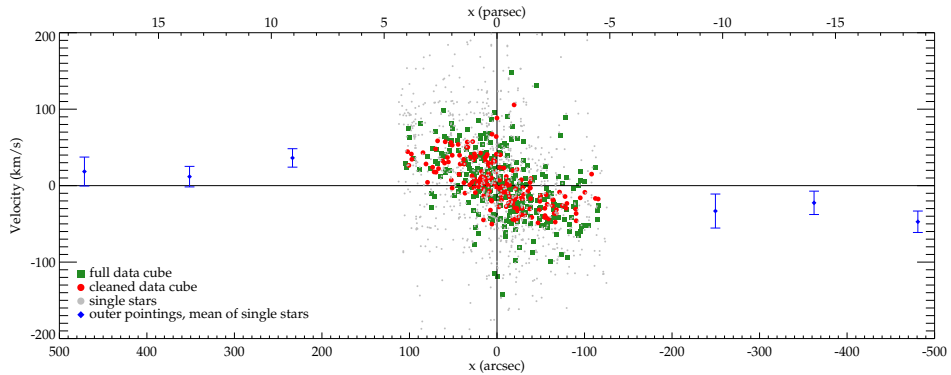


Figure 2.10: Position-velocity diagram along the Galactic plane for the velocity maps of Fig. 2.4 and 2.5. Results from our full ISAAC data cube are shown as green rectangles, red circles show the result from the cleaned data cube, which contains only faint cluster member stars. Grey dots denote velocity measurements from single stars, the blue diamonds are the mean velocities of the bright stars at the outer fields, corrected for perspective rotation.

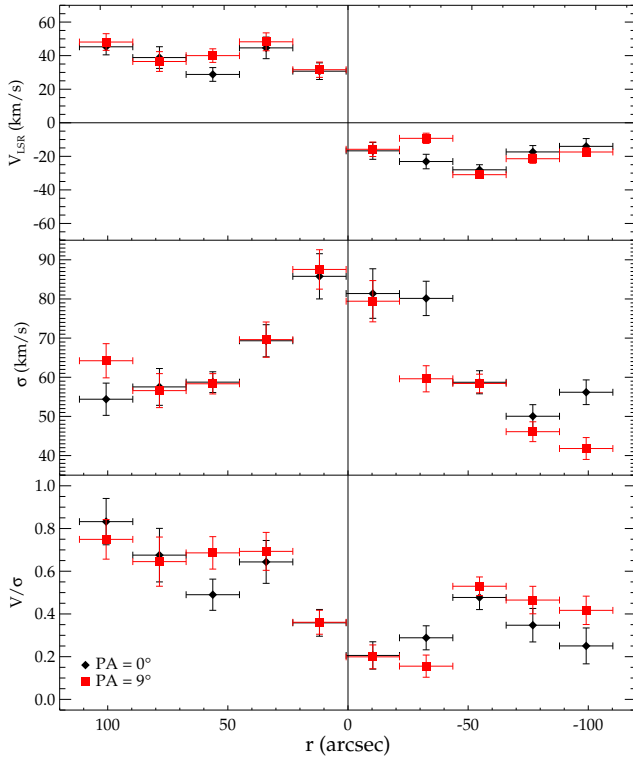


Figure 2.11: Velocity profile, velocity dispersion σ , and V/σ for a $22''$ broad slit along the Galactic plane from the cleaned data cube (black diamonds), and for a slit tilted by 9° counterclockwise with respect to the Galactic plane (red square symbols).

For further analysis we did not use the Voronoi binned velocity maps of Fig. 2.4 and 2.5, but directly binned the data cubes in major axis bins and radial annuli. In order to derive the kinematics along the photometric major axis only, we binned the cleaned data cube in rectangles, which extend over $\sim 22''$ perpendicular to the Galactic plane, i.e. $\sim 11''$ towards the Galactic North and South of Sgr A*. Each rectangle is $22''$ broad in Galactic east-west direction. This resembles a slit along the Galactic plane, centred on Sgr A* that is $22''$ wide. We summed the spectra in the rectangular bins and fitted the CO absorption lines with rPXF . The resulting velocity and velocity dispersion profiles are shown in Fig. 2.11 as black diamonds, together with the V/σ profile. Alternatively we rotated the slit axis by 9° , which is our median kinematic position angle offset found in Section 2.4.1, and applied a similar binning. The result is shown as red square symbols in Fig. 2.11.

We obtained a rotation curve with an amplitude of $\sim 40 \text{ km}\cdot\text{s}^{-1}$. As expected, the absolute velocity values are generally higher using the tilted slit than using a slit along the Galactic plane. Further, the absolute velocities are higher on the eastern side than on the western

Table 2.3: Profile of the root-mean-square velocity V_{rms} as shown in Fig. 2.12. r is the distance from Sgr A* in arcsec, V_{rms} values are in $\text{km}\cdot\text{s}^{-1}$.

r [arcsec]	V_{rms} [$\text{km}\cdot\text{s}^{-1}$] full data cube	V_{rms} [$\text{km}\cdot\text{s}^{-1}$] cleaned data cube
1.5	179 ± 20	166 ± 20
4.0	14 ± 2	136 ± 21
7.5	105 ± 8	98 ± 10
12.5	78 ± 4	73 ± 5
20.0	78 ± 3	84 ± 4
32.5	78 ± 4	71 ± 3
62.5	65 ± 2	67 ± 3
77.5	65 ± 2	62 ± 3
92.5	69 ± 2	67 ± 3
107.5	69 ± 2	61 ± 3
122.5	71 ± 3	69 ± 5
255	75 ± 3	58 ± 4
355	49 ± 4	77 ± 5
455	78 ± 3	74 ± 4
	single stars	
241	87 ± 9	
357	67 ± 7	
455	79 ± 9	

side by more than $10 \text{ km}\cdot\text{s}^{-1}$. The velocity dispersion rises only to $\sim 90 \text{ km}\cdot\text{s}^{-1}$. This can be explained by the fact that the velocity dispersion map (Fig. 2.5) has values higher than $100 \text{ km}\cdot\text{s}^{-1}$ only in few small bins in the very centre ($r \lesssim 10''$). The V/σ has a minimum close to the centre, where the velocity dispersion is highest, and higher values at larger radii. At outer radii ($r > 50'' \approx 2 \text{ pc}$), closer to the effective radius, we obtain $V/\sigma \approx 0.6$. The value of V/σ at the Galactic West is smaller than at the Galactic East, as also the absolute values of the velocities are lower.

We also computed a velocity dispersion profile within circular bins around Sgr A*. The spectra in each bin were summed up and we computed the LOSVD with pPXF. The second moment is then the root-mean-square velocity, $V_{\text{rms}} = \sqrt{V^2 + \sigma^2}$. The result is shown in Fig. 2.12 and listed in Table 2.3, the outermost data points are from our outer fields. Green rectangles denote the result from the full data cube, red circle points from the cleaned data cube. The difference between the two data cubes is mostly within the measurement uncertainties. The largest differences occur due to contamination of IRS 7 in the bin at $4''$ and another

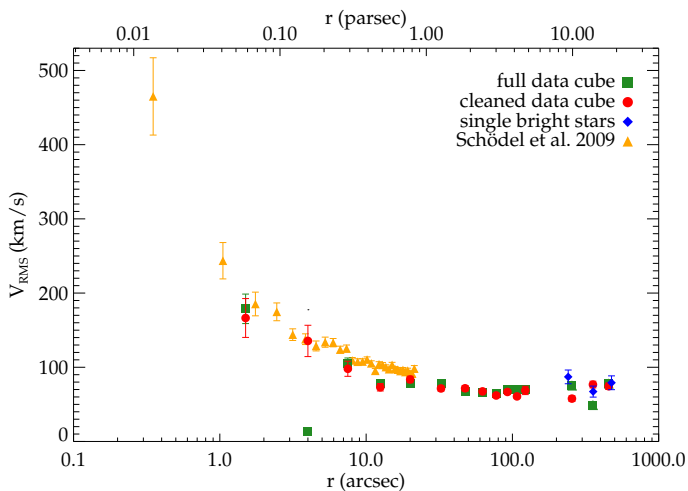


Figure 2.12: Velocity dispersion profile, obtained using circular bins around Sgr A*. The green rectangles are the data points from the full data cube, red circle points from the cleaned data cube. The large discrepancy at $r \sim 4''$ is due to the influence of the star IRS 7 on the green point. Blue diamonds are obtained from single bright stars in the outer fields. Orange triangles are proper motion data from Schödel et al. (2009).

bright star at a radius of $360''$. Most stars in the centre of the nuclear star cluster are young and do not show strong CO absorption lines that we use for our kinematic measurements. This means that the velocity dispersion we measure for the central points comes mostly from stars that lie only in projection close to Sgr A*, and the velocity dispersion at $r \lesssim 8''$ is a lower limit (Sellgren et al. 1990; Haller et al. 1996).

The surface brightness at the outer fields is lower than in the central field. After cleaning the data from bright stars and foreground stars, the S/N of the outer fields is rather low. On the other hand, bright stars can severely effect the result from the full data in the outer fields. Therefore we computed V_{rms} as a third approach from the bright stars we cut out, corrected for perspective rotation (see Section 2.3.2). This has the advantage that all stars have the same weight, irrespective of their magnitude. The results from the three approaches agree quite well at $8'$; at $4'$ and $6'$ there is more scattering.

For the central $20''$ we also plot the proper motion data of Schödel et al. (2009) for comparison (orange triangles). To extract these data along a radial profile we made circular bins around Sgr A*. Then we computed the mean velocity and velocity dispersion of each bin using a maximum likelihood approach described in Pryor & Meylan (1993). In contrast to computing the mean and standard deviation of the data, this method takes the different uncertainties for the velocity measurements into account. We used the velocities perpendicular and parallel to the Galactic plane. Each bin contains at least 21 stars. We found that the velocity dispersion perpendicular to the Galactic plane σ_b is in better agreement with our LOSVD

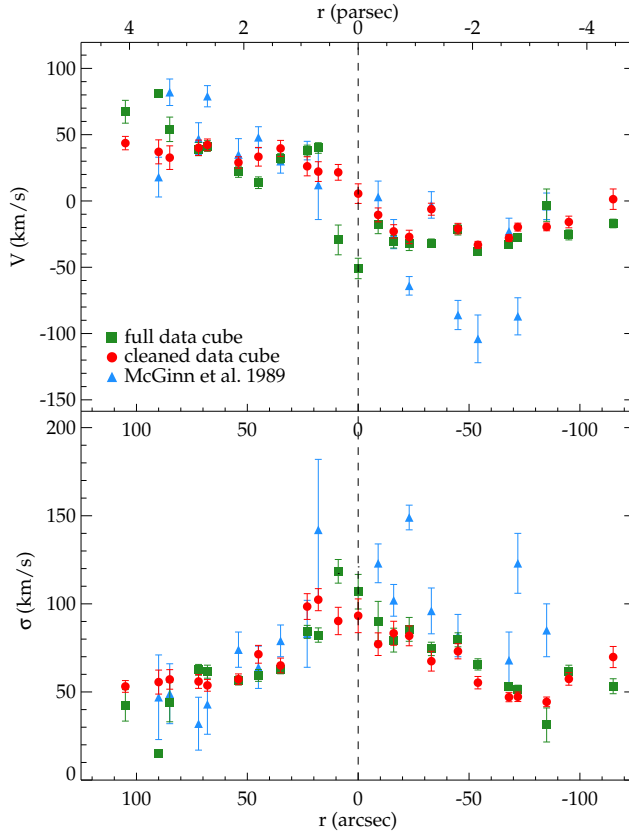


Figure 2.13: Velocity (upper panel) and velocity dispersion profile (lower panel) along the major axis, with IRS 16 as the centre. We applied the binning of McGinn et al. 1989 (blue), extended by five additional binning apertures. Results from our full ISAAC data cube are shown as green rectangles, red circles show the result from the cleaned data cube, and blue triangles denote the data from McGinn et al. (1989).

data than the velocity dispersion parallel to the Galactic plane σ_l . Parallel to the Galactic plane the velocity dispersion is higher than perpendicular to it (see Fig. 6 of Schödel et al. 2009).

The only previous observations of the Galactic centre in integrated light are from McGinn et al. (1989). They had a circular aperture of $20''$ diameter, and measured velocity and velocity dispersion profiles along the major axis (McGinn et al. 1989, Figs. 1, 4, and 5) using the first CO band head. To compare our work with these early results, we binned our data cube in exactly the same way as McGinn et al. (1989). As centre we used IRS 16C ($\alpha = 266^\circ.41705$, $\delta = -29^\circ.007826$, Henry et al. 1984), as McGinn et al. (1989) did. We applied four additional binnings which were not covered by McGinn et al. (1989). The resulting profiles are displayed in Fig. 2.13, where the upper panel is the velocity V , and the lower panel is the velocity dispersion σ , both in $\text{km}\cdot\text{s}^{-1}$. The profiles from the cleaned data cube appear smoother than the profiles from the full data cube, as the data is less affected by shot noise of dominant bright stars which can produce outliers. One such example is the bright supergiant IRS 7. This star has a big effect on the integrated spectrum in the bins centred at $r = -9''$ and $0''$. Cutting out only the star IRS 7 from the data cube containing all stars decreases the velocity measurement by more than $30\text{ km}\cdot\text{s}^{-1}$, while the velocity dispersion changes by only $\sim 14\text{ km}\cdot\text{s}^{-1}$. Using smaller apertures, this single bright star can affect the results even more. The data of McGinn et al. (1989) has more outliers and extreme velocity variations than our data, especially to the western side of Sgr A*. Schödel et al. (2009) suggested that the data of McGinn et al. (1989) may sample two different stellar populations at different depth. Then their data could hint at two distinct rotating systems in the nuclear star cluster. Our data does not confirm this large scatter in the velocity and velocity dispersion, and the profiles have a rather smooth shape. Four velocity measurements of McGinn et al. (1989) on the western side of Sgr A* have significantly higher absolute values than our data has, while the other five measurements agree with our data. They confirm that the absolute values of the velocities on the western side are lower than on the eastern side of Sgr A*. On the western side the extinction is higher than on the eastern side.

2.4.4 Distribution of young stars

We computed the CO index CO_{mag} for our sample of bright stars as defined in Section 2.3.3. Figure 2.14 shows the distribution of the CO index for all bright member stars. The value of CO_{mag} roughly correlates with the age of the stars, this means that blue data points denote stars that are more likely to be younger than stars shown in red colours. Blue filled star symbols denote stars with $CO_{\text{mag}} < 0.09$, indicating stars younger than 300 Myr. We note that the presence of foreground extinction would mean the stars we are sampling are even brighter and thus younger. Most of the 26 young stars are within 1 pc of the nuclear star cluster, confirming previous studies. For example, five of our stars lie within $0'.3$ distance of stars listed by Paumard et al. (2006). A comparison with the young star candidates of Nishiyama & Schödel (2013) results in seven matches. One of those matches has no counterpart in any previous spectroscopic study yet. Its colour in $H - K_S = 1.5$ mag, which is at our limit for

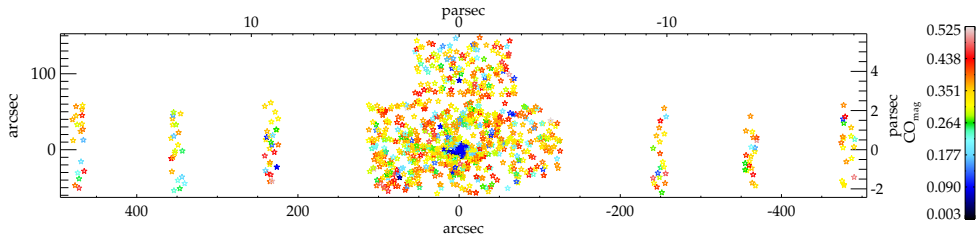


Figure 2.14: CO index map of 1153 bright stars ($K_S \leq 11.5$ mag) with $S/N > 12$. Filled blue star symbols denote stars with $CO_{\text{mag}} < 0.09$, which are younger than 300 Myr.

foreground stars. At greater distance from Sgr A*, there are only few stars with $CO_{\text{mag}} < 0.09$, and none at our outer fields at $360''$ and $480''$. But as the covered area beyond $350''$ is only about 2.1 arcmin^2 , we might simply miss the young stars.

It is possible that the young star candidates are foreground stars, although their colours in $H - K_S$ are at least 1.5 mag, and for 20 of the stars even more than 2.1 mag. The intrinsic $H - K_S$ colour for O to A type stars is about -0.1 to 0.05 (Straizys & Lazauskaitė 2009), therefore the measured colour is almost entirely caused by extinction. Schödel et al. (2010) and Fritz et al. (2011) found mean extinction values of $A_H = 4.21$ mag to 4.48 mag and $A_{K_S} = 2.42$ mag to 2.74 mag in the central region of the Galaxy. Extinction varies on arcsecond scale with a standard deviation of 0.3 mag in A_{K_S} (Schödel et al. 2010). Thus the measured colours are consistent with these stars being located in the Galactic center.

One problem of our limited spectral range is that stars with low velocities $< -250 \text{ km-s}^{-1}$ can be misidentified as a star with a low CO index. We found three such stars, which are not included in our sample of young star candidates. Observations with larger spectral range are necessary to confirm the spectral type of these stars and give a better estimation of their age.

2.5 Dynamical modelling

To measure the mass of the Milky Way nuclear star cluster and black hole we dynamically model our kinematic data. We apply axisymmetric Jeans models (Jeans 1922) to our kinematic data. We use the IDL program package JEANS ANISOTROPIC MGE DYNAMICAL MODELS (JAM) written by Cappellari (2008). In Section 2.5.1 we fit a surface brightness profile. We present the results of the Jeans models in Sections 2.5.2. Our mass profile is shown in Section 2.5.3.

2.5.1 Surface brightness profile

Light indicates the stellar density, and for a constant mass-to-light ratio (Y) also the gravitational potential of a stellar system. For the Jeans models we require a surface brightness profile. We used mid-infrared data to determine the surface brightness profile, as the interstellar extinction towards the Galactic centre reaches a minimum at $\sim 3\text{--}8 \mu\text{m}$ (Fritz et al. 2011).

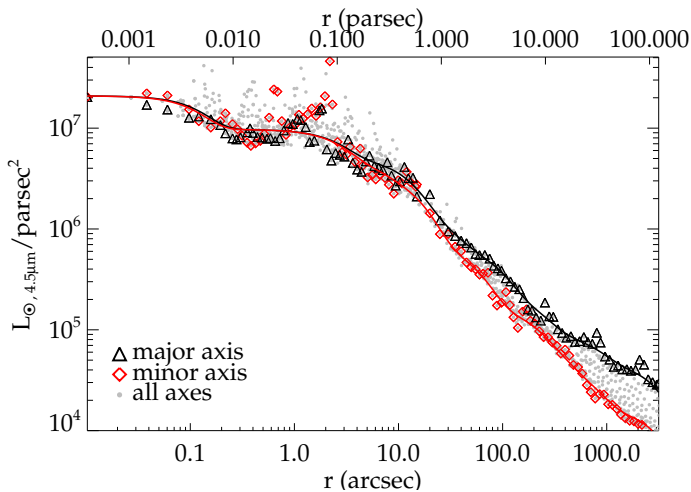


Figure 2.15: Surface brightness profile derived from a dust and extinction corrected *Spitzer*/IRAC $4.5\ \mu\text{m}$ image and NACO K_S -band mosaic for the central $30''$. Black triangles denote measurements along the major axis, and red diamonds along the minor axis, the grey data points are all measurements, at all axes. The spikes in the profile are due to individual bright stars. Solid lines illustrate the Multi-Gaussian Expansion (MGE) fit to the data.

We derived a surface brightness profile using imaging data from *Spitzer*/IRAC (Stolovy et al. 2006) at $4.5\ \mu\text{m}$. The image was dust and extinction corrected, and smoothed to a pixel scale of $5'' \cdot \text{pixel}^{-1}$. For details about the correction steps we refer to Schödel et al. (2014a). For the centre, we used a NACO K_S -band mosaic (Schödel et al. 2009) covering $40'.5 \times 40'.5$ scaled to the flux of the $4.5\ \mu\text{m}$ *Spitzer* image, with a pixel scale of $0'.027 \cdot \text{pixel}^{-1}$.

We used the MGE_FIT_SECTORS package. This is a set of IDL routines written by Cappellari (2002) to do photometric measurements directly on images and apply a Multi-Gaussian Expansion (MGE, Emsellem et al. 1994) fit to parameterise a surface brightness profile. The photometry of the two images was measured, and we determined a scale factor using the overlap region of the two images to convert the NACO image to the *Spitzer* flux. Then photometry was measured on each image along 12 angular sectors. The routine assumes four-fold symmetry and averages the measurements of four quadrants, taken along elliptical annuli with constant ellipticity ϵ .

A set of two-dimensional Gaussian functions was fitted to the combined photometric measurements. Therefore we also took the PSF of the NACO image into account. The MGE fit is not designed for a structural decomposition of the Galaxy's light profile. But Gaussians have the great advantage that deprojection can be done analytically. This procedure has been used already for galaxies (e.g. Cappellari et al. 2006), nuclear clusters (e.g. Seth et al. 2010), and globular clusters (e.g. Lützgendorf et al. 2012; Feldmeier et al. 2013). We assumed the position of Sgr A* as centre and excluded the dark $20\text{-km}\cdot\text{s}^{-1}$ -cloud and the Quintuplet cluster from the *Spitzer* image. As the central region of the $4.5\ \mu\text{m}$ emission is dominated by

Table 2.4: The Multi-Gaussian Expansion (MGE) fit parameters for the $4.5\mu\text{m}$ *Spitzer*/IRAC dust and extinction corrected image in combination with the NACO K_S -band mosaic scaled to *Spitzer* flux. I is the peak surface brightness, σ_{MGE} is the standard deviation, and q is the axial ratio of the Gaussian components.

I [$10^5 L_{\odot,4.5\mu\text{m}} \cdot \text{pc}^{-2}$]	σ_{MGE} [arcsec]	q
112	0.1	0.9
46.2	2.1	1.0
16.0	8.4	0.6
20.4	11.5	1.0
7.48	22.8	0.7
4.53	66.4	0.7
0.77	143	1.0
0.73	184	0.2
0.47	581	0.4
0.17	2705	1.0
0.31	2705	0.2

the mini-spiral and not by stellar emission, we also excluded pixels within 0.6 pc distance to Sgr A* of the *Spitzer* image from photometry measurements. The flux scaled NACO image was used out to $15''$ distance from Sgr A*. Table 2.4 lists the output of the MGE fit. The last two Gaussian components have the same value of σ_{MGE} , as they are close to the edge of the image. Figure 2.15 shows the MGE surface brightness profile along the major and minor axes.

2.5.2 Axisymmetric Jeans models

For the axisymmetric Jeans models we used the surface brightness parametrisation of Table 2.4 as an input. We assume an inclination angle of 90° , i. e. the Galaxy is seen edge-on. We fitted the model to the kinematic data. For this purpose we used the velocity maps of Fig. 2.5 of the faint stellar population, and excluded the bin with the highest uncertainty and lowest S/N. From these maps we computed the root-mean-square velocity $V_{\text{rms}} = \sqrt{V^2 + \sigma^2}$ for each bin. In all models we assumed a constant mass-to-light ratio Y . All Y values are for $4.5\mu\text{m}$ and in units of $M_{\odot}/L_{\odot,4.5\mu\text{m}}$.

For the anisotropy β ($= 1 - v_z^2/v_R^2$, Cappellari 2008) we tested different assumptions. We assumed isotropy in the central 0.5 pc (Do et al. 2013b), but fitted the anisotropy further out. Therefore we assumed different radial shapes of the anisotropy β : 1) constant anisotropy beyond 0.5 pc; 2) logarithmically increasing anisotropy beyond 0.5 pc, i.e. $\beta \propto \log(r + 0.5 \text{ pc})$; 3) linear increasing anisotropy beyond 0.5 pc, i.e. $\beta \propto r$. We have three fit parameters:

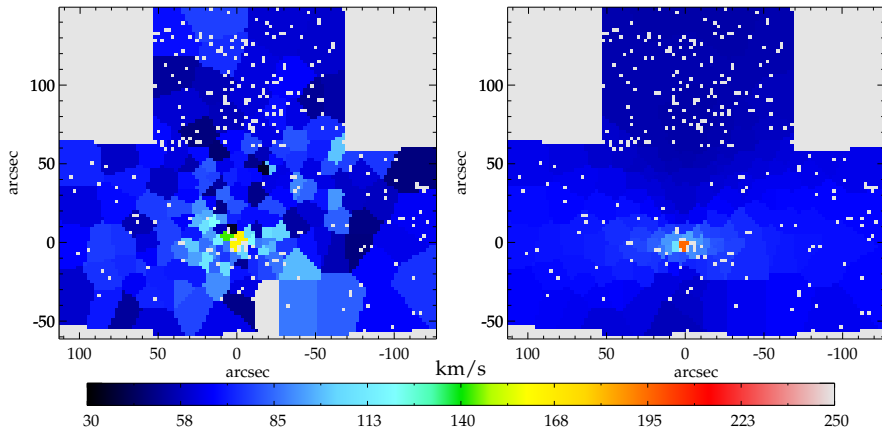


Figure 2.16: Result of the two-dimensional Jeans model with anisotropy $\beta_{\text{const}} = -0.3$, mass-to-light ratio $Y = 0.56$, and black hole mass $M_{\bullet} = 1.7 \times 10^6 M_{\odot}$. The left panel shows ISAAC data of the cleaned cube, for the root-mean-square velocity $V_{\text{rms}} = \sqrt{V^2 + \sigma^2}$, and the right panel is the best-fit model. The grey pixels mark regions, which contain no information. One bin was excluded from the fit due to its high uncertainty and low signal-to-noise, and it is also shown in grey on the left panel.

Y , $\beta_{100\text{pc}}$, and the black hole mass M_{\bullet} . As a fourth approach, we assumed constant anisotropy over the entire cluster and did not constrain the central 0.5 pc to be isotropic and fitted Y , β_{const} , and the black hole mass M_{\bullet} . We limited the value of β to $[-4; 0.9]$, since lower and higher values seem to be unrealistic.

Our best fit model has constant tangential anisotropy, the best fit parameters are $\beta_{\text{const}} = -0.3^{+0.3}_{-0.4}$, $Y = 0.56^{+0.22}_{-0.26}$, and $M_{\bullet} = (1.7^{+1.4}_{-1.1}) \times 10^6 M_{\odot}$, with $\chi_{\text{red}}^2 = 12.5$. The uncertainties are the 68 per cent confidence limits. Data and model are shown in Fig. 2.16. The left panel is the data, the right panel displays the best-fit model.

The results quoted here are from models without PSF convolution as the effect is negligible in our low spatial resolution data. In order to test this assumption we performed a PSF convolution with the seeing of the ISAAC data and found a difference that was less than 10 per cent of the uncertainties. A variation of the inclination angle to 80° has no effect on the best fit results, but increases χ_{red}^2 slightly.

The different β -profiles obtain consistent results for Y and M_{\bullet} , with only slightly higher values of χ_{red}^2 (13.0–13.4). This suggests that we cannot constrain a possible β variation over the cluster radius with our Jeans models. There is not much difference in the results if we run our models with the six outer fields or without. Using the kinematic maps containing all stars (Figure 2.4), the tangential anisotropy is increased ($\beta_{100\text{pc}}$ and $\beta_{\text{const}} \leq -0.5$), the best fit Y is lower (~ 0.32), and the black hole mass is slightly higher ($\sim 2.2 \times 10^6 M_{\odot}$). Differences to the results from the kinematic map of the cleaned data cube are less than the uncertainty limits. The χ_{red}^2 is much higher with values between 235 and 242, since the kinematic map of the full data cube is more affected by shot noise caused by single bright stars.

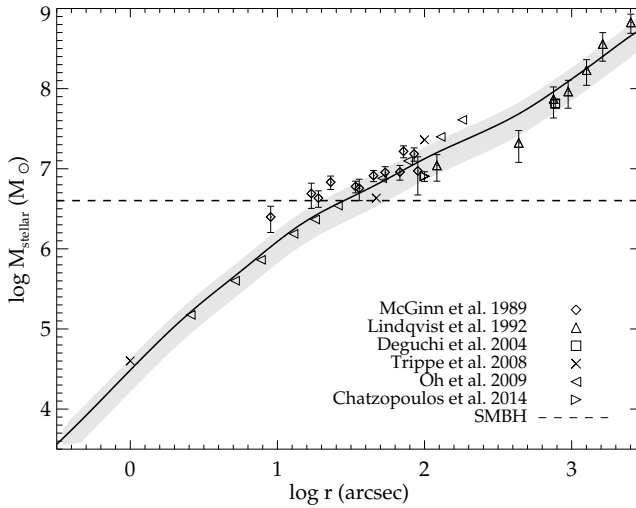


Figure 2.17: Enclosed stellar mass within a distance of $0.3''$ to $50'$ along the mean radius of the ellipses in units of M_{\odot} and in logarithmic scaling. The black line denotes a Y value of 0.56, the grey shaded contours show the uncertainty in Y of $^{+0.22}_{-0.26}$. The horizontal line is for a supermassive black hole with the mass $M_{\bullet} = 4 \times 10^6 M_{\odot}$. We also plot the results for the enclosed mass from previous studies: McGinn et al. (1989, assumed Galactocentric distance $R_0 = 8.5$ kpc), Lindqvist et al. (1992a, $R_0 = 8.5$ kpc), Deguchi et al. (2004, $R_0 = 8$ kpc), Trippe et al. (2008, $R_0 = 8$ kpc), Oh et al. (2009, $R_0 = 8$ kpc) and Chatzopoulos et al. (2015a, $R_0 = 8.3$ kpc).

As the population in the central parsec ($r \approx 13''$) is younger than at larger distances from Sgr A*, this might influence the result of the Y . We tested this by running the Jeans model without the V_{rms} data points inside $r = 10''$ and $r = 20''$. In both cases there is no difference in the best fit values of Y , M_{\bullet} and β . As another test we set the Y of the innermost five Gaussian components ($\sigma_{\text{MGE}} < 0.9$ pc) to zero before we run the Jeans models. This results in an increase of the Y of the outer components to 0.7 and M_{\bullet} to $3.4 \times 10^6 M_{\odot}$. The value of Y is within the uncertainty limits, while the black hole mass fit is significantly improved. But even with such an extreme assumption of $Y = 0$ in the central parsec, the black hole mass is too low. When we force the black hole mass to be $4 \times 10^6 M_{\odot}$, the best-fit value of Y is 0.35 and $\beta = -0.3$. This is within our uncertainties for Y .

2.5.3 Mass profile

With the mass-to-light ratio and our surface brightness profile we computed the enclosed mass of the nuclear star cluster. The light profile is parameterised by a series of Gaussians,

which is given in Table 2.4. This profile is valid out to 100 pc distance from Sgr A*. We computed the enclosed light within ellipses for each Gaussian component with the equation

$$L_j = 2\pi I_j \sigma_{\text{MGE},j}^2 q_j \left(1 - \exp\left(-\frac{x_{\text{max}}^2}{2\sigma_{\text{MGE},j}^2}\right) \right), \quad (2.3)$$

where x_{max} is the semi-major axis distance from the centre, up to which we integrate the light. Figure 2.17 illustrates the enclosed mass as a function of the mean radius of an ellipse $r = x_{\text{max}} \times \sqrt{1 - \varepsilon}$ with $\varepsilon = 0.29$ for a Y of $0.56_{-0.26}^{+0.22}$. This is the best fit result of Section 2.5.2. The uncertainty of our light profile, which we get from the uncertainty map of the *Spitzer* image, has about the same effect on the enclosed mass profile as a Y variation of 0.1.

At a distance of 10 pc from Sgr A*, the nuclear star cluster is still the dominant component of the Galaxy (Launhardt et al. 2002), it contributes more than the nuclear stellar disc. We obtain an enclosed mass of $(3.0_{-1.4}^{+1.2}) \times 10^7 M_{\odot}$ at a mean distance of 10 pc. While this mass is an extrapolation from the area where we have good sampling of the kinematics, it is more robust than previous dynamical estimates (McGinn et al. 1989; Lindqvist et al. 1992a; Trippe et al. 2008; Schödel et al. 2009).

2.6 Discussion

2.6.1 Clues to the formation of the Milky Way nuclear star cluster

Our velocity maps of the Milky Way nuclear star cluster reveal two unexpected features: (1) the offset of the rotational position angle from the Galactic plane and photometric position angle of the nuclear star cluster, and (2) indications for the presence of a rotating substructure at $r \sim 0.8$ pc rotating perpendicular to the Galactic plane.

Our kinematic analysis of the velocity map in Section 2.4.1 revealed an offset between the photometric and the kinematic position angle with a median value of $9^{\circ} \pm 3^{\circ}$ Galactic east of north. The photometric position angle is at $\sim 0^{\circ}$ (Schödel et al. 2014a). The misalignment between kinematics and morphology suggests that the overall luminosity profile is dominated by a different stellar population than the kinematics. The exact value of the position angle offset depends on the binning of the velocity map, and we use these variations for our uncertainty. Kinematic misalignment larger than 10° was already observed for galaxies of the SAURON project by Krajnović et al. (2008), but mostly in triaxial, slow-rotating galaxies. In fast-rotating galaxies, kinematic misalignment is only observed in combination with triaxial structures like bars or shells, or in the very centre of the galaxy.

In a first order approximation, the potential is spherically symmetric because a supermassive black hole is embedded in the nuclear star cluster. In a spherically symmetric system stellar orbits are approximately planar rosettes at all orientations. But the sense of rotation of some stars on inclined orbits could be reversed. Then one would observe an asymmetric velocity field. The same is valid for triaxial or flattened potentials. Triaxial tumbling systems that extend beyond the radius of influence of a central black hole have different sequences of

orbits (Heisler et al. 1982). If those orbits are populated equally, the system can be in dynamical equilibrium (Schwarzschild 1982). Then the velocity field appears symmetric relative to the short axis when observed from the Sun’s position inside the Galactic disc. However, asymmetries can be observed if a subset of inclined stellar orbits is preferentially populated.

Further, there appears to be a substructure that is red-shifted to the Galactic North ($V \approx 35 \text{ km}\cdot\text{s}^{-1}$), and blue-shifted to the Galactic South ($V \approx -25 \text{ km}\cdot\text{s}^{-1}$). This substructure rotates approximately perpendicular to the large scale sense of rotation. The sense of rotation of the well defined clockwise disc (e.g. Levin & Beloborodov 2003; Lu et al. 2009; Bartko et al. 2009; Yelda et al. 2014) is approximately opposite to the rotation we see in our data. But as we observe rather old stars, which show CO absorption lines, and the clockwise disc is seen in young stars, we do not expect the same dynamical properties.

Tremaine et al. (1975) suggested that nuclear star clusters form from infalling globular clusters. The kinematic misalignment and the perpendicular substructure could be the debris of such accretion events. Antonini et al. (2012) give a formula for the disruption radius r_{disr} at which an infalling massive star cluster is disrupted due to tidal stresses from the supermassive black hole (SMBH) in the nuclear star cluster. They found $r_{\text{disr}} \approx 1 \text{ pc}$ for the Milky Way nuclear star cluster, which is roughly equal to the core radius r_c of the old stellar distribution (0.5 pc, Buchholz et al. 2009). Antonini (2013) used an analytical model for globular cluster infall and found that the initial mass of the infalling clusters has to be at least $10^7 M_\odot$ to penetrate to a galactocentric radius of $\sim 2 \text{ pc}$. However, this model neglects internal dynamics of the infalling cluster like e.g. mass segregation. Taking this into account allows the infalling cluster to bring stars even closer to the centre (Antonini 2014). Therefore a substructure at $\sim 0.8 \text{ pc}$, like the one our data indicates, could be the remnant of a tidal disruption event.

Antonini (2014) ran N -body simulations to investigate the consecutive inspirals of 12 clusters to a Galactic centre. In this simulation only the orbits of stars from the first seven infalling clusters are close to isotropic at the end of the simulations. This is not the case for the orbits of stars from the last infalling clusters. After $\sim 3 \text{ Gyr}$ the stellar orbits are still largely correlated, and would require about 10 Gyr to reach a fully isotropic distribution (F. Antonini, personal communication, April 2014). The relaxation time of the nuclear star cluster is several Gyr at all radii, and outside of 1 pc, the relaxation time is even longer than the age of the universe (Merritt 2010). Therefore we expect the signatures of infalling clusters to remain coherent over a long period of time.

Our observation of a kinematic misalignment and a perpendicular rotating substructure can be explained by the accretion of massive star clusters. This would support the theory that the accretion of massive stellar cluster plays a role in the formation of nuclear star clusters. We plan follow-up observation with KMOS (VLT) to verify these discoveries.

2.6.2 Underestimation of the black hole mass

Our two-dimensional Jeans models in Section 2.5 resulted in a black hole mass that is lower by a factor ~ 2 than the result from direct measurements of $\sim 4 \times 10^6 M_\odot$ (Ghez et al. 2008; Gillessen et al. 2009b). Before those measurements, the black hole mass was underestimated

by other studies as well (McGinn et al. 1989; Krabbe et al. 1995; Haller et al. 1996; Genzel et al. 1996).

As shown in Fig. 2.12, the ISAAC data velocity dispersion values are lower than the proper motion data of Schödel et al. (2009). This could be due to a bias in the measurement of the velocity dispersion in the ISAAC data, and cause the underestimation of the black hole mass. We derive the kinematics from the radial velocities of old stars only, and cannot trace the young population of stars in the centre. Therefore the measured velocity dispersion is mostly from stars that lie at a large distance in front and behind of Sgr A*, and only appear to be close to the SMBH in projection (Sellgren et al. 1990). This means that the measured velocity dispersion of the central $\sim 8''$ (0.3 pc) is rather too low (e.g. Haller et al. 1996).

But as the radius of influence of the black hole extends out to 2.3 pc ($\sim 60''$, see Section 2.6.3) and the young stellar population extends only to 0.5 pc, this may not be the only reason for the too low black hole mass. To test this assumption we excluded the kinematic data of the centre out to 0.8 pc ($20''$) and found no changes in the best-fit parameters of the Jeans models. We also considered the extreme and unphysical case that the value of the mass-to-light ratio Y is zero for the Gaussian components of the potential with $\sigma_{\text{MGE}} \leq 0.8$ pc. This is motivated by the fact that the Y of young stars, which are in the central 0.5 pc, is lower than the Y of old stars. This increased the black hole mass, but only to $3.4 \times 10^6 M_{\odot}$.

Therefore the stellar population change alone cannot explain the too low black hole mass. The position angle offset may also have an effect on the black hole mass measurement in the two-dimensional Jeans models. Further, there might be a systematic bias in black hole mass measurements obtained with integrated light measurements, leading to an underestimation of black hole masses also in some other galaxies. We plan to investigate this issue in more detail in a follow-up paper.

2.6.3 Mass profile of the cluster

We obtain the cluster mass from the surface brightness assuming a constant Y . As the stellar population in the nuclear star cluster is not uniform, this may be an oversimplification. But population synthesis models showed that, compared to optical light, the mid-infrared mass-to-light ratio is rather constant. Under this assumption, McGaugh & Schombert (2013) found a mean value of $(0.5 \pm 0.1) M_{\odot}/L_{\odot,3.6\mu\text{m}}$ in disc galaxies. Meidt et al. (2014) constrained the mean value to $0.6 M_{\odot}/L_{\odot,3.6\mu\text{m}}$. The mass-to-light ratio at $4.5 \mu\text{m}$ should be similar or even less than the mass-to-light ratio at $3.6 \mu\text{m}$ (Oh et al. 2008). This is in agreement with our results from the Jeans models of $0.56^{+0.22}_{-0.26} M_{\odot}/L_{\odot,4.5\mu\text{m}}$. However, our best fit black hole mass is too low compared to direct measurements, and this might influence the outcome of Y . We tested the magnitude of this by using the black hole mass of $4 \times 10^6 M_{\odot}$ as input. Then Y decreases to 0.35, which is still above our lower limit value. This test shows that our result of Y is robust under local variations of the stellar populations, since the kinematic data covers a large enough region.

Our enclosed mass profile is shown in Fig. 2.17 using our best fit mass-to-light ratio $Y = 0.56^{+0.22}_{-0.26} M_{\odot}/L_{\odot,4.5\mu\text{m}}$ for $0.3'' < r < 50'$. This plot contains the enclosed mass from both

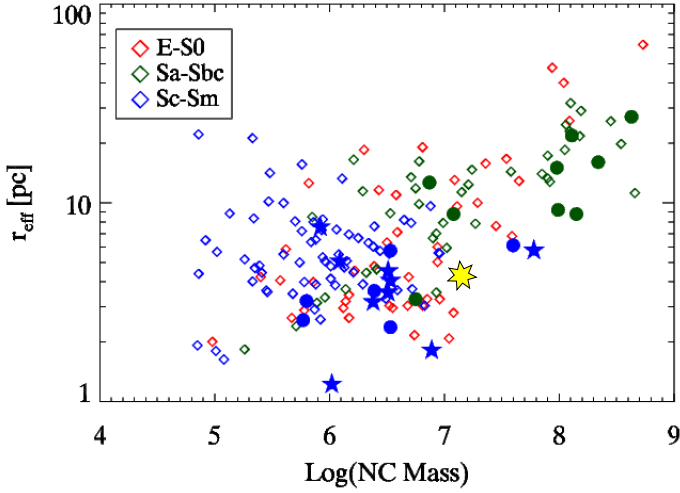


Figure 2.18: Nuclear cluster mass M_{NSC} – effective radius r_{eff} relation for nuclear star clusters, based on Seth et al. (2008a) with data from Walcher et al. (2005); Rossa et al. (2006) shown as filled symbols and Böker et al. (2002); Carollo et al. (1997, 1998, 2002); Côté et al. (2006) as open symbols. The yellow star is the result for the Milky Way nuclear star cluster within an effective radius of 4.2 pc (Schödel et al. 2014a).

the nuclear star cluster and the nuclear stellar disc, which dominates the mass at $r \gtrsim 100$ pc ($40'$). We also plot the results for the enclosed mass for various other studies, among those McGinn et al. (1989) and Lindqvist et al. (1992a) in Fig. 2.17. Those two studies assumed a Galactocentric distance of 8.5 kpc, while we assume 8.0 kpc. Further, they computed the mass by integrating the light enclosed in circles, and not ellipses, and assumed spherical symmetry. These are probably more important effects. The results of McGinn et al. (1989) for the enclosed mass tend to be higher at $r < 30''$, but we have good agreement with McGinn et al. (1989) at larger radii, and also with the results of Lindqvist et al. (1992a). One out of three of the values given by Trippe et al. (2008) is higher than our upper limit, while the other two data points agree with our results. The results of Oh et al. (2009) are in excellent agreement with our data inside $100''$. At $28_{-9}^{+28}''$ ($1.1_{-0.3}^{+1.1}$ pc), the mass of the stars equals the mass of the SMBH. Inside this radius the potential is dominated by the SMBH and therefore close to spherically symmetric. Merritt (2004) defines the radius of influence r_{infl} of a SMBH as the radius at which the enclosed mass in stars is twice the mass of the black hole. With this definition we obtain a mean radius $r_{\text{infl}} = 60_{-17}^{+54}''$ ($2.3_{-0.7}^{+2.1}$ pc). This value is in agreement with the result of 3 pc found by Alexander (2005), based on the enclosed mass of Schödel et al. (2003).

Studies of Côté et al. (2006) and Forbes et al. (2008) showed that for nuclear star clusters the effective radii increase with the luminosity of the nuclear star cluster. This indicates also a correlation of the nuclear star cluster mass M_{NSC} to r_{eff} . We plot this relation for a large number of nuclear star clusters compiled by Seth et al. (2008a) in Fig. 2.18; solid points

represent the most reliable mass estimates from Walcher et al. (2005) and Rossa et al. (2006). Other data points are from Böker et al. (2002); Carollo et al. (1997, 1998, 2002); Côté et al. (2006) and the mass estimate was derived purely photometrically. The yellow star denotes the mass of the Milky Way nuclear star cluster of $1.4 \times 10^7 M_{\odot}$ within the effective radius. The $M_{\text{NSC}} - r_{\text{eff}}$ relation breaks down for low masses. The Milky Way nuclear star cluster is within the trends defined by other clusters, but is somewhat more compact than average.

2.6.4 Anisotropy

Schödel et al. (2009) found that the velocity dispersion of the late-type stars in the cluster is consistent with isotropy. This was confirmed by Do et al. (2013b) for the inner 0.5 pc of the Galaxy. We assumed different radial anisotropy profiles, but there is no clear trend about which profile fits best. However, the models favour tangential anisotropy, and if we impose constant anisotropy throughout the model, the best-fit value is $-0.3^{+0.3}_{-0.4}$, i.e. radial anisotropy is excluded. Also our analysis of λ_R suggests the Milky Way nuclear star cluster is anisotropic. Specifically, the cluster appears to be more flattened than expected based on the observed rotation.

2.6.5 Extreme velocities for individual stars

We extracted 1375 spectra from bright stars with $K_S < 11.5$ mag from our unbinned data and fitted their velocities in Section 2.3.2. For three stars we obtained velocities higher than $250 \text{ km}\cdot\text{s}^{-1}$, they are listed in Table 2.1. One is already known as IRS 9, and at a projected distance of $8''$ from Sgr A* with $V = -340 \text{ km}\cdot\text{s}^{-1}$. Its velocity was already measured by Zhu et al. (2008) to $-347.8 \text{ km}\cdot\text{s}^{-1}$. The other stars are further out, at $80''$ and $130''$ distance, and have radial velocities of $292 \text{ km}\cdot\text{s}^{-1}$ and $-266 \text{ km}\cdot\text{s}^{-1}$. This corresponds to 3.5σ and 3.8σ in the velocity distribution of individual stars. These extreme velocities are even more surprising in their position as the local velocity dispersion around these stars is low. It is possible that these stars have been accelerated by the Hills mechanism. Hills (1988) predicted the existence of hypervelocity stars, which were ejected in a three-body encounter between the SMBH and a binary star system. Depending on the semi-major axis distance of the binary and the closest approach to the SMBH, stars can be accelerated to velocities of some $1000 \text{ km}\cdot\text{s}^{-1}$. Since the stars detected by us have velocities of $-266 \text{ km}\cdot\text{s}^{-1}$ and $292 \text{ km}\cdot\text{s}^{-1}$, they would require a proper motion component of $\sim 960 \text{ km}\cdot\text{s}^{-1}$ to reach a magnitude of the velocity vector of $\sim 1000 \text{ km}\cdot\text{s}^{-1}$. Therefore we do not consider them as strong hypervelocity star candidates. Nevertheless, these stars could have been accelerated by the Hills mechanism.

2.7 Conclusions

We obtained an integral field like spectroscopic data set of the Milky Way nuclear star cluster. These data cover the central 11 arcmin^2 (60 pc^2), and six smaller fields at larger projected distances. Those go out to $8'$ distance from Sgr A* along the Galactic Plane and cover

3.2 arcmin² in total. We set up a spectroscopic map with a pixel size of 2''22 of the central field. Additionally we constructed a spectroscopic map that was cleaned of bright stars and foreground stars. Using these data cubes, we fitted the stellar CO absorption lines and computed velocity and velocity dispersion maps.

1. We found a misalignment of the photometric and kinematic position angles by $\sim 9^\circ$ Galactic east of north. Further, we detected indications for a new kinematic substructure that is approximately aligned along the Galactic minor axis at $\sim 20''$ (0.8 pc) distance from Sgr A*. Both observations indicate to different accretion events of the Milky Way nuclear star cluster. To confirm these findings with higher spatial resolution and a wider wavelength range we plan new observations with KMOS (VLT). If confirmed, the position angle offset and the substructure give important clues to the formation history of nuclear star clusters. They support the theory that infalling massive clusters play a role in the build-up of nuclear star clusters.
2. Axisymmetric Jeans models of the velocity maps underestimated the mass of the super-massive black hole in the Galactic centre. The reason for this can partially be explained by the lack of old stars in the central 0.5 pc. Therefore our measured velocity dispersion was biased to too low values. Another possibility is that the kinematic misalignment influences the outcome of the models. We cannot exclude a systematic bias in black hole mass measurements obtained using integrated light. Such a bias could mean that we underestimate black hole masses in some other galaxies as well. Therefore we plan to investigate this issue further using additional data in a follow-up paper.
3. We fitted a surface brightness profile of the Milky Way nuclear star cluster using NACO K_S -band data and *Spitzer* photometry at $4.5 \mu\text{m}$. Our best-fit Jeans models resulted in a mass-to-light ratio $Y = 0.56_{-0.26}^{+0.22} M_\odot / L_{\odot,4.5\mu\text{m}}$. From these results we computed a profile for the enclosed mass. At a distance of $r_{\text{eff}} = 4.2$ pc from Sgr A* the cluster mass (without the black hole mass) is $(1.4_{-0.7}^{+0.6}) \times 10^7 M_\odot$. Compared to nuclear star clusters of similar size the Milky Way nuclear star cluster is rather massive.

Acknowledgements

This research was supported by the DFG cluster of excellence Origin and Structure of the Universe (www.universe-cluster.de). This publication makes use of data products from the Two Micron All Sky Survey, which is a joint project of the University of Massachusetts and the Infrared Processing and Analysis Center/California Institute of Technology, funded by the National Aeronautics and Space Administration and the National Science Foundation. This research made use of the SIMBAD database (operated at CDS, Strasbourg, France). We would like to thank the ESO staff who helped us to prepare our observations and obtain the data. A special thanks to our Telescope operator J. Navarrete, who implemented all our non-standard observing techniques. A. F. also thanks Holger Baumgardt and Eric Emsellem for helpful discussions about the project. We thank Fabio Antonini for further investigations

of his simulations on our behalf and providing us additional information. C. J. W. acknowledges support through the Marie Curie Career Integration Grant 303912. We finally thank the anonymous referee for useful comments and suggestions.

Based on observations collected at the European Organisation for Astronomical Research in the Southern Hemisphere, Chile (289.B-5010(A)).

2.8 Appendix: Persistence removal

Persistence is a known problem of infrared detectors when observing bright sources. If the exposure time is too long and the source is overexposed, there can be ghost images of the source in a subsequently taken exposure of a faint source. The magnitude of the persistence effect decreases in time according to a power-law (Dressel 2012). To avoid persistence, one should either choose short exposure times or, alternatively, make a sequence of read-outs afterwards, to flush the detector's memory of the bright source. We took acquisition images right before the object spectra, which lead to persistence in the 2D spectra. Also our 2D sky spectra are affected as we took three dithered images on source before the sky offsets to verify the position on the sky after the drift, and two dithered images on sky that also contain a few stars.

However, we developed a way to remove the persistence signature completely in our sky frames and to some extent also in the object spectra. We used the images that cause the persistence and the corresponding 2D spectra that are affected by the persistence. Removing persistence from the 2D sky spectra is rather straight forward: For every 2D sky spectrum $S_{\text{raw,sky}}$ we computed the median of each column along the dispersion axis and subtracted it from each pixel in the column, and did the same with the median along the spatial axis to get a 2D sky spectrum without any lines or stars $S_{\text{med,sky}}$. The only features left in the median subtracted 2D sky spectrum are from the persistence. Then one can simply compute a corrected 2D sky spectrum $S_{\text{cor,sky}}$

$$S_{\text{cor,sky}} = S_{\text{raw,sky}} - S_{\text{med,sky}} + \text{mean}(S_{\text{med,sky}}). \quad (2.4)$$

The clean 2D sky spectra were combined to 2D Mastersky spectra using IRAF. We also produced noise files for each sky file that contain the information about the persistence correction.

This simple approach is not possible for the 2D object spectra, as there are many stars with strong absorption lines and also an H_2 gas emission line. In contrast to the 2D sky spectra, subtracting a median leaves other strong features apart from the persistence residuals. Therefore we decided to model the persistence and subtracted the model from the 2D object spectra. To determine the persistence model parameters we used the 2D sky spectra before we applied the aforementioned correction on them.

Saturated pixels have negative counts in our images and leave persistence features in the 2D spectra taken afterwards. Persistence is also a problem if the counts of a bright source at a given pixel of the detector are above a certain threshold. First, one needs to determine

the value of this threshold. Therefore we considered only counts above a trial threshold and made a persistence mask M , where pixels with negative counts in the image as well as counts above the threshold were set to one and all other pixels were set to zero. As the raw 2D sky frames are affected by persistence coming from three images on source and two images on sky, taken $\sim 2-3$ minutes later, we made two masks, one for the images on source (M_{source}) and one for the sky images (M_{sky}). Then we used `MPFIT2DFUN.PRO` (Markwardt 2009) to fit the amplitudes of the persistence, K_{source} and K_{sky} , and a full-width-half-maximum FWHM for a Gaussian smoothing filter G_{FWHM} of the masks. The residual spectrum R is

$$R = S_{\text{med}} - G_{\text{FWHM}} * (K_{\text{source}} \times M_{\text{source}} + K_{\text{sky}} \times M_{\text{sky}}), \quad (2.5)$$

where the symbol “ $*$ ” denotes convolution. We tried different values of the mask threshold, and we found a minimum of the standard deviation of the residual spectrum R at a threshold of 33,500 counts. Therefore we defined 33,500 counts as our threshold for further corrections of images taken with an exposure time of 20s. For the images with exposure time $t = 5s$, we have a lower threshold of 24,000 counts, found by the same method.

The next step is to fit K_{source} , K_{sky} , and FWHM with the chosen threshold value of the mask for every median subtracted 2D sky spectrum $S_{\text{med,sky}}$. The persistence signal decreases in time, therefore K_{source} and K_{sky} decrease from the first to the fifth 2D sky spectrum in a sequence. We fitted the decrease of K with the power law

$$K(t) = A \times t^{-\gamma}, \quad (2.6)$$

where the parameter A is the amplitude and γ is a scale factor. We did this for K_{source} and K_{sky} separately and together, but our later analysis shows that we obtain better results when we use the result of fitting $K_{\text{source}}(t)$ alone. The parameters we used are $A = (6900 \pm 1700)$ and $\gamma = (0.98 \pm 0.04)$. The uncertainties are the formal $1-\sigma$ errors of the fit. With this knowledge we can subtract the persistence from the 2D object spectra with the equation

$$S_{\text{cor,object}} = S_{\text{raw,object}} - (G_{\text{FWHM}} * M_{\text{acq}}) \times A \times t^{-\gamma}. \quad (2.7)$$

The images causing persistence in the 2D object spectra are acquisition images. As we made acquisition offsets, we subtracted persistence caused by the acquisition image itself and from a shifted acquisition image. We have only the acquisition image itself as file, but we can identify the shift in pixels from the persistence in the 2D spectra, and we can fit the shift of the acquisition offset together with an attenuation factor α . This factor α is necessary as the offset was performed before the acquisition image was taken, and therefore the persistence signal is weaker. In this case the corrected 2D object spectra $S_{\text{cor,object}}$ are

$$S_{\text{cor,object}} = S_{\text{raw,object}} - (G_{\text{FWHM}} * M_{\text{acq}}) \times A \times t^{-\gamma} - \alpha \times (G_{\text{FWHM}} * M_{\text{acq,shifted}}) \times A \times t^{-\gamma}. \quad (2.8)$$

With these procedures it is possible to remove the persistence structures completely from the 2D sky frames and to subtract them from the 2D object spectra partially, but some residuals still remain. In some cases we made more than one acquisition offset, and furthermore it

is difficult to model the shape of the persistence, which was slightly elliptical due to the drift during the acquisition. The shape also changes depending on the area on the detector and seeing conditions. To account for uncertainties in the persistence subtraction, we made noise files that were used for the further analysis of the spectra.

To check the influence of the persistence after the correction on our results we compared two 2D spectra that cover almost the same region of the Milky Way nuclear star cluster. One 2D spectrum was not affected by the persistence, since it was the 20th exposures taken after the acquisition image. The other 2D spectrum was taken shortly after the acquisition image and was affected by persistence. We extracted several 1D spectra by summing between 45 and 100 rows of the 2D spectra. Then we fitted the CO absorption lines with `rPXF`. The signal-to-noise ratio (S/N) of the spectra taken from the file with persistence, but after our correction, is lower by ~ 27 per cent compared to the S/N of spectra from the file with no persistence. But as the effect of persistence decreases in time, not all of our data are as much affected. We estimate that in ~ 70 per cent of our spectra the decrease in S/N due to the persistence is less than 20 per cent.

2.9 Appendix: H₂ gas emission kinematics

We fitted the 1-0 Q(1) 2.4066 μm transition of H₂ to make a comparison with previous studies (e.g. Gatley et al. 1986; Yusef-Zadeh et al. 2001; Lee et al. 2008). The excellent agreement of our flux and kinematic maps with these studies shows that our data can reproduce previous results without strong biases. Figure 2.19 illustrates the results of the fitting for flux, velocity and velocity dispersion. Regions where the flux was too low and confusion with sky line residuals might be possible are not displayed. In the H₂ velocity map we can identify the northeastern and southwestern lobe of the circumnuclear disc (see Fig. 1 of Amo-Baladr3n et al. (2011) for an illustration of the central 12 pc).

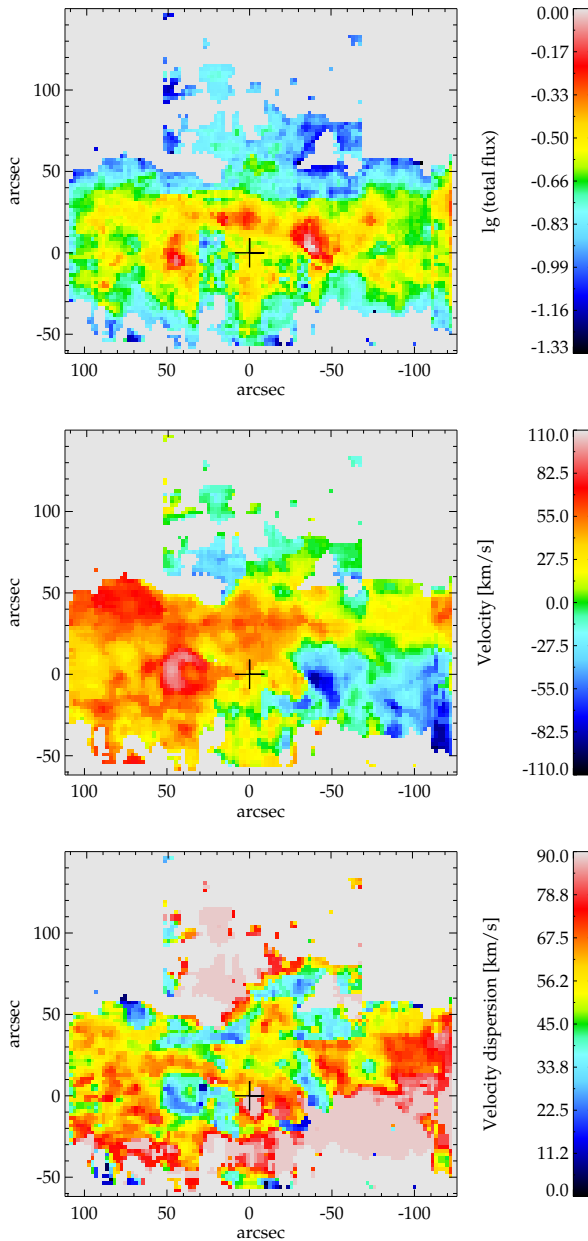


Figure 2.19: Results of the single Gaussian fit to the H_2 gas emission line. Upper panel: flux in logarithmic scaling and with respect to the maximum flux. Middle panel: velocity in $\text{km}\cdot\text{s}^{-1}$. Lower panel: velocity dispersion in $\text{km}\cdot\text{s}^{-1}$, corrected for the instrumental dispersion ($\sigma_{\text{instr}} \approx 27 \text{ km}\cdot\text{s}^{-1}$). The coordinates are centred on Sgr A* and along the Galactic plane with a position angle of $31^\circ.40$. The cross marks the position of Sgr A*.

3

Triaxial orbit-based modelling of the Milky Way nuclear star cluster

We construct triaxial dynamical models for the Milky Way nuclear star cluster using Schwarzschild's orbit superposition technique. We fit the stellar kinematic maps presented in Feldmeier et al. (2014). The models are used to constrain the supermassive black hole mass M_\bullet , dynamical mass-to-light ratio Y , and the intrinsic shape of the cluster. Our best-fitting model has $M_\bullet = (3.0_{-1.3}^{+1.1}) \times 10^6 M_\odot$, $Y = (0.90_{-0.08}^{+0.76}) M_\odot/L_{\odot,4.5\mu\text{m}}$, and a compression of the cluster along the line-of-sight. Our results are in agreement with the direct measurement of the supermassive black hole mass using the motion of stars on Keplerian orbits. The mass-to-light ratio is on the high-end of stellar population studies of other galaxies in the mid-infrared. It is possible that we underestimate M_\bullet and overestimate the cluster's triaxiality due to observational effects. The spatially semi-resolved kinematic data and extinction within the nuclear star cluster bias the observations to the near side of the cluster, and may appear as a compression of the nuclear star cluster along the line-of-sight. We derive a total dynamical mass for the Milky Way nuclear star cluster of $M_{\text{MWNSC}} = (3.1_{-0.3}^{+2.6}) \times 10^7 M_\odot$ within a radius of $r = 2 \times r_{\text{eff}} = 8.4$ pc. The best-fitting model is tangentially anisotropic in the central $r = 2$ pc of the nuclear star cluster, but close to isotropic at larger radii. Our triaxial models are able to recover complex kinematic substructures in the velocity map.

A. Feldmeier-Krause, L. Zhu, N. Neumayer, G. van de Ven, P. T. de Zeeuw, R. Schödel
submitted to MNRAS on July 22, 2016

3.1 Introduction

The Milky Way nuclear star cluster is the ideal object to study the dynamics of a stellar system around a supermassive black hole. At a distance of 8 kpc it is close enough to resolve the individual stars, and measure discrete velocities in three dimensions. Modelling the stellar kinematics can constrain the mass distribution of the star cluster, and reveal the presence of a central dark massive object. In the special case of our own Galaxy, it is possible to observe Keplerian orbits of stars around a dark, point-mass-like object in the Galactic centre. These observations constrain this dark object to be a supermassive black hole with a mass of $(4.1 \pm 0.6) \times 10^6 M_\odot$ (Ghez et al. 2008), $(4.3 \pm 0.39) \times 10^6 M_\odot$ (Gillessen et al. 2009b), or $(4.02 \pm 0.20) \times 10^6 M_\odot$ (Boehle et al. 2016). Unfortunately, similar high-resolution observations are not yet possible in other galaxies.

Already in the 1970s the requirement of a central supermassive black hole in the Galactic centre was discussed to explain observational data (e.g. Oort 1977). Several studies used stellar radial velocities to constrain the mass distribution in the Galactic centre (e.g. Rieke & Rieke 1988; McGinn et al. 1989; Sellgren et al. 1990; Haller et al. 1996; Genzel et al. 1996). Also stellar proper motions were used to study the Galactic centre mass distribution (Schödel et al. 2009). Several studies combined radial velocity and proper motion data (Trippe et al. 2008; Do et al. 2013b; Fritz et al. 2016). The mass distribution was derived using the spherical Jeans (1922) equations or the projected mass estimators of Bahcall & Tremaine (1981) for spherical systems. These studies found that a central dark mass of $2\text{--}5 \times 10^6 M_\odot$ is required to explain the observations.

Together with the increase of observational data, also the modelling became more advanced. Trippe et al. (2008) included the rotation of the nuclear star cluster in the modelling, although the rotation velocity of their data was too high (Schödel et al. 2009; Feldmeier et al. 2014). Feldmeier et al. (2014) and Chatzopoulos et al. (2015a) studied the Milky Way nuclear star cluster using axisymmetric Jeans models. Chatzopoulos et al. (2015a) showed the advantages of axisymmetric models over spherical Jeans models, which cannot explain the observed asymmetry of the velocity dispersion of proper motions parallel and perpendicular to the Galactic plane. The nuclear star cluster appears to be flattened in its light distribution (Schödel et al. 2014a) as well as in the kinematics (Chatzopoulos et al. 2015a). Most studies showed that the nuclear star cluster kinematics is in agreement with isotropy (Schödel et al. 2009; Do et al. 2013b; Chatzopoulos et al. 2015a), although the uncertainties are quite large (e.g. Do et al. 2013b). All these models assumed a constant mass-to-light ratio for the light distribution of the cluster.

In this study we relax the assumption of axisymmetry and use triaxial orbit-based Schwarzschild (1979) models. Orbit-based models make no assumptions on the velocity anisotropy of the stellar motions, as Jeans models do. Further, the higher moments of the kinematics can also be included (Rix et al. 1997), which is important to break the degeneracy of mass and anisotropy in dynamical models.

Orbit-based models are commonly used to analyse line-of-sight velocity data of other galaxies (e.g. van der Marel et al. 1998; Gebhardt et al. 2000; Valluri et al. 2005; van den

Bosch et al. 2008), and are an excellent tool to detect and measure the masses of supermassive black holes and dark matter halos. For extragalactic systems, the data are usually obtained from integrated light observations. Each data point contains the accumulated kinematics of many stars, weighted by their respective brightness. However, modelling the dynamics of integrated light data may be prone to systematic uncertainties, and bias the results of the central black hole mass. Therefore, it is interesting to test dynamical models on systems for which we know the central black hole mass from other independent measurements. The Milky Way nuclear star cluster is a good object for this kind of test. Also megamaser disc galaxies are useful to validate stellar dynamical black hole measurements. Black hole mass measurements from megamasers are very precise with uncertainties of only about 10 per cent. However, there is currently only one megamaser disc galaxy with a stellar dynamical black hole mass measurement (van den Bosch et al. 2016), NGC 4258. Different dynamical studies found either a 15 per cent lower or a 25 per cent higher black hole mass than the maser measurement (Siopis et al. 2009; Drehmer et al. 2015).

We use the triaxial orbit-based code by van den Bosch et al. (2008) to model the light distribution and line-of-sight kinematics of the Milky Way nuclear star cluster. We use the spectroscopic data cube constructed by Feldmeier et al. (2014) for the kinematic data, and derive a surface brightness distribution using *Spitzer* 4.5 μm and NACO *H*-band images. We assume a galactocentric distance of 8 kpc (Malkin 2012) and a position angle $31^\circ 40'$ East of North (J2000.0 coordinates, Reid & Brunthaler 2004) with respect to the Galactic plane. This chapter is organised as follows: We describe the kinematic and photometric data in Section 3.2. The dynamical models are introduced in Section 3.3. Section 3.4 discusses the results, and Section 3.5 summarizes the main conclusions.

3.2 Description of the data

3.2.1 Kinematic data

The line-of-sight velocity distribution (LOSVD) provides constraints on the dynamical structure of stellar systems. To extract this information, we used the near-infrared *K*-band spectroscopic data cube of Feldmeier et al. (2014), which has a pixel scale of $2''.22 \cdot \text{pixel}^{-1}$. We used the data cube that was cleaned from foreground stars and bright stars. The cleaned data cube contains the light of the old red giant star population.

We fitted the LOSVD as in Feldmeier et al. (2014), i.e. on the stellar CO absorption lines (2.2902–2.365 μm) with the IDL routine `pPXF` (Cappellari & Emsellem 2004) and the high resolution spectra of Wallace & Hinkle (1996) as template stars. We applied the same spatial binning as Feldmeier et al. (2014), resulting in 175 spatial bins. Feldmeier et al. (2014) fitted only the velocity V and velocity dispersion σ . However, we fitted in addition also higher moments of the LOSVD, in particular the Gauss-Hermite parameters h_3 and h_4 . We added noise to each of the 175 integrated light spectra in 100 Monte Carlo simulation runs and obtained a distribution for each moment of the LOSVD. The mean and standard deviation of the Monte Carlo distribution are taken as measurement and 1σ uncertainty of the kinematics.

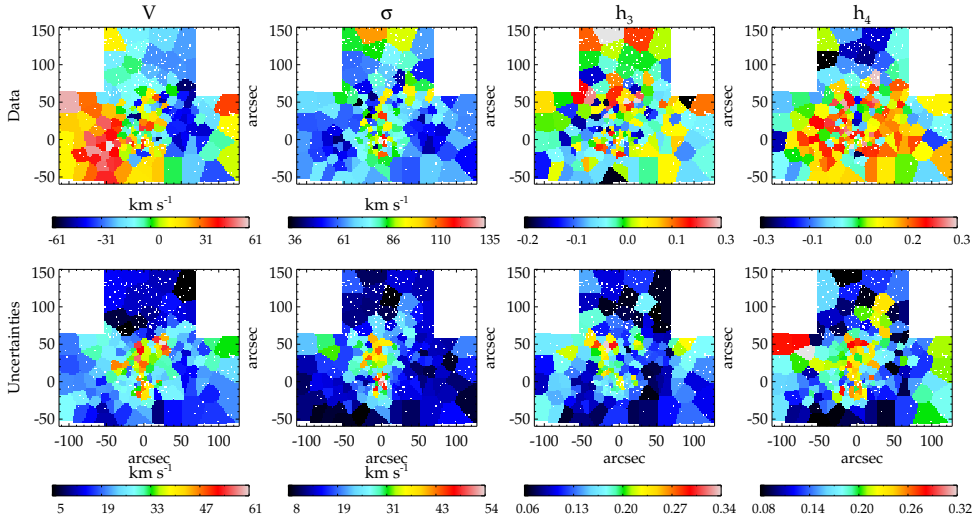


Figure 3.1: Kinematic data (top row) and respective uncertainties (bottom row). The columns denote velocity V , velocity dispersion σ , Gauss-Hermite moments h_3 , and h_4 . White pixels are due to excluded bright stars.

Since the Milky Way nuclear star cluster is at a distance of only 8 kpc, the spectroscopic observations are spatially semi-resolved. Bright stars can be resolved individually, and contribute a large fraction of the flux. For that reason we used the cleaned data cube of Feldmeier et al. (2014), where bright stars were excluded. However, the kinematic maps still show stochastic shot noise. As a consequence, the difference of the kinematics in adjacent bins can be higher than their uncertainties, which causes problems when we model the kinematics. The stochastic noise can be mistaken for signal, and this means the best fit will be achieved by modelling the shot noise. To prevent this, we increased our kinematic uncertainties ε_V such that the difference of the measurement in two adjacent bins ($V_i - V_j$) is less than the sum of their uncertainties ($\varepsilon_{V_i} + \varepsilon_{V_j}$). We do this for the uncertainty of velocity, velocity dispersion, h_3 , and h_4 , and find that it is required for about 68 per cent of the kinematic data uncertainties. Additionally, we point-symmetrise the kinematics using the procedure of van den Bosch & de Zeeuw (2010). The median uncertainties for V , σ , h_3 , and h_4 are 24.6 km·s⁻¹, 18.4 km·s⁻¹, 0.15, and 0.17. Our resulting kinematic maps are consistent with the maps of Feldmeier et al. (2014). We find rotation in the velocity map of approximately 50 km·s⁻¹ and an increase in the velocity dispersion from about 65 km·s⁻¹ towards $\sigma_{\max} = 135$ km·s⁻¹ at the centre. The kinematic maps are shown on the top row of Fig. 3.1, the uncertainties are shown on the bottom row.

3.2.2 Imaging data and surface brightness distribution

The light distribution of the nuclear star cluster traces the stellar density. We require the two-dimensional light distribution of the red giant stars, which are our kinematic tracers. The extinction is high at optical wavelengths in the Galactic centre ($A_V \sim 30$ mag, Scoville et al. 2003; Gao et al. 2013), therefore we used near- and mid-infrared images.

For the central $40''.4 \times 40''.4$ ($1.6 \text{ pc} \times 1.6 \text{ pc}$) we used the high-resolution NACO H -band mosaic of Schödel et al. (2009), which has a spatial scale of $0''.027 \cdot \text{pixel}^{-1}$. We preferred the H -band over the K -band in order to avoid light from gas emission lines in the K -band (Br γ and He I, Paumard et al. 2004). Our kinematic tracers are cool late-type stars, but there are also more than 100 hot, young stars located in the centre of the cluster, within a projected radius $r = 0.5 \text{ pc}$ ($\sim 12.8''$, Paumard et al. 2006). We masked out the young stars from the image with a 15 pixel radius. For the bright red supergiant IRS 7 we used a larger mask with a 30 pixel radius. Beyond the central 0.5 pc, the nuclear star cluster light is dominated by cool stars, and the contribution of young stars is negligible (Feldmeier-Krause et al. 2015).

For the large-scale light distribution, we used *Spitzer* IRAC images (Stolovy et al. 2006). These images were corrected for dust extinction and PAH emission by Schödel et al. (2014a). We used the extinction and emission corrected $4.5 \mu\text{m}$ image to measure the light distribution. The image was smoothed to a scale of $5'' \cdot \text{pixel}^{-1}$, and extends over $\sim 270 \text{ pc} \times 200 \text{ pc}$. We excluded a central circle with $r = 0.6 \text{ pc}$ ($\sim 15''.4$) to avoid contribution from ionised gas emission and young stars. In addition we masked out the young Quintuplet star cluster (Figer et al. 1999), and the dark $20\text{-km}\cdot\text{s}^{-1}$ -cloud M-0.13-0.08 (García-Marín et al. 2011).

We used the MGE_FIT_SECTORS package (Cappellari 2002) to derive the surface brightness distribution. The Multi-Gaussian Expansion model (Emsellem et al. 1994) has the advantage that it can be deprojected analytically. We measured the photometry of the two images along the major axis and the minor axis. The centre is the position of Sgr A*, which is the radio source associated with the Galactic centre supermassive black hole. We fitted a scale factor to match the photometry of the two images in the region where they overlap ($16'' - 27''.8$). Then we measured the photometry on each image along 12 angular sectors, and converted the NACO photometry to the *Spitzer* flux. Assuming four-fold symmetry, the measurements of four quadrants are averaged on elliptical annuli with constant ellipticity. Using the photometric measurements of the two images, we fitted a set of two-dimensional Gaussian functions, taking the point-spread-function (PSF) of the NACO image into account.

A comparison with the surface brightness profile of Fritz et al. (2016, their Fig. 2) showed that our profile is steeper in the central $\sim 30''$. A possible reason is the small overlap region of the *Spitzer* and NACO images, and that the *Spitzer* flux could be too high at the centre. Maybe the PAH emission correction of the *Spitzer* image was too low. The mid-infrared dust emission is significant out to almost $1'$. Fritz et al. (2016) used NACO H - and K_S -band images in the central $r = 20''$. Out to $1000''$ ($\sim 39 \text{ pc}$) they used *Hubble Space Telescope* WFC3 data (M127 and M153 filters) and public VISTA Variables in the Via Lactea Survey images (H - and K_S -bands, Saito et al. 2012). We lowered the intensities of the central Gaussians by scaling our averaged profile to the one-dimensional flux density profile of Fritz

Table 3.1: The Multi-Gaussian Expansion (MGE) fit parameters for the $4.5\ \mu\text{m}$ *Spitzer*/IRAC dust extinction and PAH emission corrected image in combination with the NACO *H*-band mosaic scaled to *Spitzer* flux. I_{scaled} is the peak surface brightness used in the dynamical modelling, σ_{MGE} is the standard deviation, and q is the axial ratio of the Gaussian components. I_{unscaled} is the peak surface brightness before scaling to Fritz et al. (2016).

I_{scaled} [$10^4 L_{\odot,4.5\mu\text{m}} \text{pc}^{-2}$]	σ_{MGE} [arcsec]	q	I_{unscaled} [$10^4 L_{\odot,4.5\mu\text{m}} \text{pc}^{-2}$]
0.86	1.7	0.30	312
32.4	10.4	0.34	164
89.8	15.0	0.82	257
18.5	52.1	0.95	30.0
17.0	98	0.36	29.3
7.1	154	0.95	7.4
4.8	637	0.36	4.9
3.2	2020	0.30	3.2
1.3	4590	0.81	1.3

et al. (2016). As a result the amplitudes of the inner Gaussians become smaller, but the outer Gaussians ($\sigma_{\text{MGE}} > 100'' \sim 4 \text{ pc}$) are nearly unchanged. We list the components of the Multi-Gaussian Expansion in Table 3.1 and plot the profile in Fig. 3.2.

We note that there are three main differences with the surface brightness distribution derived by Feldmeier et al. (2014): (1) We used an *H*-band instead of a K_S -band NACO image to avoid ionised gas emission; (2) We masked young stars in the NACO image to match the distribution of stars used as kinematic tracers; and (3) We scaled the central photometry to the flux density data of Fritz et al. (2016) to avoid a possible overestimation of the central flux when scaled to the *Spitzer* image. All three changes influence only the central part of the surface brightness distribution, as ionised gas emission and light from young stars are only important in the central parsec.

3.3 Dynamical models of the Milky Way nuclear star cluster

3.3.1 Schwarzschild's method

Orbit-based models or Schwarzschild models are a useful tool to model the dynamics of stellar systems by orbit superposition. The first step of Schwarzschild's method is to integrate the equations of motion for a representative library of stellar orbits in a gravitational potential Φ . Then the observables for each orbit are computed, considering projection, PSF convolution and pixel binning. The next step is to find orbital weights to combine the orbits such that they reproduce the observed data. Schwarzschild models are a powerful tool to recover

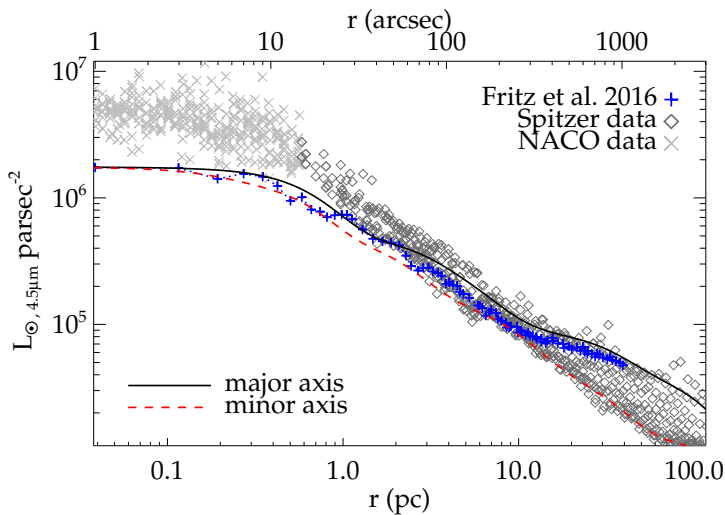


Figure 3.2: Surface brightness profile derived from a dust extinction and PAH emission corrected *Spitzer*/IRAC 4.5 μm image and NACO *H*-band mosaic for the centre, scaled to the measurements of Fritz et al. (2016, blue crosses). The black full line denotes the MGE fit along the major axis, and the red dashed line along the minor axis.

the intrinsic kinematical structure and the underlying gravitational potential (Schwarzschild 1979; van de Ven et al. 2008; van den Bosch & van de Ven 2009). We refer the reader for further details to van den Bosch et al. (2008) for implementation and van de Ven et al. (2008) for verification of the triaxial Schwarzschild code.

3.3.1.1 Mass model

We calculated orbits in the combined gravitational potential of a supermassive black hole Φ_{\bullet} and the star cluster Φ_{\star} , inferred from the imaging data. As we run triaxial models, there are three intrinsic shape parameters, p , q , and u , for the cluster. The shape parameters characterise the axis ratios for the long, intermediate and short axes x , y , and z . They are defined as $p = y/x$, $q = z/x$, and $u = x'/x$, where x' is the length of the longest axis x projected on the sky. Thus, u represents the compression of x due to projection on the sky. Each set of axis ratios refers to a set of viewing angles (θ, ϕ, ψ) . The surface brightness distribution is deprojected given the intrinsic shape parameters p, q, u , and multiplied with the dynamical mass-to-light ratio Y to get the intrinsic stellar mass density ϱ_{\star} . From Poisson's equation $\nabla^2 \Phi_{\star} = 4\pi G \varrho_{\star}$ one calculates the gravitational potential. We do this for different values of the black hole mass M_{\bullet} , dynamical mass-to-light ratio Y , and different shape parameters. In total our model has five free parameters, M_{\bullet} , Y , p , q , and u .

Besides the considered stellar population and the supermassive black hole, there are other components within the nuclear star cluster, which we neglected. We measure a dynamical

mass-to-light-ratio, which combines the stellar mass-to-light-ratio with other components. These components are the young stars, ionised gas, neutral gas, and dark matter. The young stars are at a distance of about 0.5 pc from the supermassive black hole. The lower limit of the total mass of young stars is $12\,000 M_{\odot}$ (Feldmeier-Krause et al. 2015). However, the total enclosed stellar mass in the same region is $\sim 10^6 M_{\odot}$ (Oh et al. 2009; Feldmeier et al. 2014), and the mass of the supermassive black hole is $4 \times 10^6 M_{\odot}$. The mass of the young stars is therefore probably negligible. The hot ionised gas has a mass of only a few $100 M_{\odot}$ (Ferrière 2012), and cannot influence the stellar dynamics significantly. The neutral gas in the circum-nuclear disc may contribute more mass, estimates range from $10^4 M_{\odot}$ (Etxaluze et al. 2011; Requena-Torres et al. 2012) to $10^6 M_{\odot}$ (Christopher et al. 2005), though this is probably the upper limit (Genzel et al. 2010). The circum-nuclear disc extends over a distance of about 1 pc to more than 5 pc from the centre. At 5 pc the total enclosed stellar mass is $\sim 10^7 M_{\odot}$ (McGinn et al. 1989; Feldmeier et al. 2014). We decided to neglect the mass distribution of the circum-nuclear disc in our dynamical models, since it is very uncertain, and makes up only 0.1 to 10 per cent of the stellar mass. The contribution of dark matter to the nuclear star cluster mass is also neglected. Linden (2014) show that the fraction of dark matter in the central 100 pc of the Milky Way is about 6.6 per cent, assuming the traditional dark matter profile of Navarro et al. (1996).

3.3.1.2 Orbit library

The orbit library should be as general as possible and representative for the potential. We assume that the orbits are regular and that three integrals of motion, E , I_2 , and I_3 , are conserved. The orbit families consist of box orbits, which can cross the centre and have an average angular momentum of zero, and three types of tube orbits, which avoid the centre. The tube orbits are divided in short-axis-tube orbits, which have non-zero mean angular momentum $\langle L_z \rangle$ around the short axis, outer and inner long-axis-tube orbits, which have non-zero mean angular momentum $\langle L_x \rangle$ around the long axis. The orbit grid should sample the entire phase space. It has to be dense enough to suppress discreteness noise, but integration has to be done in a reasonable amount of computing time.

We followed van den Bosch et al. (2008) and sample the orbit energy E using a logarithmic grid in radius. Each energy E is linked to the radius R_c by calculating the potential at $(x, y, z) = (R_c, 0, 0)$. We sample $N_E = 35$ energies calculated from R_c in logarithmic steps ranging from $R_c = 10^{0.5}$ to $R_c = 10^{4.2}$, i.e. $3'16$ to $4'4$ or 0.12 pc to 616.5 pc. We note that the outer radius is about 3.5 times the outermost Gaussian σ_{MGE} of the MGE fit. We tested lower values of the inner radius but found consistent results. For each energy, the starting point of an orbit is selected from a linear grid over 14 values each. For details on the orbit sampling we refer to van den Bosch et al. (2008). In total, we have $N_E \times N_{I_2} \times N_{I_3} = 35 \times 14 \times 14 = 6860$ orbits. Each orbit is integrated over 200 periods, and sampled on 100 000 points per orbit. For each orbit we store the intrinsic and projected properties. The projected orbits are stored in a (x', y', v_z) grid, with PSF convolution and pixel size of the observed data taken

into account. The velocities are stored in 183 bins between $-7.4 \sigma_{\max}$ and $+7.4 \sigma_{\max}$. These numbers guarantee a proper sampling of the observed velocity profiles (Cretton et al. 1999).

3.3.1.3 Solving the orbital weight distribution

The model has to fit the kinematic data, the intrinsic, and the projected mass distribution. The fit is done by finding a linear combination of the orbits, and solving for orbital weights γ_i . Each orbital weight corresponds to a mass on the respective orbit i , and the weights γ_i are therefore non-negative. We used the non-negative least-squares (NNLS) logarithm of Lawson & Hanson (1974), which was also used by Rix et al. (1997), van der Marel et al. (1998), and Cretton et al. (1999). One of the fitting constraints is to make sure that the model is self-consistent. It is required that the orbit superposition reproduces the intrinsic and projected aperture masses within two per cent, which is the typical accuracy of the observed surface brightness (van den Bosch et al. 2008).

3.3.2 Constraining the input parameters

We ran 4899 models with different parameter combinations of M_{\bullet} , Y , q , p , u . The black hole mass M_{\bullet} was sampled in logarithmic steps of 0.2 from 5.5 to 7.5, starting with 6.3 (i.e. $M_{\bullet} \approx 2 \times 10^6 M_{\odot}$). The mass-to-light ratio Y was linearly sampled between 0.1 and 2.0 with steps of 0.04, with a starting value of 0.6 (in units of $M_{\odot}/L_{\odot,4.5\mu\text{m}}$). The starting model had $(p, q, u) = (0.84, 0.29, 0.99)$. We sampled different combinations of (p, q, u) in steps of (0.02, 0.01, 0.01), with $0.40 < p < 0.99$, $0.05 < q < 0.29$, and $0.70 < u \leq 0.99$. We found the best fit of the five parameters by calculating the χ^2 from the kinematic measurements. The number of observables is the number of kinematic bins times the number of kinematic moments, in our case $N = 175 \times 4 = 700$.

3.3.3 Modelling results

3.3.3.1 The best-fitting model

Our best-fitting parameters are $M_{\bullet} = 3.0 \times 10^6 M_{\odot}$, $Y = 0.90$, $q = 0.28$, $p = 0.64$, $u = 0.99$. This corresponds to best-fitting viewing angles $\vartheta = 80^\circ$, $\varphi = 79^\circ$, $\psi = 91^\circ$. We show the surface brightness map and the symmetrised kinematic maps in Fig. 3.3. The upper row are the data, the lower row are the maps of the best-fitting model. The misalignment of the kinematic rotation axis with respect to the photometry, and the perpendicular rotating substructure at $\sim 20''$ (~ 0.8 pc) found by Feldmeier et al. (2014) are well reproduced in the model velocity map. The surface brightness map is reproduced within one per cent. The best fit has $\chi^2 = 290$. With $M = 5$ fitted parameters and $N = 700$ observational constraints, this means $\chi_{\text{red}}^2 = 0.42$. That χ_{red}^2 is less than one is partially due to the large uncertainties of the kinematics, and the fact that the kinematic measurements are correlated.

We illustrate the distribution of χ^2 for the 4899 models in Fig. 3.4. We plot each combination of parameters. Red colours denote low χ^2 , bluer, smaller symbols denote high χ^2 .

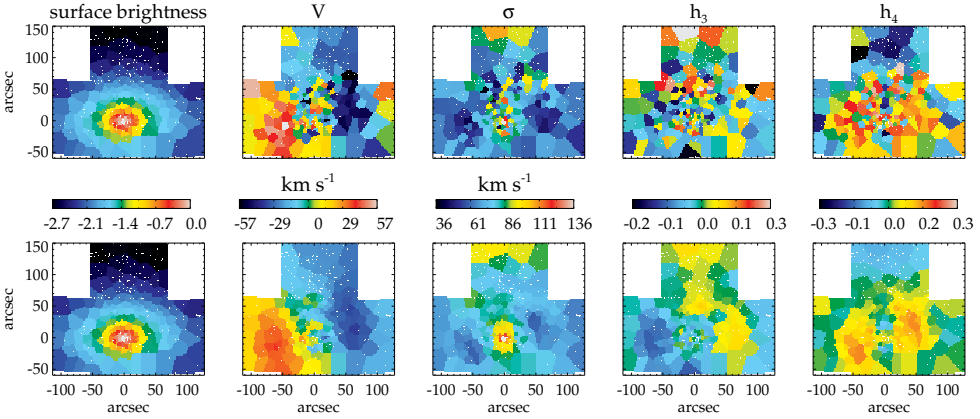


Figure 3.3: Comparison of the observed stellar surface brightness and kinematics (top row) and the best-fitting Schwarzschild model. The columns denote surface brightness, velocity V , velocity dispersion σ , Gauss-Hermite moments h_3 , and h_4 .

The black cross denotes the best-fitting model. The value of q is constrained by the surface brightness profile. As the lowest value of q_{MGE} is 0.30, the deprojected q cannot be higher. Likewise, the value of $u = 0.99$ is the boundary value of the grid. The values of q , p , and u are averaged over the entire system, i.e. the nuclear stellar disc and the embedded nuclear star cluster. The upper left panel of Fig. 3.4 shows that for each value of u , the best-fitting Y is near to 0.90. A similar behaviour is found with p and q . There is only a slight increase of the best-fitting Y with higher values of p . At the same time, the best-fitting values of M_\bullet do not vary strongly with q , p , or u (second row). The intrinsic shape parameters do not influence our best fit for M_\bullet , as this measurement is mostly made from the inner bins and the outer bins contribute little. The outer bins certainly contribute to the intrinsic shape fit. The supermassive black hole mass and the dynamical mass-to-light ratio are correlated. For higher values of Y , a lower M_\bullet fits the data.

We show how χ^2 depends on the different parameters in Fig. 3.5. The best-fitting model, which has the lowest χ^2 , is marked as blue asterisk symbol. The blue lines denote the 1σ , 2σ , and 3σ confidence limits, corresponding to $\Delta\chi^2 = 5.9$, 11.3, and 18.2. The red line illustrates the standard deviation of χ^2 itself, i.e. $\sqrt{2(N-M)} = 37.3$, where $N = 700$, and $M = 5$. This value was used as confidence limit by van den Bosch & van de Ven (2009). In Table 3.2 we list the 1σ and 3σ uncertainties.

3.3.3.2 Mass profile

We show the enclosed total mass as a function of the projected radius in Fig. 3.6, grey shaded contours are the 3σ uncertainty. The mass was computed within ellipses. We also plot the results of various other studies. Most studies assumed spherical symmetry, Feldmeier et al.

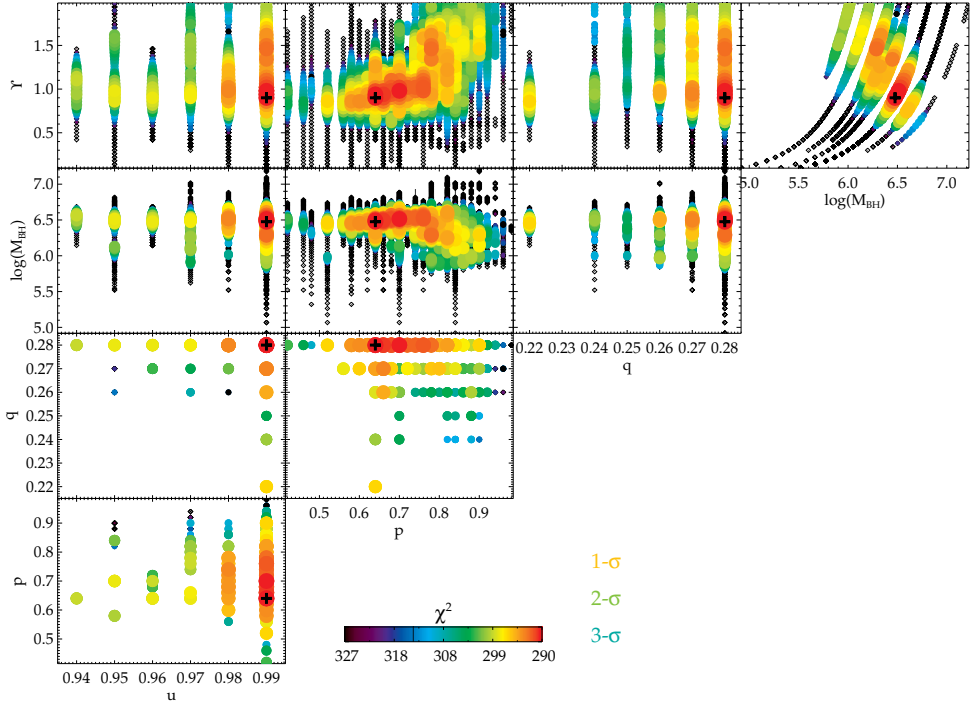


Figure 3.4: Illustration of the fitted parameter space. Each symbol denotes a model, the coloured symbols are models with $\Delta\chi^2 < \sigma_{\chi^2} = 37.3$, black diamonds are models with $\Delta\chi^2 > \sigma_{\chi^2}$. The 1σ , 2σ , and 3σ colours corresponding to $\Delta\chi^2 = 5.9$, 11.3 and 18.2 , are denoted. The black cross denotes the best-fitting model.

Table 3.2: The best-fitting model results and the 1σ and 3σ uncertainties, corresponding to $\Delta\chi^2 = 5.9$ and 18.2 .

parameter	best fit	1σ	3σ	unit
M_{\bullet}	3.0	+1.1 -1.3	+2.4 -2.3	$\times 10^6 M_{\odot}$
Y	0.90	+0.76 -0.08	+1.12 -0.32	$M_{\odot} / L_{\odot,4.5\mu\text{m}}$
q	0.28	+0.0 -0.02	+0.0 -0.06	
p	0.64	+0.18 -0.06	+0.30 -0.22	
u	0.99	+0.0 -0.01	+0.0 -0.05	

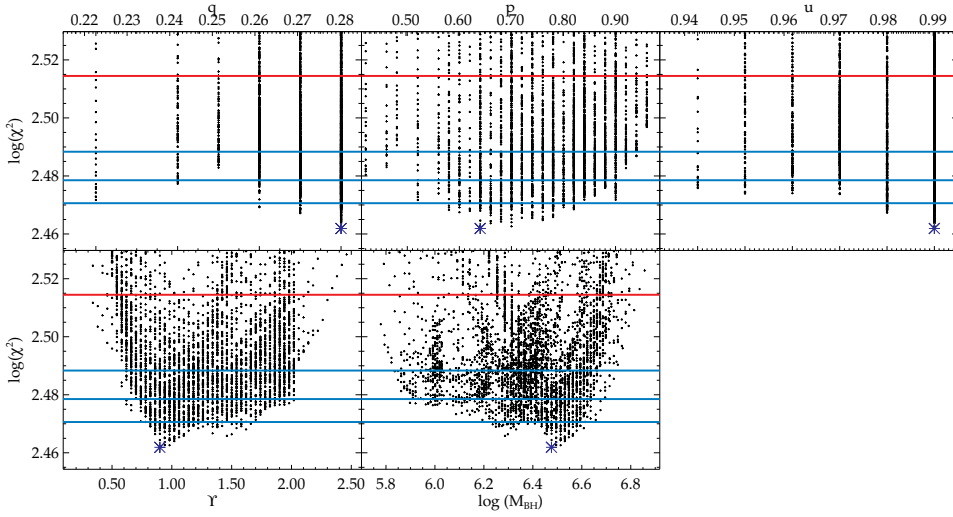


Figure 3.5: The χ^2 values plotted against the five free parameters (M_\bullet , Y , q , p , u). The best-fitting model is denoted as blue asterisk, the 1σ , 2σ , and 3σ confidence level, corresponding to $\Delta\chi^2 = 5.9$, 11.3, and 18.2, are denoted as blue lines. The red line denotes $\sigma_\chi^2 = 37.3$.

(2014) and Chatzopoulos et al. (2015a) assumed axisymmetry. Some of the studies used also different Galactocentric distances, so we scaled the masses to $R_0 = 8.0$ kpc. Our results are in agreement with other studies in the central $100''$. At larger radii $r \approx 400''$ (~ 15.5 pc) beyond the reach of our kinematic data, we obtained a higher mass than Lindqvist et al. (1992a). Their data extend to larger radii, but their assumption of spherical symmetry does no longer hold at such large radii. Launhardt et al. (2002) took the flattening of the nuclear stellar disc into account and obtained $M_\star = (8.0 \pm 2) \times 10^8 M_\odot$ within 120 pc, and in addition $M_{\text{MWNSC}} = (3 \pm 1.5) \times 10^7 M_\odot$ for the nuclear star cluster. Our best-fitting model has a total enclosed mass $M_\star = (8.8^{+7.4}_{-0.8}) \times 10^8 M_\odot$ inside an ellipse with semi-major axis distance 120 pc, which is in agreement with Launhardt et al. (2002). The enclosed stellar mass at $r = 8.4$ pc, i.e. about two times the effective radius of the nuclear star cluster, is $M_{\text{MWNSC}} = (3.1^{+2.8}_{-0.3}) \times 10^7 M_\odot$. The uncertainty comes from the 1σ uncertainty of the mass-to-light ratio Y .

The black hole influences the stellar kinematics only at the centre of the nuclear star cluster. Out to $r = 33''$ (~ 1.3 pc), the best-fitting mass of the black hole ($M_\bullet = 3.0 \times 10^6 M_\odot$) is higher than the enclosed stellar mass of our best-fitting model. Assuming $M_\bullet = 4 \times 10^6 M_\odot$, this radius increases to $41''$ (~ 1.6 pc). Merritt (2004) defined the radius of influence of a black hole as the radius where the enclosed stellar mass equals two times the black hole mass. With this definition and a black hole mass of $4 \times 10^6 M_\odot$, we obtain $r_{\text{infl}} = 71''$ (~ 2.8 pc). This value of r_{infl} is higher than the result of Feldmeier et al. (2014, $(60^{+55}_{-17})''$), as our model has less stellar mass in the centre. We have excellent agreement with Alexander (2005), who found $r_{\text{infl}} = 3$ pc. The kinematic measurements at larger radii have little influence on the black

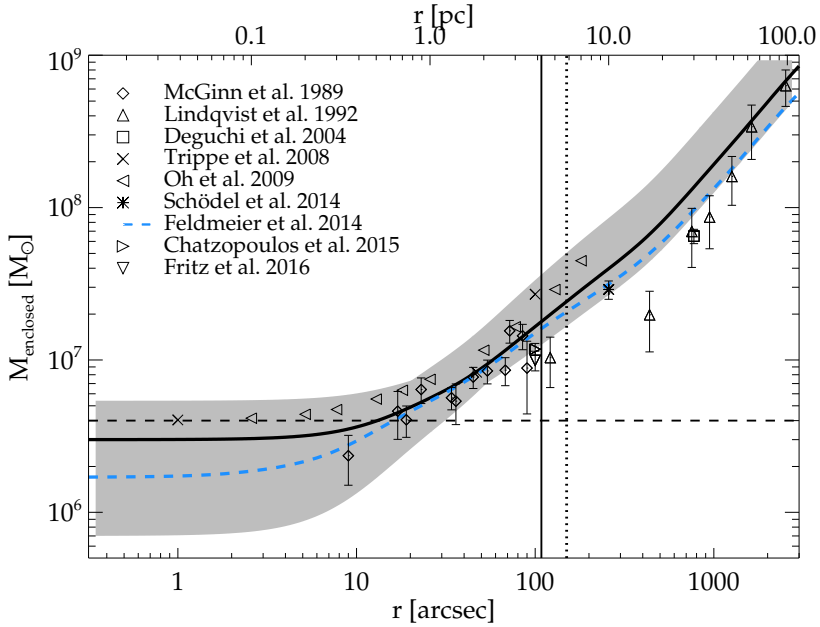


Figure 3.6: Enclosed total mass within a distance of $0'.3$ to $50'$ along the mean radius of the ellipses in units of M_{\odot} and in logarithmic scaling. The black line denotes the enclosed mass with $Y = 0.90$ and $M_{\bullet} = 3.0 \times 10^6 M_{\odot}$, the grey shaded contours are for $Y = 0.90$ $^{+1.12}_{-0.32}$ and $M_{\bullet} = (3.0^{+2.4}_{-2.3}) \times 10^6 M_{\odot}$. The horizontal line denotes a supermassive black hole with the mass $M_{\bullet} = 4 \times 10^6 M_{\odot}$. The vertical, dotted line denotes the outer edge of the kinematic data, the vertical, solid line denotes the effective radius. We also plot the results for the enclosed mass from previous studies. We scaled the masses to $R_0 = 8.0$ kpc if the study assumed a different Galactocentric distance: McGinn et al. (1989, diamonds, assumed $R_0 = 8.5$ kpc), Lindqvist et al. (1992a, upward triangles, $R_0 = 8.5$ kpc), Deguchi et al. (2004, squares), Trippe et al. (2008, x-symbol), Oh et al. (2009, leftfacing triangles), Schödel et al. (2014a, asterisk), Feldmeier et al. (2014, blue dashed line), Chatzopoulos et al. (2015a, rightfacing triangle, $R_0 = 8.3$ kpc), and Fritz et al. (2016, downward triangle, $R_0 = 8.2$ kpc).

hole mass measurement, but are important to constrain the orbital structure and dynamical mass-to-light ratio.

3.3.3.3 Internal dynamics

The best-fitting model has tangential anisotropy in the centre of the cluster. The value of the anisotropy $\beta = 1 - \sigma_t^2 / \sigma_r^2$ is negative, where σ_t is the tangential velocity dispersion and σ_r is the radial velocity dispersion. We show the anisotropy β as a function of radius in Fig. 3.7, top panel. We plot the mean anisotropy of the models within the 1σ uncertainty limit. The uncertainty of β is given by the standard deviation and is about 0.1. The plot extends to the outer edge of the kinematic data at $150''$. The vertical, solid line denotes the

photometric effective radius $r_{\text{eff}} = 4.2$ pc, the dashed line denotes the radius of influence $r_{\text{inf}} = 71''$ (~ 2.8 pc). The cluster kinematics becomes nearly isotropic at radii $r > 70''$.

We show the angular momentum distribution of the orbits in Fig. 3.8. The colours denote the density of orbits passing radius r with mean angular momentum $\langle \lambda_z \rangle$ (left panel) or $\langle \lambda_x \rangle$ (right panel). The plot of $\langle \lambda_z \rangle$ denotes rotation about the short z-axis. Orbits with $\langle \lambda_z \rangle \neq 0$ are contributed by short-axis-tube orbits, while long-axis-tube orbits have $\langle \lambda_z \rangle = 0$. On the other hand, $\langle \lambda_x \rangle$ denotes rotation about the long x-axis (bottom panel), and orbits with $\langle \lambda_x \rangle \neq 0$ are contributed by long-axis-tube orbits. Short-axis-tube orbits have $\langle \lambda_x \rangle = 0$. Long-axis-tube orbits are most important in the central 20–60'' and at larger radii $r \gtrsim 80''$. Short-axis-tube orbits, which contribute in total more mass than long-axis-tube orbits, are most important at $r = 60$ –140''. We illustrate the distribution of the stellar mass on the different orbit types also in Fig. 3.7 (bottom panel) as a function of radius. Most stars (>50 per cent) are on short-axis-tube orbits, i.e. they orbit the minor axis. Long-axis-tube orbits contribute about 40 per cent in the central 30''. They produce the perpendicular rotating substructure at $r \approx 20''$ (~ 0.8 pc) found by Feldmeier et al. (2014). At larger radii, long-axis-tube orbits contribute only about 30 per cent to the stellar mass. Box orbits contribute little mass in the centre (<10 per cent), but their fraction increases towards larger radii. At $r = 150''$ (~ 5.8 pc), they contribute 20 per cent.

3.4 Discussion

3.4.1 Difference of the resulting black hole mass

The currently best black hole mass estimate is $(4.1 \pm 0.6) \times 10^6 M_{\odot}$ (Ghez et al. 2008), $(4.3 \pm 0.39) \times 10^6 M_{\odot}$ (Gillessen et al. 2009b) or $(4.02 \pm 0.20) \times 10^6 M_{\odot}$ (Boehle et al. 2016), derived from Keplerian stellar orbits around the supermassive black hole. Using axisymmetric Jeans models and the same spectroscopic data as this study, Feldmeier et al. (2014) found a lower value of $M_{\bullet} = (1.7_{-1.1}^{+1.4}) \times 10^6 M_{\odot}$. The best fit using triaxial Schwarzschild models is $(3.0_{-1.3}^{+1.1}) \times 10^6 M_{\odot}$. This measurement is consistent with the direct measurements of Ghez et al. (2008), Gillessen et al. (2009b), and Boehle et al. (2016) within the 1σ uncertainty limit. The result is also in agreement with the lower black hole mass of Feldmeier et al. (2014). We derived a 3σ lower limit for the black hole of $0.7 \times 10^6 M_{\odot}$, and an upper limit of $5.4 \times 10^6 M_{\odot}$. We briefly discuss the model degeneracies, possible reasons for the different black hole mass measurements, and why our results are closer to the direct measurement than the black hole mass derived by Feldmeier et al. (2014).

3.4.1.1 Model degeneracies

Some model parameters seem to be correlated. This becomes clear when looking at Fig. 3.4. The best-fitting value of p apparently increases with increasing dynamical mass-to-light ratio Y (second column of the first row). However, the value of p has little effect on M_{\bullet} , as can be seen in the second column of the second row in Fig. 3.4. With a lower value of p , the

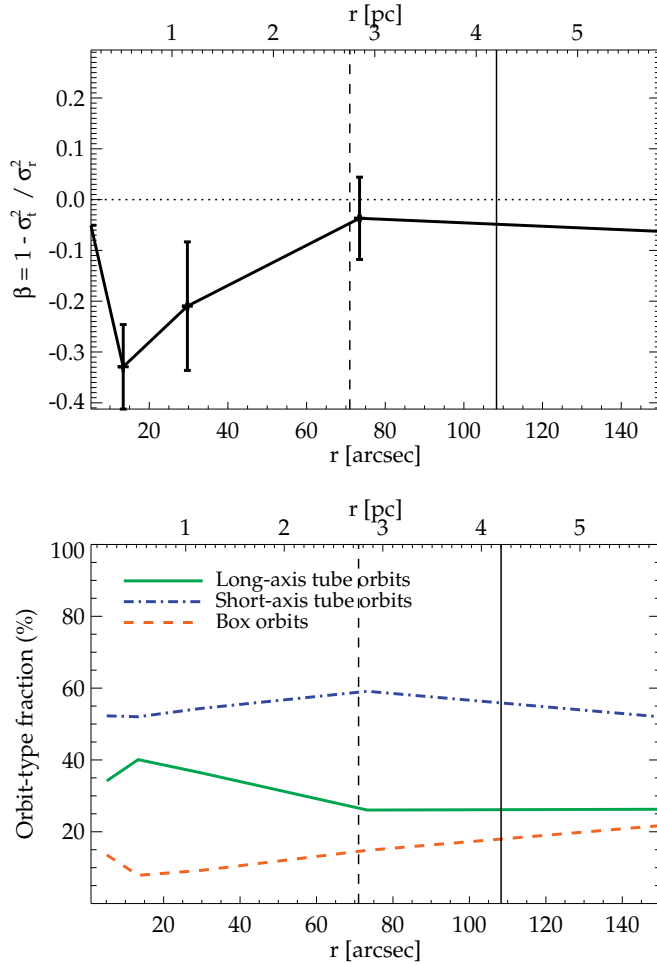


Figure 3.7: Top: Anisotropy β as a function of radius r . Negative values denote tangential anisotropy, positive values radial anisotropy. Bottom: Orbital structure of the Milky Way nuclear star cluster as a function of radius. The green, solid line denotes long-axis-tube orbits; the blue, dot-dashed line short-axis-tube orbits; the red, dashed line box orbits. The vertical, solid line denotes $r_{\text{eff}} = 4.2$ pc (Schödel et al. 2014a); the vertical, dashed line $r_{\text{infl}} = 71''$.

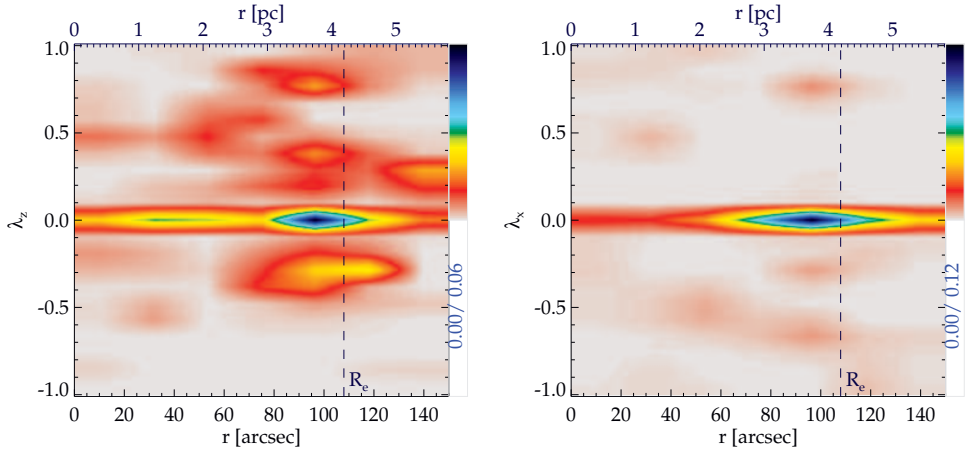


Figure 3.8: Orbit density with angular momentum λ_z (left), i.e. rotation around the short axis, and λ_x (right), i.e. rotation around the long axis. Dark, blue colour indicates higher orbit density. The vertical, dashed line denotes $r_{\text{eff}} = 4.2$ pc (Schödel et al. 2014a).

best-fitting M_\bullet decreases only slightly. At larger p , the χ^2 -contours of M_\bullet and Y broaden. This means that for a more oblate axisymmetric cluster with p closer to one, M_\bullet and Y are not as well constrained as with smaller values of p .

The dynamical mass-to-light ratio Y is inversely correlated with the black hole mass (fourth column of the first row in Fig. 3.4). The higher Y , i.e. the more massive the cluster, the less massive is the black hole. This degeneracy is often obtained in dynamical models. Valluri et al. (2004) found that the degeneracy of M_\bullet depends on how well the black hole’s sphere of influence is resolved, whereas the measurement of Y is better constrained when the data extend to larger radii. We have several kinematic data bins within the radius of influence of the supermassive black hole, and our data extend to one effective radius. This may not be sufficient to put strong constraints on Y . To get agreement with the measurement of $(4.1 \pm 0.6) \times 10^6 M_\odot$ (Ghez et al. 2008), $(4.3 \pm 0.39) \times 10^6 M_\odot$ (Gillessen et al. 2009b), and $(4.02 \pm 0.20) \times 10^6 M_\odot$ (Boehle et al. 2016), we would require a lower value of $Y \approx 0.75$.

3.4.1.2 Influence of the surface brightness profile

The shape of the surface brightness profile is important to estimate the mass of the supermassive black hole. The surface brightness profile has to represent the density of the kinematic tracer. We excluded young stars and ionised gas from the surface brightness profile, as these components contribute little mass compared to the cool, old stars we used as kinematic tracers. Excluding these components results in a lower surface brightness and stellar mass in the centre compared to Feldmeier et al. (2014). The stellar mass we obtain at $r = 32''$ (~ 1.2 pc) is $1 \times 10^6 M_\odot$ less. Our black hole mass is therefore higher, and closer to the direct measurement of $M_\bullet \approx 4 \times 10^6 M_\odot$. We ran the same axisymmetric models (Cappellari 2008), using

the same kinematic data as Feldmeier et al. (2014), but our surface brightness distribution from Table 3.1. The best fit is obtained with $M_{\bullet} = (2.8^{+1.3}_{-0.8}) \times 10^6 M_{\odot}$, $Y = 0.89^{+0.12}_{-0.19}$, and a constant anisotropy of $\beta = -0.3$. This result is in agreement with the triaxial Schwarzschild models, and confirms that the surface brightness profile has a strong influence on the results of the black hole mass and dynamical mass-to-light ratio.

3.4.1.3 Spatially varying mass-to-light ratio

We assumed a constant dynamical mass-to-light-ratio Y for the Schwarzschild models. We obtained $Y = 0.90^{+0.76}_{-0.08}$ (1σ uncertainty). The dynamical mass-to-light-ratio combines the stellar mass-to-light-ratio with other components, it is sensitive to the presence of gas or dark matter.

Our best-fitting value of $Y = 0.9$ is higher than expected from stellar-population studies at $3.6 \mu\text{m}$, which found $Y = 0.4 - 0.75$ (McGaugh & Schombert 2013; Meidt et al. 2014). At $4.5 \mu\text{m}$, Y is rather less than at $3.6 \mu\text{m}$ (Oh et al. 2008). Our measurement of Y is averaged over the entire field of the kinematic data. We cannot exclude that the stellar age or metallicity changes over the range of the kinematic data. Stellar population studies of the red giant population were mostly confined to the central 1 pc. Our knowledge of the stellar population at the outer region of our field is based on only a few bright stars (e.g. Blum et al. 2003; Feldmeier et al. 2014). But these stars are brighter and probably younger than our kinematic tracer stars. However, the mass-to-light ratio for old stars in the mid-infrared varies modestly with age and metallicity in comparison to the optical mass-to-light ratio (Meidt et al. 2014). Therefore we do not expect a change of Y by more than ~ 0.3 within the cluster. Should Y vary with radius, our mass profile (Fig. 3.6) could have a different shape. For example, if Y was lower in the centre than outside, this would increase M_{\bullet} , and there would be less mass in the stellar component.

However, the stellar mass-to-light ratio may also increase towards the central $r = 0.5$ pc, as massive stellar remnants may migrate to the centre. The mass and distribution of dark stellar remnants, i.e. stellar mass black holes and neutron stars, in the central parsec of the nuclear star cluster is uncertain. For a top-heavy initial mass function, there could be $> 1 \times 10^6 M_{\odot}$ in dark remnants (Morris 1993), though Löckmann et al. (2010) found a lower mass of about $1 \times 10^5 M_{\odot}$ for a canonical initial mass function.

In our models we neglected the mass of molecular gas in the circum-nuclear disc. The molecular gas may contribute $10^4 - 10^6 M_{\odot}$. The gas disc extends from $r \approx 1-7$ pc along the Galactic plane, but only to $r \approx 3$ pc along the minor axis (Ferrière 2012). Thus, the molecular gas is located in the central part of our spectroscopic field, but absent in the North. If the gas contributes significantly to the cluster mass, our assumption of spatially constant Y would be violated. Further, our result of Y would be higher than expected from stellar population studies. When we assume the maximum gas mass of $10^6 M_{\odot}$, the value of a constant Y decreases to about 0.85, which is within our 1σ uncertainty limit.

The spatial distribution of dark matter in the Galactic centre is uncertain. A classical cuspy Navarro et al. (1996) dark matter profile results in a dark matter fraction of about 6.6

per cent in the central 100 pc (Linden 2014). However, black hole accretion, dark matter annihilation, and scattering alter the shape of the dark matter distribution in the Galactic centre. Vasiliev & Zelnikov (2008) found that these effects produce a shallower dark matter profile in the central 2 pc than further out. The dark matter mass inferred from the classical cusp is reduced by up to 50 per cent in the central 2 pc. The contribution of dark matter to the nuclear star cluster mass should therefore be negligible. Although the dark matter distribution may be different from the luminous baryonic matter, and the dynamical mass-to-light ratio for that reason not spatially constant, the effect on the cluster mass distribution should be only minor.

3.4.2 Triaxial cluster shape

Our best-fitting model has axis ratios of $p = y/x = 0.64^{+0.18}_{-0.06}$, $q = z/x = 0.28^{+0.0}_{-0.02}$, and $u = x'/x = 0.99^{+0.0}_{-0.01}$. These axis ratios correspond to viewing angles $\vartheta = 80^\circ$, $\varphi = 79^\circ$, and $\psi = 91^\circ$. The angle ϑ denotes the polar viewing angle, φ the azimuthal viewing angle, and ψ is the misalignment angle between photometric major axis and the projected intrinsic long axis (van den Bosch et al. 2008; van den Bosch & van de Ven 2009). For the best-fitting model the angle α between the cluster's major axis and the line-of-sight is about 79° . The cluster's shape is strongly triaxial, with a triaxiality parameter $T = (1 - p^2)/(1 - q^2) = 0.64$. An oblate axisymmetric system has $T = 0$, a prolate axisymmetric system has $T = 1$.

Also the Milky Way's bulge is triaxial, the axis ratios are $p = 0.63$ and $q = 0.26$ (Wegg & Gerhard 2013). The shape was derived from the density of red clump stars in the central 800 pc of the bulge. The Milky Way bulge is much larger than the nuclear star cluster, and extends out to about 2.5 kpc. Intriguingly, the intrinsic shape parameters p and q of the Galactic bulge agree with our best-fit results for the nuclear star cluster within the error bars. The bulge has a peanut or X-shape (Nataf et al. 2010; McWilliam & Zoccali 2010). The angle α between the bulge major axis and the line-of-sight to the Galactic centre is about 27° (Rattenbury et al. 2007; Wegg & Gerhard 2013), while we obtained 79° for the nuclear star cluster.

One possible scenario for nuclear star cluster formation is that massive star clusters (10^5 – $10^7 M_\odot$) formed in the galactic disc, migrated to the galaxy's centre and merged (Neumayer et al. 2011; Guillard et al. 2016). Simulations of multiple star cluster mergers and of star cluster accretion on a nuclear stellar component can produce triaxial nuclear star clusters (Bekki et al. 2004; Hartmann et al. 2011; Perets & Mastrobuono-Battisti 2014). However, so far no systematical observational study was able to constrain the triaxial shape of nuclear star clusters in general. Hartmann et al. (2011) constrained the shape of two nuclear star clusters and found agreement with an axisymmetric shape.

3.4.3 Caveats and considerations

3.4.3.1 Regime of semi-resolved populations

We used integrated light spectroscopy to measure the stellar kinematics. This is the common approach for extragalactic systems, which have a distance of several Mpc. The measured kinematics are weighted by the respective luminosities of different stars. As the Milky Way nuclear star cluster is only 8 kpc distant, we are in the regime of semi-resolved populations. The brightest stars can be resolved individually, and these stars contribute a large fraction of the flux. A consequence of this is that individual spatial bins can be dominated by a single star. Instead of measuring the spectrum of an ensemble of stars, one measures a spectrum in which a large percentage of the flux is contributed by one single star. This causes shot noise, and high differences between neighbouring spatial bins. We accounted for this problem by excluding the brightest stars from the spectroscopic map. This method helps to significantly reduce the intrinsic scatter of the velocity dispersion (Lützgendorf et al. 2011; Bianchini et al. 2015). We further increased the kinematic uncertainties such that the data in two neighbouring bins have consistent values within their uncertainties. This helps to prevent that the models fit only stochastic shot noise. Due to the large kinematic uncertainties, the intrinsic shape parameters p , q , u , and the dynamical mass-to-light ratio Y are not very well constrained, and have large error margins.

At a distance of only 8 kpc, also the relative distances of the stars become more important. A star located on the near side of the nuclear star cluster, at a distance $d = 7.9$ kpc, contributes 1.05 times more flux than a star with the same absolute magnitude at the far side of the cluster, at $d = 8.1$ kpc. In an extragalactic system, the distance of a star at the near side and the distance of a star at the far side with respect to the observer are approximately the same, as the system is farther away. For a galaxy at $d = 5$ Mpc, a relative difference of 200 pc changes the flux only by a factor 1.00008. Even foreground stars that belong to the outer parts of the stellar system contribute roughly the same flux as a star with the same magnitude that is located in the galactic nucleus.

3.4.3.2 Interstellar extinction

Another observational complication is interstellar extinction in the Galactic centre, which varies on arcsecond scales (Schödel et al. 2010). In particular, the field of view of the kinematic data contains the so-called 20-km·s⁻¹-cloud (M-0.13-0.08, e.g. García-Marín et al. 2011) in the Galactic southwest. It lies at a projected distance of about 70'' (~ 3 pc) from the centre, and probably about 5 pc in front of Sgr A* (Ferrière 2012). This cloud blocks the light from stars of the nuclear star cluster. We cannot access the kinematics of stars behind this cloud. There is also interstellar dust within a projected distance of 20'' (~ 0.8 pc) from the centre, i.e. within the radius of influence of the black hole. This dust causes extinction within the nuclear star cluster by up to 0.8 mag (Chatzopoulos et al. 2015b). As a consequence, the two effects of dimming by distance and by extinction add up and stars that lie on the far side of the nuclear star cluster appear even more faint than the stars on the near side.

3.4.3.3 Implications

Both the semi-resolved stellar population and the inter-cluster extinction cause that our observations are biased to the near side of the nuclear star cluster. As a consequence we measured a lower limit of the velocity dispersion. Feldmeier et al. (2014) found that the velocity dispersion in the projected radial range $6'' < r < 20''$ is smaller compared to the velocity dispersion computed from proper motion data of Schödel et al. (2009), which is based on resolved stars. For resolved stars, the velocity dispersion is not weighted by the flux of the stars. An underestimated velocity dispersion means that the black hole mass measurement is biased to lower values.

This observational bias also influences the measurements of V , h_3 and h_4 . In particular, the cluster may appear compressed along the line-of-sight, and thus the value of $p = y/x = 0.64^{+0.18}_{-0.06}$ may be too low. As a consequence, $Y = 0.90^{+0.76}_{-0.08}$ would be underestimated (see second column of the first row in Fig. 3.4). However, our best-fitting result of Y is already higher than what we expect from stellar population studies (McGaugh & Schombert 2013; Meidt et al. 2014), and also higher than the result of Feldmeier et al. (2014), who found $Y = 0.56^{+0.22}_{-0.26}$. They assumed axisymmetry with $p = 1$, and thus $y = x$, i.e. the intermediate and long axis have the same length. With $p < 1$, the system extends less along the intermediate axis than in the oblate axisymmetric case.

3.4.3.4 Influence of figure rotation

The Galaxy rotates, and with it the nuclear star cluster. In a non-axisymmetric rotating system, centrifugal and Coriolis forces play a role. However, figure rotation and the resulting forces were not included in our triaxial models. Figure rotation influences the stellar orbits, and the prograde and retrograde tube orbits no longer fill the same volumes, while the box orbits acquire net mean angular momentum (e.g. Heisler et al. 1982; Schwarzschild 1982; Sellwood & Wilkinson 1993; Skokos et al. 2002). As a result, orbit-based tumbling triaxial models are computationally expensive. Other than an early attempt by Zhao (1996) no such models have been constructed that take into account kinematic data. It is difficult to predict how our results would change in a rotating model. The inferred orbital structure will be affected (depending on the tumbling speed of the nuclear star cluster), but our results on the mass distribution are likely to be fairly robust, as the assumption of a constant mass-to-light ratio is probably more important.

3.5 Summary and outlook

We constructed for the first time triaxial orbit-based Schwarzschild models of the Milky Way nuclear star cluster. We used the spectroscopic integrated light maps by Feldmeier et al. (2014) to measure the cluster kinematics of the central 60 pc^2 of the Milky Way. As photometry we used *Spitzer* $4.5\mu\text{m}$ and NACO H -band images, and measured a two-dimensional surface brightness distribution. We excluded young stars, avoided gas emission and dark

clouds. Our triaxial models were based on the code by van den Bosch et al. (2008). Our best-fitting model contains a black hole of mass $M_{\bullet} = (3.0_{-1.3}^{+1.1}) \times 10^6 M_{\odot}$, a dynamical mass-to-light ratio of $Y = (0.90_{-0.08}^{+0.76}) M_{\odot}/L_{\odot,4.5\mu\text{m}}$, and shape parameters $p = 0.64_{-0.06}^{+0.18}$, $q = 0.28_{-0.02}^{+0.0}$, and $u = 0.99_{-0.01}^{+0.0}$. Our black hole mass measurement is in agreement with the direct measurement of $M_{\bullet} = (4.1 \pm 0.6) \times 10^6 M_{\odot}$ (Ghez et al. 2008), $(4.3 \pm 0.39) \times 10^6 M_{\odot}$ (Gillessen et al. 2009b), and $(4.02 \pm 0.20) \times 10^6 M_{\odot}$ (Boehle et al. 2016). We obtain a cluster mass $M_{\text{MWNSC}} = (3.1_{-0.3}^{+2.8}) \times 10^7 M_{\odot}$ within $r = 2 \times r_{\text{eff}} = 8.4$ pc. The best-fitting model is tangentially anisotropic in the central $r = 2$ pc of the nuclear star cluster, but is close to isotropic at larger radii. The model is able to recover the long-axis rotation in the central $r = 0.8$ pc found by Feldmeier et al. (2014), and the misalignment of the kinematic rotation axis from the photometric minor axis.

There are several possible ways to extend the dynamical models in the future. One way is to include a component for the neutral gas disc inside the nuclear star cluster. If the gas mass is close to the upper limit of $10^6 M_{\odot}$, the dynamical mass-to-light ratio would probably decrease slightly, and in return would slightly increase the black hole mass. Modelling a spatially varying mass-to-light ratio may provide a better representation of the cluster's intrinsic properties. Further, proper motions can be included in combination with discrete line-of-sight velocities, as shown by van de Ven et al. (2006) and van den Bosch et al. (2006) for axisymmetric Schwarzschild models. Watkins et al. (2013) extended axisymmetric Jeans models and implemented discrete kinematic data without binning. Using discrete data means that the stars are not weighted by their luminosities. This prevents the previously discussed bias towards the near side of the cluster.

Acknowledgments

R.S. acknowledges funding from the European Research Council under the European Union's Seventh Framework Programme (FP7/2007-2013) / ERC grant agreement n. 614922. We thank Remco van den Bosch for helpful discussions about the project.

Based on observations collected at the European Organisation for Astronomical Research in the Southern Hemisphere, Chile (289.B-5010(A)).

4

KMOS view of the Galactic centre

I. Young stars are centrally concentrated

The Galactic centre hosts a crowded, dense nuclear star cluster with a half-light radius of 4 pc. Most of the stars in the Galactic centre are cool late-type stars, but there are also $\gtrsim 100$ hot early-type stars in the central parsec of the Milky Way. These stars are only 3 – 8 Myr old.

Our knowledge of the number and distribution of early-type stars in the Galactic centre is incomplete. Only a few spectroscopic observations have been made beyond a projected distance of 0.5 pc of the Galactic centre. The distribution and kinematics of early-type stars are essential to understand the formation and growth of the nuclear star cluster.

We cover the central $>4 \text{ pc}^2$ (0.75 arcmin^2) of the Galactic centre using the integral-field spectrograph KMOS (VLT). We extracted more than 1 000 spectra from individual stars and identified early-type stars based on their spectra.

Our data set contains 114 bright early-type stars: 6 have narrow emission lines, 23 are Wolf-Rayet stars, 9 stars have featureless spectra, and 76 are O/B type stars. Our wide-field spectroscopic data confirm that the distribution of young stars is compact, with 90 per cent of the young stars identified within 0.5 pc of the nucleus. We identify 24 new O/B stars primarily at large radii. We estimate photometric masses of the O/B stars and show that the total mass in the young population is $\gtrsim 12,000 M_{\odot}$. The O/B stars all appear to be bound to the Milky Way nuclear star cluster, while less than 30 per cent belong to the clockwise rotating disc. We add one new star to the sample of stars affiliated with this disc.

The central concentration of the early-type stars is a strong argument that they have formed in situ. An alternative scenario, in which the stars formed outside the Galactic centre in a cluster that migrated to the centre, is refuted. A large part of the young O/B stars is not on the disc, which either means that the early-type stars did not all form on the same disc or that the disc is dissolving rapidly.

A. Feldmeier-Krause, N. Neumayer, R. Schödel, A. Seth, M. Hilker, P. T. de Zeeuw, H. Kuntschner, C. J. Walcher, N. Lützgendorf, M. Kissler-Patig
Astronomy & Astrophysics, Volume 584, id.A2, 27 pp, 12/2015

4.1 Introduction

Nuclear star clusters are a distinct component at the centre of many galaxies. The central region of ~ 75 – 80 per cent of spiral galaxies (Carollo et al. 1998; Böker et al. 2002; Georgiev & Böker 2014) and spheroidal galaxies (Côté et al. 2006; den Brok et al. 2014) contains a nuclear star cluster. Nuclear star clusters are located at a distinguished spot in a galaxy: The centre of the galaxy’s gravitational potential (Neumayer et al. 2011). Galaxies grow by mergers and accretion, so that infalling gas and stars can finally end up in the centre of a galaxy. Nuclear regions therefore have very high densities. Many nuclear star clusters also contain a supermassive black hole (e.g. Seth et al. 2008a; Graham & Spitler 2009). The nuclear regions of galaxies are of special interest for galaxy formation and evolution studies because of the scaling correlations between the mass of the nuclear star cluster and other galaxy properties, such as the galaxy mass (e.g. Wehner & Harris 2006; Rossa et al. 2006; Ferrarese et al. 2006; Scott & Graham 2013).

The nuclear star cluster of the Milky Way (MW) is the best-studied case of a galaxy nucleus. The cluster was first detected by Becklin & Neugebauer (1968) in the infrared. It has a half-light radius or effective radius r_{eff} of ~ 110 – $127''$ (4.2 – 5 pc, Schödel et al. 2014a; Fritz et al. 2016) and a mass of $M_{\text{MWNSC}} = (2.5 \pm 0.4) \times 10^7 M_{\odot}$ (Schödel et al. 2014a). The central parsec of the Milky Way nuclear star cluster is extensively studied. At a distance of only ~ 8 kpc (Ghez et al. 2008; Gillessen et al. 2009a; Chatzopoulos et al. 2015a), it is possible to spatially resolve single stars. Monitoring of single stars over more than a decade led to an accurate measurement of the mass of the Milky Way central supermassive black hole: $M_{\bullet} = 4.3 \times 10^6 M_{\odot}$ (Eckart et al. 2002; Ghez et al. 2005, 2008; Gillessen et al. 2009b). The black hole is connected to the radio source Sagittarius A* (Sgr A*).

Within the central ~ 2 pc around Sgr A* lie ionised gas streamers, concentrated in three spiral arms (e.g. Ekers et al. 1983; Herbst et al. 1993). They are called the minispiral or Sgr A West. The brightest features of the minispiral are the Northern Arm (NA), Eastern Arm (EA), Bar, and Western Arc (WA, e.g. Paumard et al. 2004; Zhao et al. 2009; Lau et al. 2013).

To understand the formation and growth of nuclear star clusters, it is important to study the stellar populations. Despite the complications from extinction and reddening, near-infrared spectroscopy can be used to examine stellar ages. For instance, studies of individual stars by Blum et al. (2003) and Pfuhl et al. (2011) suggested that the dominant populations in the Milky Way nuclear star cluster are older than 5 Gyr.

Studies have shown that star formation in nuclear star clusters continues until the present day (Walcher et al. 2006). Observations of nuclear clusters in edge-on spirals reveal that young stars are located in flattened discs (Seth et al. 2006, 2008b). These younger components have a wide range of scales but most frequently appear to be centrally concentrated (Lauer et al. 2012; Carson et al. 2015). The Galactic centre likewise contains a young population of stars. Within the central parsec ($r < 0.5$ pc) are $\gtrsim 100$ hot early-type stars. These young stars are O- and B-type supergiants, giants, main-sequence stars, and post-main-sequence Wolf-Rayet (WR) stars (e.g. Krabbe et al. 1995; Ghez et al. 2003; Paumard et al. 2006; Bartko et al. 2010; Do et al. 2013a). The young stars formed about 3 – 8 Myr ago (e.g.

Krabbe et al. 1995; Paumard et al. 2006; Lu et al. 2013). Dynamically, the young stars can be sorted into three different groups: (1) stars within $r < 0.03$ pc ($0.8''$) are in an isotropic cluster, also known as S-star cluster. Most of the $\gtrsim 20$ stars are B-type main-sequence stars. Then there are (2) stars on a clockwise (CW) rotating disc with $r \approx 0.03$ – 0.5 pc (0.8 – $13''$) distance to Sgr A*, and (3) stars at the same radii as the stars in group (2), but not on the CW disc. It is under debate if there is a second, counter-clockwise rotating disc of stars within this group (Genzel et al. 2003; Paumard et al. 2006; Bartko et al. 2009; Lu et al. 2009, 2013; Yelda et al. 2014). The stars in groups (2) and (3) have similar stellar populations (Paumard et al. 2006). It is unclear whether the stars of group (1) are the less massive members of the outer young population or if they were formed in one or several distinct star formation events.

Most of the early-type stars are located within the central 1 pc, but it is unclear if this is just an observational bias. Previous spectroscopic studies were mostly obtained within a radius of 0.5 pc ($\sim 12''$). Bartko et al. (2010) observed various fields with SINFONI and covered a surface area of ~ 500 arcsec². However, the fields are asymmetrically distributed and mostly lie within $12''$ ($\lesssim 0.5$ pc) distance from the centre. Do et al. (2013a) observed an area of 113.7 arcsec² along the CW disc. Their observations extend out to 0.58 pc. Støstad et al. (2015) mapped an additional 80 arcsec² out to 0.92 pc and found a break in the distribution of young stars at 0.52 pc. No previous spectroscopic study has fully sampled regions beyond the CW disc. For this reason, we obtained *K*-band spectroscopy of the central $64''.9 \times 43''.3$ (2.51 pc \times 1.68 pc) of the Milky Way using the *K*-band Multi-Object-Spectrograph (KMOS, Sharples et al. 2013) on the ESO/VLT. We covered an area of 2700 arcsec² (0.75 arcmin², >4 pc²), centred on Sgr A* and symmetric in Galactic coordinates. From this data set we extracted spectra for more than 1000 individual stars and obtained a map of the minispiral. We aim to classify the stars into late-type stars and early-type stars. For this purpose we use the CO absorption line as distinction. After the classification we investigate the properties of the two different classes. Late-type stars will be treated separately in Chapter 5.

We here consider young populations of stars including O/B type stars, emission-line stars, and stars with featureless spectra. We also present the intensity maps of ionised Brackett (Br) γ and He gas and of molecular H₂ gas. Over a nearly symmetric area of >4 pc² we investigate the presence and spatial distribution of early-type stars. Furthermore, we derive photometric masses and collect the kinematics of the O/B stars. In addition, we examine the spectral subclasses of the emission-line stars.

This paper is organised as follows: In Sect. 4.2 we describe the observations and data reduction. We outline the data analysis in Sect. 4.3. Our results are presented in Sect. 4.4 and are discussed in Sect. 4.5. We conclude with a summary in Sect. 4.6.

4.2 Observations and data reduction

4.2.1 Spectroscopic observations

Our spectroscopic observations were obtained with KMOS at VLT-UT1 (Antu) on September 23, 2013 during the KMOS science verification. KMOS consists of 24 IFUs with a field

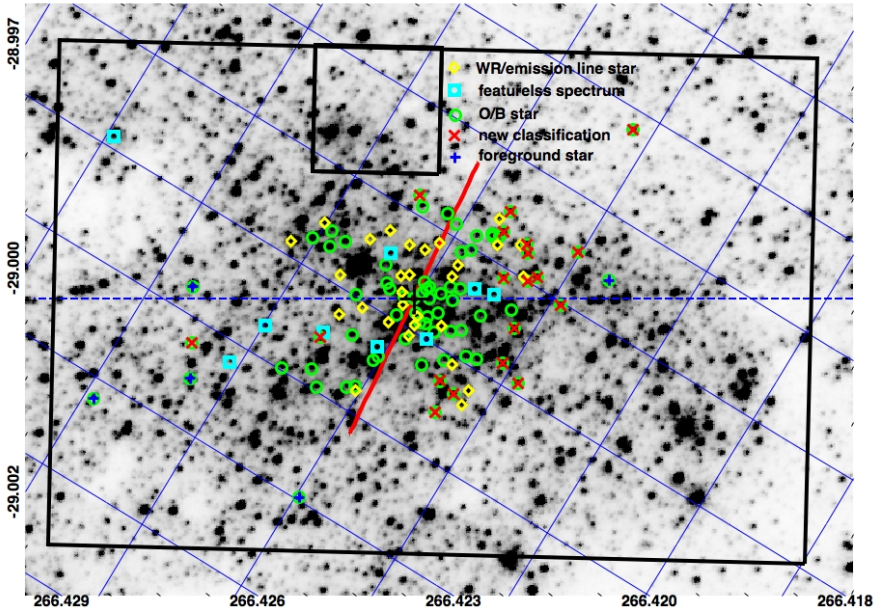


Figure 4.1: Field of view and spatial distribution of early-type stars in the Milky Way nuclear star cluster. The black box shows the KMOS $64''.9 \times 43''.3$ field of view, i.e. $2.51 \text{ pc} \times 1.68 \text{ pc}$, the small square in the upper middle was not observed due to the inactive IFU 13. Blue lines are the equatorial coordinate grid with a spacing of $10''$. The dashed blue horizontal line denotes the orientation of the Galactic plane. The black cross shows the position of Sgr A*. The underlying image is from HST/NICMOS (Dong et al. 2011), aligned along Galactic coordinates. The yellow diamond symbols denote confirmed Wolf-Rayet (WR) and emission-line stars; cyan squares stars with featureless spectra; green circles O/B stars; red x-symbols new young star candidates; blue plus-symbols probable foreground stars. The red line denotes the line of nodes of the clockwise-rotating disc of young stars.

of view of $2''.8 \times 2''.8$ each. We observed in mosaic mode using the large configuration. This means that all 24 IFUs of KMOS are in a close arrangement, and an area of $64''.9 \times 43''.3$ ($\sim 2880 \text{ arcsec}^2$) is mapped with 16 dithers. There is a gap in the mosaic of $10''.8 \times 10''.8$ because one of the arms (IFU 13) was not working properly and had to be parked during the observations (see Fig. 4.1). Therefore the total covered area is $\sim 2700 \text{ arcsec}^2$, corresponding to $\sim 4 \text{ pc}^2$. We observed two full mosaics of the same area with 16 dithers per mosaic. The mosaics are centred on $\alpha=266^\circ.4166$ and $\delta=-29^\circ.0082$ with a rotator offset angle at 120° . We chose the rotator offset angle such that the long side of a mosaic is almost aligned with the Galactic plane ($31^\circ.40$ east of north, J2000.0 coordinates, Reid & Brunthaler 2004). The rotator angle only deviates by $1^\circ.40$ from the Galactic plane. Thus the covered area is approximately point-symmetric with respect to Sgr A*.

We used KMOS in the K -band ($\sim 1.934 - 2.460 \mu\text{m}$) with a spectral resolution $R = \frac{\lambda}{\Delta\lambda} \sim 4300$, which corresponds to a FWHM of 5.55 \AA measured on the sky lines. The pixel

scale is $\sim 2.8 \text{ \AA} \cdot \text{pixel}^{-1}$ in the spectral direction and $0''.2 \text{ pixel}^{-1} \times 0''.2 \text{ pixel}^{-1}$ in the spatial direction. Each of the mosaic tiles consists of two 100 s exposures. We observed one quarter of a mosaic on a dark cloud (G359.94+0.17, $\alpha \approx 266^\circ.2$, $\delta \approx -28^\circ.9$, Dutra & Bica 2001) for sky subtraction. B dwarfs were observed for telluric corrections.

4.2.2 Data reduction

For data reduction we used the KMOS pipeline Software Package for Astronomical Reduction with KMOS (SPARK, Davies et al. 2013) in ESO Recipe Execution Tool (EsoREX). This package contains routines for processing dark frames, flat field exposures, arc frames obtained using argon and neon arc lamps, and standard star exposures. For the telluric spectra we used an IDL routine that removes the Br γ absorption line from each telluric spectrum. The routine fits the Br γ line with a Lorentz profile and subtracts the fit from the telluric spectrum. It also divides the telluric spectrum by a blackbody spectrum to remove the stellar continuum.

We reduced both science and sky exposures by applying the following steps: flat fielding, wavelength calibration, cube construction, telluric correction, and spatial illumination correction (using flat-field frames). The four sky exposures were average combined to a master sky, which we subtracted from the object cubes. We used the method described by Davies (2007), in which the sky cube is scaled to the object cube based on OH line strengths before subtraction. Then we removed the cosmic rays from each object cube with a 3D version of L.A.CosMIC (van Dokkum 2001) provided by Davies et al. (2013).

We extracted the spectra from the 736 data cubes using PAMPELMUSE, a software package written by Kamann et al. (2013). PAMPELMUSE was designed for extracting spectra from IFU observations of crowded stellar fields and enables clean extraction of stars even when their separation is smaller than the seeing. The program requires an accurate star catalogue. We used the catalogue provided by Schödel et al. (2010, and in prep.), which was obtained from NACO and HAWK-I observations. We ran PAMPELMUSE separately for every IFU because the astrometry of a mosaic cube is not accurate enough and because the point-spread function (PSF) of the observations varies in time. As a consequence, the PSF in a mosaic varies between the individual 16 dither positions.

Within PAMPELMUSE, the routine INITFIT uses the source list and produces a simulated image with the spatial resolution of KMOS. This image is then used as a first guess for the position of the stars in the data cubes. Since the PSF varies with wavelength, CUBEFIT runs the PSF-fitting for each layer of the data cube. We restricted the PSF to a circular shape. This means that the PSF is defined by two variables, the FWHM and the β -parameter of the Moffat profile. The PSF variables, the coordinates, and the flux were fitted iteratively and for each layer of the data cube in the wavelength interval of $[2.02 - 2.42 \mu\text{m}]$. We excluded wavelength regions with prominent gas emission lines (e.g. H₂, Br γ , He) from the fit.

The coordinates and the PSF vary only smoothly with wavelength, and the routine POLYFIT fits a 1D polynomial to the coordinate and PSF parameters as a function of wavelength. The goodness of the PSF fit depends on the number of bright stars in the IFU. For IFUs without

bright stars in the field of view we used the PSF that was determined from IFUs with bright stars in the FOV. However, the PSF varies in time. Therefore we inspected the PSF fits for the 23 data cubes, where each data cube corresponds to a specific IFU. We did this separately for each exposure and selected the best PSF fits per exposure. We combined the best FWHM and best β of one exposure to a mean FWHM and mean β , both as a function of wavelength. The FWHM lies between two to three pixels for the 32 exposures because the seeing also changed from $0''.7$ to $1''.3$ during the night. With the knowledge of the PSF of each exposure and the star coordinates, the routine CUBEFIT was run again to determine the flux for each star on all layers of the data cubes.

After extracting background-subtracted spectra with PAMPELMUSE, we shifted each spectrum to the local standard of rest. PAMPELMUSE extracted $\sim 12\,000$ spectra of more than 4 000 different stars with $K_S < 17$ mag in the KMOS field of view. We discarded all spectra with a signal-to-noise ratio (S/N) below 10 or negative flux, leaving $\sim 3\,000$ spectra. The S/N for each extracted spectrum was calculated by PAMPELMUSE with Eq. 16 of Kamann et al. (2013). We combined the two spectra of each star from the two exposures. For ~ 180 stars we had even more than two spectra from the two mosaics, since PAMPELMUSE also extracted spectra from stars that were centred outside of the field of view of the IFU. We combined the spectra with the best S/N to one spectrum per star by taking a noise-weighted mean. The S/N between the individual exposures typically differed by less than 10. We obtained spectra for more than 1 000 individual stars with a formal total S/N > 10 .

We also constructed a mosaic using the data cubes from all 32 exposures. This mosaic extends over $64''.9 \times 43''.3$, with a gap for the inactive IFU 13. To determine the astrometry of the mosaic, we used the $1.9\,\mu\text{m}$ image of the *Hubble Space Telescope* (HST)/NICMOS Paschen- α Survey of the Galactic centre (Wang et al. 2010; Dong et al. 2011) as a reference. This image has a pixel scale of $0''.1\text{ pixel}^{-1}$. We collapsed the KMOS mosaic data cube to an image and rebinned it to the HST pixel scale. The two images were iteratively cross correlated. Although the two images cover different wavelength regions, a large enough number of stars is detected in both images to line the frames up. Finally, we applied a correction to the local standard of rest. This mosaic data cube was used to measure the gas emission lines of the minispiral and circumnuclear ring.

4.3 Data analysis

4.3.1 Photometry

To be able to determine the spectral classes and colours of the stars, we complemented our spectroscopic data set with photometric measurements. Schödel et al. (2010, and in prep.) observed the Milky Way nuclear star cluster with NACO and HAWK-I and constructed a star catalogue. This catalogue provides J (HAWK-I), H , and K_S (HAWK-I and NACO) photometry. The NACO catalogue extends over the central $\sim 40'' \times 40''$, HAWK-I data were used for regions farther out.

The brightest stars are saturated in the HAWK-I and NACO images, and we complemented our photometry with other star catalogues. We used photometry from the SIRIUS catalogue (Nishiyama et al. 2006) for eight stars, and for three further bright stars without HAWK-I, NACO or SIRIUS photometry, we used photometry from the 2MASS catalogue (Skrutskie et al. 2006). For almost 1 000 stars we have the JHK_S photometry from either NACO/HAWK-I, SIRIUS or 2MASS, for a further 100 stars we only have HK_S photometry. For two stars we have no K_S photometry, but JH photometry.

To obtain clean photometry, we corrected for interstellar extinction. In the Galactic centre, extinction varies on arcsecond scales (e.g. Scoville et al. 2003; Schödel et al. 2010; Fritz et al. 2011). The typical extinction values are about 2.5 mag in the K_S band, 4.5 mag in the H band, and more than 7 mag in the J band. We used the extinction map and the extinction law derived from Schödel et al. (2010)¹ for the extinction correction of the photometry. About 350 (~30 per cent) of the stars are outside the field of view of the extinction map. For these we assumed that the extinction is the mean value of the extinction map $A_{K_S} = 2.70$ mag.

The extinction map was created after excluding foreground stars. Therefore, any foreground star will be strongly over-corrected to very negative colours. The intrinsic colours of cluster members are in a very narrow range of about $-0.13 \text{ mag} < (H - K_S) < 0.38 \text{ mag}$ (Schödel et al. 2010; Do et al. 2013a; Schödel et al. 2014b; Cox 2000, Table 7.6, and 7.8). We used this knowledge to identify foreground stars. Stars with a bluer extinction-corrected $(H - K_S)_0$ colour than the intrinsic colour are foreground stars. To account for uncertainties in the extinction correction, we used a larger colour interval and classified a foreground star when the extinction-corrected $(H - K_S)_0$ colour was less than -0.5 mag.

Identifying background stars is less obvious. Very red stars may not be background stars, but be embedded in local dust features or have dusty envelopes. Viehmann et al. (2006) showed that several red sources in the Galactic centre are not background stars, but bow-shock sources. For red sources we have to consider the spectral type and the surroundings of the star to decide whether it is locally embedded or a background star.

4.3.2 Completeness

It is important to know how complete our spectroscopic data set is up to a given magnitude. Completeness is influenced by various factors, for example the depth of the observation, the spatial resolution, but also the stellar number density of the observed field. In a dense environment, crowding becomes stronger, and fewer faint stars can be detected.

We used the photometric catalogue by Schödel et al. (2010, and in prep.) to extract the stars, which means that our spectroscopic data set can at best be as complete as the photometric catalogue. Our data have a lower spatial resolution than the images used to produce the photometric catalogue, and therefore the completeness of our data set must be lower. The photometric catalogue contains $\gtrsim 6\,000$ stars in the KMOS field of view. PAMPELMUSE

¹We downloaded the extinction map from the CDS database. It turned out that the astrometry of the extinction map was wrong by a scale factor of 60. We reported this issue to CDS, and the astrometry was fixed on 26th March, 2015.

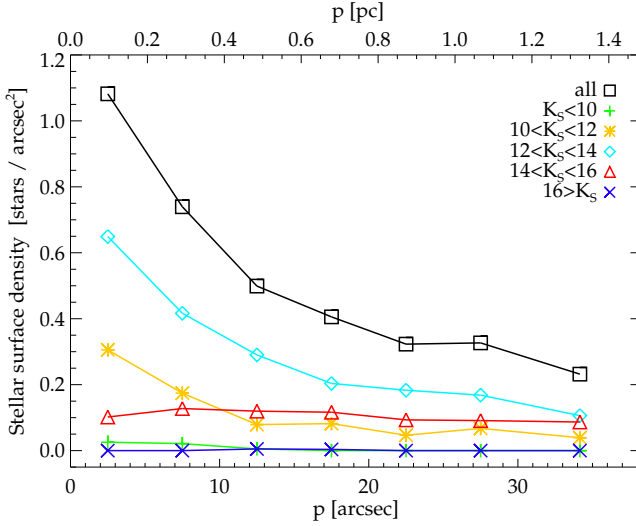


Figure 4.2: Number density profile of the spectroscopic data set in different magnitude bins.

Table 4.1: Completeness limits of the spectroscopic data set for different radial bins.

distance p [arcsec]	80 % completeness at K_S [mag]	50 % completeness at K_S [mag]
$p < 5$	13.0 ± 0.3	13.8 ± 0.1
$5 \leq p < 10$	13.3 ± 0.1	14.1 ± 0.1
$p \geq 10$	13.5 ± 0.2	14.1 ± 0.2

extracted spectra from more than 4 000 stars with $K_S < 17$ mag. Only $\sim 1\,000$ of these have a spectrum with a S/N greater than 10. We determined the completeness of the spectroscopic data set by comparing our data set with the photometric catalogue in different magnitude bins. We assumed that the photometric catalogue is complete to 100 per cent up to $K_S = 15$ mag, at least at a projected distance $p > 10''$ from Sgr A*.

The effect of crowding is illustrated in Fig. 4.2. We plot the number density profile of our spectroscopic data set as a function of the projected distance p to Sgr A* in different magnitude bins. Most of the stars are in the magnitude bin of $12 \leq K_S [\text{mag}] \leq 14$. The number density of bright stars with $10 \leq K_S [\text{mag}] \leq 14$ decreases with increasing radius in the central $10''$, while the number density of faint stars in the magnitude bin $14 \leq K_S [\text{mag}] \leq 16$ is nearly constant in the same radial range and even slightly increases. The reason for this is crowding: There are more bright stars in the centre of the cluster, and they outshine the faint stars. Therefore we miss more faint stars in the centre than farther out. This effect was shown in previous studies (e.g. Schödel et al. 2007; Do et al. 2009; Bartko et al. 2010).

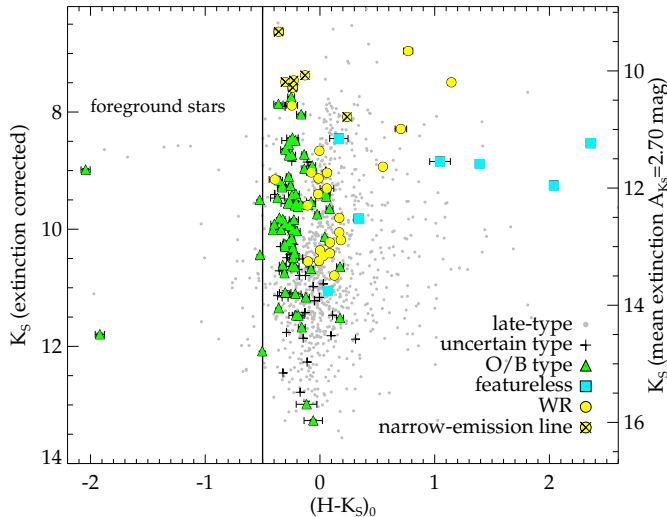


Figure 4.3: Colour-magnitude diagram of the stars within the KMOS field of view with extracted spectra and H and K_S photometry, after extinction correction. Stars with colours $(H-K_S)_0 < -0.5$ mag are most likely foreground stars (left of the vertical line). Different symbols and colours denote different types of stars. Yellow circles denote emission-line/WR stars; cyan squares sources with featureless spectra; green triangles O/B type stars; grey dots late-type stars; black plus-signs stars of uncertain type. The right y -axis denotes the K_S magnitude after extinction correction, with a mean extinction of $A_{K_S} = 2.70$ mag.

As a result of the higher crowding in the centre, the completeness limits depend on the distance from the centre. For this reason we determined the completeness separately for stars located within $p < 5''$ from Sgr A*, stars with $5'' \leq p < 10''$, and stars beyond $10''$. The spectroscopic completeness was then estimated by comparing the number of stars as a function of magnitude $N(K_S)$ in the spectroscopic data set with the total number of stars from the photometric catalogue. We calculated the fraction of stars that are missing in the spectroscopic data set for different magnitude bins to correct our number density results by that fraction. To derive the fraction of missing stars, we binned the stars in magnitude bins of ΔK_S . We varied the size of the magnitude bins to test the effect of the magnitude binning. We tried $\Delta K_S = 0.7$ mag, $\Delta K_S = 0.5$ mag, and $\Delta K_S = 0.3$ mag. The difference gives the uncertainties of the completeness limits. We list our 80 and 50 per cent completeness limiting magnitudes in Table 4.1 for the three different radial bins. At greater distances, the completeness limits are shifted to fainter stars than in the centre as a result of crowding. The completeness limits did not vary beyond their uncertainty when we chose slightly different radial bins.

We investigated the effect of source confusion on our ability to classify stars. We conclude that crowding only has a minor effect on our completeness limit, and the S/N degradation does not severely affect our ability to classify stars brighter than our completeness limit.

4.3.3 Spectral identification of late- and early-type stars

We visually investigated the spectra and classified the stars into three categories: (a) late-type stars, (b) early-type stars, and (c) uncertain type. Late-type stars are rather cool and have CO absorption lines. Most of them are of old to intermediate age (Pfuhl et al. 2011), although there are exceptions such as the red supergiant IRS 7, which is only ~ 7 Myr old (Carr et al. 2000). Late-type stars are in the majority with ~ 990 stars. They will be analysed in detail in Chapter 5.

Early-type stars can be separated into emission-line stars, O/B stars, and featureless spectra. The data set contains 29 stars with emission lines, 23 of which are Wolf-Rayet (WR) stars and six stars have narrow emission lines (see Sect. 4.4.2.3). The O/B star spectra have no CO lines but rather He and/or H (Br γ) absorption lines. Our data set contains 76 O/B stars (see Sect. 4.4.1). A further nine stars have featureless spectra without strong absorption or emission features, but strongly increasing continuum (see Sect. 4.4.3). They are associated with bow shocks. The remaining 40 spectra are in category (c) of uncertain type, mostly because the S/N was too low or because the spectra are contaminated by the light of nearby brighter stars.

Figure 4.3 shows a colour-magnitude diagram (CMD) using H and K_S after extinction correction. The location of these stars is also indicated in Fig. 4.1 with the same colour coding. We would like to point out that almost all WR stars are redder than the O/B stars. This is because they have evolved off the main sequence and may be producing dust. Therefore, the observed mean position of the WR stars on the red side of the CMD supports our stellar classification and the accuracy of the CMD.

4.3.4 Deriving stellar kinematics

Stellar kinematics are useful to study the origin of the early-type stars. In this section we describe our routine to fit the radial velocities of O/B stars.

The broad lines of the Wolf-Rayet stars make it difficult to determine their radial velocities. The lines are mostly a combination of several blended lines, and the stars have fast winds and outflows. For the featureless sources no spectral lines can be fitted. For the O/B stars we used the penalized pixel-fitting (pPXF) routine to fit the Br γ and He lines (Cappellari & Emsellem 2004). We used template spectra from three different libraries: Wallace & Hinkle (1996), Hanson et al. (2005), and KMOS B-main-sequence stars. The KMOS B-main-sequence stars were observed in our program as telluric standard stars. From Hanson et al. (2005) we only used the O/B stars that were observed with ISAAC/VLT ($R \sim 8000$). We measured the radial velocities of the O/B templates by fitting the Br γ line and shifted the templates to the rest wavelength. The high-resolution templates were convolved with a Gaussian to match the spectral resolution of the KMOS data. Then we ran pPXF on our data.

The uncertainty of the radial velocity was measured using Monte Carlo simulations. We added random noise to the spectra and fitted the radial velocities in 100 runs. The standard deviation of the 100 measurements was our uncertainty. The results are listed in Table 4.6 and are analysed in Sect. 4.4.5. The wavelength region of the He I and Br γ absorption lines also

shows He I and Br γ emission from ionised gas (see Sect. 4.4.2.1). The program PAMPELMUSE subtracts the background when extracting the stellar spectra, but the surrounding gas emission increases the noise in this wavelength region. This induces high uncertainties in our radial velocity measurements. For this reason, the median value of the radial velocity uncertainty is $\sigma_{\text{median}} \approx 60 \text{ km}\cdot\text{s}^{-1}$. We compared our radial velocity measurements with the data of Bartko et al. (2009) and Yelda et al. (2014). There are nine stars with independent radial velocity measurements from this work and the previous studies. Using these stars, we can estimate the so-called true external σ of our measurement, meaning that we can test whether we over- or underestimate the uncertainties. The procedure was described by Reijns et al. (2006). First, we measured the mean velocity offsets $\langle v_i - v_j \rangle$ ($i = 1, 2, 3; j = 2, 3, 1$) between each pair of the three studies for the overlap stars and the respective standard deviation $\sigma_{v_i-v_j}^2$. Because $\sigma_{v_i-v_j}^2 = \sigma_{v_i}^2 + \sigma_{v_j}^2$, we can calculate the true σ_{v_i} ($i = 1, 2, 3$) from the three measurements of $\sigma_{v_i-v_j}^2$.

A comparison of the external error σ_{ext} with the mean error σ_{mean} of the individual radial velocity measurements indicates whether we over- or underestimate the uncertainty. The external error $\sigma_{\text{ext}} = 45 \text{ km}\cdot\text{s}^{-1}$ for our radial velocities is smaller than the mean error σ_{mean} of the nine overlap stars. σ_{ext} is approximately 0.7 times the mean error σ_{mean} . Of the nine stars with three independent radial velocity measurements, five stars in our data set have a high S/N (>56 (Id 109, 205, 294, 331, 372)), but four stars (Id 707, 1123, 1238, 2233) have a low S/N (<30). The velocities of three of these four stars with low S/N agree with the measurement of Bartko et al. (2009) or Yelda et al. (2014) within the uncertainties. However, we consider the radial velocity measurements of the five stars with the higher S/N more reliable. The external error calculated from the five stars with high S/N is $\sigma_{\text{ext}} = 27 \text{ km}\cdot\text{s}^{-1}$. This is 0.8 times the mean error σ_{mean} , thus our errors appear to be accurate to within 20 per cent. Although nine independent radial velocity measurements are not enough for an accurate determination of σ_{ext} , our analysis indicates that we do not underestimate the radial velocity errors.

4.4 Results

Here we first present the O/B type stars, and we derive their masses from the photometry. We obtain maps of the emission line flux that is generated by the minispiral and the circumnuclear ring. For stars with narrow emission lines and Wolf-Rayet stars we show spectra and the spectral classification, followed by the spectra of featureless sources. We finally present the spatial distribution of the early-type stars. We also investigate the O/B star kinematics and stellar orbits.

4.4.1 O/B type stars

4.4.1.1 Identifying O/B stars

O/B-stars have effective temperatures of $T_{\text{eff}} > 10,000$ K (e.g. Martins et al. 2005; Crowther et al. 2008). The most prominent lines in O/B giant K -band spectra are the He I ($2.058 \mu\text{m}$, $2.113 \mu\text{m}$ and $\sim 2.164 \mu\text{m}$), H I (4-7) Br γ ($2.166 \mu\text{m}$), and He II ($2.1885 \mu\text{m}$) lines (Hanson et al. 2005). The $2.113 \mu\text{m}$ complex is also partly generated by N III. These lines appear mostly in absorption, but can also be in emission or absent, depending on the spectral type (Morris et al. 1996).

Previous studies found ~ 100 O/B supergiants, giants, and main-sequence stars in the innermost parsec of the Galaxy (e.g. Paumard et al. 2006; Bartko et al. 2009; Do et al. 2013a; Støstad et al. 2015). Our spectroscopic data set contains 76 O/B stars, 52 of which were reported in previous spectroscopic studies, but 24 sources appear not to have been identified before, due primarily to the wider field of view of our observations relative to previous spectroscopic studies.

The spectra of the newly identified O/B stars are shown in Fig. 4.4. Five of them are probably foreground stars, as they have very blue colours (Id 436, 663, 1104, 3308, and 3339, $(H - K_S)_0 = -2.04, -0.53, -0.52, -0.50,$ and -1.92 mag). For one of the O/B stars (Id 982) we had to assume a mean extinction value of $A_{K_S} = 2.70$ mag because this star is beyond the field of view of the extinction map of Schödel et al. (2010). This means there is a large uncertainty in the star's colour of $(H - K_S)_0 = 0.04$ mag. If the local extinction is higher than the assumed mean extinction value of $A_{K_S} = 2.70$ mag, this could mean that this star also is a foreground star. For the star Id 2048 we have no colour information and cannot determine whether this star is a foreground star.

We list our sample of O/B-type stars in Table 4.4. This table provides the star Id, right ascension R.A., declination Dec (in equatorial coordinates), the offset coordinates Δ R.A. and Δ Dec with respect to Sgr A*, the magnitude K_S , remarks on the star colour, the star name and type (if available), and a note to the respective reference.

The O/B-type stars were identified by inspecting the spectra of all stars in our data set. To verify our visual classification, we measured the equivalent widths (EW) of the $^{12}\text{CO}(2,0)$ line at $2.2935 \mu\text{m}$, and the Na I doublet at $2.2062 \mu\text{m}$ and $2.2090 \mu\text{m}$. We used the definitions of band and continuum from Frogel et al. (2001). For the late-type stars we obtain a mean value of $EW_{\text{CO,LT}} = 18.30$ ($EW_{\text{Na,LT}} = 4.60$) with a standard deviation of $\sigma_{\text{CO,LT}} = 5.20$ ($\sigma_{\text{Na,LT}} = 2.13$). The mean uncertainty is only $\Delta EW_{\text{CO,LT}} = 0.39$ ($\Delta EW_{\text{Na,LT}} = 0.25$). For the O/B stars, the equivalent widths for CO and Na are lower, with a mean value of $EW_{\text{CO,O/B}} = -0.76$ and $\sigma_{\text{CO,O/B}} = 3.25$ ($EW_{\text{Na,O/B}} = 0.47$ and $\sigma_{\text{Na,O/B}} = 1.75$). This means that the equivalent width of the CO line of O/B stars is on average more than 3.67σ smaller than for late-type stars, and the equivalent width of Na is $\sim 1.97\sigma$ smaller. We list the equivalent widths of CO and Na for the O/B stars in Table 4.5.

O/B giants and supergiants have observed magnitudes of $K_S = 11 - 13$ mag at the Galactic centre, while O/B main-sequence stars have $K_S = 13 - 15$ mag (Eisenhauer et al. 2005; Paumard et al. 2006). To estimate the luminosity class of the O/B stars in our sample, we

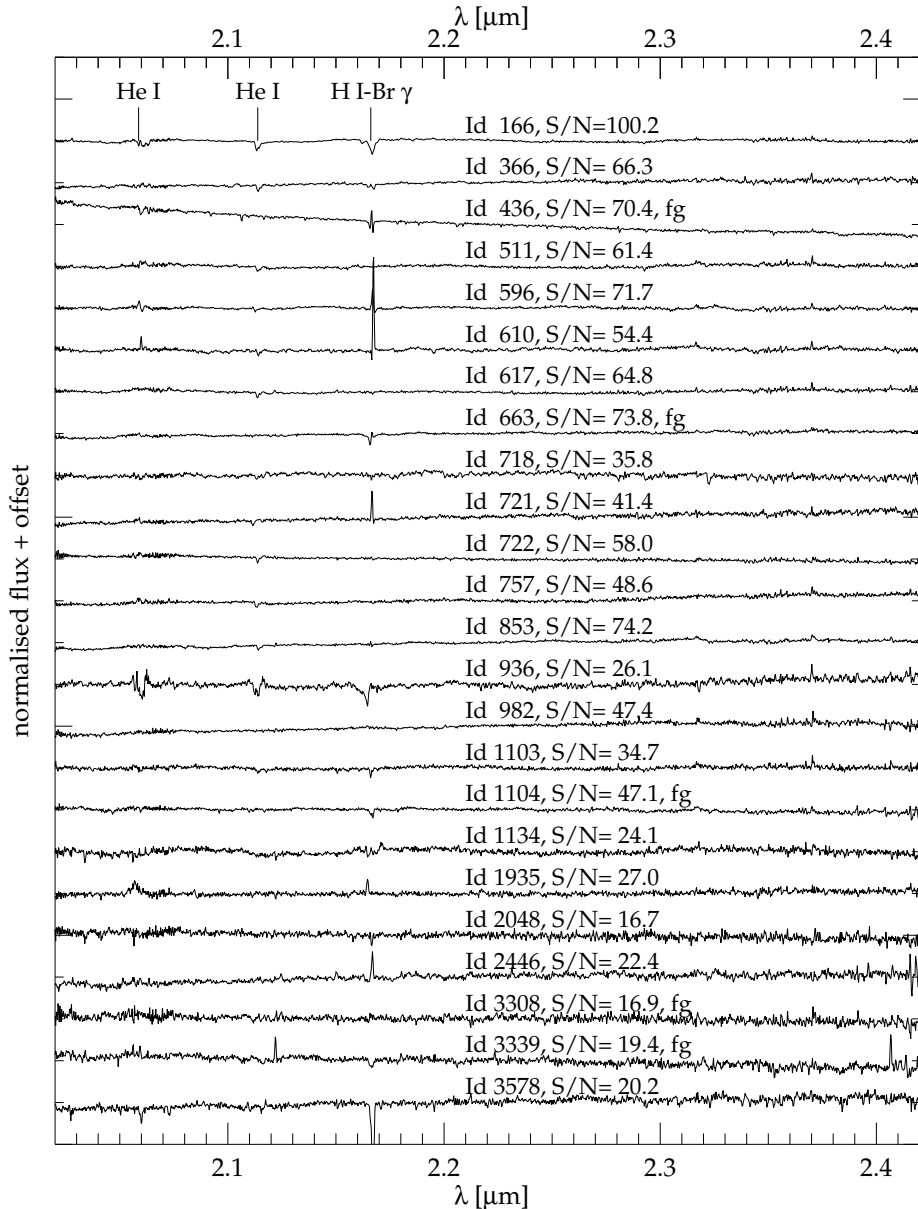


Figure 4.4: Spectra of the newly identified O/B type stars. The fluxes are normalised and an offset is added to the flux. The spectra are not shifted to rest wavelength. The numbers denote the identification numbers of the stars as listed in Tables 4.4, 4.5, and 4.6. We also show the S/N and denote probable foreground stars with “fg”.

corrected the K_S magnitude using the extinction map provided by Schödel et al. (2010) and added a mean extinction of $A_{K_S} = 2.70$ mag to the K_S magnitude. We chose $A_{K_S} = 2.70$ mag since this is the mean value of A_{K_S} from Schödel et al. (2010) in our field of view. The resulting values are given in Table 4.4 (see also the right y-axis in Fig. 4.3). With this rough magnitude cut, we estimate that about 70 per cent of the O/B stars in our data set are giants or supergiants, and 30 per cent are main-sequence stars.

4.4.1.2 Mass estimates and dust extinction

To determine the spectral type of O/B stars in the K band, the data quality has to be very high. The He I line at $2.058 \mu\text{m}$ is in a region of high telluric absorption and low S/N. The minispiral emission increases the noise at $2.058 \mu\text{m}$ and $2.166 \mu\text{m}$. Since the gas emission is spatially highly variable, the background subtraction is imperfect. But even without these difficulties, a spectral classification is complicated. Hanson et al. (2005) collected K -band spectra of O and early-B stars of known spectral type. They found that for a determination of T_{eff} and $\log(g)$, the spectral resolution should be $R \approx 5000$ or higher. Furthermore, a $\text{S/N} > 100$ is desirable. For the stars in our data set, these conditions are not fulfilled. Therefore we cannot place more constraints on the spectral types of our O/B star sample.

Nevertheless, we can estimate the mass of the O/B stars under some assumptions from the photometry. The intrinsic colour of O/B stars is in a very narrow range close to $(H - K_S)_0 \approx -0.1$ mag (Cox 2000, Table 7.6, and 7.8). Therefore the wide spread of the O/B stars over ~ 1 mag on the CMD (Fig. 4.3) is mostly due to imperfect extinction correction. For the extinction correction we used the extinction map of Schödel et al. (2010). It was derived by averaging over several stars and is therefore only an approximation to the real local extinction. However, because we spectroscopically selected the stars and all O/B stars have intrinsic colours $(H - K_S)_0 \approx -0.1$ mag, we can use the photometric colours to obtain independent extinction estimates. We assumed an extinction law of $A_\lambda \propto \lambda^{-\alpha}$ to calculate the true extinction for each single O/B star and its true magnitude $K_{S,0}$. We used the extinction law coefficient of $\alpha=2.21$ (Schödel et al. 2010). The results for $K_{S,0}$ and A_{K_S} are listed in Cols. 4 and 5 of Table 4.5 for the 73 O/B stars with H and K_S photometry. The uncertainty $\sigma_{K_{S,0}}$ contains the propagated error of the measured photometry σ_H and σ_{K_S} , the error of the true intrinsic colour σ_{H-K_S} , the extinction-law coefficient uncertainty σ_α , and the Galactocentric distance uncertainty σ_{R_0} .

The derived extinction values A_{K_S} range from 0.42 mag for probable foreground stars to 3.06 mag. The median extinction value of O/B stars that are not flagged as foreground stars is 2.48 mag with a standard deviation of 0.22 mag. The extinction derived from the extinction map is mostly higher, with a median of $A_{K_S} = 2.63$ mag and a standard deviation of 0.15 mag. We plot the extinction derived from the intrinsic colours against the extinction from the extinction map of Schödel et al. (2010) in Fig. 4.5. For the two stars Id 436 and 3339 it is obvious that they are foreground stars, the extinction derived from the intrinsic colour is lower by more than 2 mag than A_{K_S} from the extinction map. We also classified the three

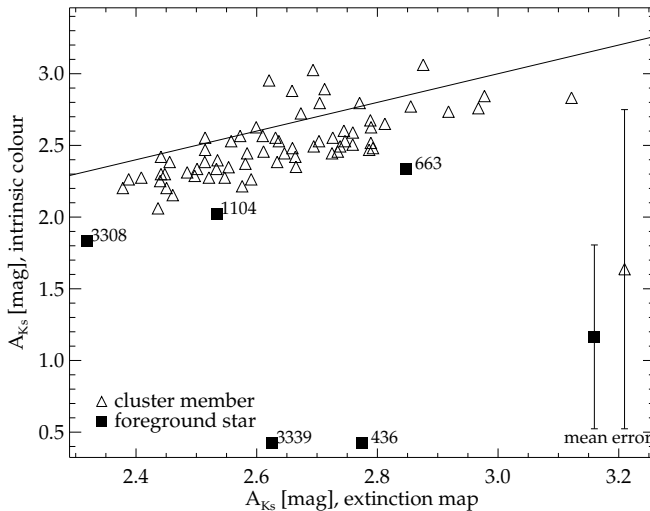


Figure 4.5: Comparison of the extinction A_{K_S} in magnitudes derived from the intrinsic colour with the extinction from the extinction map of Schödel et al. (2010) for O/B stars. The black line denotes the 1:1 line; filled squares foreground stars; open triangles cluster member stars. Typical error bars are shown in the lower right corner.

stars Id 663, 1104, and 3308 as foreground stars. With the large uncertainty of the extinction, these stars might be cluster member stars.

There appears to be a systematic offset between the extinction: A_{K_S} derived from intrinsic colours is mostly lower by ~ 0.2 mag than the value of A_{K_S} from the extinction map. We varied different input parameters to test their effect on our result of A_{K_S} . A lower value of $(H - K_S)_0$ than -0.1 mag is unlikely. However, when we changed the extinction law coefficient α from 2.21 (Schödel et al. 2010) to 2.1, the offset of 0.2 mag disappeared. Previous studies measured α in the range of 2.0 to 2.64 (Gosling et al. 2009; Stead & Hoare 2009; Nishiyama et al. 2009; Schödel et al. 2010). The value of α has the largest uncertainty and can therefore alone account for the offset.

We also used isochrones to estimate the stellar mass given the position of the star in the CMD. We used the isochrones of Bressan et al. (2012), Chen et al. (2014a) and Tang et al. (2014) downloaded at ² with solar metallicity. Ramírez et al. (2000) found that the iron abundance [Fe/H] of the Galactic centre stars is roughly solar. However, the α -element abundance is super-solar (Cunha et al. 2007; Martins et al. 2008). Paumard et al. (2006) and Lu et al. (2013) showed that the young population in the Galactic centre is 3 – 8 Myr old. We used isochrones in this age interval with a spacing of $\Delta(\log(\text{age}/\text{yr})) = 0.01$. The isochrones are for 2MASS photometry, therefore we shifted the colours to our ESO photometry using the equations given by Carpenter (2001, 2003 version at ³).

²<http://stev.oapd.inaf.it/cmd>

³<http://www.astro.caltech.edu/~jmc/2mass/v3/transformations/>

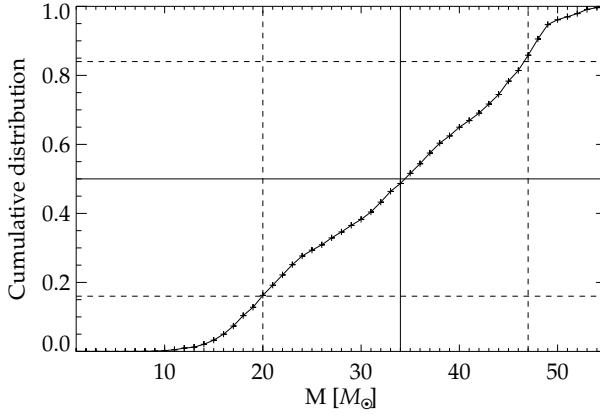


Figure 4.6: Cumulative mass distribution of star Id 617. The horizontal lines denote 0.16, 0.5, and 0.86 percentiles, the vertical lines denote the corresponding masses. We derived a mass of $M_{\star} = 34^{+13}_{-14} M_{\odot}$ for this star.

For the O/B stars in our data set we computed the likelihood \mathcal{L} of $(H - K_S)_0 = (H - K_S)_{\text{iso}}$ and $K_{S,0} = K_{S,\text{iso}}$

$$\mathcal{L} = \frac{1}{\sqrt{2\pi}\sigma_{K_{S,0}}} \exp\left(-\frac{1}{2}\left(\frac{K_{S,0} - K_{S,\text{iso}}}{\sigma_{K_{S,0}}}\right)^2\right) \times \frac{1}{\sqrt{2\pi}\sigma_{(H-K_S)_0}} \exp\left(-\frac{1}{2}\left(\frac{(H - K_S)_0 - (H - K_S)_{\text{iso}}}{\sigma_{(H-K_S)_0}}\right)^2\right),$$

where $(H - K_S)_{\text{iso}}$ and $K_{S,\text{iso}}$ are the isochrone points from all isochrones in our age interval. To each isochrone point there is a corresponding stellar mass M_{\star} . Because we used various isochrones, there can be different stellar mass values for the same value of $(H - K_S)_{\text{iso}}$ and $K_{S,\text{iso}}$. We have a distribution of stellar masses, and we used the likelihood to calculate the probability mass function of the stellar mass for each O/B star separately. In Table 4.5 we list the median mass of each star in the probability function (column M_{\star}), the uncertainties are derived from the 0.16 and 0.84 percentiles. Figure 4.6 shows the cumulative mass distribution of star Id 617 as an example. The masses of our O/B star sample range from $43 M_{\odot}$ for the brightest stars to only $7 M_{\odot}$ for a probable foreground star. When we used isochrones with a slightly higher metallicity, we obtained lower stellar masses in most cases. However, the results agree within their uncertainties.

We estimated the total mass of the young star cluster with some assumptions. In Sect. 4.3.1 we have shown that the 80 per cent completeness limit is at $K_S \approx 13.2$ mag. When we consider only O/B stars with $K_S \leq 13.2$ mag and with $M_{\star} \geq 30 M_{\odot}$, the mass function is approximately complete. The initial mass function (IMF) of young stars in the Galactic centre is top-heavy (Bartko et al. 2010; Lu et al. 2013). We fitted the IMF $dN/dm = A \times m^{-\alpha}$ to the observed mass function in the mass interval $[30 M_{\odot}; 43 M_{\odot}]$, where we have 51 stars. We

used the software MPFIT (Markwardt 2009) to fit the coefficient A and use α values from the literature. We refrained from fitting α . The covered mass interval and the number of stars are too small to constrain the shape of the IMF. Then we integrated the IMF from $[1 M_{\odot}; M]$ to obtain the total mass of the young star cluster. As our mass function contains only O/B stars and no emission-line stars, which are also young and in the same mass interval, we derived only a lower limit for the young star cluster mass.

Assuming an IMF with $\alpha=1.7$ (Lu et al. 2013) and $M=150 M_{\odot}$, we obtain $M_{\text{young}, M \leq 150 M_{\odot}}^{\alpha=1.7} = 21,000 M_{\odot}$, and with $\alpha = 0.45$ (Bartko et al. 2010), we obtain $M_{\text{young}, M \leq 150 M_{\odot}}^{\alpha=0.45} = 32,000 M_{\odot}$. With an upper integration limit of $M = 80 M_{\odot}$, the young cluster mass is $M_{\text{young}, M \leq 80 M_{\odot}}^{\alpha=1.7} = 16,000 M_{\odot}$ for $\alpha = 1.7$ and $M_{\text{young}, M \leq 80 M_{\odot}}^{\alpha=0.45} = 12,000 M_{\odot}$ for $\alpha = 0.45$. We thus give $M_{\text{total, young}} \sim 12,000 M_{\odot}$ as a lower limit for the mass of the young star cluster. When we consider the lower mass limits of the stars, the total mass is decreased to $M_{\text{young}, M \leq 80 M_{\odot}}^{\alpha=1.7} = 6,000 M_{\odot}$ ($M_{\text{young}, M \leq 80 M_{\odot}}^{\alpha=0.45} = 10,000 M_{\odot}$). The binning uncertainty is also of the order $\sim 3,000 M_{\odot}$.

4.4.2 Emission line sources

There are three sources of emission lines in the Galactic centre: (a) Extended ionised gas streamers, the so-called minispiral, or Sgr A East; (b) molecular gas; and (c) emission-line stars, which mostly are WR stars.

4.4.2.1 Ionised gas streamers

The gas streamers of the minispiral can be seen in our data in the H I (4-7) Br γ 2.166 μm and He I 2.058 μm ($2s^1S-2p^1P^0$) lines. We fitted Gaussians to the H I Br γ and He I 2.058 μm emission lines using the KMOS mosaic. The resulting flux maps are shown in Fig. 4.7 for Br γ and in Fig. 4.8 for He I emission. The images are oriented in the Galactic coordinate system and are centred on Sgr A*, which is shown as a red or black cross. We chose the applied flux scaling in the Figs. 4.7 and 4.8 to show the extended minispiral structure, but the flux of the emission lines is not saturated in the data. The H I Br γ emission is stronger than the He I emission, therefore the He I map is noisier.

The gas emission is very bright and complicates the measurement of equivalent widths of the He I and H I Br γ absorption features of O/B-type stars. Since the gas emission is also highly variable on small spatial scales, we refrained from modelling the gas emission. PAMPELMUSE subtracted the surrounding background from the spectra, but residuals remain in our data. Subtracting the gas emission close to the star can be complicated even for high-angular resolution data (see Paumard et al. 2006). However, as the gas emission lines are very narrow compared to emission lines from Wolf-Rayet stars and because most emission-line stars have additional C or N lines, we can distinguish between the different emission line sources.

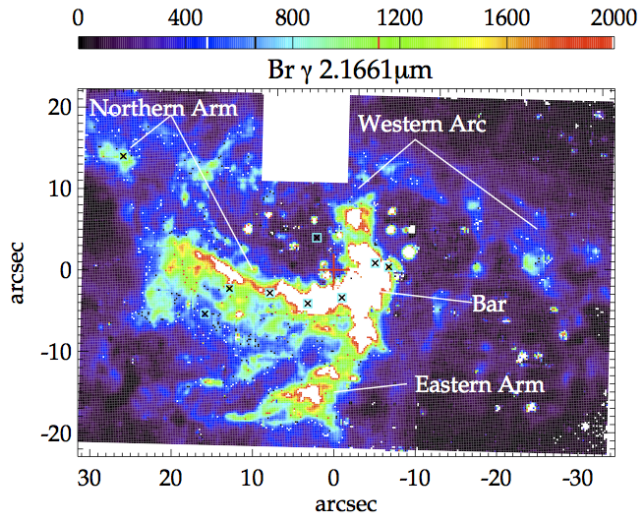


Figure 4.7: Emission line map of Br γ gas at 2.1661 μ m of the full KMOS mosaic. The axes show the distance from Sgr A* (red plus sign) in Galactic coordinates. Black crosses with cyan surrounding square symbols denote the positions of the sources with featureless spectra (see Sect. 4.4.3). The flux of Br γ emission is not saturated, but the scaling was set low in order to show the fainter, extended structure of the minispiral.

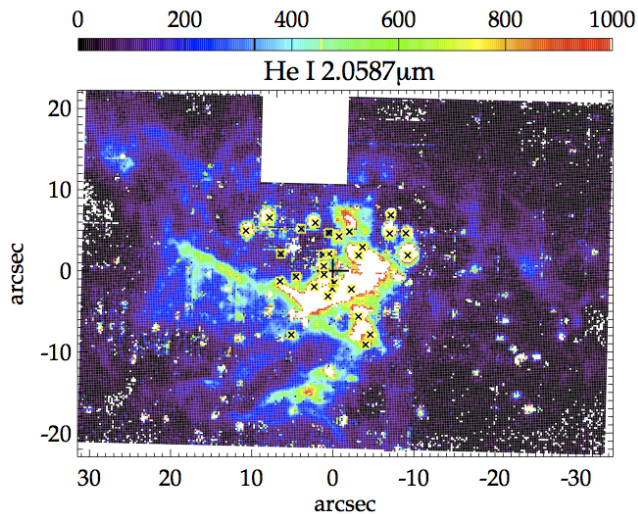


Figure 4.8: Same as Fig. 4.7 for He I gas at 2.0587 μ m. The black plus sign denotes the position of Sgr A*. The He I emission line is weaker than the Br γ line. Black crosses with yellow surrounding square symbols denote the positions of the emission-line stars (see Sect. 4.4.2.3). The He I line flux is not saturated in the data, but we set the scaling in this image low in order to show the extended structure of the minispiral.

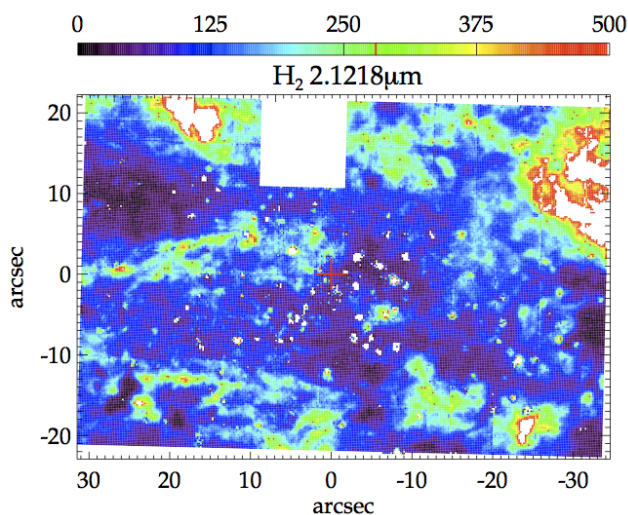


Figure 4.9: Same as Fig. 4.7 for H_2 gas at $2.1218\ \mu\text{m}$. The red plus sign denotes the position of Sgr A*. The H_2 line flux is not saturated in the data, but we set the scaling in this image low in order to show the extended structure of the gas.

4.4.2.2 Molecular gas

The molecular gas in the Galactic centre is concentrated in a circumnuclear ring (CNR). This clumpy gas ring extends over a projected distance of ~ 1.6 to 7 pc ($41''$ – $3'$, e.g. Yusef-Zadeh et al. 2001; Lee et al. 2008; Smith & Wardle 2014) and rotates with $\sim 110\ \text{km}\cdot\text{s}^{-1}$ (Christopher et al. 2005; Feldmeier et al. 2014). The gas ring consists of two prominent symmetric lobes north-east and south-west of Sgr A*.

Our data set maps only the inner edge of the circumnuclear ring. We fitted Gaussians to the H_2 emission line at $2.1218\ \mu\text{m}$ ($1-0\ \text{S}(1)$) using the KMOS mosaic. Figure 4.9 shows the H_2 flux map in the Galactic coordinate system. There are several gas streamers and clumpy structures within the projected distance of the circumnuclear ring.

4.4.2.3 Emission-line stars: Spectral classification

Stars with a He I $2.058\ \mu\text{m}$ emission line can belong to many different types such as WR stars, intermediate types such as Ofpe/WN9 (O-type spectra with additional H, He, and N emission lines, and other peculiarities), and luminous blue variable (LBV) stars. Paumard et al. (2001) suggested two classes of He I $2.058\ \mu\text{m}$ emission-line stars in the Galactic centre: Stars with narrow emission lines ($\text{FWHM}\sim 200\ \text{km}\cdot\text{s}^{-1}$) and stars with very broad emission lines ($\text{FWHM}\sim 1\ 000\ \text{km}\cdot\text{s}^{-1}$). Paumard et al. (2001) roughly sorted narrow-line stars into LBV-type stars, with temperatures of $10,000$ – $20,000$ K, and broad-line stars to WR-type stars,

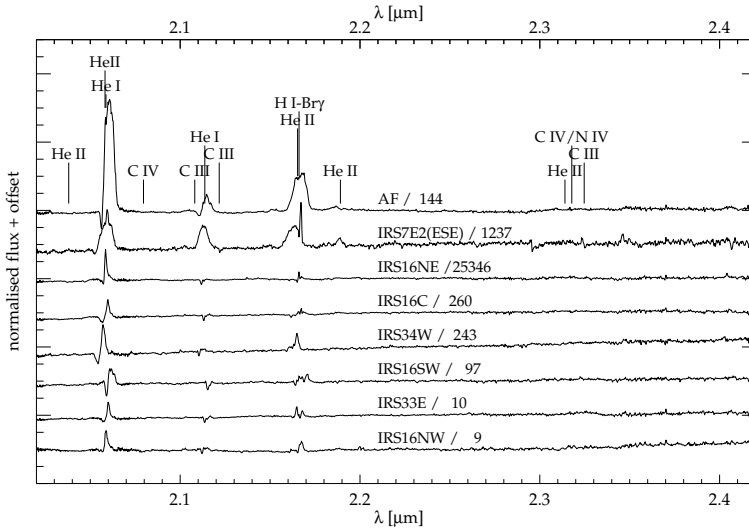


Figure 4.10: Spectra of stars with narrow emission lines and Wolf-Rayet stars. The lower six spectra are Ofpe/WN9 stars with narrow emission lines (FWHM $\sim 200 \text{ km-s}^{-1}$). Fluxes are normalised and an offset is added to the flux. The spectra are not shifted to rest wavelength. The narrow emission line in the $2.167 \mu\text{m}$ emission line of spectrum Id 1237 is a residual of poorly subtracted minispiral emission.

with higher temperatures of $>30,000 \text{ K}$. In broad-line star spectra the lines have a higher peak value above the continuum than in narrow-line star spectra.

Wolf-Rayet (WR) stars are evolved, massive stars ($>20 M_{\odot}$ while on the main sequence, Sander et al. 2012). Their spectra show strong emission lines because these stars are losing mass. Figer et al. (1997) provided a list of WR emission lines in the K -band; among them the He I, He II, H I, N III, C III, and C IV transitions. WR stars can be sorted into WN and in WC types. WN-type spectra are dominated by nitrogen lines and WC-type spectra are dominated by carbon and oxygen.

We have 29 spectra with a He I $2.058 \mu\text{m}$ emission line/WR stars. These stars are already known, for instance from Krabbe et al. (1995), Blum et al. (2003) and Paumard et al. (2006). We list these stars in Table 4.2, and their spatial distribution is shown in Fig. 4.1 with yellow symbols. The spectra are shown in Figs. 4.10, 4.11, and 4.12. In some spectra the residual from the minispiral gas emission after the subtraction is still visible, for example in Id. 1237/IRS 7E2 (ESE) at $\sim 2.167 \mu\text{m}$. The brightest WR stars are also visible in the emission line maps in Figs. 4.7 and 4.8 as bright point sources. As a result of their large FWHM, the emission lines are blends of several lines. Therefore radial velocity measurements of WR stars are highly uncertain with our data. Tanner et al. (2006) obtained high-resolution spectra and measured the radial velocities of emission lines stars in the Galactic centre.

Paumard et al. (2006) listed eight stars in their Table 2 as Ofpe/WN9 stars because they showed narrow emission lines and a He I complex at $2.113 \mu\text{m}$. The KMOS spectra of these

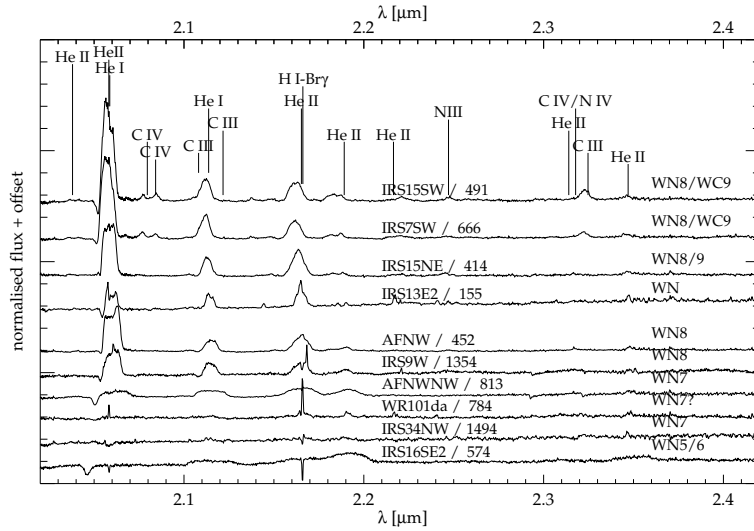


Figure 4.11: Spectra of Wolf-Rayet stars of type WN and WN/WC, ordered by increasing WN-type from bottom to top. The fluxes are normalised and an offset is added to the flux. The spectra are not shifted to rest wavelength.

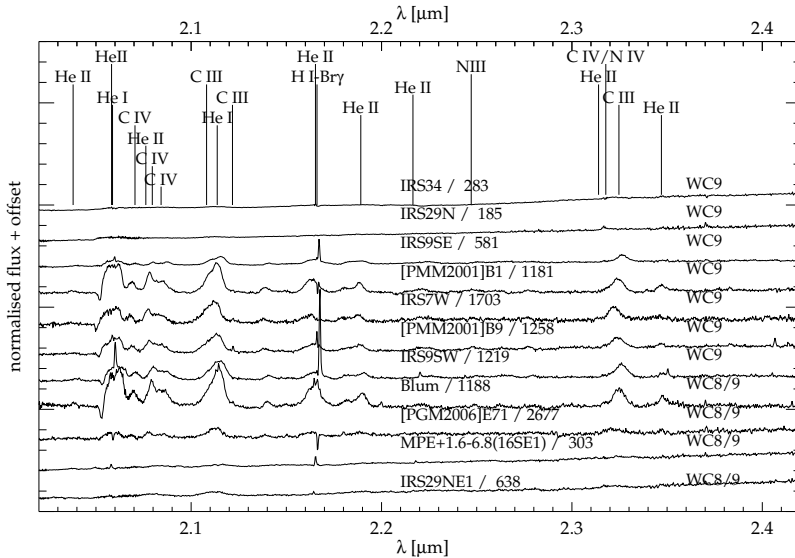


Figure 4.12: Spectra of Wolf-Rayet stars of type WC. The classification from Paumard et al. (2006, PGM06) is written for all spectra. The narrow emission line at $2.167 \mu\text{m}$ of spectrum Id 784 is a residual of the subtracted minispiral emission. The fluxes are normalised and an offset is added to the flux. The spectra are not shifted to rest wavelength.

stars are shown in Fig. 4.10. All spectra have P Cygni profiles at $2.058 \mu\text{m}$, at the He I line. This indicates that these stars are a source of strong stellar winds ($\sim 200 \text{ km}\cdot\text{s}^{-1}$). However, two of the stars (Id 144/AF and Id 1237/IRS 7E2 (ESE)) look different in our data from the other Ofpe/WN9 stars. They have significantly broader lines, with FWHM $\sim 700 \text{ km}\cdot\text{s}^{-1}$ instead of $\sim 200 \text{ km}\cdot\text{s}^{-1}$. The $2.113 \mu\text{m}$ feature is mostly in emission and not in absorption, in contrast to the other six as Ofpe/WN9 identified stars. Furthermore, a feature at He II $2.1891 \mu\text{m}$ appears in emission. Figer et al. (1997) showed that the ratio between the $2.1891 \mu\text{m}$ feature and the $2.11 \mu\text{m}$ feature is strongly correlated with subtypes for WN stars and increases with earlier subtype. This $2.1891 \mu\text{m}$ feature is also present in the other WN stars of our data (see Fig. 4.11). Therefore we conclude that the stars Id 144/AF and Id 1237/IRS 7E2 (ESE) are not Ofpe/WN9 stars but are hotter stars, such as WN8 or WN9. Tanner et al. (2006) also classified star AF (Id 1206) as a broad emission-line star.

The spectra of stars classified as WN stars in Paumard et al. (2006) are shown in Fig. 4.11. WN stars can be separated into an early (WN2 to WN6) and a late group (WN6 to WN9). The only early WN star in our data, Id 574/IRS 16SE2, is a WN5/6 star (Horrobin et al. 2004). The spectrum of Id 155/IRS 13E2 is classified as that of an WN star by Paumard et al. (2006) without further specification. We find that this spectrum resembles the late WN8 spectra of Id 452/AFNW and Id 1354/IRS 9W. Stars Id 784/WR101da and Id 1494/IRS34 NW were classified as WN7 stars. Their spectra have only weak emission lines, for example at $2.189 \mu\text{m}$ (He II) and $2.347 \mu\text{m}$ (He II).

Star Id 491/IRS 15SW was classified as a transition-type WN8/WC9 star by Paumard et al. (2006). In addition to the aforementioned He I and He II emission lines, the spectrum shows the C IV doublet at 2.0796 and $2.0842 \mu\text{m}$, and C III at $\sim 2.325 \mu\text{m}$ in emission. These features are much weaker than the He and H lines. The spectrum of Id 666/IRS 7SW has the same C IV and C III lines, although it was classified as WN8 by Paumard et al. (2006). Therefore we suggest that Id 666/IRS 7SW is a WN/WC transition-type star like Id 491/IRS 15SW.

WC stars have C III and C IV emission lines that are about as strong as the He lines. Figure 4.12 shows the spectra of WC stars in our data set. The classifications are adopted from Paumard et al. (2006). We find that for stars Id 185/IRS 29N, Id 283/IRS 34, Id 303, and Id 638/IRS 29NE1 the emission lines are rather weak. This cannot be caused by the S/N, which is higher than 55 for all of the four spectra. The continua of these four spectra show a steep rise with wavelength, and these stars are also very red ($(H - K_S)_0 > 0.54 \text{ mag}$). This suggests that these stars are embedded in dust (Geballe et al. 2006). The continuum emission from the surrounding dust dilutes the stellar spectral lines (for a discussion see Appendix 4.7).

In summary, we confirm that 29 stars are emission-line stars. We classify the stars Id 144/AF and Id 1237/IRS 7E2 as broad emission-line stars and the star Id 666/IRS 7SW as a WN8/WC9 star, in contrast to Paumard et al. (2006). Four of the stars (Id 185/IRS 29N, Id 283/IRS 34, Id 303, and Id 638/IRS 29NE1) have only weak emission lines, which can be explained by bright surrounding dust. Despite their red colours, we do not consider them to be background stars. We discuss these findings in Appenix 4.7.

Table 4.2: Emission-line and Wolf-Rayet stars

Id	RA [$^{\circ}$]	Dec [$^{\circ}$]	Colour	Name	Type	PGM06 ^d	S/N
9	266.4168	-29.00748	...	IRS16NW	Ofpe/WN9 ^b	E19	96
10	266.4171	-29.00870	...	IRS33E	Ofpe/WN9 ^b	E41	91
97	266.4172	-29.00808	...	IRS16SW	Ofpe/WN9 ^b	E23	82
243	266.4155	-29.00740	red	IRS34W	Ofpe/WN9 ^b	E56	71
260	266.4171	-29.00764	...	IRS16C	Ofpe/WN9 ^b	E20	102
25346	266.4177	-29.00757	...	IRS16NE	Ofpe/WN9 ^b	E39	95
144	266.4148	-29.00974	...	AF	WN ^a	E79	78
155	266.4158	-29.00831	...	IRS13E2	WN ^a	E51	46
414	266.4172	-29.00458	...	IRS15NE	WN8/9 ^b	E88	55
452	266.4144	-29.00883	...	AFNW	WN8 ^b	E74	69
491	266.4163	-29.00504	...	IRS15SW	WN8/WC9 ^b	E83	50
574	266.4178	-29.00814	...	IRS16SE2	WN5/6 ^b	E40	34
666	266.4156	-29.00647	...	IRS7SW	WN8/WC9 ^a	E66	60
784	266.4154	-29.00827	...	WR101da	WN7? ^b	E60	39
813	266.4138	-29.00854	...	AFNWNW	WN7 ^b	E81	57
1237	266.4182	-29.00647	...	IRS7E2(ESE)	WN ^a	E70	36
1354	266.4178	-29.00939	...	IRS9W	WN8 ^b	E65	36
1494	266.4156	-29.00704	...	IRS34NW	WN7 ^b	E61	34
185	266.4163	-29.00742	red	IRS29N	WC9 ^b	E31	82
283	266.4152	-29.00762	red	IRS34	WC9 ^c	...	167
303	266.4174	-29.00813	red	MPE+1.6-6.8	WC8/9 ^b	E32	69
581	266.4186	-29.01009	...	IRS9SE	WC9 ^b	E80	91
638	266.4165	-29.00725	red	IRS29NE1	WC8/9 ^b	E35	55
1181	266.4198	-29.00775	...	[PMM2001]B1	WC9 ^b	E78	39
1188	266.4141	-29.00930	...	Blum	WC8/9 ^b	E82	21
1219	266.4182	-29.01005	...	IRS9SW	WC9 ^b	E76	42
1258	266.4178	-29.00686	...	[PMM2001]B9	WC9 ^b	E59	40
1703	266.4161	-29.00616	...	IRS7W	WC9 ^b	E68	20
2677	266.4173	-29.00601	WC8/9 ^b	E71	27

Notes. ^(a) Spectral classification from this work ^(b) Spectral type from Paumard et al. (2006)
^(c) Spectral type from Blum et al. (2003) ^(d) PGM06 refers to the nomenclature of Paumard et al. (2006)

4.4.3 Featureless spectra

Previous studies pointed out that several sources apparently have featureless, steep K -band spectra in the Galactic centre. For example, the spectra of IRS 3 and IRS 1W show no detectable emission or absorption features (e.g. Krabbe et al. 1995; Blum et al. 2003). These sources are often extended in mid-infrared images, and it was shown that they are bow shocks. Bow shocks are caused by bright emission-line stars that either have strong winds or move

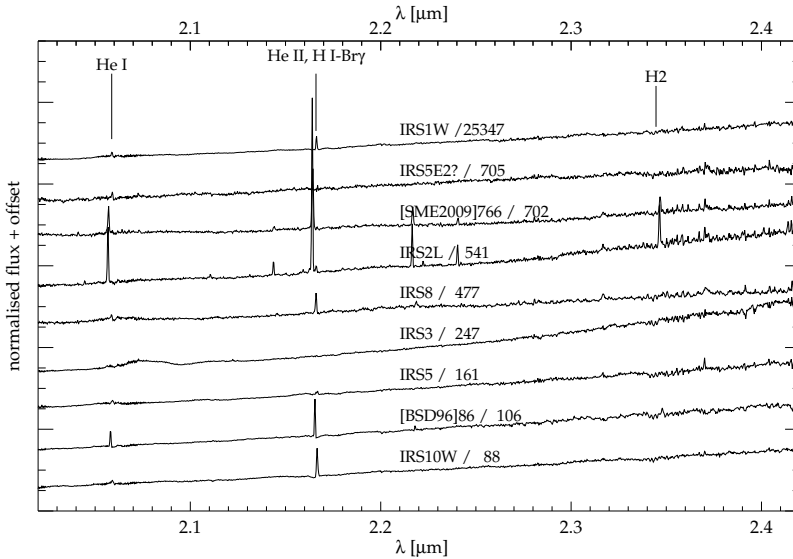


Figure 4.13: Featureless spectra. Emission lines are due to imperfect background subtraction and caused by He I, H I, and H₂ gas emission. The fluxes are normalised and an offset is added to the flux. The spectra are not shifted to rest wavelength.

through the minispiral (e.g. Tanner et al. 2005, 2006; Geballe et al. 2006; Viehmann et al. 2006; Perger et al. 2008; Buchholz et al. 2009; Sanchez-Bermudez et al. 2014).

We detected several featureless sources in our KMOS data. They are listed in Table 4.3, and their spectra are shown in Fig. 4.13. The first column of Table 4.3 denotes the Id, R.A., and Dec from our catalogue. Most of the sources with featureless spectra are located close to the minispiral. The last column of Table 4.3 gives their location within the minispiral. We also indicate their positions in Fig. 4.7. Many of the stars are either connected with the Northern Arm (NA) or the Bar. Only star Id 247/IRS 3 is in a region of low ionised gas emission. Nevertheless, it is the most reddened of these sources.

Bow shocks arise through the interaction of the interstellar medium (like the minispiral gas) with the material expelled from mass-losing stars. The central sources of Id 161/IRS 5 and Id 25347/IRS 1W are probably WR stars (Tanner et al. 2005; Sanchez-Bermudez et al. 2014). The source Id 247/IRS 3 was classified as WC5/6 (Horrobin et al. 2004) and as an AGB star (Pott et al. 2005). The spectrum of Id 247/IRS 3 shows a broad emission bump at 2.078 μm , but this could be caused by the close WN5/6 star IRS 3E. This star is rather faint ($K_S = 14.1$ mag), however, compared to star Id 247 ($K_S = 11.2$ mag), and therefore the spectrum has a too low S/N and is missing from our list of WR stars.

The spectrum of Id 477/IRS 8 in our data is nearly featureless, but Geballe et al. (2006) were able to separate the spectrum of IRS 8 into the contribution of the bow shock and the actual star, IRS 8*. They showed that star IRS 8* has several weak emission and absorption

Table 4.3: Stars with featureless spectra

Id	RA [°]	Dec [°]	Colour	Name	Type	S/N	location
88	266.4189	-29.00637	...	IRS10W	...	110	NA
106	266.4176	-29.00855	red	[BSD96]86	...	116	Bar
161	266.4196	-29.00512	?	IRS5	WR ^f	102	NA
247	266.4161	-29.00676	red	IRS3	WC5/6 ^c /AGB ^d	94	-
477	266.4173	-28.99969	red	IRS8	O5-6 ^e	58	NA-edge
541	266.4157	-29.00891	red	IRS2L	...	51	Bar
702	266.4156	-29.00938	...	[SME2009]766	...	51	Bar
705	266.4209	-29.00485	...	IRS5NE?	G8 III ^g	48	NA
25347	266.4185	-29.00766	?	IRS1W	Be ^{?b} /WR ^f	125	NA

Notes. ^(a) K_S magnitudes from Schödel et al. (2010), if available ^(b) Spectral type from Paumard et al. (2006) ^(c) Spectral type from Horrobin et al. (2004) ^(d) Spectral type from Pott et al. (2005) ^(e) Spectral type from Geballe et al. (2006) ^(f) Spectral type from Tanner et al. (2005), Sanchez-Bermudez et al. (2014) ^(g) Spectral type from Perger et al. (2008)

lines and classified IRS 8* as O star. One star in our sample of featureless sources (Id 705) was classified as a late-type star by Perger et al. (2008).

These featureless sources are also very red in $H - K_S$, as we show in Fig. 4.3. We find that of all of the sources, the spectra of Id 247/IRS 3 and Id 541/IRS 2L have the steepest continuum rise to longer wavelengths (slope $m = \Delta\text{flux}/\Delta\lambda = 4.2$ and 3.3, respectively). These sources are probably not background stars, but surrounding dust causes the reddening.

In brief, many stars with featureless spectra were either classified as young emission-line or O-type star, or their red colour and continuum shape suggest that they are young, embedded stars. Therefore we also consider these stars as young early-type stars of the Milky Way nuclear star cluster.

4.4.4 Spatial distribution of early-type stars

Our wide-field study of early-type stars confirms the results of previous studies in smaller regions (e.g. Støstad et al. 2015). Young stars are mostly concentrated at $p < 0.5$ pc (see Fig. 4.1). Previous spectroscopic data sets were spatially asymmetric with respect to Sgr A* and therefore were potentially biased. For example, Do et al. (2013a) observed the Galactic centre along the projected disc of young stars. Our data set is completely symmetric with respect to Sgr A* out to $p = 12''$ (~ 0.47 pc). In the radial range to $p = 21''$ (0.84 pc) we only miss a small field of $10''.8 \times 10''.8$, therefore the area is complete to 91 per cent out to $p = 21''$ (0.84 pc). The spatially nearly full coverage allows us to study the spatial distribution of early-type stars.

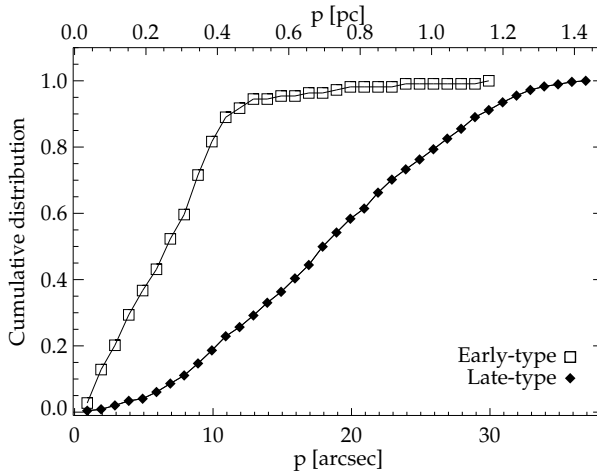


Figure 4.14: Cumulative number counts of early-type stars (open square symbols) and late-type stars (filled diamonds) as a function of projected distance p from Sgr A*, normalised to one. Foreground stars were excluded.

Figure 4.14 shows the cumulative number counts of our observed early-type stars and late-type stars normalised to one, as a function of projected distance p to Sgr A*. Most of the early-type stars lie within the central parsec and reach a cumulative frequency of 0.9 at $p = 12''$ (0.47 pc), whereas the late-type stars are distributed throughout the entire cluster range. For this plot we did not correct for completeness. Including a completeness correction would steepen the lines in the innermost regions even more. The median projected distance to the centre is only $6''.6$ (~ 0.26 pc) for the early-type stars, but $19''$ (0.74 pc) for the late-type stars. We list the projected distance p to Sgr A* for the O/B stars in Table 4.6. The outermost O/B star that is not a foreground star is Id 982 with $p = 23''.6$ (0.92 pc). Only the featureless source Id 477/IRS 8 has a larger distance $p = 29''.4$ among the early-type stars.

While we benefit from the large spatial coverage, our data set lacks the spatial resolution and the higher completeness of other studies (e.g. Bartko et al. 2010; Do et al. 2013a). In Sect. 4.3.2 we calculated the fraction of stars that we missed in different radial and magnitude bins. We used three radial bins ($p < 5''$, $5'' \leq p < 10''$, and $p \geq 10''$) and magnitude bins with a width of $\Delta K_S = 0.5$ mag. We corrected our number counts of early-type stars in the different magnitude and radial bins by including the fraction of missed stars. Then we computed a completeness-corrected stellar number density of bright stars with $K_S < 14.3$ mag. We find excellent agreement with the results of Do et al. (2013a, $K' < 14.3$ mag), as shown in Fig. 4.15. Our data set extends to larger radii beyond $10''$. There are only a few stars in this region, and the number density of bright early-type stars decreases by more than two orders of magnitude from the centre to a projected distance of $p = 1$ pc.

Inspection of Fig. 4.1 shows that the distribution of early-type stars (i.e. O/B stars, emission-line stars, and sources with featureless spectra) appears elongated, primarily along

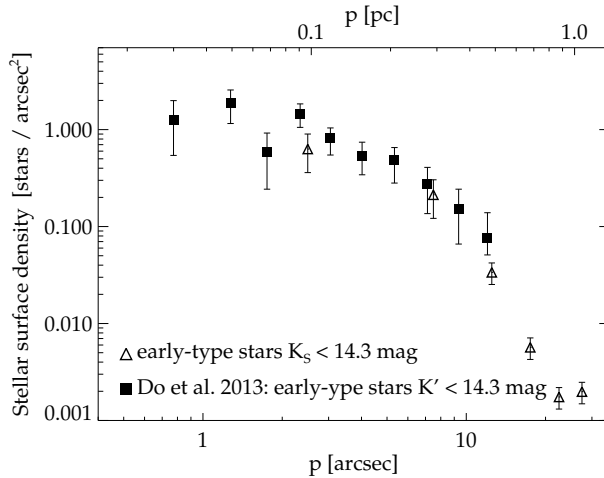


Figure 4.15: Stellar surface density profile for all early-type stars (O/B, emission line stars, and sources with featureless spectra). We exclude possible foreground stars and apply a completeness correction (see Sect. 4.3.1). We consider only stars brighter than $K_S=14.3$ mag. Open triangles denote this study, filled squares the results of Do et al. (2013a).

the Galactic plane. However, there is a slight misalignment of the distribution of early-type stars with respect to the Galactic plane. Most early-type stars beyond 0.5 pc ($\sim 12''.8$) are either in the Galactic north-west (NW, top right), or south-east (SE, bottom left) quadrant. We note that on larger scales the rotation axis also seems offset from the Galactic plane in a similar direction (Feldmeier et al. 2014). The early-type stars are more centrally concentrated in the north-east (NE) and south-west (SW) fields than in the SE and NW fields. The median projected distances \hat{p} are $\hat{p}_{NE} = 0.19$ pc ($5''.0$) and $\hat{p}_{SW} = 0.23$ pc ($5''.8$) in the NE and SW field, but $\hat{p}_{SE} = 0.26$ pc ($6''.6$) and $\hat{p}_{NW} = 0.30$ pc ($7''.8$) in the SE and NW fields.

To quantify a possible asymmetric distribution, we compared the number of early-type stars in the different quadrants Galactic NE, SE, SW, and NW. The centre is the position of Sgr A*. We corrected for the slightly asymmetrically covered area and compared the number of stars N_{field} in different fields. Probable foreground stars were not taken into account. We find that there are about the same number of early-type stars in the NE, SE and SW fields, but ≈ 1.4 times more early-type stars in the NW quadrant (corresponding to more than ten stars). This is in contrast to the distribution of late-type stars, for which there are the fewest stars in the Galactic NW.

As some of the early-type stars in the central ~ 0.5 pc are on a disc, asymmetry is not unexpected. However, Fig. 4.1 shows that the line of nodes of the disc is $\sim 60^\circ$ offset from the Galactic plane. The early-type stars also appear offset from the Galactic plane, but not by as much. An important observational bias is introduced by the spatially variable extinction. This is also shown in Fig. 4.1. In the underlying $1.90 \mu\text{m}$ image there are some patchy regions with less flux, for instance in the SW corner of the image. We detect fewer stars in these regions

and find an asymmetric spatial distribution of early-type stars. As our extinction map does not extend to this region, we cannot quantify the effect of the variable extinction. Thus we cannot conclude whether dust alone can explain the asymmetry.

4.4.5 Kinematics of early-type stars

The early-type stars in the Galactic centre can be distributed into different groups based on their kinematics. In the central $p < 0.03$ pc ($\sim 0''.8$) is the S-star cluster. This group of ≥ 20 stars has high orbital eccentricities e ($\bar{e} = 0.8$, Gillessen et al. 2009b). Most of the stars are B-type main-sequence stars ($K_s \geq 14$ mag). These stars are mostly too faint and too crowded to be in our data set. The only exception is S2 (Id 2314), which is one of the brightest S-stars with $K_s = 14.1$ mag (for a Table of 51 sources in the S-star cluster see Sabha et al. 2010).

At greater distances, 0.03 pc $< p < 0.5$ pc (0.8 – $13''$), there is a clockwise (CW) rotating disc of young stars with moderate orbital eccentricities ($e \approx 0.3$). This disc contains WR, O, and B stars (Yelda et al. 2014). Not all stars in this radial range lie on the disc, there is also a more isotropic off-disc population. The disc and off-disc populations are very similar and probably coeval (Paumard et al. 2006). It is not yet settled whether there is a second, counterclockwise rotating disc. To assess whether a star belongs to the disc or not and if the star is on a bound orbit, we have to know the stellar kinematics.

We measured the radial velocities of O/B stars as described in Sect. 4.3.4, and Table 4.6 lists the radial velocities v_z of the O/B stars. When no good radial velocity measurement was possible with our spectra, we list the radial velocity of Bartko et al. (2009), Yelda et al. (2014), or an error-weighted mean of their measurements. Furthermore, we match the O/B stars of our data set with the proper motions of Yelda et al. (2014) and Schödel et al. (2009). These measurements are also listed in Table 4.6 as v_{RA} and v_{Dec} . To transfer the proper motion velocities into $\text{km}\cdot\text{s}^{-1}$, we assumed a Galactocentric distance of $R_0 = 8$ kpc.

About 20 young stars are on the CW disc (Yelda et al. 2014). The CW disc has the orbital parameters inclination $i = 130^\circ$ and ascending node $\Omega = 96^\circ$ (e.g. Yelda et al. 2014; Bartko et al. 2009; Lu et al. 2009; Paumard et al. 2006). The stars on the CW disc are approaching (negative radial velocity, $v_z < 0$) in the equatorial North-West, and receding (positive radial velocity, $v_z > 0$) in the equatorial South-East. Based on this simple criterion, we can exclude the membership of 23 stars of our O/B star sample, 7 of which are newly identified O/B stars. We list in the second last column of Table 4.6 whether v_z agrees with the rotation of the CW disc or not. If the entry in the sixth column of Table 4.6 is 0, a membership to the CW disc is not possible according to v_z , given the longitude of the ascending node Ω is 96° . If the disc is warped, as found by Bartko et al. (2009), the value of Ω would change with the distance to Sgr A*. Then the radial velocity criterion would exclude one star less.

The stellar kinematics are illustrated in Fig. 4.16. For 45 O/B stars we have the radial velocity and proper motions, and for 22 stars proper motions alone. The directions of the arrows denote the proper motion direction, the lengths of the arrows denote the proper motion velocity v_{pm} assuming a distance of 8 kpc. Additionally, we overplot the kinematics of the emission-line stars with 27 radial velocities adopted from Tanner et al. (2006), and 28 proper

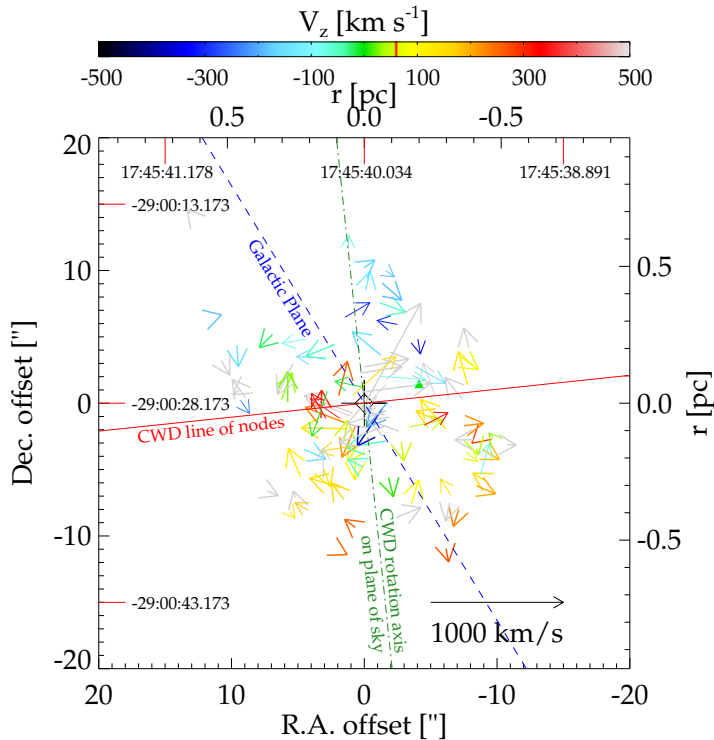


Figure 4.16: Three-dimensional stellar kinematics of the O/B stars and emission line stars (smaller arrows). The arrows denote the proper motions, colours signify different radial velocities v_z . The black cross indicates the position of Sgr A*. The coordinates show the offset to Sgr A* in equatorial coordinates, the numbers at the top and left denote absolute equatorial coordinates. The Galactic plane is plotted as a blue dashed line; the line of nodes of the clockwise disc with $\Omega = 96^\circ$ as a red line; the projected rotation axis of the clockwise disc as a green dot-dashed line.

motion measurements as slightly smaller arrows. Proper motions are taken from Yelda et al. (2014) if available, and from Schödel et al. (2009) otherwise. Because we used the disc parameters of Yelda et al. (2014) in our analysis, we give preference to the proper motions derived by this study.

4.4.6 O/B star orbits

To identify stars on radial or tangential orbits, the angular momentum $j_z = xv_y - yv_x$ can be used, or as suggested by Madigan et al. (2014), j_z normalised to the maximum angular momentum at projected radius p

$$h = \frac{xv_y - yv_x}{\sqrt{GM_\bullet p}}. \quad (4.1)$$

x and y denote the distance to Sgr A* in equatorial coordinates, v_x and v_y are the proper motions in the same coordinate system, $M_\bullet = 4.3 \times 10^6 M_\odot$ (Ghez et al. 2008; Gillessen et al. 2009b) is the mass of the supermassive black hole, and G is the gravitational constant.

The h -value constrains the stellar orbital eccentricity and shows whether the star is on a projected orbit that is clockwise (CW) tangential ($h \approx 1$) or counterclockwise tangential ($h \approx -1$). We also list h in Table 4.6. If h is negative, this star is probably not a member of the CW disc, although the radial velocity v_z may agree with the CW disc. A value of $h \approx 0$ does in principle mean the star is on a radial projected orbit. But this can have different reasons: Either the star has a high orbital eccentricity ($e \gtrsim 0.8$), a highly inclined orbit ($i \gtrsim 70^\circ$, with 90° meaning edge-on), or both. If we have both proper motion and radial velocity for a star, we can compare the magnitude of the proper motion velocity $v_{\text{pm}} = (v_{\text{RA}}^2 + v_{\text{Dec}}^2)^{1/2}$ to the total three-dimensional velocity v_{tot} . If the proper motion velocity is much lower than the radial velocity, that is, the three-dimensional velocity vector is mainly pointing along our line of sight, the star is on a close to edge-on orbit. For example, a value of $v_{\text{pm}}/v_{\text{tot}} \leq 0.2$ indicates a high inclination of the orbit. Then a low value of $|h|$ tells us nothing about the eccentricity of the stellar orbit.

Twenty-four stars have $|h| \leq 0.2$, suggesting a high eccentricity e , a high inclination i , or both. For 18 of these stars we have kinematics in three dimensions, thus we can infer for three stars that they have orbits with high inclination, they are marked with a footnote in Table 4.6 (Id 483, 728, and 853). On the other hand, we have 11 stars with $|h| \leq 0.2$, for which the ratio $|v_{\text{pm}}|/v_{\text{tot}} \geq 0.6$ indicates a rather low inclination. Therefore the orbits of these stars have truly high eccentricities.

Although a low value of $|h|$ does not necessarily mean a radial orbit, a value of $h > 0.6$ is an indication that a star is on the CW disc. Our data set contains 14 stars (~ 20 per cent) with $h > 0.6$, for eight (~ 12 per cent) of them v_z also agrees with the CW disc, but for four of them it does not. Only one star of the new O/B stars is a good candidate for being on the CW disc: Id 596 has $h = 0.82$ and is at a distance of $p = 7''.35$ (~ 0.3 pc) from Sgr A*.

To determine the full orbit of a star and thereby constrain the disc membership, it is also necessary to consider the distance of the star along the line of sight. Lu et al. (2009) and Yelda et al. (2014) included measurements of the plane-of-sky acceleration to constrain the stars' line-of-sight distances to Sgr A*. To better constrain the orbital parameters, previous studies (e.g. Lu et al. 2009; Bartko et al. 2009; Yelda et al. 2014; Sanchez-Bermudez et al. 2014) computed density maps of the orbital planes and ran Monte Carlo simulations.

For one star, Id 96, the value of $|h|$ is even higher than 1: $h = -1.05$. According to Madigan et al. (2014), this means the star is still on a bound orbit, as $|h| \leq \sqrt{2}$. But it requires the semi-major axis of the stellar orbit to be larger than p , and the star is closer to pericenter than apocenter.

Feldmeier et al. (2014) detected two high-velocity stars at $p = 3$ pc ($80''$) and $p = 5$ pc ($130''$) with $v_z = 292 \text{ km}\cdot\text{s}^{-1}$ and $-266 \text{ km}\cdot\text{s}^{-1}$. Our data set also contains stars with high velocities. To check if the O/B stars are bound to the nuclear star cluster, we plot the total velocity v_{tot} against the projected distance p to Sgr A* in Fig. 4.17. For stars without a radial velocity measurement we plot v_{pm} , which is only a lower limit of v_{tot} . The colour-coding

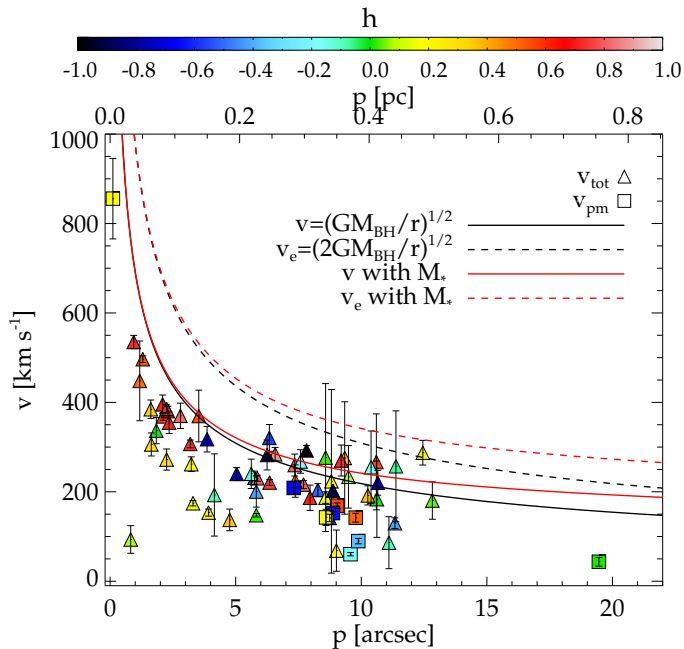


Figure 4.17: Velocity profile for the O/B stars. The total velocity is plotted against the projected distance p to Sgr A*. Triangles denote fully known kinematics in three dimensions, squares denote only two-dimensional projected proper motion measurements and are therefore only lower limits of the total velocity. The colour-coding illustrates the normalised angular momentum $h = (xv_y - yv_x) / (\sqrt{GM_\bullet p})$. The full black line denotes the velocity profile for a central point mass with $M_\bullet = 4.3 \times 10^6 M_\odot$; the dashed line the escape velocity v_e for such a point mass. Red lines mean that we also consider a stellar mass M_* .

denotes the value of h . The full black line denotes the Keplerian velocity with a single point mass in the centre with mass $M_\bullet = 4.3 \times 10^6 M_\odot$. When we also take the stellar mass into account, the velocity increases. To illustrate this, we plot the velocity as a red line when we assume the stellar mass profile from Feldmeier et al. (2014). Most stars lie below this line and must therefore be bound to the Milky Way nuclear star cluster.

The dashed lines show the escape velocity v_e . Only one star has a velocity close to the escape velocity: Id 722. It is at a projected distance of $12''.45$ with $v_{\text{tot}} = (287 \pm 27) \text{ km}\cdot\text{s}^{-1}$. The proper motion of this star also points away from Sgr A*. For Fig. 4.17 we plot only the projected distances of the stars, which are only lower limits. The true distance of star Id 722 might well be larger. But when we consider the stellar mass distribution, the star's velocity is lower than the escape velocity. The normalised angular momentum is $h = 0.16$, and if one takes the stellar mass into account for h as well, $|h|$ becomes even smaller. This indicates that this star with $M_\star = 32 \pm 14 M_\odot$ is on a radial orbit, but the star is still gravitationally bound to the Milky Way nuclear star cluster.

Some of the stars have large velocity uncertainties. Six stars may have velocities above the escape velocity (Id 366, 511, 610, 617, 728, and 853), four of them (610, 617, 728, 853) also have a low value of $|h| < 0.2$, suggesting either a high eccentricity or inclination in their orbits. To better constrain the stellar orbits, a more accurate radial velocity measurement is required.

4.5 Discussion

4.5.1 Detection of 19 new O/B stars

Our sample of 76 O/B stars mostly consists of previously known O/B stars. However, 24 O/B stars have not been reported before, and 19 of these O/B stars are probably also cluster member stars. Three stars (Id 663, 1104, and 3308) are possibly foreground stars, while two stars (Id 436, 3339) are definitely foreground stars.

To verify our classification as O/B type stars, we measured the equivalent widths of the CO line at $2.2935 \mu\text{m}$ and the Na I doublet at $\sim 2.206 \mu\text{m}$ in Sect. 4.4.1 and compared the result to the mean value of the late-type stars. For most of the O/B stars, the equivalent widths deviate by $\sim 3\sigma$ from the mean value of late-type stars for the CO line and by $\sim 2\sigma$ from the mean late-type star value for Na I.

Only ten O/B stars have $EW_{\text{CO}} > 2.7 \text{ \AA}$, i.e. within 3σ of the late-type stars' mean value ($EW_{\text{CO,LT}} = 18.3 \text{ \AA}$). However, six of these ten stars have been classified as O/B stars in previous studies. For the other four stars (Id 718, 2446, 3308, and 3578), the significance of either the CO non-detection or of the Na non-detection is at least 2.7σ . The S/N of the spectra is in the range of 16.9 to 35.8, this is rather low compared to the O/B star median S/N of 46. It is possible that the low S/N or poorly subtracted light from surrounding late-type stars produces a weak CO line signal. If these stars indeed have weak CO lines, the low values of EW_{CO} ($3.2 \text{ \AA} - 8.3 \text{ \AA}$) would suggest effective temperatures $T_{\text{eff}} > 4500 \text{ K}$ (Pfuhl et al. 2011). Then these stars could be of intermediate age ($\sim 100 \text{ Myr}$).

4.5.2 O/B star mass estimates

We estimated the masses of the O/B stars in Sect. 4.4.1.2 based on the assumptions that the intrinsic colours $(H - K_S)_0$ are in a narrow range, close to -0.10 mag (Straizys & Lazauskaitė 2009), their metallicity is roughly solar (Ramírez et al. 2000), and their ages are in the range of $3 - 8 \text{ Myr}$ (Paumard et al. 2006; Lu et al. 2013). This means that we assumed the same age for the new O/B star detections as for the previously known O/B star population, for which this age estimate was derived. This may be an oversimplification. The new O/B-type stars are at larger projected distances from Sgr A* and may have formed in a different star formation event. This means that their age and metallicity may be different. Some of these stars have a mass of approximately $10 M_{\odot}$. Renzini et al. (1992) showed that a star with a mass $M_{\star} = 9 M_{\odot}$ and solar metallicity spends $\sim 20 \text{ Myr}$ on the main sequence. This means that these stars may be much older than $3 - 8 \text{ Myr}$. On the other hand, among the newly

classified O/B stars are also several bright, massive stars ($M_\star > 20 M_\odot$). These stars must be younger and close to the age of 3 – 8 Myr. The spectra of the newly identified O/B stars with $S/N \gtrsim 50$ contain a He I absorption line at $2.113 \mu\text{m}$. Hanson et al. (1996) showed that this line disappears in early O stars. Therefore the stars with $2.113 \mu\text{m}$ absorption are later than O7 V, O7 III, or O9 I. This suggests that the new O/B stars belong to the same population as the already classified O/B stars, none of which is earlier than O7 (Paumard et al. 2006).

The estimated mass in Table 4.5 is the median of the distribution of possible stellar masses weighted by the likelihood of the star position in the colour magnitude diagram. We considered the uncertainty of the Galactocentric distance σ_{R_0} , the extinction law coefficient σ_α , the photometry (σ_H and σ_{K_S}), and the intrinsic colour $\sigma_{(H-K_S)_0}$ in the propagated uncertainty. For the brightest of these stars we derive median masses of more than $40 M_\odot$. Such a high mass was observed for O6 I or O6 V stars (Cox 2000, Table 15.8). But the stars with reported spectral type in our sample are of type O8 and later. For example, we derive a mass of $M_\star = (41^{+9}_{-13}) M_\odot$ for the O8–9.5 star Id 331. Stars of this spectral type have masses of $\sim 28 M_\odot$ (O8 I star) and lower (Cox 2000, Table 15.8). This suggests that we rather overestimate the stellar masses.

We showed that the derived value for the extinction A_{K_S} from intrinsic colours is lower than the value of A_{K_S} from the extinction map adopted from Schödel et al. 2010 (see Fig. 4.5). We would find better agreement by assuming an extinction law exponent of $\alpha = 2.1$ instead of $\alpha = 2.21$ (Schödel et al. 2010). Then the derived magnitudes $K_{S,0}$ of the stars would be higher, that is, the stars would be fainter. We tested if this would lower the stellar masses, but found that it is only a minor effect. For most of the stars the lower limit of our mass estimate agrees with the mass expected for the spectral type.

4.5.3 Total mass of young stars

We calculated a lower limit for the total mass of young stars to $M_{\text{young}, M \leq 150 M_\odot}^{\alpha=1.7} = 21,000 M_\odot$ assuming a top-heavy initial mass function (IMF) with slope $\alpha = 1.7$ (Lu et al. 2013) and a maximum stellar mass $M = 150 M_\odot$. This result agrees with the cluster total mass found by Lu et al. (2013) of 14,000 to 37,000 M_\odot in the same integration range [$1 M_\odot$; $150 M_\odot$]. With an extremely top-heavy IMF ($\alpha = 0.45$, Bartko et al. 2010), the mass is even higher $M_{\text{young}, M \leq 150 M_\odot}^{\alpha=0.45} = 32,000 M_\odot$, but still in agreement with Lu et al. (2013). We integrated up to stars with $M = 150 M_\odot$, but the most massive star in the Galactic centre has only $M_\star = 80 M_\odot$ (Martins et al. 2007). When we integrate in the interval [$1 M_\odot$; $80 M_\odot$], the cluster mass is only $M_{\text{young}, M \leq 80 M_\odot}^{\alpha=1.7} = 16,000 M_\odot$, for $\alpha = 1.7$, and $M_{\text{young}, M \leq 80 M_\odot}^{\alpha=0.45} = 12,000 M_\odot$ for $\alpha = 0.45$. We thus give $M_{\text{total, young}} \sim 12,000 M_\odot$ as a lower limit for the mass of the young star cluster.

For these calculations we assumed that the present-day mass function slope is the same as the IMF slope, but this is only valid for a simple stellar population (Elmegreen & Scalo 2006). This is a reasonable assumption, since we used stars in the mass range [$30 M_\odot$; $45 M_\odot$] to fit the IMF, and these stars should all be younger than 8 Myr. As we scaled the IMF only to the observed mass function of O/B stars and did not consider the massive and young emission-line stars, the derived total cluster mass is only a lower limit.

4.5.4 Disc membership

We estimated if an O/B star can be a member of the clockwise (CW) disc based on the stellar angular momentum h and on the stellar radial velocity v_z . As the disc is receding in the SE and approaching in the NW, we can exclude the membership of stars with $v_z > 0$ that are located in the NW and of stars with $v_z < 0$ that are located in the SE. We can also exclude stars with an angular momentum $h \lesssim 0.5$ if we can show that the orbit is not edge-on. This allowed us to exclude the CW disc membership for 53 stars (>69 per cent) in our O/B star sample, of which 16 stars are newly classified O/B stars. When we assume that the CW disc is warped, as found by Bartko et al. (2009), these numbers change by only one star (54 stars, >72 per cent).

A disc fraction of $\lesssim 30$ per cent agrees with the results of Yelda et al. (2014), who studied the kinematics of O/WR stars and found a disc fraction of about 20 per cent. Yelda et al. (2014) also showed that the significance of the disc decreases with distance to Sgr A*. Our sample of new O/B stars mostly lies at $\sim 10''$ (0.4 pc), that is, close to the assumed outer edge of the CW disc at $\sim 13''$ (0.5 pc). It might be that the outer edge of the disc is even closer to Sgr A* (Støstad et al. 2015).

On the other hand, we found ten stars (one new) for which a membership to the CW disc is possible based on their proper motions, projected location, and radial velocity. However, this does not mean that these stars are necessarily members of the CW disc, as the three-dimensional location with respect to Sgr A* was not taken into account. We were unable to constrain whether the remaining 13 O/B stars might be members of the CW disc or not. The radial velocity uncertainty allows both a receding and an approaching motion, there is no proper motion available, or the inclination i is too high to determine the angular momentum h . Three of these undetermined stars are probably foreground stars.

For a better determination of the stellar orbits, a more sophisticated analysis such as that reported by Lu et al. (2009), Bartko et al. (2009), Yelda et al. (2014), and Sanchez-Bermudez et al. (2014), is necessary. In the future, the missing proper motions and radial velocities that are missing so far will probably also be available (Pfuhl et al. in prep.).

4.5.5 Origin of the early-type stars

Our data set covers the central $2.51 \text{ pc} \times 1.68 \text{ pc}$ ($> 4 \text{ pc}^2$) of the Galactic centre. No previous study covered such a large region with a comparable spatial resolution. We were able to extract stars as faint as $K_S = 15 \text{ mag}$ with a completeness of 80 per cent at $K_S \approx 13.5 \text{ mag}$. For the bright supergiants and giant stars with $K_S < 13 \text{ mag}$, we can assume that our data set is roughly complete out to $p = 0.84 \text{ pc}$ ($21''$).

Bright O/B stars with $K_S < 13 \text{ mag}$ have a well-determined age of 3 – 8 Myr. We can add the red supergiant IRS 7, the emission-line stars, and sources with featureless spectra and $K_S < 13 \text{ mag}$, which are in the same age range. Then we find that 90 per cent of these 79 massive stars are located within $p = 0.44 \text{ pc}$ ($11''.4$). This confirms the finding of Støstad et al. (2015) that the cluster of young stars has an outer edge at approximately $13''$ (0.52 pc). This

central confinement can help to constrain the origin and formation scenarios for the young stars.

It was suggested that young stars in the Galactic centre were formed in a massive young star cluster that fell towards the centre from $r \gtrsim 10$ pc (Gerhard 2001; McMillan & Portegies Zwart 2003). In this scenario the infalling cluster is stripped and disrupted. But then we would expect a higher number of young stars beyond $p = 0.5$ pc (Fujii et al. 2010; Perets & Gualandris 2010). Our data set contains only three bright early-type stars (and three faint early-type stars) beyond $p = 0.5$ pc, but 76 (23) within $p = 0.5$ pc. An infalling cluster would leave a trail of early-type stars, but we find no evidence for such a structure. It might be possible that the infalling cluster had been mass segregated and left a trail of fainter early-type stars that we could not detect. But other studies with a smaller spatial coverage but higher completeness for fainter stars were likewise unable to detect any signs of a trail (Bartko et al. 2010; Støstad et al. 2015).

The late-type stars are much less concentrated than the early-type stars. This agrees with the findings in other nuclear star clusters (e.g. Seth et al. 2010; Georgiev & Böker 2014; Carson et al. 2015). The old component of the nuclear star cluster is often spheroidal and more extended than the disc of young stars. One counterexample is NGC 4244, where the blue disc is more extended than the older spheroidal component (Seth et al. 2008b). Seth et al. (2006) argued that young stellar discs in nuclear star clusters have a lifetime of $\lesssim 1$ Gyr before being disrupted. In other nuclear star clusters, the young discs are often aligned with the host galaxy disc (e.g. NGC 404, NGC 4244, and NGC 4449; Seth et al. 2006, 2008b; Georgiev & Böker 2014). This is not the case for the CW disc in the Galactic centre. The projected distribution of young stars beyond $p = 0.47$ pc ($12''$) appears to be elongated along the Galactic plane, but slightly misaligned to it. It is unclear if this effect is only caused by the variable extinction.

The CW disc of young stars can be explained by in situ star formation in a dense disc or stream around Sgr A* (Levin & Beloborodov 2003; Paumard et al. 2006). The material would come from infalling molecular clumps and gas clouds (e.g. Wardle & Yusef-Zadeh 2008; Gualandris et al. 2012; Emsellem et al. 2015). As the stars are very concentrated in the centre, the star-forming region must have had a size of $r \lesssim 0.5$ pc. However, the majority of the early-type stars in the Galactic centre are not on the CW disc (see Sect. 4.5.4 and Yelda et al. 2014). As the stars are only 3 – 8 Myr old, the young stars either did not all form in a disc or the disc is dissolving more rapidly than expected.

One possible disruption scenario is the infall of another molecular cloud to the Galactic centre (Mapelli et al. 2013). This cloud is disrupted in the supermassive black hole potential and forms an irregular, dense gas disc. Perturbations induced from this gas disc might be able to dismember the CW disc of young stars (Mapelli et al. 2013). This could explain the isotropic cluster of young stars in the same radial range as the CW disc. However, other reasons that cause an instability of the CW disc are also possible (e.g. Hobbs & Nayakshin 2009; Chen & Amaro-Seoane 2014). More simulations and theoretical work are needed to explore the possibilities.

4.5.6 Early-type stars beyond the central 0.5 pc

There are only six stars with projected distances $p > 0.5$ pc. These are three O/B stars (Id 982, 2048, and 2446) and three featureless sources (Id 161, 477, and 705). However, the classification of two of the O/B stars as cluster member stars is uncertain. Id 982 is located outside the coverage of the extinction map by Schödel et al. (2010), therefore the colour has a large uncertainty. Id 2048 lacks full colour information.

Id 2446 at $p = 0.75$ pc ($19''.5$) is the only outer O/B star with available proper motions. The proper motion vector points away from Sgr A*, but the velocity is low enough for the star to be bound to the cluster ($v_{\text{pm}} = 43.5 \pm 9.6$ km·s⁻¹). The angular momentum is $h = 0.01$, which means that the star is on a radial projected orbit.

Two of the three featureless sources beyond 0.5 pc (Id 161/IRS 5 and 705/IRS 5NE) are part of the IRS 5 complex (Perger et al. 2008). Viehmann et al. (2006) pointed out that the IRS 5 sources are remarkably bright in the mid-infrared, but less prominent in the near-infrared. The O/B star Id 483/IRS 5SE also belongs to this group. IRS 5SE consists of two components, IRS 5SE1 and IRS 5SE2 (Viehmann et al. 2006), which cannot be resolved in our data set. In this region we have two additional spectra that we were unable to classify (IRS 5S and IRS 5E); the remaining stars in this area have late-type signatures.

Id 477/IRS 8 is a special case. This featureless source has the largest distance to Sgr A* of all early-type stars in our field of view. Geballe et al. (2006) classified IRS 8 as an O5–O6 giant or supergiant. This makes IRS 8 the earliest O/B star in the Galactic centre. All the O/B stars within $p = 0.5$ pc are of type O8 and later. This would make IRS 8 the youngest known star in the Galactic centre. However, Geballe et al. (2006) suggested that IRS 8 originally was a member of a close binary and was rejuvenated.

4.6 Summary

We observed the central >4 pc² of the Galactic centre with the integral field spectrograph KMOS. Among more than 1 000 spectra from single stars were 114 early-type star spectra. We analysed these early-type spectra, and found the following:

1. We detected 24 previously unknown O/B-type stars. Of these, 19 stars are probable cluster members. The new O/B stars are at projected distances of 0.3 pc–0.92 pc and cover masses from about 10 – 40 M_{\odot} .
2. We derived a lower mass limit for the young cluster mass $M_{\text{total,young}} = 12,000 M_{\odot}$. We used different initial mass function slopes from the literature and integrated in the range [1 M_{\odot} ; 80 M_{\odot}].
3. With our spatially extended and nearly symmetric coverage, we studied the spatial distribution of early-type stars. We found that the early-type stars are strongly concentrated in the projected central $p = 0.4$ pc and that only a few stars lie beyond 0.5 pc.

This contradicts a scenario where the early-type stars formed outside the Galactic centre in a massive cluster that fell towards the centre and depleted the stars at their current location. This formation scenario would leave behind a trail of early-type stars at projected distances of $p > 0.5$ pc, which we did not detect. This is a strong argument for the in situ formation of the early-type stars.

4. We studied the kinematics of the O/B stars and showed that one of the new O/B stars is a good candidate to be a member of the clockwise rotating disc. However, the majority (≥ 69 per cent) of the O/B stars is not on the disc. This means that either these stars have not formed on the clockwise disc or that the disc is already strongly disrupted. We found no stars that are unbound to the Milky Way nuclear star cluster.

Acknowledgements

This research was supported by the DFG cluster of excellence Origin and Structure of the Universe (www.universe-cluster.de). C. J. W. acknowledges support through the Marie Curie Career Integration Grant 303912. This publication makes use of data products from the Two Micron All Sky Survey, which is a joint project of the University of Massachusetts and the Infrared Processing and Analysis Center/California Institute of Technology, funded by the National Aeronautics and Space Administration and the National Science Foundation. This research made use of the SIMBAD database (operated at CDS, Strasbourg, France).

We would like to thank the ESO staff who helped us to prepare our observations and obtain the data. Special thanks go to Alex Agudo Berbel, Yves Jung, Ric Davis, and Lodovico Coccato for advice and assistance in the data reduction process. We are also grateful to Sebastian Kamann for providing us with his code PAMPELMUSE. We thank Morgan Fouesneau, Iskren Georgiev, and Paco Najarro for discussions and suggestions. We finally thank the anonymous referee for comments and suggestions.

Based on observations collected at the European Organisation for Astronomical Research in the Southern Hemisphere, Chile (60.A-9450(A)).

4.7 Appendix: Spectral classification of emission-line stars

We have spectra of 29 emission line stars. These stars were classified in previous studies as either Ofpe/WN9 type, WN, or WC type stars. Ofpe/WN9 types have narrower lines and are cooler ($T_{\text{eff}}=10,000\text{--}20,000$ K) than WN and WC stars ($T_{\text{eff}}>30,000$ K). We found some disagreement with previously reported spectral classifications for some of the emission-line stars.

Id 144/AF and Id 1237/IRS 7E2(ESE): We find that the two stars Id 144/AF and Id 1237/IRS 7E2(ESE), which were listed as Ofpe/WN9 by Paumard et al. (2006), have broad emission lines and are rather WN8 or WN9 stars. Paumard et al. (2006) stated that their spectra of these stars are of high quality. But we also have a high S/N, 78.2 for Id 144/AF and

35.6 for Id 1237/IRS 7E2. Furthermore, the high-resolution spectra of Tanner et al. (2006) agree with Id 144/AF being a broad emission-line star, but they have no data for Id 1237/IRS 7E2(ESE). Paumard et al. (2003) also found a broad He I line in the spectrum of Id 144/AF. The resolving power R reported by Tanner et al. (2006) was 14,000 and 23,300, but only 1 500 and 4 000 in the data used by Paumard et al. (2006). Our data set with $R \approx 4\,300$ agrees with the high-resolution results from Tanner et al. (2006). Because of their broad emission lines (FWHM $\sim 700\text{ km}\cdot\text{s}^{-1}$) and the resemblance of the spectra of Id 144/AF and Id 1237/IRS 7E2 with the WN8 and WN9 spectra in our data set, we classify Id 144/AF and Id 1237/IRS 7E2 as broad emission-line stars, probably WN8 or WN9. Id 1237/IRS 7E2 was also classified as a WN8 star by Martins et al. (2007). Martins et al. (2007) used non-LTE atmosphere models to derive the properties of Galactic centre stars. For Id 144/AF they found a degeneracy between the effective temperature T_{eff} and the helium abundance $[He/H]$. In addition, the wind of this star could be stronger than the wind of the Ofpe/WN9 stars, and Id 144/AF may be more evolved. Martins et al. (2007) suggested that Ofpe/WN9 stars evolve to WN8 stars.

Id 666/IRS 7SW: We reclassify the star Id 666/IRS 7SW as WN8/WC9. This star was classified as WN8 in Paumard et al. (2006). The C III and C IV lines distinguish a WN8/WC9 star from a WN8 star. These lines are weaker than the He and H lines. Therefore a low S/N can lead to a misidentification as a WN8 star, but Paumard et al. (2006) state that their spectrum of Id. 666/IRS 7SW is of high quality. Our spectrum of this star has a S/N of 59.9, and we can clearly identify the C IV doublet at $2.0796\ \mu\text{m}$, and $2.0842\ \mu\text{m}$ C III at $2.325\ \mu\text{m}$ (see Fig. 4.11). The spectrum is very similar to the spectrum of the WN8/WC9 star Id 491/IRS 15SW, therefore we conclude that Id 666/IRS 7SW is also a WN8/WC9 type star. The two stars Id 491/IRS 15SW and Id 666/IRS 7SW are also in a similar location at the colour-magnitude diagram ($(H - K_S)_0 = -0.02\ \text{mag}$ and $-0.11\ \text{mag}$, $K_{S,0} = 9.40\ \text{mag}$ and $9.59\ \text{mag}$, Fig. 4.3), which confirms their similarity. This classification agrees with that of Martins et al. (2007).

Id 185/IRS 29N, Id 283/IRS 34, Id 303, and Id 638/IRS 29NE1: Four of the eleven WC stars have only shallow emission lines in our data set. These stars are Id 185/IRS 29N, Id 283/IRS 34, Id 303, and Id 638/IRS 29NE1. The lines are very broad, but only weakly pronounced. Previous studies (Paumard et al. 2001; Tanner et al. 2006) did not detect any distinct He I emission for Id 185/IRS 29N, while Paumard et al. (2003) reported a broad He I emission line for the same star. Tanner et al. (2006) suggested that Id 638/IRS 29NE1 is variable and that the spectral features changed with time. Rafelski et al. (2007) studied the light curve of IRS 29N over a time line of ten years and found photometric variability. They suggested that these sources could be a wind-colliding binary system. Gamen et al. (2012) showed that stars can change their spectra within months.

Apart from the weak but broad lines, all the four sources are also very red ($(H - K_S)_0 > 0.55\ \text{mag}$). Their continua rise steeply with wavelength. This is an indication that these sources are embedded in dust (see e.g. Geballe et al. 2006 for IRS 8). The continuum in the spectra might not be the stellar continuum, but the continuum of the circumstellar dust, which dominates the lines (Figer et al. 1999; Chiar & Tielens 2001). Therefore the emission lines appear only as weak, broad bumps in the spectrum.

Circumstellar dust is common for WC9 stars such as Id 185/IRS 29N and Id 283/IRS 34. For earlier types such as WC8, dust formation is rather uncommon and might indicate colliding winds (Sander et al. 2012). The two stars Id 303 and Id 638/IRS 29NE1 are WC8/9 stars. Id 303 is located close to the minispiral, at least in projection. So it might be a bow-shock that causes the reddening of Id 303. The bow-shock sources Id 161/IRS 5 and Id 25347/IRS 1W are probably also embedded WR stars (Tanner et al. 2005; Sanchez-Bermudez et al. 2014), but their emission lines are outshone by the bow-shock continuum. Id 638/IRS 29NE1, however, is not located inside the minispiral. But as mentioned earlier, the spectral features seem to change with time. This could be explained by circumstellar dust.

Id 243/IRS 34W: The star with a narrow emission line, Id 243/IRS 34W, has moderate reddening ($(H - K_S)_0 = 0.24$ mag) and a steeply rising continuum. As Paumard et al. (2003) already pointed out, this star is fainter than the other stars with narrow emission lines (see also the colour-magnitude diagram, yellow circle with black cross, Fig. 4.3). The star Id 243/IRS 34W shows a long-term photometric variability (Ott et al. 1999; Paumard et al. 2003). Therefore this star may also be dust embedded. Id 243/IRS 34W is a LBV candidate, and Humphreys et al. (1999) showed for the case η Carinae that LBV eruptions are accompanied with circumstellar dust obscurations.

4.8 Appendix: O/B star tables

Table 4.4: O/B stars I.

Id	R.A. [$^{\circ}$]	Dec [$^{\circ}$]	Δ R.A. [$''$]	Δ Dec [$''$]	K_S^a [mag]	Name	Type	Note ^b
64	266.4174	-29.0077	-1.63	0.57	10.7	IRS16CC	O9.5-B0.5	4, 5
96	266.4144	-29.0074	6.61	1.39	10.4	3
109	266.4172	-29.0083	-1.06	-1.92	10.6	...	B0.5-1	4, 5
166	266.4140	-29.0094	7.66	-5.79	11.3	1, 5, 7
205	266.4188	-29.0077	-5.31	0.27	11.2	IRS1E	B1-3	4
209	266.4157	-29.0099	3.01	-7.57	11.2	3?
227	266.4174	-29.0096	-1.55	-6.34	11.4	...	?	2
230	266.4168	-29.0054	0.08	8.52	11.2	...	O9-B	2, 5
273	266.4168	-29.0050	-0.00	10.20	11.4	...	O9-B	2, 5
294	266.4168	-29.0085	0.08	-2.30	11.1	IRS33N	B0.5-1	4, 5
331	266.4171	-29.0083	-0.57	-1.72	11.3	IRS16SSW	O8-9.5	4
366	266.4171	-29.0104	-0.57	-9.37	11.6	1, 5
372	266.4183	-29.0088	-3.83	-3.48	11.8	4
^{fg} 436	266.4197	-29.0032	-7.62	16.76	11.7	1, 7
443	266.4173	-29.0082	-1.22	-1.48	12.1	IRS16SSE1	O8.5-9.5	4
445	266.4165	-29.0057	0.98	7.57	11.7	...	O9-B	2, 5
483	266.4203	-29.0060	-9.24	6.63	12.0	IRS5SE	B3	8

Table 4.4: continued.

Id	R.A. [$^{\circ}$]	Dec [$^{\circ}$]	Δ R.A. [$''$]	Δ Dec [$''$]	K_S^a [mag]	Name	Type	Note ^b
507	266.4163	-29.0086	1.39	-2.85	11.9	...	O8.5-9.5	2
508	266.4187	-29.0078	-4.90	0.10	12.2	...	O9.5-B2II	4
511	266.4146	-29.0100	6.03	-8.01	12.1	1, 5
516	266.4175	-29.0066	-1.88	4.42	11.4	...	B0-3	2
562	266.4169	-29.0076	-0.16	0.84	12.3	S1-3	?	4
567	266.4185	-29.0070	-4.57	2.96	11.9	3, 5
596	266.4184	-29.0094	-4.07	-5.53	12.3	1
610	266.4185	-29.0098	-4.40	-7.10	12.0	1
617	266.4142	-29.0095	7.17	-6.22	12.5	1
^{fg} 663	266.4237	-29.0025	-18.37	18.99	12.2	1
668	266.4171	-29.0080	-0.73	-0.73	12.5	4
707	266.4173	-29.0086	-1.30	-2.92	12.3	...	B0-3	4, 5
716	266.4173	-29.0098	-1.30	-7.24	12.6	3
718	266.4161	-29.0102	2.04	-8.62	12.7	1
721	266.4190	-29.0064	-5.88	5.16	12.2	1
722	266.4149	-29.0109	5.21	-10.94	12.7	1
725	266.4160	-29.0084	2.20	-2.11	12.3	...	O9-B0	2
728	266.4142	-29.0086	6.93	-2.96	12.4	3
757	266.4140	-29.0088	7.58	-3.52	12.1	1, 5
762	266.4179	-29.0081	-2.77	-1.11	12.2	IRS16SE3	O8.5-9.5	4
785	266.4171	-29.0090	-0.57	-4.13	12.3	...	B0-1	4
838	266.4146	-29.0068	6.13	3.53	12.3	3
847	266.4160	-29.0086	2.37	-2.90	12.1	...	B0-1	2
853	266.4173	-29.0110	-1.22	-11.33	12.4	1
890	266.4203	-29.0069	-9.15	3.21	12.9	6
900	266.4163	-29.0080	1.39	-0.57	12.6	...	O8.5-9.5	4
936	266.4148	-29.0099	5.46	-7.50	12.7	1
941	266.4169	-29.0072	-0.24	2.27	12.5	...	O9-B0	4
951	266.4199	-29.0066	-8.17	4.37	13.0	...	OB	2
958	266.4142	-29.0088	7.18	-3.42	12.6	3
973	266.4149	-29.0084	5.22	-1.93	14.2	3?
974	266.4178	-29.0092	-2.61	-4.93	13.0	3
[?] 982	266.4098	-29.0102	18.81	-8.47	12.8	1
1048	266.4198	-29.0075	-8.00	0.99	13.1	4
1103	266.4134	-29.0087	9.13	-3.13	16.0	1
^{fg} 1104	266.4218	-29.0042	-13.43	12.87	13.1	1
1123	266.4164	-29.0079	1.14	-0.43	12.9	...	O8-9.5	4
1134	266.4151	-29.0094	4.73	-5.58	15.7	1
1238	266.4163	-29.0078	1.47	0.04	13.3	...	O9-9.5	2
1245	266.4197	-29.0077	-7.59	0.43	13.4	4

Table 4.4: continued.

Id	R.A. [$^{\circ}$]	Dec [$^{\circ}$]	Δ R.A. [$''$]	Δ Dec [$''$]	K_S^a [mag]	Name	Type	Note ^b
1327	266.4151	-29.0082	4.73	-1.32	12.7	3
1350	266.4163	-29.0094	1.55	-5.61	13.3	3
1474	266.4168	-29.0071	-0.00	2.75	13.0	...	O8-9	4
1534	266.4163	-29.0083	1.39	-1.70	13.3	...	O-B	4
1554	266.4145	-29.0083	6.36	-1.70	13.2	3?
1619	266.4166	-29.0081	0.65	-1.05	14.2	S1-8	...	4
1643	266.4164	-29.0053	1.15	9.06	13.8	...	O9-B0	2
1892	266.4164	-29.0068	1.06	3.63	13.5	...	O8-9	2
1935	266.4143	-29.0066	6.70	4.21	13.4	1
[?] 2048	266.4134	-29.0106	9.12	-9.87	15.7	1
2233	266.4166	-29.0079	0.73	-0.34	13.8	S0-14	O9.5-B2	4
2314	266.4168	-29.0078	0.08	0.05	14.4	S2,S0-2	B0-2	4
2420	266.4169	-29.0096	-0.08	-4.81	13.9	4
2446	266.4210	-29.0039	-11.14	14.28	14.1	1
^{fg} 3308	266.4136	-29.0115	8.54	-13.40	14.8	1
^{fg} 3339	266.4231	-29.0079	-16.65	-0.45	14.5	1
3578	266.4192	-29.0097	-6.19	-6.61	14.2	1
[?] 3773	266.4142	-29.0086	7.01	-2.75	14.9	...	O-B	2
[?] 11652	266.4145	-29.0077	6.28	0.30	3?

Notes. Identification number Id, the coordinates in RA and Dec, and the offset coordinates from Sgr A* Δ RA and Δ Dec in arcseconds (R.A._{SgrA*}=266 $^{\circ}$.41684, Dec_{SgrA*}=-29 $^{\circ}$.00781056). We mark the five probable foreground stars with ^{fg}, and stars with unknown colour with [?] in the Id column. If the star was previously listed and classified, we denote the name and type. Column “Note” lists the reference to the stellar identification as an early-type star. ^(a) K_S magnitudes from Schödel et al. (2010), extinction corrected and shifted to a common extinction of $A_{K_S} = 2.70$ mag; ^(b) (1) First spectroscopic classification reported in this work; (2) Spectral type from Paumard et al. (2006); (3) Spectral type from Bartko et al. (2009); (4) Spectral type from Do et al. (2013a); (5) Photometric early-type candidate from Nishiyama & Schödel (2013); (6) Classified as early-type star by Støstad et al. (2015); (7) Early-type star candidate from Feldmeier et al. (2014); (8) Classified as early-type star by Perger et al. (2008).

Table 4.5: O/B stars II.

Id	Extinction map		Intrinsic colour			EW_{CO}	EW_{Na}
	$K_{S,0}$ [mag]	A_{K_S} [mag]	$K_{S,0}$ [mag]	A_{K_S} [mag]	M_{\star} [M_{\odot}]		
64	8.04	2.63	8.12 ± 1.15	2.55 ± 1.14	42^{+10}_{-11}	-3.0	1.0
96	7.74	2.92	7.92 ± 1.23	2.74 ± 1.21	43^{+9}_{-12}	-5.3	-0.5
109	7.87	2.79	8.18 ± 1.11	2.47 ± 1.10	42^{+10}_{-11}	-3.0	0.3

Table 4.5: continued.

Id	Extinction map		Intrinsic colour			M_{\star} [M_{\odot}]	EW_{CO}	EW_{Na}
	$K_{S,0}$ [mag]	A_{K_S} [mag]	$K_{S,0}$ [mag]	A_{K_S} [mag]				
166	8.56	2.58	8.77 ± 1.07	2.37 ± 1.05	41^{+10}_{-12}	-1.8	0.4	
205	8.48	2.66	8.66 ± 1.12	2.48 ± 1.10	41^{+10}_{-12}	0.9	-0.6	
209	8.49	2.53	8.68 ± 1.07	2.34 ± 1.04	41^{+10}_{-12}	-2.0	3.1	
227	8.73	2.51	8.77 ± 1.11	2.47 ± 1.10	41^{+10}_{-12}	0.7	-0.9	
230	8.49	2.58	8.63 ± 1.10	2.44 ± 1.09	41^{+10}_{-11}	-0.6	0.9	
273	8.74	2.48	8.91 ± 1.04	2.31 ± 1.03	41^{+9}_{-13}	-0.3	-0.0	
294	8.44	2.76	8.61 ± 1.17	2.59 ± 1.15	41^{+10}_{-12}	0.3	3.6	
331	8.64	2.74	8.89 ± 1.13	2.49 ± 1.11	41^{+9}_{-13}	-0.4	0.8	
366	8.92	2.51	8.88 ± 1.15	2.55 ± 1.13	41^{+9}_{-13}	-2.1	-1.5	
372	9.11	2.50	9.31 ± 1.03	2.29 ± 1.02	39^{+10}_{-13}	-3.6	0.8	
436	8.99	2.78	11.34 ± 0.29	0.42 ± 0.23	19^{+18}_{-3}	1.3	1.6	
443	9.39	2.71	9.21 ± 1.30	2.89 ± 1.29	39^{+11}_{-13}	3.8	-1.0	
445	8.97	2.61	9.01 ± 1.15	2.57 ± 1.14	40^{+10}_{-13}	-0.2	0.6	
483	9.26	2.44	9.45 ± 1.02	2.25 ± 1.00	38^{+10}_{-14}	1.4	0.4	
507	9.25	2.73	9.52 ± 1.11	2.46 ± 1.09	38^{+10}_{-14}	-2.2	2.5	
508	9.53	2.60	9.50 ± 1.18	2.63 ± 1.17	38^{+11}_{-14}	-1.6	1.2	
511	9.40	2.41	9.53 ± 1.03	2.28 ± 1.01	38^{+10}_{-14}	-2.1	-0.3	
516	8.74	2.97	8.95 ± 1.24	2.76 ± 1.23	40^{+10}_{-12}	4.6	1.6	
562	9.56	2.51	9.69 ± 1.07	2.38 ± 1.06	37^{+11}_{-14}	-4.0	1.0	
567	9.17	2.79	9.48 ± 1.12	2.48 ± 1.10	38^{+10}_{-14}	-0.6	0.9	
596	9.59	2.57	9.59 ± 1.15	2.57 ± 1.14	38^{+10}_{-15}	-1.3	-0.9	
610	9.29	2.72	9.57 ± 1.10	2.44 ± 1.09	38^{+10}_{-15}	-5.6	-1.3	
617	9.81	2.46	10.12 ± 0.97	2.15 ± 0.96	34^{+13}_{-14}	-0.2	0.5	
663	9.50	2.85	10.02 ± 1.05	2.33 ± 1.04	35^{+12}_{-15}	1.9	0.4	
668	9.84	2.61	9.99 ± 1.11	2.46 ± 1.09	35^{+12}_{-15}	1.3	-1.0	
707	9.62	2.79	9.74 ± 1.20	2.67 ± 1.19	37^{+11}_{-15}	1.1	-2.2	
716	9.92	2.58	10.28 ± 1.00	2.21 ± 0.99	33^{+13}_{-14}	0.4	0.0	
718	10.01	2.50	10.17 ± 1.06	2.34 ± 1.04	34^{+13}_{-15}	3.5	3.9	
721	9.53	2.69	9.73 ± 1.12	2.49 ± 1.11	37^{+11}_{-15}	-1.8	0.1	
722	10.02	2.44	10.39 ± 0.93	2.06 ± 0.92	32^{+14}_{-14}	-1.2	-0.6	
725	9.57	2.75	9.78 ± 1.14	2.53 ± 1.13	37^{+11}_{-15}	-8.7	-0.4	
728	9.65	2.66	9.43 ± 1.29	2.88 ± 1.28	39^{+10}_{-15}	-4.4	-1.5	
757	9.42	2.70	9.59 ± 1.14	2.53 ± 1.12	38^{+10}_{-15}	-3.1	-1.2	
762	9.47	2.59	9.80 ± 1.03	2.26 ± 1.01	37^{+10}_{-15}	1.2	2.8	
785	9.60	2.74	9.74 ± 1.17	2.60 ± 1.16	37^{+11}_{-15}	-1.0	-2.3	
838	9.58	2.86	9.66 ± 1.24	2.77 ± 1.23	37^{+11}_{-15}	-1.5	1.0	
847	9.45	2.88	9.26 ± 1.37	3.06 ± 1.36	39^{+11}_{-14}	-4.8	0.7	

Table 4.5: continued.

Id	Extinction map		Intrinsic colour			M_{\star} [M_{\odot}]	EW_{CO}	EW_{Na}
	$K_{S,0}$ [mag]	A_{K_S} [mag]	$K_{S,0}$ [mag]	A_{K_S} [mag]				
853	9.75	2.70	9.65 ± 1.25	2.80 ± 1.24	37^{+11}_{-15}	-0.3	1.1	
890	10.16	2.38	10.34 ± 0.99	2.20 ± 0.98	33^{+13}_{-15}	-4.0	1.5	
900	9.95	2.65	10.15 ± 1.10	2.44 ± 1.09	34^{+13}_{-15}	-6.7	0.2	
936	10.03	2.39	10.16 ± 1.02	2.26 ± 1.01	34^{+13}_{-14}	-3.2	-2.9	
941	9.83	2.79	10.10 ± 1.13	2.52 ± 1.12	35^{+12}_{-16}	1.3	1.9	
951	10.30	2.45	10.55 ± 0.99	2.20 ± 0.98	30^{+15}_{-13}	2.7	1.8	
958	9.91	2.66	10.15 ± 1.09	2.42 ± 1.08	34^{+13}_{-15}	-2.7	-1.4	
973	11.47	2.98	11.61 ± 1.28	2.84 ± 1.26	17^{+21}_{-7}	-0.8	-0.6	
974	10.26	2.63	10.51 ± 1.07	2.38 ± 1.06	31^{+15}_{-14}	3.2	0.7	
982	10.14	... ^a	9.96 ± 2.74	2.87 ± 2.06	35^{+14}_{-20}	0.3	-0.5	
1048	10.41	2.45	10.56 ± 1.03	2.30 ± 1.02	30^{+15}_{-13}	-3.1	0.7	
1103	13.27	2.67	13.22 ± 1.23	2.72 ± 1.21	11^{+8}_{-4}	-0.9	-0.4	
1104	10.44	2.53	10.95 ± 0.91	2.02 ± 0.90	23^{+20}_{-8}	2.7	0.1	
1123	10.22	2.55	10.42 ± 1.06	2.35 ± 1.05	32^{+14}_{-14}	2.4	3.7	
1134	12.99	2.44	13.01 ± 1.11	2.42 ± 1.08	11^{+8}_{-3}	-5.3	-1.7	
1238	10.64	2.62	10.31 ± 1.32	2.95 ± 1.31	33^{+14}_{-16}	-5.7	-2.0	
1245	10.65	2.44	10.79 ± 1.03	2.30 ± 1.02	26^{+18}_{-11}	1.0	-0.5	
1327	10.01	3.12	10.30 ± 1.27	2.83 ± 1.26	33^{+14}_{-15}	-1.1	-0.7	
1350	10.62	2.55	10.88 ± 1.03	2.28 ± 1.01	24^{+20}_{-9}	2.6	3.6	
1474	10.32	2.79	10.48 ± 1.18	2.63 ± 1.17	31^{+15}_{-14}	1.1	1.0	
1534	10.64	2.73	10.81 ± 1.15	2.55 ± 1.14	26^{+19}_{-11}	-7.9	-0.0	
1554	10.49	2.81	10.65 ± 1.19	2.65 ± 1.18	29^{+16}_{-13}	-2.3	-0.3	
1619	11.48	2.64	11.58 ± 1.14	2.53 ± 1.13	17^{+20}_{-6}	-4.3	1.4	
1643	11.08	2.52	11.32 ± 1.04	2.28 ± 1.02	19^{+21}_{-7}	2.1	0.3	
1892	10.75	2.76	11.00 ± 1.13	2.51 ± 1.11	23^{+20}_{-9}	5.8	1.6	
1935	10.68	2.77	10.65 ± 1.25	2.80 ± 1.24	29^{+16}_{-14}	-2.2	1.4	
2048	13.00	2.64	-3.8	-2.6	
2233	11.11	2.54	11.24 ± 1.08	2.40 ± 1.07	20^{+21}_{-8}	-3.1	6.7	
2314	11.68	2.46	11.75 ± 1.07	2.38 ± 1.06	17^{+18}_{-7}	-0.3	2.8	
2420	11.16	2.56	11.19 ± 1.14	2.53 ± 1.12	20^{+21}_{-8}	5.5	0.5	
2446	11.35	2.67	11.66 ± 1.06	2.35 ± 1.04	17^{+19}_{-6}	3.2	2.5	
3308	12.09	2.32	12.57 ± 0.83	1.83 ± 0.82	12^{+9}_{-3}	4.4	-2.1	
3339	11.80	2.63	14.00 ± 0.29	0.42 ± 0.23	7^{+8}_{-1}	2.1	4.4	
3578	11.52	2.69	11.18 ± 1.35	3.03 ± 1.34	21^{+22}_{-9}	8.3	-1.2	
3773	12.22	2.70	0.0	0.9	
11652	...	2.77	-5.0	-0.1	

Notes. K_S magnitudes taken from Schödel et al. (2010), extinction corrected with the extinction map from Schödel et al. (2010); extinction A_{K_S} adopted from the map of Schödel et al. (2010); $K_{S,0}$ magnitude assuming an intrinsic colour of $(H - K_S)_0 = -0.1$ mag for O/B stars; corresponding extinction A_{K_S} ; stellar mass M_\star using isochrones with 3–8 Myr age and solar metallicity. The last two columns denote the equivalent widths (EW) of CO and Na.^(a) Beyond extinction map from Schödel et al. (2010).

Table 4.6: O/B stars III.

Id	p [$''$]	v_{RA} [$\text{km}\cdot\text{s}^{-1}$]	v_{Dec} [$\text{km}\cdot\text{s}^{-1}$]	v_z [$\text{km}\cdot\text{s}^{-1}$]	v_z on disk ^g	h	S/N
64	2.11	-65 ± 4^b	257 ± 4	256 ± 12^c	1	0.56	88
96	7.82	69 ± 9^b	250 ± 9	136 ± 17^c	0	-1.05	82
109	2.30	350 ± 1^b	6 ± 1	149 ± 27^c	1	0.63	92
166	10.62	85 ± 5^a	52 ± 4	154 ± 102^c	0	0.01	100
205	6.35	-82 ± 8^b	202 ± 6	32 ± 16^c	1	0.75	77
209	8.27	-54 ± 3^a	177 ± 6	87 ± 31^c	0	-0.51	38
227	6.57	229 ± 2^b	68 ± 3	154 ± 28^c	1	0.89	84
230	8.58	-35 ± 7^b	144 ± 6	-114 ± 20^c	1	0.15	81
273	10.26	-79 ± 7^b	59 ± 8	-165 ± 25^c	1	0.37	95
294	2.25	137 ± 1^b	-210 ± 1	105 ± 61^c	1	0.30	85
331	1.84	100 ± 1^b	-234 ± 1	221 ± 45^c	1	-0.01	56
366	9.34	80 ± 4^a	61 ± 4	257 ± 135^c	1	0.37	66
372	5.75	-163 ± 1^b	-72 ± 2	-148 ± 23^c	0	-0.54	71
436	19.09	77 ± 33^c	70
443	2.09	301 ± 1^b	116 ± 1	229 ± 36^c	1	0.61	47
445	7.70	-195 ± 7^b	-71 ± 6	-61 ± 21^c	1	0.81	54
483	12.83	-10 ± 4^a	3 ± 4	-180 ± 42^c	0	0.04^h	78
507	3.19	300 ± 1^b	-49 ± 2	-46 ± 57^c	...	0.74	66
508	5.86	1 ± 21^b	229 ± 6	24 ± 25^f	...	0.80	62
511	10.60	40 ± 5^a	-127 ± 6	231 ± 124^c	0	0.54	61
516	5.04	219 ± 8^b	-87 ± 8	-46 ± 64^c	...	-0.76	70
562	0.94	-520 ± 1^b	66 ± 1	110 ± 72^c	1	0.72	22
567	6.25	116 ± 6^b	-228 ± 6	-120 ± 77^c	0	-0.92	75
596	7.35	91 ± 5^a	212 ± 4	120 ± 52^c	1	0.82	71
610	8.81	14 ± 5^a	50 ± 7	-217 ± 211^c	0	0.18	54
617	10.39	-143 ± 3^a	-60 ± 7	202 ± 102^c	0	-0.17	64
663	28.81	-7 ± 24^c	73
668	1.18	367 ± 13^a	130 ± 12	-221 ± 179^c	0	0.50	40
707	3.30	-27 ± 1^b	164 ± 1	53 ± 20^d	1	0.15	28
716	7.37	94 ± 8^b	125 ± 9	160 ± 50^e	1	0.47	48

Table 4.6: continued.

Id	p [""]	v_{RA} [km·s ⁻¹]	v_{Dec} [km·s ⁻¹]	v_z [km·s ⁻¹]	v_z on disk ^g	h	S/N
718	8.87	-187 ± 5 ^a	76 ± 7	9 ± 88 ^c	...	-0.87	35
721	8.74	100 ± 6 ^a	-98 ± 3	-22 ± 44 ^c	...	-0.59	41
722	12.45	-21 ± 6 ^a	-103 ± 8	268 ± 30 ^c	0	0.16	57
725	3.23	220 ± 1 ^b	80 ± 2	117 ± 37 ^c	0	0.20	41
728	8.58	6 ± 10 ^b	-5 ± 8	277 ± 166 ^c	0	0.03 ^h	26
757	9.49	-124 ± 4 ^a	-73 ± 3	184 ± 89 ^c	0	0.10	48
762	3.53	-5 ± 1 ^b	209 ± 1	305 ± 70 ^e	1	0.54	25
785	4.15	5 ± 1 ^b	-162 ± 2	104 ± 170 ^c	...	-0.08	38
838	7.96	-138 ± 11 ^b	-98 ± 9	78 ± 64 ^c	0	0.61	68
847	3.92	-19 ± 1 ^b	-143 ± 2	52 ± 23 ^c	0	0.24	46
853	11.38	-14 ± 4 ^a	-8 ± 6	257 ± 124 ^c	1	-0.07 ^h	74
890	11.34	-64 ± 4 ^a	-108 ± 6	31 ± 45 ^c	...	-0.42	54
900	1.62	293 ± 1 ^b	-99 ± 1	-229 ± 35 ^c	1	0.34	30
936	9.78	31 ± 8 ^a	-139 ± 10	0.51	26
941	2.35	-314 ± 1 ^b	50 ± 1	157 ± 55 ^c	1	0.71	45
951	10.66	-13 ± 8 ^b	-161 ± 8	-150 ± 40 ^e	0	-0.67	59
958	9.01	-13 ± 9 ^b	-49 ± 8	46 ± 68 ^c	...	0.18	24
973	6.34	190 ± 5 ^a	221 ± 11	133 ± 70 ^c	0	-0.57	50
974	5.82	-51 ± 1 ^b	-134 ± 2	140 ± 50 ^e	1	-0.41	45
982	23.64	47
1048	9.57	50 ± 3 ^a	-35 ± 5	-0.18	50
1103	11.10	-68 ± 15 ^a	-2 ± 16	53 ± 92 ^c	...	-0.08	34
1104	20.45	57 ± 10 ^a	66 ± 7	123 ± 51 ^c	...	0.10	47
1123	1.30	188 ± 1 ^b	-280 ± 1	-364 ± 10 ^d	1	0.53	26
1134	7.78	24
1238	1.64	152 ± 1 ^b	-182 ± 1	-193 ± 41 ^d	1	0.32	24
1245	9.04	102 ± 7 ^a	135 ± 6	0.56	32
1327	5.62	168 ± 8 ^b	74 ± 8	155 ± 50 ^e	0	-0.12	44
1350	5.82	-37 ± 1 ^b	-143 ± 2	10 ± 50 ^e	...	0.03	34
1474	2.80	-335 ± 1 ^b	59 ± 1	145 ± 72 ^c	0	0.82	28
1534	2.25	355 ± 1 ^b	-126 ± 2	-83 ± 42 ^c	1	0.75	29
1554	7.58	-149 ± 11 ^b	18 ± 11	222 ± 31 ^c	0	-0.20	50
1619	1.20	102 ± 94 ^c	0	...	19
1643	9.20	-148 ± 7 ^b	-130 ± 6	-185 ± 50 ^e	1	0.72	32
1892	3.86	216 ± 2 ^b	176 ± 2	-153 ± 60 ^c	1	-0.74	16
1935	8.87	39 ± 4 ^a	147 ± 3	-0.64	26

Table 4.6: continued.

Id	p [$''$]	v_{RA} [$\text{km}\cdot\text{s}^{-1}$]	v_{Dec} [$\text{km}\cdot\text{s}^{-1}$]	v_z [$\text{km}\cdot\text{s}^{-1}$]	v_z on disk ^g	h	S/N
2048	14.50	130 ± 52^c	0	...	16
2233	0.82	82 ± 1^b	-35 ± 1	-28 ± 104^c	...	0.08	23
2314	0.11	-415 ± 30^a	748 ± 102	0.20	25
2420	4.76	113 ± 1^b	60 ± 2	-51 ± 65^f	...	0.36	19
2446	19.46	28 ± 6^a	33 ± 11	0.01	22
3308	16.67	8 ± 3^a	141 ± 5	-104 ± 73^c	...	-0.46	16
3339	19.70	76 ± 60^c	19
3578	9.88	-82 ± 6^a	-36 ± 4	-0.37	20
3773	8.60	143 ± 18^a	-1 ± 10	0.20	34
11652	7.31	131 ± 9^a	163 ± 17	-0.66	15

Notes. The table lists: Projected distance to Sgr A* p in arcseconds; proper motions v_{RA} and v_{Dec} are taken from previous studies; the radial velocity v_z is adopted from this and previous studies; h is the normalised projected angular momentum, signal-to-noise ratio S/N. ^(a) Proper motions from Schödel et al. (2009); ^(b) Proper motions from Yelda et al. (2014); ^(c) Radial velocity from this work; ^(d) Radial velocity is error-weighted mean from Bartko et al. (2009) and Yelda et al. (2014); ^(e) Radial velocity from Bartko et al. (2009); ^(f) Radial velocity from Yelda et al. (2014); ^(g) disc membership excluded if 0, possible if 1 (based on v_z); ^(h) High inclination (based on $v_{\text{pm}}/v_{\text{tot}}$).

5

KMOS view of the Galactic centre

II. Metallicity distribution of late-type stars

Knowing the metallicity distribution of stars in the Galactic centre has important implications for the formation history of the Milky Way nuclear star cluster. However, this distribution is not well known, and is currently based on a small sample of fewer than 100 stars. We obtained near-infrared K -band spectra of more than 700 late-type stars in the central 4 pc^2 of the Milky Way nuclear star cluster with the integral-field spectrograph KMOS (VLT). We analyse the medium-resolution spectra using a full-spectral fitting method employing the Göttingen Spectral library of synthetic PHOENIX spectra. The derived stellar metallicities range from metal-rich $[M/H] > +0.3$ dex to metal-poor $[M/H] < -1.0$ dex, with a fraction of $5.2^{+6.0}_{-3.1}$ per cent metal-poor ($[M/H] \leq -0.5$ dex) stars. The metal-poor stars are distributed over the entire observed field. The origin of metal-poor stars remains unclear. They could originate from infalling globular clusters. For the metal-rich stellar population ($[M/H] > 0$ dex) a globular cluster origin can be ruled out. As there is only a very low fraction of metal-poor stars in the central 4 pc^2 of the Galactic centre, we believe that our data can discard a scenario in which the Milky Way nuclear star cluster is purely formed from infalling globular clusters.

A. Feldmeier-Krause, W. Kerzendorf, N. Neumayer, R. Schödel, F. Nogueras-Lara, T. Do,
P. T. de Zeeuw, H. Kuntschner

submitted to MNRAS on May 20, 2016

5.1 Introduction

A dense concentration of stars is located within the central 10 pc of our Galaxy. These stars form the Milky Way’s nuclear star cluster. The centre of this star cluster hosts the Milky Way’s supermassive black hole, Sgr A*. It is unclear how the nuclear star cluster and the supermassive black hole formed and evolved. Many other galaxies host either a nuclear star cluster, a central supermassive black hole, or both (e.g. Böker et al. 2002; Côté et al. 2006; Seth et al. 2008a; Graham & Spitler 2009; Neumayer & Walcher 2012).

Two main formation scenarios for nuclear star clusters have been proposed. The stars may have formed “in-situ”, i.e., in the centre of the galaxy where they are located now (e.g. Loose et al. 1982; Schinnerer et al. 2008; Seth et al. 2008b; Pflamm-Altenburg & Kroupa 2009). The second possibility is that the stars formed in clusters further out. Star clusters might have migrated to the centre of the galaxy to form the nuclear star cluster (e.g. Tremaine et al. 1975; Capuzzo-Dolcetta & Mocchi 2008; Agarwal & Milosavljević 2011; Gnedin et al. 2014; Antonini 2013). In particular, massive globular clusters may have fallen into galactic nuclei through dynamical friction and thus have seeded nuclear star clusters (e.g. Antonini et al. 2012). Studying the stellar populations of the nuclear star cluster will shed light on the formation scenario, possibly distinguishing between the presented scenarios. In particular, the stellar metallicity distribution is useful to infer the formation history of the nuclear star cluster. A narrow distribution of age and metallicity would suggest that all stars formed from the same gas cloud in one single burst of star formation. On the other hand, a spread in age and metallicity would reveal several star formation events, or even continuous star formation. An inhomogeneous distribution of the metallicity over the nuclear star cluster might be produced by the migration of star clusters with different intrinsic metallicities from the outskirts to the centre of the galaxy (Perets & Mastrobuono-Battisti 2014). In particular, if globular clusters have contributed significant mass to a nuclear star cluster, then we would expect to find a considerable fraction of low-metallicity stars in it, as globular cluster stars have typically low metallicities, $[Fe/H]$. In the Milky Way globular clusters, $[Fe/H]$ ranges from -2.37 dex to 0.0 dex with a median at $[Fe/H] = -1.32$ dex (Harris 1996, 2010 edition). Only about 10 per cent of the Milky Way globular clusters have metallicities $[Fe/H]$ greater than -0.5 dex (Bica et al. 2006).

Due to its proximity, the Milky Way nuclear star cluster is the perfect laboratory to study the composition and structure of a nuclear star cluster. The cluster is at a distance of approximately 8 kpc (Ghez et al. 2008; Gillessen et al. 2009a; Chatzopoulos et al. 2015a). It has a mass of $\sim 2.5 \times 10^7 M_{\odot}$ (Schödel et al. 2014a; Feldmeier et al. 2014) and a half-light radius of 4.2 pc (Schödel et al. 2014a). Many of the stars observed in the Galactic centre are cool late-type stars. They are distributed throughout the cluster (Feldmeier-Krause et al. 2015). Most of the cool stars are red giants that formed several Gyr ago, though some late-type stars are younger supergiant stars (Blum et al. 2003; Pfuhl et al. 2011). Several red giants of intermediate age (50–500 Myr) have been found as well (Nishiyama et al. 2016). With the exception of short-lived O/B stars and bright A-stars, main sequence stars are too faint to be detected and studied with current instrumentation in the crowded Milky Way centre.

Despite being the arbiter for a number of important questions, there exist only few measurements of iron abundance and metallicity in the Galactic centre. Lately, the Gaia-ESO Survey and the Apache Point Observatory Galactic Evolution Experiment (APOGEE) measured metallicity and abundances for several thousand stars of the Milky Way (Mikolaitis et al. 2014; Holtzman et al. 2015). But in the centre of the Milky Way, measurements are hindered by high extinction ($A_V = 30$ mag, Scoville et al. 2003). Infrared spectroscopy is required, preferentially in the near-infrared K -band, where extinction decreases to about $A_K = 2.5$ mag (e.g. Cl  net et al. 2001; Sch  del et al. 2010). Ram  rez et al. (2000) and Ryde & Schultheis (2015) measured the iron abundance of fewer than 20 stars in the Galactic centre using high-resolution spectroscopy and found a mean iron abundance near solar, $\langle [Fe/H] \rangle = +0.1$ dex. Recently, Do et al. (2015) measured the overall metallicity $[M/H]$ on a larger sample of 83 stars and found a large spread, from $[M/H] \lesssim -1.0$ dex to $[M/H] \gtrsim +0.5$ dex. Their sample is concentrated in the central 1 pc, where adaptive optics is most useful. Further out, in the inner Galactic bulge, Schultheis et al. (2015) found also evidence for metal-poor K/M giants with $[M/H] = -1$ dex. The α -elements of these metal-poor stars seem to be enhanced (Schultheis et al. 2015). Concerning metal-rich stars ($[Fe/H] > 0$ dex) in the Galactic centre, Cunha et al. (2007) and Ryde & Schultheis (2015) found enhanced Ca abundances ($0 \text{ dex} \lesssim [Ca/Fe] \lesssim +0.5 \text{ dex}$), while Ryde & Schultheis (2015) and Ryde et al. (2016) found lower Mg and Si abundances ($-0.2 \lesssim [\alpha/Fe] \lesssim +0.2 \text{ dex}$).

A systematic metallicity study of a large sample of stars beyond the central $r = 0.5$ pc of the Milky Way nuclear star cluster has been missing so far. In this study, we present the spectra of more than 700 late-type stars located in an area $>4 \text{ pc}^2$ of the Galactic centre. The spectra were obtained with the integral-field spectrograph KMOS (Sharples et al. 2013) in the near-infrared K -band. We measure the stellar parameters effective temperature T_{eff} , and overall metallicity $[M/H]$ with full spectral fitting for more than 700 stars and study their spatial distribution. The outline of this chapter is as follows: We present the data set in Section 5.2. We outline the full spectral fitting routine and the error estimation in Section 5.3. In Section 5.4 we present our results, and discuss them in Section 5.5. The conclusion follows in Section 5.6.

5.2 Data set

5.2.1 Observations and data reduction

Our spectroscopic observations were performed with KMOS on 2013 September 23, during the KMOS science verification at VLT-UT1 (Antu). We observed an area of 2700 arcsec^2 , which corresponds to approximately 4 pc^2 at a distance of 8 kpc. The field extends over $64'9 \times 43'3$, centred on $\alpha = 266^\circ.4166$ and $\delta = -29^\circ.0082$, with a gap of $10'8 \times 10'8$ in the Galactic North-East direction, since one of the 24 KMOS integral-field units (IFUs) was inactive (IFU 13, see Fig. 1 of Feldmeier-Krause et al. 2015).

The spectra were taken in the K -band ($\sim 19\,340 - 24\,600 \text{ \AA}$). The KMOS scale is $\sim 2.8 \text{ \AA} \cdot \text{pixel}^{-1}$ in the spectral direction. The spatial scale is $0'2 \cdot \text{pixel}^{-1} \times 0'2 \cdot \text{pixel}^{-1}$. We observed

the field twice with 100 s exposure time each. For sky subtraction we made an offset to a dark cloud (G359.94+0.17, $\alpha \approx 266^\circ 2$, $\delta \approx -28^\circ 9$, Dutra & Bica 2001). Further, we observed B dwarfs for telluric corrections. Data reduction was performed with the ESO pipeline and standard recipes for dark correction, flat fielding, wavelength calibration, and illumination correction. For sky subtraction we used the method by Davies (2007), which is implemented in the pipeline. We removed cosmic rays with the method by van Dokkum (2001). For further details on the data reduction we refer to Feldmeier-Krause et al. (2015).

We extracted spectra of more than 1 000 individual stars with PAMPELMUSE (Kamann et al. 2013). The spectra have a formal signal-to-noise >10 . In PAMPELMUSE stars are deblended with a point spread function (PSF) fitting technique. Spectra from stars are also extracted when the stars' PSFs are centred outside of the field of view of the IFU. Therefore we have more than two exposures for some of the stars.

5.2.2 Spectral resolution

The spectral resolution of KMOS varies spatially for the 24 different IFUs (e.g. Gazak et al. 2015). We measured the line-spread-function of each IFU separately on the reconstructed sky data cubes in order to create a resolution map for each IFU. The line-spread function is reasonably well described with a Gaussian, and we fitted three different sky lines in the wavelength region of $\lambda = 21\,900 - 22\,400 \text{ \AA}$ for all 23 used IFUs separately. We calculated average resolution maps from four sky exposures for each IFU, and smoothed the maps using a Gaussian with width $\sigma = 1 \text{ pix}$, roughly corresponding to the seeing during the observations. We find that the spectral resolution $R = \lambda/\Delta\lambda$ varies between 3 310 to 4 660 for the 23 different active IFUs on the three different KMOS detectors. On a single IFU, the spectral resolution has a standard deviation of about 30 to 150. The standard deviation of the spectral resolution R over all IFUs is 300, this is 7 per cent of the mean value. We use the respective R values for fitting the stellar spectra.

5.2.3 Data selection

For this paper we only regard late-type stars, i.e., cool stars with molecular CO absorption lines at $\lambda \geq 22\,935 \text{ \AA}$. Spectra of early-type stars are presented in Feldmeier-Krause et al. (2015). We visually inspected the spectra and identified 982 stars as late-type stars based on the prominent CO lines.

In addition to the spectroscopy, we have photometry obtained with HAWKI-I and NACO from Schödel et al. (2010) and Nogueras-Lara et al. (in prep.) in the J (HAWKI-I), H (HAWKI-I and NACO), and K_S (HAWKI-I and NACO) bands. Since the brightest stars can be saturated in the HAWKI-I and NACO images, we complemented the photometry with the SIRIUS catalogue (Nishiyama et al. 2006) for six late-type stars. For two further bright late-type stars with neither HAWKI-I, NACO nor SIRIUS photometry due to saturation, we used 2MASS (Skrutskie et al. 2006) photometry.

We corrected the photometry for dust extinction using the extinction map and extinction law of Schödel et al. (2010), which was derived with NACO data. This extinction map covers about 70 per cent of our stars. For stars outside the field of view of the Schödel et al. (2010) extinction map, we used the extinction map of Noguerras-Lara et al. (in prep.) derived from HAWK-I data. It has lower spatial resolution, but covers the entire field of view of the KMOS data.

The $H - K_S$ colour can be used to identify foreground stars. The intrinsic $H - K_S$ colour ranges from about -0.13 mag to $+0.38$ mag (Do et al. 2013a; Schödel et al. 2014b). We assumed that stars with significantly bluer extinction-corrected $(H - K_S)_0$ colour are over-corrected foreground stars. We classified a star as foreground star when $(H - K_S)_0 < -0.5$ mag. Including zero point uncertainties, the uncertainty of the H - and K_S -band magnitudes in our photometry is less than ten per cent, so $(H - K_S)_0 < -0.5$ mag corresponds to a three-sigma exclusion criterion. We excluded 62 stars with this criterion. For eleven stars we do not have photometry in both bands. We excluded these eleven stars in our later analysis, since they might be foreground stars. In our selected data set, the extinction corrected K_S -band magnitudes range from 4.91 to 13.56 mag, with a median of 10.49 mag. For a colour-magnitude-diagram of the data set we refer to Feldmeier-Krause et al. (2015).

5.2.4 Spectral indices

Spectral indices in the K -band are correlated with the spectral type of a star, and can be used for a rough spectral classification and effective temperature estimate (e.g. Ivanov et al. 2004; Silva et al. 2008). The most prominent spectral feature of cool stars are the CO absorption lines ($\lambda \geq 22\,935$ Å) and the Na I doublet at 22 062 and 22 090 Å. In this section, we calibrate the CO equivalent width (EW_{CO}) and the Na equivalent width (EW_{Na}) on a spectral library and present the measurements on our data set. The EW_{CO} and EW_{Na} measurements confirm our classification as late-type stars quantitatively. Further, we obtain some constraints on the effective temperature T_{eff} and surface gravity $\log(g)$ that are useful as priors for the full spectral fitting.

5.2.4.1 Calibrating spectral indices with a spectral library

We measured the spectral indices EW_{CO} and EW_{Na} using different spectral libraries with known spectral types for calibration. The spectral libraries are listed in Table 5.1. We used the spectral index definitions of Frogel et al. (2001). All spectra were degraded to the same spectral resolution of the KMOS data before we computed the indices. The spectral resolution of the KMOS detector varies for the different IFUs (see Section 5.2.2). We tested the effect of the spectral resolution by degrading the spectral library to $R = 3\,000$, and found no systematic difference in the result compared to the spectral indices obtained with $R = 4\,350$. The difference is less than 1 per cent for all indices. This test shows that equivalent width measurements are robust under moderate spectral resolution variations. Since the results with $R = 3\,000$ are consistent with the results at KMOS resolution, we included spectra from Wal-

Table 5.1: Spectral libraries in the K -band

Library	Resolution ($R = \lambda/\Delta\lambda$)	Spectral type	Luminosity class	Spectral region [\AA]
Wallace & Hinkle (1996)	$\geq 45,000$	F8–M8	I–V	20 195–23 960
Wallace & Hinkle (1997)	3 000	O4–M7	I–V	20 202–24 096
Winge et al. (2009), NIFS v1.5	6 000	G8–M3	I–III	20 700–24 700
Winge et al. (2009), NIFS v2.0	6 000	G8–M3	I–III	20 200–24 300
Winge et al. (2009), GNIRS	18,000	F7–M0	II–V	21 800–24 250

lace & Hinkle (1997, $R = 3\,000$)¹ to obtain a larger sample. We also tested the influence of the continuum shape on index measurements by reddening the library spectra with the mean extinction in our field-of-view, $A_{K_S} = 2.7$ mag. For the CO and Na equivalent width measurements the effect is less than 1 per cent, though it is about 7.3 per cent when we instead compute the D_{CO} index as defined by Mármol-Queraltó et al. (2008).

Giant stars with luminosity class II–IV have a mean value for EW_{CO} of approximately 13 \AA , and the maximum value is about 25 \AA . We expect that the majority of the stars in our data set are giants. However, we also computed EW_{CO} for the supergiant and dwarf stars in our spectral library. Supergiants have larger values of EW_{CO} , with a mean at 20 \AA , and values up to 33 \AA . Since no giant star has a larger value of EW_{CO} than 25 \AA , we can assume that stars in our data set with $EW_{CO} > 25$ \AA are either M-type supergiants, or have a higher metallicity, as CO absorption strength also increases with metallicity (e.g. Houdashelt et al. 1992 for $[Fe/H] < 0$ dex). The mean value of EW_{Na} is about 2 \AA for giant stars and about 3 \AA for supergiants. We further found that all stars with a detectable CO line, from dwarfs over giants to supergiants, have effective temperatures $T_{\text{eff}} \lesssim 6\,000$ K. Since all the stars in our data set have CO lines, their temperatures are probably $\lesssim 6\,000$ K. We derived a new $T_{\text{eff}} - EW_{CO}$ relation for giant stars. The results are presented in Appendix 5.7.

5.2.4.2 Late-type star classification

To verify our classification as late-type stars, we measured spectral indices on our data set. We computed the equivalent widths of the first CO band head and the Na I doublet as defined by Frogel et al. (2001). Before computing the spectral indices, we measured the radial velocities of the stellar spectra and shifted the spectra to rest wavelength. To obtain the velocities we used the IDL routine `pPXF` (Cappellari & Emsellem 2004) as in Feldmeier et al. (2014), with the high resolution spectra of Wallace & Hinkle (1996) as templates. The wavelength range of the fit is from 21 500 to 23 900 \AA .

The late-type stars have mean values of $EW_{CO,LT} = 18.30$ \AA and $EW_{Na,LT} = 4.60$ \AA . The stars we classified as early-type O/B stars have smaller equivalent widths, with a mean value

¹We excluded stars that are also in the sample of Wallace & Hinkle (1996), and the star HR8530/HD212320, which was classified as M6III star by Wallace & Hinkle (1997), but was listed as G6III star by McWilliam (1990).

of $EW_{\text{CO,O/B}} = -0.76 \text{ \AA}$ and $EW_{\text{Na,O/B}} = 0.47 \text{ \AA}$ (see also Feldmeier-Krause et al. 2015). There is a clear distinction between the distribution of the EW_{CO} of the early- and late-type stars, which confirms our visual classification. Our data set contains 66 stars with $EW_{\text{CO}} > 25 \text{ \AA}$, which might suggest that these stars are supergiants. Among those stars, 47 are rather bright ($K_{S,0} \leq 10 \text{ mag}$) giving further support to those objects being supergiants at the Galactic centre. The CO strength in Galactic centre supergiants is normal in comparison to disc stars (Blum et al. 1996).

The Na I doublet lines are rather strong for most stars in the data set, with a mean value of $EW_{\text{Na}} = 4.60 \text{ \AA}$, while the giant stars in the spectral library have $EW_{\text{Na}} \leq 4.5 \text{ \AA}$. Blum et al. (1996) showed that stars in the Galactic centre have higher Na I and Ca I line strengths compared to disc stars with similar CO strengths. Also the high-resolution spectra studied by Cunha et al. (2007) and Ryde & Schultheis (2015) have high $[Ca/Fe]$ abundances. We show three example spectra in Fig. 5.1. The Na I and Ca I line regions are marked as grey shaded areas. Na is produced in massive stars in SN II (Kobayashi et al. 2006) and in intermediate-mass AGB stars (Karakas 2010). In contrast to Na, Ca is an α -element. The Na I lines are blended with other elements, e.g. Sc, Si, Fe, V, and CN lines (Wallace & Hinkle 1996). One or several of these elements might be enhanced and produce the large Na I equivalent width.

5.3 Full spectral fitting

We fitted the spectra of our KMOS data set using the `STARKit` code (Kerzendorf & Do 2015) also used by Do et al. (2015). This code interpolates on a grid of synthetic spectra and utilises the Bayesian sampler `MULTINEST` (Feroz et al. 2009; Buchner et al. 2014). In the following we give a short outline of our assumptions and used parameters. For details on the Bayesian sampling procedure we refer to Do et al. (2015).

5.3.1 Fitting method and assumptions

We fitted the effective temperature T_{eff} , metallicity $[M/H]$, surface gravity $\log(g)$, and radial velocity v_z . $[\alpha/Fe]$ was fixed to zero and stellar rotation was ignored. Most of the stars in our data set are red giants, which have too low rotational velocities to be resolved with our data ($< 10 \text{ km}\cdot\text{s}^{-1}$, Oke & Greenstein 1954; Gray 1989). Our spectral grid consists of the model spectra from the PHOENIX spectral library (Husser et al. 2013), with stellar parameters in the range $T_{\text{eff}} = [2300 \text{ K}, 12,000 \text{ K}]$ with a step size of $\Delta T_{\text{eff}} = 100 \text{ K}$, $[M/H] = [-1.5 \text{ dex}, +1.0 \text{ dex}]$, $\Delta[M/H] = 0.5 \text{ dex}$, $\log(g) = [0.0 \text{ dex}, 6.0 \text{ dex}]$, $\Delta \log(g) = 0.5 \text{ dex}$. The synthetic spectra have a resolution of $R = 500,000$. We convolved the spectra to the same spectral resolution as the KMOS spectra. We took the different spectral resolutions obtained on the 23 different IFUs into account (see Section 5.2.2). The prior of the metallicity $[M/H]$ was set uniform in the range $[-1.5 \text{ dex}, +1.0 \text{ dex}]$. The surface gravity can be constrained by the K_S -band magnitude, as shown by Do et al. (2015). Stars brighter than $K_S = 12 \text{ mag}$ have a lower surface gravity. Therefore we set the uniform priors for $\log(g)$ in the range $2.0 \text{ dex} < \log(g) < 4.5 \text{ dex}$ for stars with $K_{S,0} \geq 12 \text{ mag}$, and to $0.0 \text{ dex} < \log(g) < 4.0 \text{ dex}$

for stars with $K_{S,0} < 12$ mag. In addition, we chose $0.0 \text{ dex} < \log(g) < 2.0 \text{ dex}$ for all stars with $K_{S,0} \leq 10$ mag and $EW_{\text{CO}} > 25 \text{ \AA}$, and $0.0 \text{ dex} < \log(g) < 4.0 \text{ dex}$ for all stars with $K_{S,0} > 10$ mag and $EW_{\text{CO}} > 25 \text{ \AA}$, as these stars are potentially supergiants (see Section 5.2.4).

The continua of the spectra were not normalised or straightened. Still, we did not use the continuum shape to constrain the effective temperature, as interstellar dust and extinction also affect the continuum shape and might bias our results for the stellar parameters. We fitted the spectral continuum with a fifth degree polynomial function, to minimise the difference between the observed and model spectrum. The model spectra were multiplied with the polynomial to match the continuum shape of the data.

We fitted the spectra in the wavelength range $\lambda = [20\,900 \text{ \AA}, 22\,900 \text{ \AA}]$, i.e., we excluded the molecular CO absorption lines from the stellar parameter fit. Do et al. (2015) showed that fitting the spectrum in the CO line region can introduce significant biases in $\log(g)$ and $[M/H]$. The reason is probably that molecular lines are not as reliable as atomic lines in synthetic spectra. Since the Na and Ca lines of Galactic centre stars are strong compared to normal disc stars (see Section 5.2.4.2 and Blum et al. 1996), we excluded these lines from the stellar parameter fit. In particular, we excluded the wavelength regions $\lambda = [22\,027 \text{ \AA}, 22\,125 \text{ \AA}]$ and $\lambda = [22\,575 \text{ \AA}, 22\,685 \text{ \AA}]$. However, we included the Na I and Ca I lines in the fit of the radial velocity v_z . We limited the radial velocity v_z to $[-500 \text{ km}\cdot\text{s}^{-1}; +500 \text{ km}\cdot\text{s}^{-1}]$. For spectra with strong Brackett- γ gas contamination emitted by the minispiral (for a Brackett- γ flux map extracted from our data see Feldmeier-Krause et al. 2015), we also excluded the region $\lambda = [21\,621 \text{ \AA}, 21\,696 \text{ \AA}]$ from the fit. Figure 5.1 shows three spectra in the fitted wavelength region. The excluded Na I and Ca I line regions are shaded in gray. The Brackett- γ line region, which was excluded for spectra with strong gas contamination, is shaded in light blue. Even though we excluded these regions, there are several other absorption lines in the spectra, some of them are marked with blue vertical dashed lines and labelled on top of the plot. The list of absorption lines we labelled is not complete, there are more lines visible in the spectra.

5.3.2 Error estimation

5.3.2.1 Statistical uncertainties

We fitted the spectra of 907 stars. We selected spectra with high fitted signal-to-noise ($S/N = \text{median}(\text{spectrum})/\sigma(\text{residual spectrum}) > 15$, where the residual spectrum equals observed spectrum minus best fit spectrum), and with low one-sigma uncertainties ($\sigma_{T_{\text{eff}}} < 250 \text{ K}$, $\sigma_{[M/H]} < 0.25 \text{ dex}$, $\sigma_{\log(g)} < 1 \text{ dex}$). For stars with several exposures, we took the mean of the stellar parameters obtained by the individual fits as our measurement. In many cases, the standard deviation of the results from fitting the single exposures of the same star is larger than the one-sigma fit uncertainties. For these stars we used the standard deviations as statistical uncertainties. We estimated the uncertainties of 230 stars with only one exposure from the median uncertainties of the other fits. The mean statistical uncertainties, either directly from the fits or the standard deviations, are $\sigma_{T_{\text{eff}}} = 83 \text{ K}$, $\sigma_{[M/H]} = 0.11 \text{ dex}$, $\sigma_{\log(g)} = 0.16 \text{ dex}$, and $\sigma_{v_z} = 2.9 \text{ km s}^{-1}$.

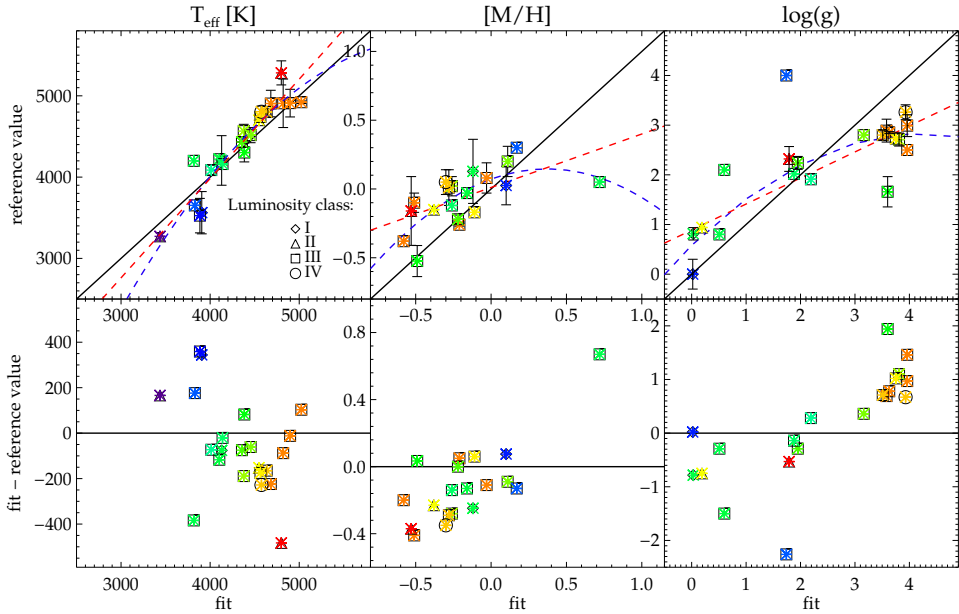


Figure 5.2: Comparison of the best-fitting stellar parameters with the reference values of stars from the spectral library. Left panel: T_{eff} in K for 22 stars; middle panel: $[M/H]$ in dex for 19 stars; right panel: $\log(g)$ in dex for 20 stars. Upper panel: fit result plotted against the reference value, lower panel: fit result plotted against residual (fit result – reference value). The different symbols denote different luminosity classes, colours mark the same star. The black line is the one-to-one line, the red dashed line is a linear fit to the data, the blue dashed line a quadratic fit.

One of the reasons for different results of single exposures of the same star are so-called fringes or ripples (Neeser et al. 2016). Fringes are visible as wavy pattern in the continuum of the spectrum. Fringes can arise when the star is located at the edge of the IFU, or is spatially undersampled. Fortunately, stars that are close to the edge of the IFU have often more than two exposures. The standard deviation of the individual measurements gives a good estimation for the uncertainty of the parameter fit. In some cases the standard deviation is very high. We conclude that the fit did not work properly for at least one of the exposures in such a case. We excluded stars with high statistical uncertainties.

5.3.2.2 Systematic uncertainty of synthetic model spectra

We determined systematic uncertainties by applying the full spectral fitting routine on stars from a spectral library. We selected stars from Wallace & Hinkle (1996) and Winge et al. (2009), for which previous measurements of the stellar parameters are listed in Soubiran et al. (2010). All the spectra were convolved to the KMOS spectral resolution. The GNIRS stars from Winge et al. (2009) cover a smaller wavelength range than our fitting interval, so we fitted those stars from $\lambda = [21\,800 \text{ \AA}; 22\,900 \text{ \AA}]$. We put constraints on $\log(g)$ based

on the luminosity class (see also Do et al. 2015): Giant stars with luminosity class III were constrained to the interval $\log(g) = [0.5 \text{ dex}, 4 \text{ dex}]$, supergiants and bright giants (luminosity class I and II) had $\log(g) = [0 \text{ dex}, 2 \text{ dex}]$. Subgiants (luminosity class IV) were constrained to $\log(g) = [2 \text{ dex}, 5.5 \text{ dex}]$. We did not include main sequence stars (luminosity class V), since we do not expect any dwarf stars in our data set except foreground stars. Even the faintest star in our data set with $K_S = 16.9 \text{ mag}$ is too bright to be a cool main sequence star in the Galactic centre, whereas hot main sequence stars (O/B/A-type) are not late-type stars and therefore excluded from the data set. In total we fit 22 reference spectra with known T_{eff} , for 19 reference spectra we also know $[M/H]$, and for 20 stars $\log(g)$. We fitted each spectrum twice, we computed the standard deviation of the residual spectrum after the first fit and used it as uniform noise spectrum in the second fit. We show a comparison of the fitted results to the reference results in Fig. 5.2. The values of T_{eff} are in good agreement, the mean and standard deviation of the fit residuals are $\langle \Delta T_{\text{eff}} \rangle = -58 \text{ K}$, $\sigma_{\Delta T_{\text{eff}}} = 205 \text{ K}$, $\langle \Delta [M/H] \rangle = -0.1 \text{ dex}$, $\sigma_{\Delta [M/H]} = 0.24 \text{ dex}$, $\langle \Delta \log(g) \rangle = 0.2 \text{ dex}$, $\sigma_{\Delta \log(g)} = 1.0 \text{ dex}$. To some extent, the scatter and offsets are caused by the different methods and assumptions used by the different studies that measured the reference stellar parameters. But as argued by Do et al. (2015), offsets are also due to systematics in the model spectra. We added the standard deviations in quadrature to our statistical uncertainties to account for the systematics of the model spectra.

The systematic uncertainty values we obtained are lower than the systematic uncertainties found by Do et al. (2015). The reason for this is twofold. Do et al. (2015) used the MARCS grid (Gustafsson et al. 2008) and not the PHOENIX grid (Husser et al. 2013), and they used the IRTF SPEX library (Rayner et al. 2009) as reference stars. The IRTF stellar library has a spectral resolution of $R \approx 2000$. The MARCS grid was computed with different stellar abundances and atomic line lists than the PHOENIX synthetic spectra. We tested the MARCS grid for our reference stars and found $\langle \Delta T_{\text{eff}} \rangle = -38 \text{ K}$, $\sigma_{\Delta T_{\text{eff}}} = 268 \text{ K}$, $\langle \Delta [M/H] \rangle = -0.33 \text{ dex}$, $\sigma_{\Delta [M/H]} = 0.25 \text{ dex}$, $\langle \Delta \log(g) \rangle = 1.2 \text{ dex}$, $\sigma_{\Delta \log(g)} = 0.7 \text{ dex}$. There appears to be a systematic offset to higher values of $\log(g)$ and lower values of $[M/H]$ compared to the reference values. Hence, we decided to use the PHOENIX synthetic spectra. However, there are also some systematic offsets when we use the PHOENIX grid. The effective temperature tends to be overestimated at $T_{\text{eff}} \lesssim 4000 \text{ K}$ (by up to 360 K, see lower left panel of Fig. 5.2), but rather underestimated at $T_{\text{eff}} \gtrsim 4500 \text{ K}$ (by up to 480 K). On the other hand, the results for $\log(g)$ are rather too high at $\log(g) \gtrsim 2.5 \text{ dex}$, but too low at $\log(g) \lesssim 1 \text{ dex}$. The metallicities of most spectra are in good agreement with the reference metallicities. We show two reference star fits in Fig. 5.3. We plotted the GNIRS spectrum of HD206067 (bottom, black). For this star our results (red) are in good agreement with the reference stellar parameters (blue). There is one outlier for the metallicity results. The fit of the NIFS spectrum of the K4 III star HD121447 indicated a very high metallicity ($[M/H] \gtrsim +0.72 \pm 0.05 \text{ dex}$), though the reference iron abundance is roughly solar ($[Fe/H] = +0.05 \text{ dex}$, Smith 1984). The observed spectrum from Winge et al. (2009), the best-fitting model spectrum, and a model spectrum with the reference stellar parameters are shown in Fig. 5.3 (top). By eye one can hardly decide which model spectrum fits the data better, however, some lines (marked with black dot-dashed vertical lines) are recovered better by our best fit than by the model with

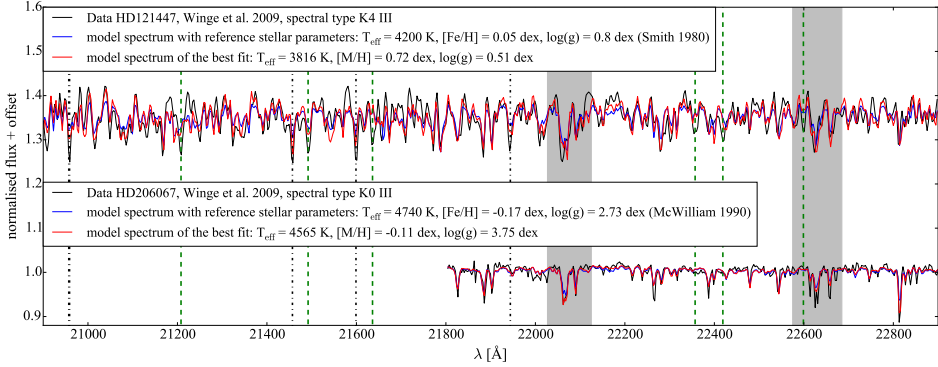


Figure 5.3: Top: NIFS spectrum of HD121447 (Winge et al. 2009, black), a PHOENIX (Husser et al. 2013) model spectrum with the reference values found by Smith (1984, blue), and a model spectrum with the best-fitting results we obtained (red). Vertical dashed green lines denote spectral lines that are not or barely seen in the model spectra, black dot-dashed lines denote spectral lines that are better recovered by a spectrum with higher metallicity. Bottom: GNIRS spectrum of HD206067 (Winge et al. 2009, black), our results (red) are in good agreement with the reference values found by McWilliam (1990, blue). Grey contours mark regions that were excluded from the fit.

the reference values. There are some lines in the observed spectrum, which are not in the model spectra. Some of these lines are marked as green dashed vertical lines in Fig. 5.3. We conclude that fits, which obtain high metallicities $[M/H] \gtrsim +0.5$ dex, must be considered suspect. We note that we did not test our method on stars with high metallicities beyond $[M/H] = +0.3$ dex. As can be seen from Fig. 5.2, the fitted results in T_{eff} appear to be very robust. A large discrepancy in the fitted metallicity or surface gravity still produces good results in T_{eff} .

5.3.2.3 Total uncertainties

We took different uncertainties into account and added them in quadrature. These uncertainties are (1) the statistical uncertainties, either the one-sigma fitting uncertainties or the standard deviation of several exposures of the same star and (2) systematic uncertainties of the synthetic model spectra. The systematic uncertainties are dominating the total uncertainty for most of the stars. The mean total uncertainties of our sample of stars are $\sigma_{T_{\text{eff}}} = 230$ K, $\sigma_{[M/H]} = 0.27$ dex, $\sigma_{\log(g)} = 1.04$ dex, $\sigma_{v_z} = 2.9$ km·s⁻¹. The mean statistical and total uncertainties are plotted as error bars in Fig. 5.4.

5.4 Results

Our data set contains 982 stars in the central $64''.9 \times 43''.3$ of the Milky Way, for which we fitted stellar parameters. We excluded several stars due to low signal-to-noise ratio or large

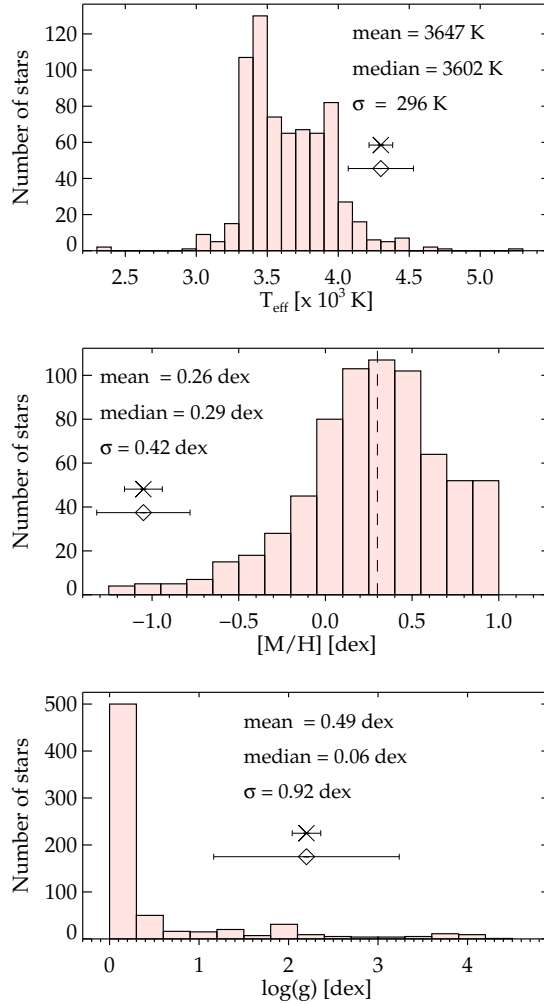


Figure 5.4: Histograms of the stellar parameters for 687 stars with $(H - K_S)_0 = [-0.5 \text{ mag}; 0.8 \text{ mag}]$, from top to bottom: effective temperature T_{eff} , metallicity $[M/H]$, surface gravity $\log(g)$. The error bar denotes the mean statistical uncertainty (cross symbol) and mean total uncertainty (diamond symbol) of the measurements.

uncertainties (Section 5.3.2.1). Stars with a rather blue colour, or no colour information, may be foreground stars, and not belong to the Milky Way nuclear star cluster. We excluded those 73 stars, which leaves 705 stars. A further 18 stars have rather red colours, they are probably locally embedded in dust, but might also be background stars. Figure 5.4 illustrates the distribution of the stellar parameter results for 687 stars, which are probably cluster members, with extinction corrected colour $(H - K_S)_0 = [-0.5 \text{ mag}, 0.8 \text{ mag}]$. The mean statistical and total uncertainties for the stellar parameter measurements are shown as error bars.

5.4.1 Effective temperatures

As expected, the late-type stars are mostly cool, with a mean temperature $\langle T_{\text{eff}} \rangle \approx 3650 \text{ K}$ (upper panel of Fig. 5.4). This means the stars are mostly late K-type stars or M-type stars (Cox 2000). As shown in Section 5.3.2.2, we rather overestimate low temperatures and underestimate high temperatures. This indicates that the distribution of T_{eff} might be too narrow. To estimate this effect we made a linear fit to the T_{eff} measurements of reference stars (red dashed line in upper left panel of Fig. 5.2). We shifted our T_{eff} measurements using this relation, which broadens the T_{eff} distribution by 77 K. Only one star (Id 2164) has a temperature higher than 5000 K, in agreement with a G-type star. Also the CO equivalent width is rather low (4.32 Å), which confirms the higher effective temperature.

5.4.2 Metallicities

The mean metallicity is $\langle [M/H] \rangle = +0.26 \text{ dex}$, this means that most stars are metal-rich. The standard deviation of $[M/H]$ is 0.42 dex. The metallicity distribution is shown on the middle panel of Fig. 5.4 for 687 likely cluster member stars. We found several metal-poor stars. Our data contain 156 stars with $[M/H] < 0 \text{ dex}$, from which 37 stars have $[M/H] \leq -0.5 \text{ dex}$ and 8 stars even $[M/H] \leq -1.0 \text{ dex}$. One of the metal-poor stars with $[M/H] \leq -0.5 \text{ dex}$ has a rather red colour ($(H - K_S)_0 = 0.84 \text{ mag}$), it might either be locally embedded or a background star. Our data set contains $(5.2^{+6.0}_{-3.1})$ per cent low-metallicity stars (i.e. $[M/H] \leq -0.5 \text{ dex}$), and $(22.8^{+24.5}_{-12.6})$ per cent sub-solar metallicity stars ($[M/H] \leq 0.0 \text{ dex}$).

Several stars are close to the boundary metallicity of the grid at $[M/H] = +1 \text{ dex}$. This would mean that these stars are super-metal-rich. However, there is probably a problem with the fit or the spectral grid. We only tested the metallicity measurement on reference stars with $[M/H] \lesssim +0.3 \text{ dex}$. We indicated this metallicity as a vertical dashed line in the middle panel of Fig. 5.4. We cannot say whether our method works for stars with a higher metallicity. Further, we showed in Section 5.3.2.2 that the metallicity of a star with $[M/H] > 0 \text{ dex}$ was overestimated by nearly 0.7 dex. We conclude that stars with a metallicity $[M/H] \gtrsim +0.3 \text{ dex}$ are probably metal-rich ($[M/H] \gtrsim 0 \text{ dex}$), however, with our method and models at moderate spectral resolution we cannot determine the metallicity to a higher accuracy. Figure 5.1 shows three spectra with different metallicities $[M/H] = -0.89, +0.25,$ and $+0.69 \text{ dex}$. Their effective temperatures and surface gravities are very similar. These spectra have fitted signal-to-noise values of $S/N > 30$. For all three spectra the Na doublet

and Ca triplet lines (marked as grey shaded area) are deeper than in the best-fitting spectra. For the metal-poor star, many of the other lines are fit reasonably well, e.g. the Fe lines at 21 290, 21 782, 21 901, 22 266, or 22 399 Å, which are blended with Ti, Si, or Sc. The lines at 21 290, 21 782, and 21 901 Å are also fit well for the spectrum with $[M/H] = +0.25$ dex. However, in particular the spectrum with the highest metallicity $[M/H] = +0.69$ dex has many lines that are deeper than the model spectrum. This confirms that the stars with a best-fitting metallicity $[M/H] > +0.3$ dex are definitely very interesting targets to be followed-up with high resolution spectroscopy. At this point, it would be premature to claim that these stars are indeed super-metal-rich.

5.4.3 Surface gravities

The surface gravity is mostly low, in agreement with cool giant ($\log(g) < 3.0$ dex) and supergiant ($\log(g) < 1.5$ dex) stars (lower panel of Fig. 5.4). For most stars we obtained a value of $\log(g)$ close to zero, at the edge of the PHOENIX spectral grid. This suggests that the value of $\log(g)$ might be even negative, as for M-type supergiants. However, we showed in Section 5.3.2.2 that $\log(g)$ is rather underestimated at low values of $\log(g)$, and the systematic uncertainty is 1 dex. Therefore we consider the results of $\log(g)$ as highly uncertain.

We fitted the surface gravity together with the other stellar parameters but treated it mostly as a nuisance parameter, rather than an actual measurement. We did this to avoid any biases that may be introduced by fixing $\log(g)$ to a wrong value. As we showed in Section 5.3.2.2, fitting a discrepant value in $\log(g)$ does not directly translate into a wrong value for the effective temperature or metallicity. Some of the most discrepant results for $\log(g)$ give very good results for T_{eff} and $[M/H]$.

5.4.4 Radial velocities

We fitted the radial velocities together with the stellar parameters. They range from -268.8 to $+313.6$ $\text{km}\cdot\text{s}^{-1}$. The mean velocity of 705 stars with $(H - K_S)_0 > -0.5$ mag is $\langle v_z \rangle = +7.6 \pm 3.6$ $\text{km}\cdot\text{s}^{-1}$. The disagreement from zero is probably due to the asymmetric spatial distribution of stars in our data set, with 410 stars in the Galactic East, and 295 stars in the Galactic West. The velocity dispersion $\langle \sigma_z \rangle = 96.2 \pm 2.6$ $\text{km}\cdot\text{s}^{-1}$. We computed the mean velocity and velocity dispersion with the maximum likelihood approach (Pryor & Meylan 1993), which takes the individual velocity uncertainties into account.

We also considered the Galactic East and Galactic West separately. We obtained for the 410 stars in the Galactic East $\langle v_z \rangle = +24.6 \pm 4.8$ $\text{km}\cdot\text{s}^{-1}$, $\langle \sigma_z \rangle = 96.4 \pm 3.4$ $\text{km}\cdot\text{s}^{-1}$, and $\langle v_z \rangle = -16.2 \pm 5.3$ $\text{km}\cdot\text{s}^{-1}$, $\langle \sigma_z \rangle = 90.7 \pm 3.8$ $\text{km}\cdot\text{s}^{-1}$ for the 295 stars in the Galactic West. The mean radial velocity confirms the rotation of the Milky Way nuclear star cluster by approximately 20 $\text{km}\cdot\text{s}^{-1}$ within the central 1.2 pc ($30''$), as found by McGinn et al. (1989) and also Feldmeier et al. (2014) from a different data set.

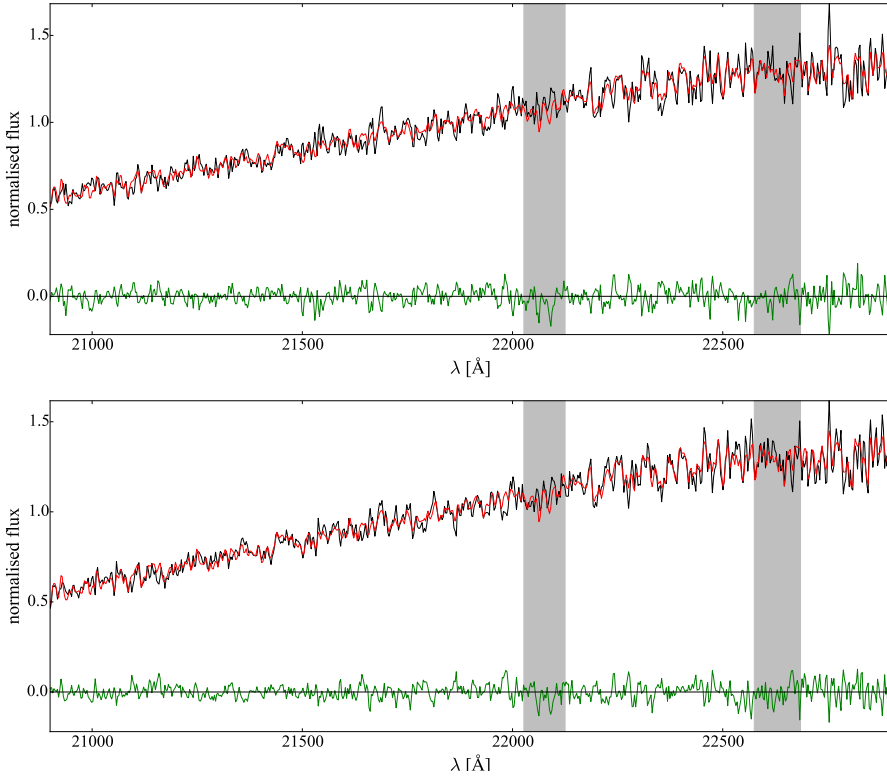


Figure 5.5: Spectra of the long-period variable star Id 649 in black. We fit the two exposures separately, the best fit (red) is obtained at $T_{\text{eff}} = 2\,300$ K, $[M/H] = +0.99$ dex, $\log(g) = 5$ dex. Green circles denote the fit residuals. The flux of the spectrum increases towards longer wavelengths. The fits have $\chi^2_{\text{red}} = 11.6$ and 14.2, and $S/N = 20.6$ and 22.5.

5.4.5 Long-period variable stars

Our data contain six stars with $T_{\text{eff}} < 3\,000$ K, five of them have an effective temperature close to the edge of the PHOENIX grid, at $T_{\text{eff}} = 2\,300$ K. We checked those stars in the SIMBAD database (Wenger et al. 2000) and found that four of the stars were classified as long-period variables or Mira stars (Id 158, 221, 25349, 25389) by Reid et al. (2003) and Matsunaga et al. (2009). Such stars are mostly M-type giants or supergiants, with periods of few to several hundred days. However, long-period variables can also be carbon rich (C-type stars), or zirconium rich (S-type stars), and Mira stars can be oxygen-rich or carbon-rich (Cox 2000).

The six stars are rather bright, with observed magnitudes ranging from $K_S = 9$ to 12.3 mag. This also indicates that the stars are supergiant and bright giant stars, however, we obtained $\log(g)$ values ranging from 1.5 to 5.6 dex. We conclude that the PHOENIX spectral grid is not suitable to obtain the surface gravity of C-type, S-type or oxygen rich long-period variable stars. Many Mira stars suffer from rapid mass loss. These stars are often embedded in

dust, which causes reddening. Indeed, three of these six cool stars have rather red extinction-corrected colours ($(H - K_S)_0 = 0.93 - 2.12$ mag). This reddening makes it hard to classify the six cool stars as member or background stars. Further, all six stars have a steeply rising continuum (slope $m = \Delta\text{flux}/\Delta\lambda = 3.2$ to 4.8 , see also Fig. 5.5), at least 3 times steeper than most other stars. This also indicates that the stars are embedded in dust, and our photometric extinction correction was possibly too low.

5.4.6 Spatial distribution and kinematics of metal-poor stars

We investigated if the metal-poor stars show any kind of peculiar spatial distribution. For this purpose, we counted the number of metal-poor stars ($[M/H] \leq -0.5$) in circular annuli around Sgr A*. We chose the bins such that each bin contains at least five metal-poor stars. The fraction of metal-poor stars divided by the total number of late-type stars is shown in the upper panel of Fig. 5.6. The uncertainties come from the total uncertainty of $[M/H]$. We did not find a significant change of the fraction of metal-poor stars in the range of 0 to 1.4 pc projected distance from the centre. Further, we divided the data set in eight segments, and computed the fraction of metal-poor stars with respect to the total number of stars as a function of the position angle. The result is shown in Fig. 5.6 (lower panel). We found that the fraction of metal-poor stars is highest in the Galactic North East, and lower in the Galactic South. But again, the uncertainties are too high for this trend to be significant.

We show a completeness corrected surface number density profile of metal-poor stars (grey triangles) and metal-rich stars ($[M/H] \geq 0.0$ dex, open diamond symbols) in Fig. 5.7. We used the same method as in Feldmeier-Krause et al. (2015) to construct the profile, i.e. we corrected the number counts in different magnitude and radial bins for completeness, and counted the stars in rings around Sgr A*. The surface number density of early-type stars is denoted with filled square symbols. The decrease of the early-type star density with larger radii is steep, over more than two orders of magnitude. The density of stars with $[M/H] \geq 0.0$ dex and $K_S < 14$ mag is nearly constant, and decreases only by a factor $\lesssim 3$. There is much scatter in the surface number density of metal-poor stars.

We also illustrate the spatial distribution of the 705 stars with $(H - K_S)_0 > -0.5$ mag in Fig. 5.8. The upper panel is colour-coded with the metallicity $[M/H]$, and metal-poor stars ($[M/H] \leq -0.5$ dex) are highlighted as square symbols. The middle panel is colour-coded with the effective temperature. Metal-poor stars are rather hotter than the other stars, with $\langle T_{\text{eff}} \rangle = 3980$ K. Only one is a long-period variable star with a low temperature of 2300 K. We already discussed in Section 5.4.5 that long-period variable stars can have an unusual chemical composition, and therefore the results are uncertain.

The radial velocity v_z is illustrated in the lower panel of Fig. 5.8. The metal-poor stars also rotate around Sgr A*, and their mean velocity and velocity dispersion are $\langle v_z \rangle = +76.8$ km·s⁻¹, $\sigma_z = 101.9$ km·s⁻¹ in the Galactic East, $\langle v_z \rangle = -15.2$ km·s⁻¹, $\sigma_z = 124.3$ km·s⁻¹ in the Galactic West, and $\langle v_z \rangle = +47.0$ km·s⁻¹, $\sigma_z = 116.4$ km·s⁻¹ in the entire field. The velocity dispersion is similar to the velocity dispersion of all stars ($\sigma_z = 94.6 \pm 2.6$ km·s⁻¹, Section 5.4.4). We also matched the stars with the proper motion data of Schödel et al. (2009), and found

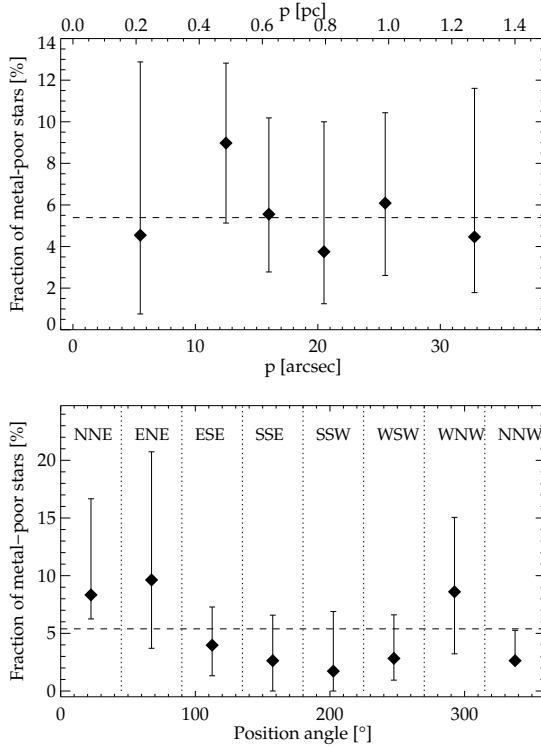


Figure 5.6: Fraction of metal-poor stars ($[M/H] \leq -0.5$ dex) as a function of projected distance p from Sgr A* (upper panel), and as function of the position angle (Galactic East of North) centred on Sgr A* (lower panel).

400 matches. The proper motions of the metal-poor stars are plotted as black arrows in Fig. 5.8. The average velocity dispersion over two dimensions for 21 metal-poor stars with proper motions ($\sigma_{2d} = 89.8 \text{ km}\cdot\text{s}^{-1}$) is in agreement with the velocity dispersion of the other stars ($\sigma_{2d} = 100.3 \pm 3.7 \text{ km}\cdot\text{s}^{-1}$). As for the radial velocities, the absolute two-dimensional velocity of the metal-poor stars ($\langle v_{2d} \rangle = 126.3 \text{ km}\cdot\text{s}^{-1}$) is in agreement with the two-dimensional velocity of the other 379 stars ($\langle v_{2d} \rangle = 127.5 \pm 3.3 \text{ km}\cdot\text{s}^{-1}$). Altogether the kinematics of the metal-poor stars are not significantly distinct from the kinematics of the other stars.

5.4.7 Influence of radial velocity shift

Depending on the radial velocity of a star, a slightly different wavelength region is fitted. In this section we test if this has a strong effect. We fitted the spectra as observed in the fixed wavelength interval $\lambda = [20\,900 \text{ \AA}, 22\,900 \text{ \AA}]$. But since the stars have velocities in the range of $v_z = [-269 \text{ km}\cdot\text{s}^{-1}; 314 \text{ km}\cdot\text{s}^{-1}]$, some spectra are shifted with respect to the rest wavelength by up to 22 \AA . This means we fit the stars in different rest wavelength intervals, and

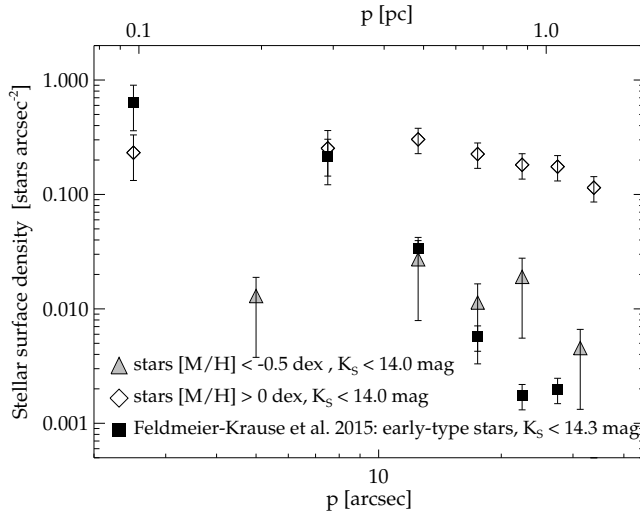


Figure 5.7: Completeness corrected stellar surface number density profile for stars brighter than $K_S = 14.0$ mag. Grey triangles denote metal-poor stars ($[M/H] \leq -0.5$ dex), open diamond symbols denote super-solar metallicity stars ($[M/H] \geq 0.0$ dex). Filled square symbols illustrate the distribution of early-type stars.

some lines at the edge of $\lambda = [20\,900 \text{ \AA}, 22\,900 \text{ \AA}]$ may be part of the fit or not, depending on the stellar radial velocity. To test the magnitude of this effect, we shifted 50 spectra to the rest wavelength, and fitted the spectra at slightly shifted wavelength regions, at $\lambda = [20\,900 \text{ \AA}, 22\,900 \text{ \AA}]$, $\lambda = [20\,920 \text{ \AA}, 22\,920 \text{ \AA}]$, and $\lambda = [20\,880 \text{ \AA}, 22\,880 \text{ \AA}]$. The offset of $\pm 20 \text{ \AA}$ corresponds to $\pm 270 \text{ km}\cdot\text{s}^{-1}$. For these 50 spectra we found that the median of the stellar parameter change is $\Delta T_{\text{eff}} = 3 \text{ K}$, $\Delta[M/H] = +0.01$ dex, $\Delta \log(g) = +0.01$ dex, $\Delta v_z = 0.3 \text{ km}\cdot\text{s}^{-1}$ with standard deviations of $\sigma_{\Delta T_{\text{eff}}} = 44 \text{ K}$, $\sigma_{\Delta[M/H]} = 0.1$ dex, $\sigma_{\Delta \log(g)} = 0.6$ dex, and $\sigma_{\Delta v_z} = 0.7 \text{ km}\cdot\text{s}^{-1}$. This means that a shift in the radial velocity does not bias the results of the stellar parameters, though it can change the results. The difference is usually less than the uncertainties.

5.4.8 Influence of spectral resolution

As we showed in Section 5.2.2, the spectral resolution depends on the used IFU. For the spectral fits we took the different spectral resolutions into account. In this section we test if a lower spectral resolution obtains consistent results with a higher spectral resolution, and how a mismatch of the data and model spectral resolution affects the results.

We used the spectral library and convolved the spectra to the minimum and maximum spectral resolution of the KMOS data ($R = 3\,300$ and $4\,660$). We fitted the spectra with $R = 3\,300$ using model spectra at $R = 4\,660$, and the spectra with $R = 4\,660$ using model spectra at $R = 3\,300$. The results of T_{eff} , $\log(g)$ and v_z change only slightly, and there are no systematic

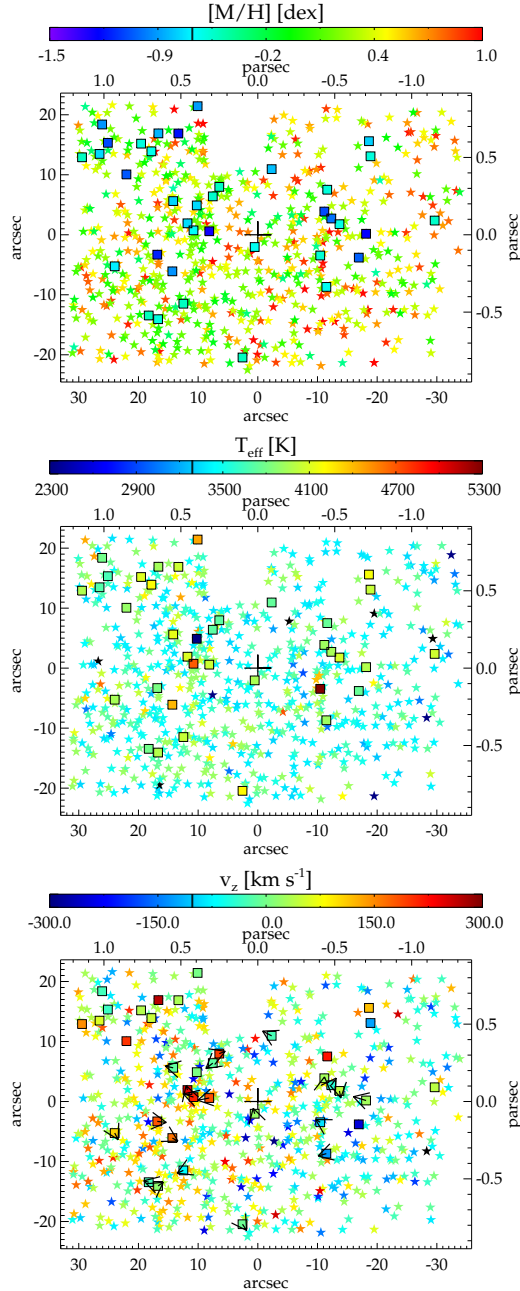


Figure 5.8: Spatial distribution of 705 stars with $(H - K_S)_0 > -0.5$ mag in offset coordinates from the central supermassive black hole, Sgr A*, illustrated as black cross. Galactic North is up. The colours denote the metallicity $[M/H]$ (upper panel), effective temperature T_{eff} (middle panel) and radial velocity v_z (lower panel). The square symbols highlight metal-poor stars with $[M/H] \leq -0.5$ dex. Black arrows denote proper motions of metal-poor stars.

offsets. Only the metallicity is affected. In particular, when fitting the data with models that have a higher spectral resolution, the metallicity is shifted by $\langle \Delta[M/H] \rangle = +0.1$ dex with $\sigma_{\Delta[M/H]} = 0.06$ dex. On the other hand, fitting data using model spectra that have a lower spectral resolution, the metallicity is shifted by $\langle \Delta[M/H] \rangle = -0.09$ dex with $\sigma_{\Delta[M/H]} = 0.05$ dex.

We repeated the fits using model spectra convolved to the correct respective spectral resolution. The mean differences and standard deviations at the different spectral resolutions are small compared to the uncertainties. We conclude that a variation of the spectral resolution does not bias our results when the correct spectral resolution is adopted for each spectrum.

5.5 Discussion

In this section we discuss our results of the stellar metallicities, and compare them with other metallicity measurements. We argue that the stars in our data set are likely members of the nuclear star cluster. From the stellar K -band magnitude we infer the luminosity classes and conclude that the metal-poor stars are consistent with globular cluster stellar populations. We finally discuss implications for the formation of the Milky Way nuclear star cluster.

5.5.1 Detection of stars with low metallicity $[M/H] \lesssim -0.5$ dex

We measured the metallicities of 705 stars in the near-infrared K -band with medium spectral resolution. We detected 37 stars with $[M/H] \lesssim -0.5$ dex, this is 5.2 per cent of the stars in our sample. Their mean magnitude $K_{S,0} = 13.18$ mag is similar to the mean magnitude of the stars with $[M/H] > -0.5$ dex ($K_{S,0} = 13.04$ mag). We could not calibrate the metallicity measurements with metal-poor library stars with $[M/H] < -0.5$ dex. Therefore, we could not test if we can differentiate between stars with $[M/H] = -0.5$ dex and $[M/H] = -1.0$ dex. But we showed in Section 5.3.2.2 that our method is able to differentiate metal-poor ($[M/H] < -0.3$ dex) from metal-rich stars ($[M/H] > +0.0$ dex).

Our metallicity results are in agreement with the results of Do et al. (2015), who measured the metallicities of 83 Galactic centre stars. Do et al. (2015) used the same fitting procedure as this work, but their data have a higher spatial and spectral resolution ($R = 5400$). Further, they used the MARCS grid (Gustafsson et al. 2008). We matched their 83 stars with our data set. To obtain a match, the distance of two stars has to be less than $0''.3$, and the difference in K_S -band magnitude not more than 0.4 mag. With these conditions we have 29 stars in common. The temperatures and metallicities are in reasonable agreement, with $\langle \Delta T_{\text{eff}} \rangle = -2.6$ K, $\sigma_{\Delta T_{\text{eff}}} = 148$ K, $\langle \Delta[M/H] \rangle = -0.32$ dex, $\sigma_{\Delta[M/H]} = 0.35$ dex. The values of $\log(g)$ have a larger disagreement than expected from fitting the spectral library in Section 5.3.2.2, with $\langle \Delta \log(g) \rangle = -2.6$ dex, $\sigma_{\Delta \log(g)} = 0.9$ dex. This is caused by the low surface gravities obtained with the PHOENIX grid, and the tendency of the MARCS grid to higher surface gravities (see Fig. 2 of Do et al. 2015). The radial velocity is also offset by $\langle \Delta v_z \rangle = 28.9$ km·s⁻¹, $\sigma_{v_z} = 7.5$ km·s⁻¹, but this is simply due to the fact that Do et al. (2015) did not shift their

spectra to the local standard of rest, as we did. This is a shift of less than 2 \AA , and should therefore not affect the results severely (see Section 5.4.7).

5.5.2 Note of caution on the measurement of high metallicities

Our results suggest that most stars are metal-rich, i.e., $[M/H] > 0.0$ dex. For more than 75 per cent of the stars we obtain a metallicity $[M/H] > 0.0$ dex, and for about 28 per cent even $[M/H] > +0.5$ dex. The measurements of high metallicities have to be regarded with caution. Our metallicity measurements are differential and may not be correct in absolute values.

As Do et al. (2015) pointed out, there might be systematic effects due to the use of medium resolution spectroscopy. Differences between metal-rich and solar-metallicity spectra are not as pronounced as differences between metal-poor and solar-metallicity spectra. We showed in Section 5.3.2.2 on the fit of a reference star that the metallicity can be overestimated by almost 0.7 dex. Figure 5.3 illustrates that several lines of the spectrum (black) are deeper than the lines of the best-fitting model spectrum (red). The model spectrum with the reference stellar parameters (blue) of Smith (1984) is a worse fit. A similar effect can be seen in the KMOS data. In Fig. 5.1 we showed the spectrum of a star with supposedly high metallicity ($[M/H] = +0.69$ dex, bottom spectrum). Although the model spectrum (red) has a high metallicity, several lines of the observed spectrum (black) are still deeper and not fitted well. It might be that the used model spectra are not ideal to fit red giants with high metallicities at medium spectral resolution. Maybe the assumption of solar α -abundances causes problems at high metallicities. Alternatively, the line strengths of strong lines in the model spectra may be too low if the microturbulence assumed by Husser et al. (2013) was too low. Further, the synthetic spectra were computed assuming LTE, which may affect our results (Lind et al. 2012; Bergemann & Nordlander 2014). The Gaia-ESO Survey and the Apache Point Observatory Galactic Evolution Experiment (APOGEE) measured metallicities for several thousand stars of the Milky Way (Mikolaitis et al. 2014; Holtzman et al. 2015). They found some stars with high metallicities $[M/H] \approx +0.5$ dex. However, their spectra are at shorter wavelengths than our data, and we cannot compare their spectra of metal-rich stars to our data. In summary, we cannot rule out that some of the stars in our data set have high metallicities. But since the spectra of the alleged super-metal-rich stars are not fitted well, we do not claim the detection of such stars.

Nevertheless, we conclude that most of the stars in our data set are metal-rich ($[M/H] > +0.0$ dex). Studies of the Milky Way bulge and disc showed that the metallicity increases towards the center (e.g. Zoccali et al. 2008; Ness & Freeman 2016; Hayden et al. 2015), with the most metal-rich stars concentrated to the plane. Therefore it is not surprising to find metal-rich stars in the Galactic centre. To verify the metallicity measurements, observations with higher spectral resolution are required. A subsample of the metal-poor stars and some metal-rich stars observed with high-resolution spectroscopy would be useful to calibrate our measurements, and to measure abundance ratios, such as $[Na/Fe]$, and $[Ca/Fe]$. But also the applied tools should be improved. As the Galactic centre stars seem to be enhanced in some elements, synthetic spectra with higher element abundances are probably more suitable

to fit the spectra. At the moment, PHOENIX spectra with $[\alpha/Fe] > 0$ dex are only available for $[M/H] = 0.0$ dex. We plan to implement different α -abundances to the spectral fit in the future. In addition, a larger spectral library in the K -band at high to medium spectral resolution will be useful. In the near future, the X-SHOOTER spectral library (Chen et al. 2014b) will provide near-infrared spectra, which will be very useful to study the Milky Way nuclear star cluster.

5.5.3 Metallicity distribution

The metallicity distribution is important to derive the fraction of metal-poor and metal-rich stars. This information is essential to reconstruct the star formation history. We obtained a mean metallicity $\langle [M/H] \rangle = +0.26$ dex. The standard deviation of $[M/H]$ is 0.42 dex.

Other studies obtained similar results for the metallicity distribution in the Galactic centre. Do et al. (2015) found a mean value of $\langle [M/H] \rangle = +0.4$ dex and a standard deviation of 0.4 dex for a sample of 83 stars. Further out, in the inner Galactic bulge, Schultheis et al. (2015) measured the metallicities of 33 stars and obtained a mean metallicity $\langle [M/H] \rangle = +0.4$ dex with a dispersion of 0.55 dex. They also found eight low-metallicity stars with $[M/H] \approx -1.0$ dex and enhanced α -element abundance. Our metallicity measurements are in agreement. Due to the larger number of stars in our sample, we were able to find a continuous metallicity distribution. The metallicity distribution is rather smooth, and we do not see signs of a second peak at $[M/H] = -1.0$ dex, as indicated by the smaller samples of Do et al. (2015) and Schultheis et al. (2015). Our metallicity distribution has a negative skewness, which was also found for the metallicity distribution of the inner Galactic disc using APOGEE data (Hayden et al. 2015). However, we note that we did not measure systematic uncertainties for metallicities $[M/H] < -0.5$ dex and $[M/H] > +0.3$ dex on reference stars, but assumed the same systematic uncertainties as in the range -0.5 dex $< [M/H] < +0.3$ dex. The shape of the metallicity distribution at low ($[M/H] < -0.5$ dex) and high ($[M/H] > 0.3$ dex) metallicities may be influenced by unknown systematic effects. Nevertheless, the spread of the metallicity distribution by about 0.4 dex means that the chemical composition of the stars in the Galactic centre is inhomogeneous.

5.5.4 Contamination from foreground or background sources

We checked the membership of a star to the Milky Way nuclear star cluster based on the extinction corrected colours. We identified foreground stars, e.g., from the Galactic bulge or disc, with their blue colours. But as we do not know exactly the extinction along the line-of-sight, it is possible that some stars of our sample are bar or bulge stars with rather high extinction. However, their number density should be lower than the number density of Galactic centre stars. Clarkson et al. (2012) studied a $12'' \times 12''$ field near the Arches cluster, about 26 pc in projection away from our field. Their data contain only one field star with $K < 13.8$ mag, identified by proper motions. This translates to a number density of 0.007 inner bulge stars per arcsec². In our field of 2 700 arcsec², we estimate the number of inner bulge

stars to approximately 19, but this estimate is based on a small field with only one foreground star in our magnitude range.

We also checked if the kinematics of the stars contain any hints on the cluster membership. For this reason we matched the stars in our data set with the proper motion data of Schödel et al. (2009). We obtained 400 matches, all within the central $p = 25''$ (~ 0.97 pc) of the nuclear star cluster. Most of the stars have a lower velocity than the escape velocity, and their kinematics are in agreement with being bound to the nuclear star cluster. There is one exception with a significantly higher velocity than the escape velocity, this is the potential runaway star found by Schödel et al. (2009). It has a proper motion velocity of $424 \text{ km}\cdot\text{s}^{-1}$. Schödel et al. (2009) suggested that this star might escape the Milky Way nuclear star cluster. About 40 per cent of the stars move against the main direction of rotation of the nuclear star cluster. Several stars in the Galactic East have a negative velocity v_z , and likewise, several stars in the Galactic West have a positive velocity. But this does not mean that these stars do not belong to the nuclear star cluster. They may be on bound counter-rotating tube orbits or on box orbits.

There might be some stars from the nuclear stellar disc with similar colours as the stars of the nuclear star cluster. The nuclear stellar disc and the nuclear star cluster form the nuclear stellar bulge. The nuclear stellar disc extends over $p \approx 120$ pc, and dominates over the nuclear star cluster at $p \gtrsim 30$ pc (Launhardt et al. 2002). We are not able to distinguish if a star is from the nuclear star cluster or the nuclear stellar disc based on the extinction or kinematics.

5.5.5 Luminosity classes and implications for stellar ages

The K_S -band magnitude can be used to infer the luminosity class of the stars, and estimate their age. The extinction corrected magnitudes of the stars in our data set range from $K_{S,0} < 6$ to $K_{S,0} \approx 13.5$ mag, with a median at $K_{S,0} = 10.4$ mag.

Stars with magnitudes $K_{S,0} \lesssim 5.7$ mag are red supergiants (Blum et al. 2003), but supergiants may be as faint as approximately 7.5 mag (Blum et al. 1996, 2003). Red supergiants are massive ($M > 10 M_\odot$, Cox 2000) and young, only a few 10^7 yr old (Greggio & Renzini 2011). For five stars in the range $5.7 \text{ mag} \lesssim K_{S,0} \lesssim 7.5 \text{ mag}$, one cannot distinguish supergiants from (bright) giant stars based on the magnitude. Blum et al. (2003) suggested that it is more likely for the stars to be (bright) giants.

Red giant stars have masses of about 0.3 to $10 M_\odot$, and ages $\gtrsim 1$ Gyr. The stars with $K_{S,0} > 7.5$ mag are probably red giant stars. This means 99 per cent of the stars in our data set are red giants. The red clump is a subgroup of red giants, their magnitude is roughly $K_{S,0} = 12.9$ mag (Schödel et al. 2010). Only about 1.5 per cent of the stars in our data set are faint enough for the red clump. Another subgroup of red giant stars are the bright asymptotic giant branch (AGB) stars. AGB stars have masses in the range $0.5 M_\odot \lesssim M \lesssim 10 M_\odot$ (Blum et al. 1996). They have two phases, the early AGB (E-AGB) phase, and a later thermally pulsing AGB (TP-AGB) phase. During the later phase, material from the core is mixed with the surface material. The six long-period variables (Section 5.4.5) are probably such AGB stars. TP-AGB stars are rather bright, with $K_{S,0} \lesssim 8.4$ mag for solar and higher metallicities

and ages >1 Gyr (PARSEC evolutionary tracks, Bressan et al. 2012; Rosenfield et al. 2016). About 50 stars (7 per cent) in our sample could be TP-AGB stars, based on their K_S -band magnitudes. Fainter stars could be E-AGB stars ($6.9 \text{ mag} \lesssim K_{S,0} \lesssim 12 \text{ mag}$, 93 per cent) or normal red giant branch stars ($7.5 \text{ mag} \lesssim K_{S,0} \lesssim 16.4 \text{ mag}$, 99 per cent). As the time a star spends on the red giant branch is about forty times longer than the time spent as AGB star (Greggio & Renzini 2011), it is more likely for a star to be on the red giant branch.

The metal-poor stars in our data set have magnitudes ranging from $K_{S,0} = 7.2$ to 12.6 mag and temperatures from $3\,660$ to $5\,300 \text{ K}$, except for one cooler long-period variable star. We compared the location of the stars in a $T_{\text{eff}} - K_{S,0}$ diagram with the PARSEC evolutionary tracks (Bressan et al. 2012). Using $[M/H] = -0.5$ and -1.0 dex for the tracks, we find that the metal-poor stars have ages ≥ 1 Gyr, and initial masses $M_{\text{ini}} \lesssim 2 M_{\odot}$. Tracks with age 10 Gyr and masses $M_{\text{ini}} \lesssim 1 M_{\odot}$ are also in agreement with the stellar effective temperatures and magnitudes. This means the stellar ages and masses are consistent with stars in Galactic globular clusters.

5.5.6 Clues to the formation of the Milky Way nuclear star cluster

There is a large spread of metallicities ranging from metal-poor stars ($[M/H] \lesssim -1.0$ dex) to metal-rich stars ($[M/H] \gtrsim +0.2$ dex) in the late-type giant star population of the Milky Way nuclear star cluster. This means that the cluster did not form from one homogeneous gas cloud in one single star burst.

The metal-poor stars in the Milky Way nuclear star cluster may have formed in an early starburst in-situ, or somewhere else in the Galaxy and migrated to the centre. The stars might have migrated from the Milky Way bulge to the centre, as the inner bulge also contains some metal-poor stars (Schultheis et al. 2015; Ness & Freeman 2016). Another possibility is that the stars formed in a star cluster, potentially a globular cluster, that migrated to the centre of the Milky Way. The Milky Way globular cluster system has a bimodal metallicity distribution, with about 71 per cent metal-poor ($[Fe/H] \lesssim -0.75$ dex) and 29 per cent metal-rich ($-0.75 \lesssim [Fe/H] \lesssim 0.0$ dex) globular clusters (Bica et al. 2006). The sub-solar metallicity stars in the Milky Way nuclear star cluster have similar metallicities as the “metal-rich” Milky Way Globular clusters.

Aharon & Perets (2015) studied the in-situ formation scenario for nuclear star clusters. Depending on where the star formation occurs dominantly, in the center or in the outskirts of the nuclear star cluster, the cluster would have a positive or negative age gradient. But also the consecutive infall of multiple stellar clusters creates an age and stellar population gradient in the nuclear star cluster (Perets & Mastrobuono-Battisti 2014). We investigated the radial distribution of metal-poor stars, but we were not able to find any significant difference with respect to metal-rich stars. The number of metal-poor stars is too low, and the uncertainties are too high to discern the spatial distributions. We found indications for a slight overabundance of metal-poor stars in the Galactic North East. If this observation is confirmed, it would rather suggest a later infall scenario than in-situ formation. If the old, metal-poor stars have formed in-situ, they should be distributed isotropically now. However, this assumption needs

to be confirmed in three-dimensional simulations of in-situ nuclear star cluster formation. The kinematics of the metal-poor stars are not significantly different from the kinematics of the other stars. The dynamical evolution of the different formation scenarios needs to be studied further in simulations.

The infall of globular clusters to the centre of the Milky Way cannot explain the large fraction of metal-rich ($[M/H] > 0.0$ dex) stars. These stars must have formed from enriched gas within the Milky Way, as their metallicities are inconsistent with the observed Milky Way globular cluster metallicities. Metal-rich stars formed either directly in the Galactic centre, or in an enriched star cluster within the Milky Way that migrated to the Galactic centre.

5.6 Conclusions

We observed the central 4 pc^2 of the Milky Way nuclear star cluster in the K -band with the integral field spectrograph KMOS. We analysed the spectra of more than 700 late-type stars. We found that the equivalent width of the Na I doublet line region is enhanced with respect to stellar library spectra. Using full spectral fitting we derived effective temperatures and metallicities of 705 stars of the Milky Way nuclear star cluster. Most stars are red K- and M-type giants with temperatures $T_{\text{eff}} = 3\,000 - 5\,000$ K. The metallicities range from sub-solar $[M/H] < -1.0$ dex to super-solar $[M/H] > +0.3$ dex, with a standard deviation of 0.42 dex. The fraction of low-metallicity stars with $[M/H] \leq -0.5$ dex is $(5.2_{-3.1}^{+6.0})$ per cent. The spatial distribution and kinematics of metal-poor stars are consistent with metal-rich stars. The metal-poor stars might come from infalling globular clusters. However, our data set is dominated by metal-rich stars, for which the origin from a globular cluster infall can be ruled out.

Acknowledgments

R.S. acknowledges funding from the European Research Council under the European Union's Seventh Framework Programme (FP7/2007-2013) / ERC grant agreement n. 614922. This publication makes use of data products from the TwoMicron All Sky Survey, which is a joint project of the University of Massachusetts and the Infrared Processing and Analysis Center/California Institute of Technology, funded by the National Aeronautics and Space Administration and the National Science Foundation. This research made use of the SIMBAD database (operated at CDS, Strasbourg, France). We thank Nikolay Kacharov, and Iskren Georgiev for discussions and suggestions. Thanks to Ariane Lançon for helpful discussions. We finally thank the anonymous referee for comments and suggestions.

Based on observations collected at the European Organisation for Astronomical Research in the Southern Hemisphere, Chile (60.A-9450(A)).

5.7 Appendix: The $T_{\text{eff}} - EW_{\text{CO}}$ relation for giants

We calibrated the relation of the effective temperature T_{eff} with the CO equivalent width EW_{CO} as defined by Frogel et al. (2001) using the stars of the spectral library. We considered 69 stars with luminosity classes II–IV. EW_{CO} was computed with $R = 3\,000$ for stars from Wallace & Hinkle (1997), and $R = 4\,350$ for the other stars in the spectral library.

The effective temperature T_{eff} is given for the stars in the GNIRS library in Winge et al. (2009), for the other stars we complemented T_{eff} with entries from the stellar parameter catalogue PASTEL (Soubiran et al. 2010). For stars with more than one entry we used the mean of the various measurements, and the standard deviation as uncertainty $\sigma_{T_{\text{eff}}}$. When there was no entry of T_{eff} for a star in the PASTEL catalogue, we used our knowledge of the spectral type. We used the list given in Lang (1992), where T_{eff} is listed for various spectral types, and for dwarfs, giants, and supergiants separately. When necessary, we interpolated linearly between the spectral classes. We compared the Lang (1992) values for T_{eff} with the values given in Table 7.5, 7.6 and 7.7 in Cox (2000) and in Table 15.7 in Cox (2000). We used the scatter between these three different spectral type– T_{eff} tables to estimate the uncertainty $\sigma_{T_{\text{eff}}}$.

Figure 5.9 shows the relation between T_{eff} and EW_{CO} for 69 stars with luminosity classes II–IV from the spectral libraries. We made a linear fit to the data in the range below 6 000 K and found the relation

$$T_{\text{eff}} = 5\,677^{\pm 21} \text{K} - 106.3^{\pm 3.0} \text{K}\text{\AA}^{-1} \times EW_{\text{CO}}, \quad (5.1)$$

where EW_{CO} is in \AA , and T_{eff} in K. The uncertainties are the formal fit uncertainties. The residual scatter is 163 K. Our best-fitting result is shown as red line in Fig. 5.9. We also show the three-degree-polynomial fit of Pfuhl et al. (2011) as blue dot-dashed line. Pfuhl et al. (2011) used 33 giant stars from spectral libraries at lower spectral resolution ($R \approx 3\,000$ and $R \approx 2\,000$). Our $T_{\text{eff}} - EW_{\text{CO}}$ relation is in agreement with their relation for $T_{\text{eff}} \gtrsim 3\,000$ K. However, at $T_{\text{eff}} \lesssim 3\,000$ K, the Pfuhl et al. (2011) relation declines faster than our linear fit. The different result of the relation can be explained by the larger sample and the different values of T_{eff} that we use. We included larger uncertainties $\sigma_{T_{\text{eff}}}$ than Pfuhl et al. (2011), since we took several measurements of T_{eff} for a star into account. We did not make a metallicity cut for the stars, since for many stars in the stellar library the metallicity is not known. When we just use a subsample of 39 spectra with near solar-metallicity in the range $-0.5 \text{ dex} < [M/H] < +0.5 \text{ dex}$, the relation changes within the formal fit uncertainties. Schultheis et al. (2016) showed that the $T_{\text{eff}} - EW_{\text{CO}}$ relation does not depend on the metallicity in the temperature range 3 200–4 500 K and metallicities $[Fe/H]$ from -1.2 dex to $+0.5 \text{ dex}$. We conclude that our $T_{\text{eff}} - EW_{\text{CO}}$ relation is robust in this temperature and metallicity range.

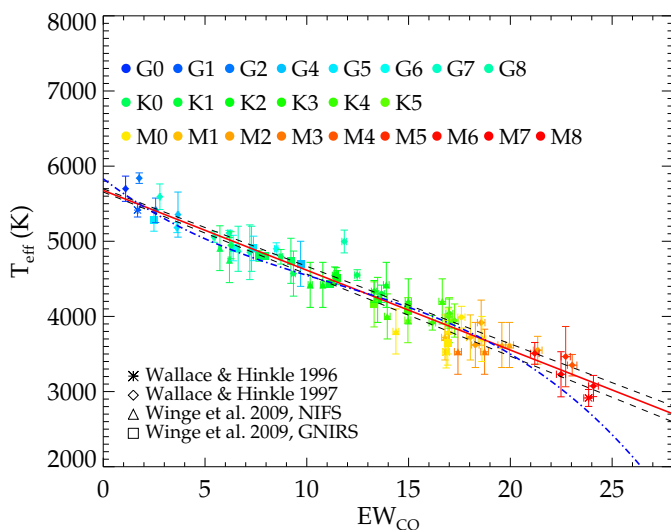


Figure 5.9: Relation between effective Temperature T_{eff} and the equivalent width EW_{CO} for 69 template stars with luminosity class II–IV. The different colours denote different spectral types, the symbols denote the library from which the spectrum is taken. The red line is a linear fit to the data, the black dashed lines show the formal uncertainty of the linear fit. The blue dot-dashed line is the $T_{\text{eff}} - EW_{\text{CO}}$ relation as derived by Pfuhl et al. (2011).

Bibliography

- Agarwal, M. & Milosavljević, M. 2011, *ApJ*, 729, 35
- Aharon, D. & Perets, H. B. 2015, *ApJ*, 799, 185
- Alexander, T. 2005, *Phys. Rep.*, 419, 65
- Amico, P., Cuby, J.-G., Devillard, N., et al. 2002, *ISAAC Data Reduction Guide 1.5*
- Amo-Baladrón, M. A., Martín-Pintado, J., & Martín, S. 2011, *A&A*, 526, A54
- Antonini, F. 2013, *ApJ*, 763, 62
- Antonini, F. 2014, *ApJ*, 794, 106
- Antonini, F., Capuzzo-Dolcetta, R., Mastrobuono-Battisti, A., et al. 2012, *ApJ*, 750, 111
- Bahcall, J. N. & Tremaine, S. 1981, *ApJ*, 244, 805
- Balcells, M., Graham, A. W., & Peletier, R. F. 2007, *ApJ*, 665, 1084
- Baldassare, V. F., Reines, A. E., Gallo, E., et al. 2015, *ApJ*, 809, L14
- Barth, A. J., Martini, P., Nelson, C. H., et al. 2003, *ApJ*, 594, L95
- Bartko, H., Martins, F., Fritz, T. K., et al. 2009, *ApJ*, 697, 1741
- Bartko, H., Martins, F., Trippe, S., et al. 2010, *ApJ*, 708, 834
- Becklin, E. E., Matthews, K., Neugebauer, G., et al. 1978, *ApJ*, 219, 121
- Becklin, E. E. & Neugebauer, G. 1968, *ApJ*, 151, 145
- Bekki, K., Couch, W. J., Drinkwater, M. J., et al. 2004, *ApJ*, 610, L13
- Bergemann, M. & Nordlander, T. 2014, *ArXiv e-prints*
- Bianchini, P., Norris, M. A., van de Ven, G., et al. 2015, *MNRAS*, 453, 365
- Bica, E., Bonatto, C., Barbuy, B., et al. 2006, *A&A*, 450, 105
- Blum, R. D., Ramírez, S. V., Sellgren, K., et al. 2003, *ApJ*, 597, 323
- Blum, R. D., Sellgren, K., & Depoy, D. L. 1996, *AJ*, 112, 1988
- Boehle, A., Ghez, A. M., Schödel, R., et al. 2016, *ArXiv e-prints*
- Böker, T. 2010, in *IAU Symposium*, Vol. 266, 58–63
- Böker, T., Laine, S., van der Marel, R. P., et al. 2002, *AJ*, 123, 1389
- Böker, T., Sarzi, M., McLaughlin, D. E., et al. 2004, *AJ*, 127, 105
- Bressan, A., Marigo, P., Girardi, L., et al. 2012, *MNRAS*, 427, 127
- Buchholz, R. M., Schödel, R., & Eckart, A. 2009, *A&A*, 499, 483
- Buchner, J., Georgakakis, A., Nandra, K., et al. 2014, *A&A*, 564, A125
- Cappellari, M. 2002, *MNRAS*, 333, 400
- Cappellari, M. 2008, *MNRAS*, 390, 71
- Cappellari, M., Bacon, R., Bureau, M., et al. 2006, *MNRAS*, 366, 1126
- Cappellari, M. & Copin, Y. 2003, *MNRAS*, 342, 345
- Cappellari, M. & Emsellem, E. 2004, *PASP*, 116, 138
- Capuzzo-Dolcetta, R. & Mocchi, P. 2008, *ApJ*, 681, 1136
- Carollo, C. M., Stiavelli, M., de Zeeuw, P. T., et al. 1997, *AJ*, 114, 2366
- Carollo, C. M., Stiavelli, M., & Mack, J. 1998, *AJ*, 116, 68

- Carollo, C. M., Stiavelli, M., Seigar, M., et al. 2002, *AJ*, 123, 159
- Carpenter, J. M. 2001, *AJ*, 121, 2851
- Carr, J. S., Sellgren, K., & Balachandran, S. C. 2000, *ApJ*, 530, 307
- Carson, D. J., Barth, A. J., Seth, A. C., et al. 2015, *AJ*, 149, 170
- Chaisson, E. & McMillan, S. 1993, *Astronomy today*
- Chanamé, J., Kleyna, J., & van der Marel, R. 2008, *ApJ*, 682, 841
- Chatzopoulos, S., Fritz, T. K., Gerhard, O., et al. 2015a, *MNRAS*, 447, 948
- Chatzopoulos, S., Gerhard, O., Fritz, T. K., et al. 2015b, *MNRAS*, 453, 939
- Chen, X. & Amaro-Seoane, P. 2014, *ApJ*, 786, L14
- Chen, Y., Girardi, L., Bressan, A., et al. 2014a, *MNRAS*, 444, 2525
- Chen, Y.-P., Trager, S. C., Peletier, R. F., et al. 2014b, *A&A*, 565, A117
- Chiar, J. E. & Tielens, A. G. G. M. 2001, *ApJ*, 550, L207
- Christopher, M. H., Scoville, N. Z., Stolovy, S. R., et al. 2005, *ApJ*, 622, 346
- Clarkson, W. I., Ghez, A. M., Morris, M. R., et al. 2012, *ApJ*, 751, 132
- Clénet, Y., Rouan, D., Gendron, E., et al. 2001, *A&A*, 376, 124
- Côté, P., Piatek, S., Ferrarese, L., et al. 2006, *ApJS*, 165, 57
- Cox, A. N., ed. 2000, *Allen's Astrophysical Quantities*, 4th edn.
- Cretton, N., de Zeeuw, P. T., van der Marel, R. P., et al. 1999, *ApJS*, 124, 383
- Crowther, P. A., Lennon, D. J., Walborn, N. R., et al. 2008, in *Mass Loss from Stars and the Evolution of Stellar Clusters*, Vol. 388, 109
- Cunha, K., Sellgren, K., Smith, V. V., et al. 2007, *ApJ*, 669, 1011
- Davies, R. I. 2007, *MNRAS*, 375, 1099
- Davies, R. I., Agudo Berbel, A., Wiezorrek, E., et al. 2013, *A&A*, 558, A56
- De Lorenzi, F., Hartmann, M., Debattista, V. P., et al. 2013, *MNRAS*, 429, 2974
- Deguchi, S., Imai, H., Fujii, T., et al. 2004, *PASJ*, 56, 261
- den Brok, M., Peletier, R. F., Seth, A., et al. 2014, *MNRAS*, 445, 2385
- Do, T., Ghez, A. M., Morris, M. R., et al. 2009, *ApJ*, 703, 1323
- Do, T., Kerzendorf, W., Winsor, N., et al. 2015, *ApJ*, 809, 143
- Do, T., Lu, J. R., Ghez, A. M., et al. 2013a, *ApJ*, 764, 154
- Do, T., Martinez, G. D., Yelda, S., et al. 2013b, *ApJ*, 779, L6
- Dong, H., Wang, Q. D., Cotera, A., et al. 2011, *MNRAS*, 417, 114
- Drehmer, D. A., Storch-Bergmann, T., Ferrari, F., et al. 2015, *MNRAS*, 450, 128
- Dressel, L. 2012, *Wide Field Camera 3 Instrument Handbook for Cycle 21 v. 5.0*
- Dutra, C. M. & Bica, E. 2001, *A&A*, 376, 434
- Eckart, A., Genzel, R., Ott, T., et al. 2002, *MNRAS*, 331, 917
- Eisenhauer, F., Genzel, R., Alexander, T., et al. 2005, *ApJ*, 628, 246
- Ekers, R. D., van Gorkom, J. H., Schwarz, U. J., et al. 1983, *A&A*, 122, 143
- Elmegreen, B. G. & Scalo, J. 2006, *ApJ*, 636, 149
- Emsellem, E., Cappellari, M., Krajnović, D., et al. 2011, *MNRAS*, 414, 888
- Emsellem, E., Cappellari, M., Krajnović, D., et al. 2007, *MNRAS*, 379, 401
- Emsellem, E., Monnet, G., & Bacon, R. 1994, *A&A*, 285, 723
- Emsellem, E., Renaud, F., Bournaud, F., et al. 2015, *MNRAS*, 446, 2468

- Etzaluze, M., Smith, H. A., Tolls, V., et al. 2011, *AJ*, 142, 134
- Feldmeier, A., Lützgendorf, N., Neumayer, N., et al. 2013, *A&A*, 554, A63
- Feldmeier, A., Neumayer, N., Seth, A., et al. 2014, *A&A*, 570, A2
- Feldmeier-Krause, A., Neumayer, N., Schödel, R., et al. 2015, *A&A*, 584, A2
- Feroz, F., Hobson, M. P., & Bridges, M. 2009, *MNRAS*, 398, 1601
- Ferrarese, L., Côté, P., Dalla Bontà, E., et al. 2006, *ApJ*, 644, L21
- Ferrière, K. 2012, *A&A*, 540, A50
- Figier, D. F., McLean, I. S., & Morris, M. 1999, *ApJ*, 514, 202
- Figier, D. F., McLean, I. S., & Najarro, F. 1997, *ApJ*, 486, 420
- Filippenko, A. V. & Ho, L. C. 2003, *ApJ*, 588, L13
- Forbes, D. A., Lasky, P., Graham, A. W., et al. 2008, *MNRAS*, 389, 1924
- Fritz, T. K., Chatzopoulos, S., Gerhard, O., et al. 2016, *ApJ*, 821, 44
- Fritz, T. K., Gillessen, S., Dodds-Eden, K., et al. 2011, *ApJ*, 737, 73
- Frogel, J. A., Stephens, A., Ramírez, S., et al. 2001, *AJ*, 122, 1896
- Fujii, M., Iwasawa, M., Funato, Y., et al. 2010, *ApJ*, 716, L80
- Gamen, R., Arias, J. I., Barbá, R. H., et al. 2012, *A&A*, 546, A92
- Gao, J., Li, A., & Jiang, B. W. 2013, *Earth, Planets, and Space*, 65, 1127
- García-Marín, M., Eckart, A., Weiss, A., et al. 2011, *ApJ*, 738, 158
- Gatley, I., Jones, T. J., Hyland, A. R., et al. 1986, *MNRAS*, 222, 299
- Gazak, J. Z., Kudritzki, R., Evans, C., et al. 2015, *ApJ*, 805, 182
- Geballe, T. R., Najarro, F., Rigaut, F., et al. 2006, *ApJ*, 652, 370
- Gebhardt, K., Adams, J., Richstone, D., et al. 2011, *ApJ*, 729, 119
- Gebhardt, K., Richstone, D., Kormendy, J., et al. 2000, *AJ*, 119, 1157
- Genzel, R., Eisenhauer, F., & Gillessen, S. 2010, *Reviews of Modern Physics*, 82, 3121
- Genzel, R., Schödel, R., Ott, T., et al. 2003, *ApJ*, 594, 812
- Genzel, R., Thatte, N., Krabbe, A., et al. 1996, *ApJ*, 472, 153
- Georgiev, I. Y. & Böker, T. 2014, *MNRAS*, 441, 3570
- Georgiev, I. Y., Böker, T., Leigh, N., et al. 2016, *MNRAS*, 457, 2122
- Gerhard, O. 2001, *ApJ*, 546, L39
- Ghez, A. M., Duchêne, G., Matthews, K., et al. 2003, *ApJ*, 586, L127
- Ghez, A. M., Salim, S., Hornstein, S. D., et al. 2005, *ApJ*, 620, 744
- Ghez, A. M., Salim, S., Weinberg, N. N., et al. 2008, *ApJ*, 689, 1044
- Gillessen, S., Eisenhauer, F., Fritz, T. K., et al. 2009a, *ApJ*, 707, L114
- Gillessen, S., Eisenhauer, F., Trippe, S., et al. 2009b, *ApJ*, 692, 1075
- Gnedin, O. Y., Ostriker, J. P., & Tremaine, S. 2014, *ApJ*, 785, 71
- Gosling, A. J., Bandyopadhyay, R. M., & Blundell, K. M. 2009, *MNRAS*, 394, 2247
- Graham, A. W. & Spitler, L. R. 2009, *MNRAS*, 397, 2148
- Gray, D. F. 1989, *ApJ*, 347, 1021
- Greene, J. E. 2012, *Nature Communications*, 3, 1304
- Greggio, L. & Renzini, A. 2011, *Stellar Populations. A User Guide from Low to High Redshift*
- Gualandris, A., Mapelli, M., & Perets, H. B. 2012, *MNRAS*, 427, 1793

- Guillard, N., Emsellem, E., & Renaud, F. 2016, ArXiv e-prints
- Gültekin, K., Richstone, D. O., Gebhardt, K., et al. 2009, *ApJ*, 698, 198
- Gustafsson, B., Edvardsson, B., Eriksson, K., et al. 2008, *A&A*, 486, 951
- Habing, H. J. & Olofsson, H. 2004, *Asymptotic giant branch stars*, Astronomy and astrophysics library (New York, Berlin: Springer.)
- Haller, J. W., Rieke, M. J., Rieke, G. H., et al. 1996, *ApJ*, 456, 194
- Hanson, M. M., Conti, P. S., & Rieke, M. J. 1996, *ApJS*, 107, 281
- Hanson, M. M., Kudritzki, R.-P., Kenworthy, M. A., et al. 2005, *ApJS*, 161, 154
- Häring, N. & Rix, H.-W. 2004, *ApJ*, 604, L89
- Harris, W. E. 1996, *AJ*, 112, 1487
- Hartmann, M., Debattista, V. P., Seth, A., et al. 2011, *MNRAS*, 418, 2697
- Hayden, M. R., Bovy, J., Holtzman, J. A., et al. 2015, *ApJ*, 808, 132
- Heisler, J., Merritt, D., & Schwarzschild, M. 1982, *ApJ*, 258, 490
- Henry, J. P., Depoy, D. L., & Becklin, E. E. 1984, *ApJ*, 285, L27
- Herbst, T. M., Beckwith, S. V. W., Forrest, W. J., et al. 1993, *AJ*, 105, 956
- Hills, J. G. 1988, *Nature*, 331, 687
- Hobbs, A. & Nayakshin, S. 2009, *MNRAS*, 394, 191
- Holtzman, J. A., Shetrone, M., Johnson, J. A., et al. 2015, *AJ*, 150, 148
- Horrobin, M., Eisenhauer, F., Tecza, M., et al. 2004, *Astronomische Nachrichten*, 325, 88
- Houdashelt, M. L., Frogel, J. A., & Cohen, J. G. 1992, *AJ*, 103, 163
- Hubble, E. P. 1926, *ApJ*, 64
- Humphreys, R. M., Davidson, K., & Smith, N. 1999, *PASP*, 111, 1124
- Husser, T.-O., Wende-von Berg, S., Dreizler, S., et al. 2013, *A&A*, 553, A6
- Ivanov, V. D., Rieke, M. J., Engelbracht, C. W., et al. 2004, *ApJS*, 151, 387
- Jeans, J. H. 1922, *MNRAS*, 82, 122
- Kamann, S., Wisotzki, L., & Roth, M. M. 2013, *A&A*, 549, A71
- Karakas, A. I. 2010, *MNRAS*, 403, 1413
- Kenyon, S. J., Bromley, B. C., Geller, M. J., et al. 2008, *ApJ*, 680, 312
- Kerzendorf, W. & Do, T. 2015, *starkit: First real release*
- Kleinmann, S. G. & Hall, D. N. B. 1986, *ApJS*, 62, 501
- Kobayashi, C., Umeda, H., Nomoto, K., et al. 2006, *ApJ*, 653, 1145
- Koleva, M., Prugniel, P., de Rijcke, S., et al. 2011, *MNRAS*, 417, 1643
- Kormendy, J. & Bender, R. 1996, *ApJ*, 464, L119
- Kormendy, J. & Richstone, D. 1995, *ARA&A*, 33, 581
- Krabbe, A., Genzel, R., Eckart, A., et al. 1995, *ApJ*, 447, L95
- Krajnović, D., Bacon, R., Cappellari, M., et al. 2008, *MNRAS*, 390, 93
- Krajnović, D., Cappellari, M., de Zeeuw, P. T., et al. 2006, *MNRAS*, 366, 787
- Lang, K. R. 1992, *Astrophysical data: Planets and stars*
- Lau, R. M., Herter, T. L., Morris, M. R., et al. 2013, *ApJ*, 775, 37
- Lauer, T. R., Bender, R., Kormendy, J., et al. 2012, *ApJ*, 745, 121
- Launhardt, R., Zylka, R., & Mezger, P. G. 2002, *A&A*, 384, 112
- Lawson, C. L. & Hanson, R. J. 1974, *Solving least squares problems*

- Lee, S., Pak, S., Choi, M., et al. 2008, *ApJ*, 674, 247
- Leigh, N., Böker, T., & Knigge, C. 2012, *MNRAS*, 424, 2130
- Levin, Y. & Beloborodov, A. M. 2003, *ApJ*, 590, L33
- Lind, K., Bergemann, M., & Asplund, M. 2012, *MNRAS*, 427, 50
- Linden, T. 2014, in *The Galactic Center: Feeding and Feedback in a Normal Galactic Nucleus*, Vol. 303, 403–413
- Lindqvist, M., Habing, H. J., & Winnberg, A. 1992a, *A&A*, 259, 118
- Lindqvist, M., Winnberg, A., Habing, H. J., et al. 1992b, *A&AS*, 92, 43
- Liu, H. B., Hsieh, P.-Y., Ho, P. T. P., et al. 2012, *ApJ*, 756, 195
- Löckmann, U., Baumgardt, H., & Kroupa, P. 2010, *MNRAS*, 402, 519
- Loose, H. H., Kruegel, E., & Tutukov, A. 1982, *A&A*, 105, 342
- Lu, J. R., Do, T., Ghez, A. M., et al. 2013, *ApJ*, 764, 155
- Lu, J. R., Ghez, A. M., Hornstein, S. D., et al. 2009, *ApJ*, 690, 1463
- Lützgendorf, N., Kissler-Patig, M., Gebhardt, K., et al. 2012, *A&A*, 542, A129
- Lützgendorf, N., Kissler-Patig, M., Noyola, E., et al. 2011, *A&A*, 533, A36
- Lyubenova, M., van den Bosch, R. C. E., Côté, P., et al. 2013, *MNRAS*, 431, 3364
- Madigan, A.-M., Pfuhl, O., Levin, Y., et al. 2014, *ApJ*, 784, 23
- Malkin, Z. 2012, *ArXiv e-prints*
- Mapelli, M., Gualandris, A., & Hayfield, T. 2013, *MNRAS*, 436, 3809
- Markwardt, C. B. 2009, in *Astronomical Data Analysis Software and Systems XVIII*, Vol. 411, 251
- Mármol-Queraltó, E., Cardiel, N., Cenarro, A. J., et al. 2008, *A&A*, 489, 885
- Martins, F., Genzel, R., Hillier, D. J., et al. 2007, *A&A*, 468, 233
- Martins, F., Hillier, D. J., Paumard, T., et al. 2008, *A&A*, 478, 219
- Martins, F., Schaerer, D., & Hillier, D. J. 2005, *A&A*, 436, 1049
- Matsunaga, N., Kawadu, T., Nishiyama, S., et al. 2009, *MNRAS*, 399, 1709
- Matthews, L. D., Gallagher, III, J. S., Krist, J. E., et al. 1999, *AJ*, 118, 208
- McGaugh, S. & Schombert, J. 2013, *ArXiv e-prints*
- McGinn, M. T., Sellgren, K., Becklin, E. E., et al. 1989, *ApJ*, 338, 824
- McMillan, S. L. W. & Portegies Zwart, S. F. 2003, *ApJ*, 596, 314
- McWilliam, A. 1990, *ApJS*, 74, 1075
- McWilliam, A. & Zoccali, M. 2010, *ApJ*, 724, 1491
- Meidt, S. E., Schinnerer, E., van de Ven, G., et al. 2014, *ApJ*, 788, 144
- Merritt, D. 2004, *Coevolution of Black Holes and Galaxies*, 263
- Merritt, D. 2010, *ApJ*, 718, 739
- Mikolaitis, Š., Hill, V., Recio-Blanco, A., et al. 2014, *A&A*, 572, A33
- Milosavljević, M. 2004, *ApJ*, 605, L13
- Misgeld, I. & Hilker, M. 2011, *MNRAS*, 414, 3699
- Moorwood, A., Cuby, J.-G., Biereichel, P., et al. 1998, *The Messenger*, 94, 7
- Morris, M. 1993, *ApJ*, 408, 496
- Morris, P. W., Eenens, P. R. J., Hanson, M. M., et al. 1996, *ApJ*, 470, 597
- Nataf, D. M., Udalski, A., Gould, A., et al. 2010, *ApJ*, 721, L28

- Navarro, J. F., Frenk, C. S., & White, S. D. M. 1996, *ApJ*, 462, 563
- Neeser, M., Coccato, L., Jung, Y., et al. 2016, *Reflex KMOS Tutorial Issue 1.6*
- Ness, M. & Freeman, K. 2016, *PASA*, 33, e022
- Neumayer, N. & Walcher, C. J. 2012, *Advances in Astronomy*, 2012
- Neumayer, N., Walcher, C. J., Andersen, D., et al. 2011, *MNRAS*, 413, 1875
- Nishiyama, S., Nagata, T., Kusakabe, N., et al. 2006, *ApJ*, 638, 839
- Nishiyama, S. & Schödel, R. 2013, *A&A*, 549, A57
- Nishiyama, S., Schödel, R., Yoshikawa, T., et al. 2016, *A&A*, 588, A49
- Nishiyama, S., Tamura, M., Hatano, H., et al. 2009, *ApJ*, 696, 1407
- Oh, S., Kim, S. S., & Figer, D. F. 2009, *Journal of Korean Astronomical Society*, 42, 17
- Oh, S.-H., de Blok, W. J. G., Walter, F., et al. 2008, *AJ*, 136, 2761
- Oka, T., Nagai, M., Kamegai, K., et al. 2011, *ApJ*, 732, 120
- Oke, J. B. & Greenstein, J. L. 1954, *ApJ*, 120, 384
- Oort, J. H. 1977, *ARA&A*, 15, 295
- Ott, T., Eckart, A., & Genzel, R. 1999, *ApJ*, 523, 248
- Paumard, T., Genzel, R., Martins, F., et al. 2006, *ApJ*, 643, 1011
- Paumard, T., Maillard, J.-P., & Morris, M. 2004, *A&A*, 426, 81
- Paumard, T., Maillard, J. P., Morris, M., et al. 2001, *A&A*, 366, 466
- Paumard, T., Maillard, J.-P., & Stolovy, S. 2003, *Astronomische Nachrichten Supplement*, 324, 303
- Perets, H. B. & Gualandris, A. 2010, *ApJ*, 719, 220
- Perets, H. B. & Mastrobuono-Battisti, A. 2014, *ApJ*, 784, L44
- Perger, M., Moulataka, J., Eckart, A., et al. 2008, *A&A*, 478, 127
- Pflamm-Altenburg, J. & Kroupa, P. 2009, *MNRAS*, 397, 488
- Pfuhl, O., Fritz, T. K., Zilka, M., et al. 2011, *ApJ*, 741, 108
- Phillips, A. C., Illingworth, G. D., MacKenty, J. W., et al. 1996, *AJ*, 111, 1566
- Pott, J.-U., Eckart, A., Glindemann, A., et al. 2005, *The Messenger*, 119, 43
- Pryor, C. & Meylan, G. 1993, in *Structure and Dynamics of Globular Clusters*, Vol. 50, 357
- Rafelski, M., Ghez, A. M., Hornstein, S. D., et al. 2007, *ApJ*, 659, 1241
- Ramírez, S. V., Sellgren, K., Carr, J. S., et al. 2000, *ApJ*, 537, 205
- Rattenbury, N. J., Mao, S., Sumi, T., et al. 2007, *MNRAS*, 378, 1064
- Rayner, J. T., Cushing, M. C., & Vacca, W. D. 2009, *ApJS*, 185, 289
- Reid, M. J. & Brunthaler, A. 2004, *ApJ*, 616, 872
- Reid, M. J., Menten, K. M., Genzel, R., et al. 2003, *ApJ*, 587, 208
- Reid, M. J., Menten, K. M., Trippe, S., et al. 2007, *ApJ*, 659, 378
- Reijns, R. A., Seitzer, P., Arnold, R., et al. 2006, *A&A*, 445, 503
- Renzini, A., Greggio, L., Ritossa, C., et al. 1992, *ApJ*, 400, 280
- Requena-Torres, M. A., Güsten, R., Weiß, A., et al. 2012, *A&A*, 542, L21
- Rieke, G. H. & Rieke, M. J. 1988, *ApJ*, 330, L33
- Rix, H.-W., de Zeeuw, P. T., Cretton, N., et al. 1997, *ApJ*, 488, 702
- Rosenfield, P., Marigo, P., Girardi, L., et al. 2016, *ApJ*, 822, 73
- Rossa, J., van der Marel, R. P., Böker, T., et al. 2006, *AJ*, 132, 1074

- Ryde, N. & Schultheis, M. 2015, *A&A*, 573, A14
- Ryde, N., Schultheis, M., Grieco, V., et al. 2016, *AJ*, 151, 1
- Sabha, N., Witzel, G., Eckart, A., et al. 2010, *A&A*, 512, A2
- Saito, R. K., Hempel, M., Minniti, D., et al. 2012, *A&A*, 537, A107
- Sanchez-Bermudez, J., Schödel, R., Alberdi, A., et al. 2014, *A&A*, 567, A21
- Sander, A., Hamann, W.-R., & Todt, H. 2012, *A&A*, 540, A144
- Schinnerer, E., Böker, T., & Meier, D. S. 2003, *ApJ*, 591, L115
- Schinnerer, E., Böker, T., Meier, D. S., et al. 2008, *ApJ*, 684, L21
- Schödel, R., Eckart, A., Alexander, T., et al. 2007, *A&A*, 469, 125
- Schödel, R., Feldmeier, A., Kunneriath, D., et al. 2014a, *A&A*, 566, A47
- Schödel, R., Feldmeier, A., Neumayer, N., et al. 2014b, *Classical and Quantum Gravity*, 31, 244007
- Schödel, R., Merritt, D., & Eckart, A. 2009, *A&A*, 502, 91
- Schödel, R., Najarro, F., Muzic, K., et al. 2010, *A&A*, 511, A18
- Schödel, R., Ott, T., Genzel, R., et al. 2003, *ApJ*, 596, 1015
- Schödel, R., Yelda, S., Ghez, A., et al. 2013, *MNRAS*, 429, 1367
- Schultheis, M., Cunha, K., Zasowski, G., et al. 2015, *A&A*, 584, A45
- Schultheis, M., Ryde, N., & Nandakumar, G. 2016, *A&A*, 590, A6
- Schwarzschild, M. 1979, *ApJ*, 232, 236
- Schwarzschild, M. 1982, *ApJ*, 263, 599
- Scott, N. & Graham, A. W. 2013, *ApJ*, 763, 76
- Scoville, N. Z., Stolovy, S. R., Rieke, M., et al. 2003, *ApJ*, 594, 294
- Sellgren, K., McGinn, M. T., Becklin, E. E., et al. 1990, *ApJ*, 359, 112
- Sellwood, J. A. & Wilkinson, A. 1993, *Reports on Progress in Physics*, 56, 173
- Seth, A., Agüeros, M., Lee, D., et al. 2008a, *ApJ*, 678, 116
- Seth, A. C., Blum, R. D., Bastian, N., et al. 2008b, *ApJ*, 687, 997
- Seth, A. C., Cappellari, M., Neumayer, N., et al. 2010, *ApJ*, 714, 713
- Seth, A. C., Dalcanton, J. J., Hodge, P. W., et al. 2006, *AJ*, 132, 2539
- Sharples, R., Bender, R., Agudo Berbel, A., et al. 2013, *The Messenger*, 151, 21
- Siegel, M. H., Dotter, A., Majewski, S. R., et al. 2007, *ApJ*, 667, L57
- Silva, D. R., Kuntschner, H., & Lyubenova, M. 2008, *ApJ*, 674, 194
- Siopis, C., Gebhardt, K., Lauer, T. R., et al. 2009, *ApJ*, 693, 946
- Skokos, C., Patsis, P. A., & Athanassoula, E. 2002, *MNRAS*, 333, 847
- Skrutskie, M. F., Cutri, R. M., Stiening, R., et al. 2006, *AJ*, 131, 1163
- Smith, I. L. & Wardle, M. 2014, *MNRAS*, 437, 3159
- Smith, V. V. 1984, *A&A*, 132, 326
- Soubiran, C., Le Campion, J.-F., Cayrel de Strobel, G., et al. 2010, *A&A*, 515, A111
- Stead, J. J. & Hoare, M. G. 2009, *MNRAS*, 400, 731
- Stolovy, S., Ramirez, S., Arendt, R. G., et al. 2006, *Journal of Physics Conference Series*, 54, 176
- Støstad, M., Do, T., Murray, N., et al. 2015, *ApJ*, 808, 106
- Straižys, V. & Lazauskaitė, R. 2009, *Baltic Astronomy*, 18, 19

- Tang, J., Bressan, A., Rosenfield, P., et al. 2014, MNRAS, 445, 4287
- Tanner, A., Figer, D. F., Najarro, F., et al. 2006, ApJ, 641, 891
- Tanner, A., Ghez, A. M., Morris, M. R., et al. 2005, ApJ, 624, 742
- Tremaine, S. D., Ostriker, J. P., & Spitzer, Jr., L. 1975, ApJ, 196, 407
- Trippe, S., Gillessen, S., Gerhard, O. E., et al. 2008, A&A, 492, 419
- Turner, M. L., Côté, P., Ferrarese, L., et al. 2012, ApJS, 203, 5
- Valluri, M., Ferrarese, L., Merritt, D., et al. 2005, ApJ, 628, 137
- Valluri, M., Merritt, D., & Emsellem, E. 2004, ApJ, 602, 66
- van de Ven, G., de Zeeuw, P. T., & van den Bosch, R. C. E. 2008, MNRAS, 385, 614
- van de Ven, G., van den Bosch, R. C. E., Verolme, E. K., et al. 2006, A&A, 445, 513
- van den Bosch, R., de Zeeuw, T., Gebhardt, K., et al. 2006, ApJ, 641, 852
- van den Bosch, R. C. E. & de Zeeuw, P. T. 2010, MNRAS, 401, 1770
- van den Bosch, R. C. E., Greene, J. E., Braatz, J. A., et al. 2016, ApJ, 819, 11
- van den Bosch, R. C. E. & van de Ven, G. 2009, MNRAS, 398, 1117
- van den Bosch, R. C. E., van de Ven, G., Verolme, E. K., et al. 2008, MNRAS, 385, 647
- van der Marel, R. P., Cretton, N., de Zeeuw, P. T., et al. 1998, ApJ, 493, 613
- van Dokkum, P. G. 2001, PASP, 113, 1420
- Vasiliev, E. & Zelnikov, M. 2008, Phys. Rev. D, 78, 083506
- Viehmann, T., Eckart, A., Schödel, R., et al. 2006, ApJ, 642, 861
- Volonteri, M. 2010, A&A Rev., 18, 279
- Walcher, C. J., Böker, T., Charlot, S., et al. 2006, ApJ, 649, 692
- Walcher, C. J., van der Marel, R. P., McLaughlin, D., et al. 2005, ApJ, 618, 237
- Wallace, L. & Hinkle, K. 1996, ApJS, 107, 312
- Wallace, L. & Hinkle, K. 1997, ApJS, 111, 445
- Wang, Q. D., Dong, H., Cotera, A., et al. 2010, MNRAS, 402, 895
- Wardle, M. & Yusef-Zadeh, F. 2008, ApJ, 683, L37
- Watkins, L. L., van de Ven, G., den Brok, M., et al. 2013, MNRAS, 436, 2598
- Wegg, C. & Gerhard, O. 2013, MNRAS, 435, 1874
- Wehner, E. H. & Harris, W. E. 2006, ApJ, 644, L17
- Wenger, M., Ochsenein, F., Egret, D., et al. 2000, A&AS, 143, 9
- Winge, C., Riffel, R. A., & Storchi-Bergmann, T. 2009, ApJS, 185, 186
- Yelda, S., Ghez, A. M., Lu, J. R., et al. 2014, ApJ, 783, 131
- Yusef-Zadeh, F., Braatz, J., Wardle, M., et al. 2008, ApJ, 683, L147
- Yusef-Zadeh, F., Stolovy, S. R., Burton, M., et al. 2001, ApJ, 560, 749
- Zhao, H. 1996, MNRAS, 283, 149
- Zhao, J.-H., Morris, M. R., Goss, W. M., et al. 2009, ApJ, 699, 186
- Zhu, Q., Kudritzki, R. P., Figer, D. F., et al. 2008, ApJ, 681, 1254
- Zoccali, M., Hill, V., Lecureur, A., et al. 2008, A&A, 486, 177
- Zoccali, M., Renzini, A., Ortolani, S., et al. 2003, A&A, 399, 931

Nederlandse samenvatting

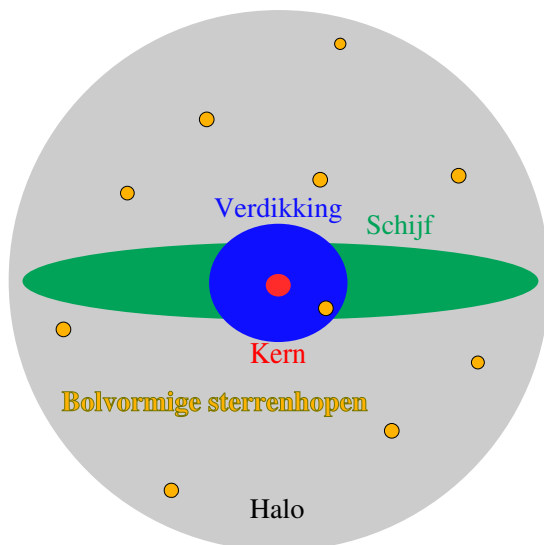
Sterrenstelsels

Op een heldere, maanloze nacht kan men aan de hemel een vage lichtende band zien, zelfs zonder telescoop. Deze band bestaat uit miljarden sterren en heet de Melkweg. Figuur R1 toont een afbeelding van de Melkweg. Daarnaast zijn er overal nog tal van kleinere nevels te zien (zie bijv. rechtsonder in figuur R1). In de jaren twintig van de vorige eeuw bewees Edwin Hubble dat veel van deze nevels sterrenstelsels zijn. Ze liggen op grote afstanden buiten de Melkweg. De Melkweg is slechts één van de miljarden sterrenstelsels in het heelal.

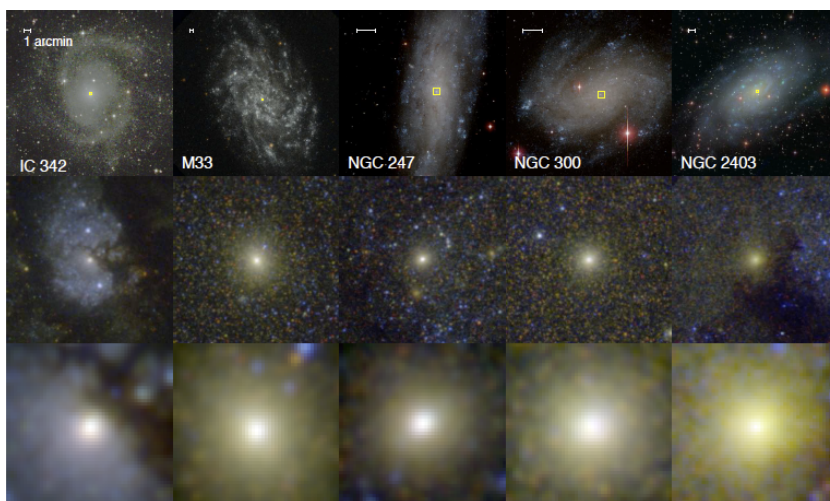


Figuur R1: De Melkweg (afbeelding van Serge Brunier).

Sterrenstelsels bestaan uit sterren, planeten, gas, stof en een onzichtbare component, die donkere materie wordt genoemd. Donkere materie vertoont geen wisselwerking met licht, dus het kan niet zonder meer gezien worden met een telescoop. Deze donkere materie in de galactische halo is echter nodig om de bewegingen van sterren en gas in de sterrenstelsels te verklaren. Sterrenstelsels worden omringd door bolvormige sterrenhopen of bolhopen. Deze sterrenhopen zijn ronde, dichtbevolkte voorwerpen in de galactische halo, vooral bestaande uit oude, metaalarme sterren. Veel sterrenstelsels zijn zogeheten spiraalstelsels, zoals de Melkweg. Er bestaan ook stelsels zonder bijzondere eigenschappen; zij worden elliptische sterrenstelsels genoemd. Figuur R2 toont een schematisch zijaanzicht van de Melkweg. Het gas en stof bevinden zich hoofdzakelijk in de galactische schijf en kern. De meeste sterren bevinden zich ook in de schijf en de kern, evenals in de verdikking.



Figuur R2: Schematisch zijaanzicht van de Melkweg. De onderdelen zijn niet op schaal getekend.



Figuur R3: Afbeeldingen van spiraalstelsels met een centrale sterrenhoop, overgenomen van Carson et al. (2015). De bovenste rij toont de volledige sterrenstelsels, de middelste rij zoomt in op de binnenste delen (ca. 500×500 vierkante lichtjaar) en de onderste rij toont de centrale sterrenhopen in het midden van elk stelsel (ca. 80×80 vierkante lichtjaar). De schaallijnen bovenin geven $1'$ weer (ca. 2400 lichtjaar).

Centrale sterrenhopen

In de jaren negentig hebben sterrenkundigen de binnenste delen van sterrenstelsels in kaart gebracht met de ruimtetelescoop *Hubble* en met telescopen op aarde met spiegels van 8 tot 10 meter in doorsnee. Veel stelsels zijn in het centrum zeer helder vanwege een dichtbevolkte sterrenhoop, ook wel een centrale sterrenhoop genoemd. Enkele afbeeldingen van sterrenstelsels met een centrale sterrenhoop zijn te zien in figuur R3. Centrale sterrenhopen bevatten vele miljoenen sterren met een gezamenlijke massa van ongeveer één miljoen tot honderd miljoen maal de massa van de zon. Zo'n 50 tot 75% van alle sterrenstelsels, waaronder de Melkweg, hebben een centrale sterrenhoop. Dit soort sterrenhopen komen vooral voor in stelsels van lage tot gemiddelde massa. Zware, heldere stelsels bevatten geen centrale sterrenhoop. Sterrenkundigen willen onderzoeken hoe centrale sterrenhopen ontstaan en waarom ze niet in alle sterrenstelsels voorkomen.

Hoe zwaarder of helderder een sterrenstelsel is, des te zwaarder is ook de centrale sterrenhoop in dat stelsel. Zulke correlaties zijn interessant, want ze geven mogelijk inzicht in de gezamenlijke evolutie van het sterrenstelsel en zijn kern. De sterrenhopen hebben stralen van 3 tot 30 lichtjaar, terwijl de bijbehorende stelsels ruwweg 1000 tot 100.000 lichtjaar groot zijn. De correlaties kunnen iets zeggen over de natuurlijke processen die de vorm bepalen van de binnenste delen van sterrenstelsels. Sterrenkundigen hebben twee verschillende theorieën voorgesteld voor het ontstaan van centrale sterrenhopen: (a) gas uit het sterrenstelsel hoopt zich in het centrum op en sterren ontstaan ter plaatse in de kern van het stelsel; of (b) sterren ontstaan in dichtbevolkte hopen elders in het stelsel, bijv. in bolvormige sterrenhopen. Deze bolhopen bewegen vervolgens naar binnen toe en worden de centrale sterrenhoop. Het is ook mogelijk dat beide processen bijdragen aan de vorming van centrale sterrenhopen.

De sterren in een centrale sterrenhoop zijn niet allemaal even oud. De leeftijden variëren van slechts een paar miljoen jaar tot tien miljard jaar. De hopen bevatten dus meerdere "sterpopulaties". Sterpopulaties kunnen verschillen qua leeftijd, maar ook qua chemische samenstelling, want de sterren zijn niet op hetzelfde moment en uit hetzelfde materiaal ontstaan. De sterpopulaties kunnen een karakteristieke ruimtelijke verdeling hebben of op een bepaalde manier bewegen. Onderzoek naar de eigenschappen van verschillende populaties is zinvol om het ontstaan en de ontwikkeling van centrale sterrenhopen te ontrafelen.

Superzware zwarte gaten

Het is moeilijk om je een zwart gat voor te stellen: een voorwerp zó zwaar dat niets eruit kan ontsnappen. Zwarte gaten zijn onzichtbaar; alle materie of straling die erin terecht komt, kan nooit meer weg. Een zwart gat beïnvloedt de omringende sterren en gas via de zwaartekracht. Uit de bewegingen van de sterren in omloopbanen rond een zwart gat kunnen we de aanwezigheid van dat zwarte gat afleiden.

Superzware zwarte gaten zijn tienduizend tot tien miljard maal zo zwaar als de zon. Zij bevinden zich in het midden van de meeste sterrenstelsels, met name in zware stelsels. Er is nog altijd onduidelijkheid over hoe superzware zwarte gaten ontstaan en hoe ze groeien.

Eenzijds zouden zwarte gaten het eindproduct kunnen zijn van de levenscyclus van sterren, anderzijds zouden ze ook direct kunnen ontstaan uit ineenslopende gaswolken in het jonge heelal. Deze kleine zwarte gaten zouden dan snel groter moeten zijn geworden, anders is er geen verklaring voor de aanwezigheid van superzware zwarte gaten toen het heelal nog maar een miljard jaar oud was.

De Melkweg bevat ook een superzwaar zwart gat, gelegen binnenin de centrale sterrenhoop. De sterren aldaar worden al meer dan tien jaar nauwlettend in de gaten gehouden. Het is inmiddels duidelijk dat ze elliptische banen beschrijven rond een onzichtbaar voorwerp. Op basis van deze omloopbanen is de massa van het zwarte gat bepaald op vier miljoen zonsmassa's.

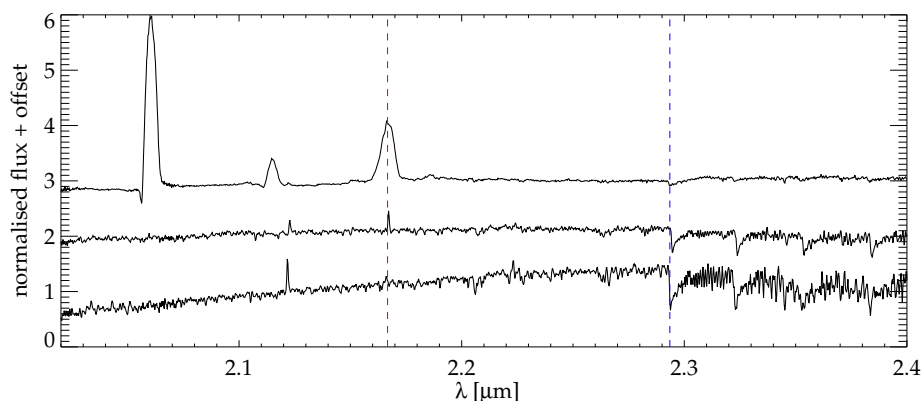
Het direct meten van de omloopbanen van de sterren rond een zwart gat is vooral nog alleen mogelijk in de Melkweg. Er bestaan een aantal alternatieve methodes om superzware zwarte gaten in andere sterrenstelsels te vinden. Eén zo'n methode is het gebruik van dynamische modellen om de totale massaverdeling van een bepaalde groep sterren te bepalen. Dit soort modellen bootsen de waarnemingen en de gemeten bewegingen van de zichtbare sterren na. Aangezien de individuele omloopbanen beïnvloed worden door de zwaartekracht van het gehele stelsel, geven de dynamische modellen als resultaat de volledige massaverdeling, inclusief de massa van onzichtbare onderdelen zoals zwarte gaten en donkere materie.

Spectroscopie

Een spectrograaf splitst licht op in een spectrum, oftewel een grafiek van de lichtsterkte als functie van de golflengte. Spectra bevatten een schat aan informatie over de lichtbron. Er kunnen lijnen zichtbaar zijn in een spectrum, ofwel helder tegen een donkere achtergrond (emissie), ofwel donker tegen een heldere achtergrond (absorptie). Deze lijnen zijn het gevolg van wisselwerkingen tussen elektromagnetische straling en materie. De golflengte, sterkte en breedte van de lijnen zeggen iets over de eigenschappen van de lichtbron. Figuur R4 toont de spectra van drie sterren. De rode en blauwe streepjeslijnen geven respectievelijk een emissie- en een absorptielijn aan.

Elke lijn in een spectrum wordt veroorzaakt door een bepaald soort materie, zoals een atoom of een molecuul. De sterkte of intensiteit van de lijn hangt af van het aantal atomen of moleculen in de ster. Een ijzerlijn wordt bijvoorbeeld sterker als de ster meer ijzer bevat. De lijnsterkte hangt ook af van de oppervlaktetemperatuur van de ster. Sommige lijnen zijn alleen zichtbaar boven of onder een bepaalde temperatuur. Door de sterktes van alle lijnen in een spectrum te meten, kunnen we dus het metaalgehalte en de effectieve temperatuur van de ster bepalen. De sterkte van de absorptielijnen in figuur R4 verschilt per ster. Bovendien bevat het bovenste spectrum enkele emissielijnen die niet in de andere spectra zichtbaar zijn, omdat die van koudere sterren komen.

Als de lichtbron zich ten opzichte van de waarnemer beweegt, verschuiven de spectraallijnen naar een andere golflengte. Dit heet het dopplereffect. Door de golflengte van een bepaalde lijn te meten, kunnen we dus de snelheid uitrekenen waarmee de ster naar ons toe



Figuur R4: Spectra van drie verschillende sterren zoals gemeten met de instrumenten ISAAC en KMOS op de *Very Large Telescope* in Chili. De lichtsterkte (*flux*) is uitgezet tegen de golflengte (λ) in het nabije infrarood. De rode en blauwe streepjeslijnen geven aan waar zich respectievelijk een emissie- en een absorptielijn bevinden. Het bovenste spectrum komt van een hetere ster dan de onderste twee spectra.

of van ons af beweegt. De spectra in figuur R4 zijn onderling iets verschoven in golflengte, omdat ze afkomstig zijn van sterren met verschillende snelheden.

In ver van ons verwijderde sterrenstelsels zijn de sterren te zwak om individuele spectra te kunnen meten. We kunnen wel het gezamenlijke spectrum van een groep sterren waarnemen. Zo'n spectrum bevat het licht van vele sterren naar rato van hun onderlinge helderheid. De gemeten snelheid, effectieve temperatuur en metaalgehalte zijn dus een gewogen gemiddelde van de sterren die bijdragen aan het spectrum. Aangezien echter niet alle sterren dezelfde snelheid hebben, zijn de spectraallijnen van de hele groep breder dan die van individuele sterren. Deze lijnverbreding is beperkt als alle sterren min of meer even snel en in dezelfde richting bewegen, maar het effect is groter als de mate van willekeurige bewegingen (oftewel de snelheidsspreiding) van de sterren groot is. De snelheidsspreiding hangt af van de totale massaverdeling (lichte en donkere materie) en is dus van groot belang voor de eerder genoemde dynamische modellen.

Dit proefschrift

In dit proefschrift bestuderen we de ontstaansgeschiedenis van de centrale sterrenhoop in de Melkweg. De afmetingen van de sterrenhoop zijn vrij typisch voor een centrale sterrenhoop, met een straal van ongeveer 14 lichtjaar. De centrale sterrenhoop van de Melkweg bevindt zich op zo'n 26.000 lichtjaar van de aarde. Daarmee is hij de dichtstbijzijnde centrale sterrenhoop in het heelal en kan hij in meer detail bestudeerd worden dan de centrale sterrenhopen



Figuur R5: Afbeelding van de binnenste 45×30 vierkante lichtjaar van de Melkweg, waar de centrale sterrenhoop zich bevindt (uit het VVV-project, Saito et al. 2012).

in andere sterrenstelsels. We tonen een afbeelding van onze centrale sterrenhoop in figuur R5.

In **hoofdstuk 2** bekijken we de bewegingen en massaverdeling van de centrale sterrenhoop van de Melkweg. We gebruiken de spectrograaf ISAAC (werkend in het nabije infrarood, met een lange waarneemsleuf) op de *Very Large Telescope* (VLT) in Chili om een groot gebied van 640 vierkante lichtjaar van de centrale sterrenhoop in kaart te brengen. We nemen ook zes kleinere gebieden waar tot een maximale straal van 62 lichtjaar langs het galactische vlak. De data omvatten het volledige zwaartekrachtsbereik van ongeveer negen lichtjaar (straal) van het superzware zwarte gat. We meten de snelheid langs de gezichtslijn en de intensiteit van de absorptielijn van CO in 1375 spectra van individuele sterren. Met behulp van spectra van het geïntegreerde licht van de rode reuzensterren maken we kaarten van de snelheden en snelheidsspreidingen. De snelheidskaart toont de draaiing van de centrale sterrenhoop en andere, complexere patronen. In het bijzonder ontdekken we dat de draaias 9° is gekanteld ten opzichte van de fotometrische korte as, en we vinden aanwijzingen voor een draaiende substructuur die op een straal van ongeveer 2,6 lichtjaar loodrecht op het galactisch vlak staat. Deze structuren kunnen het gevolg zijn van specifieke momenten van accretie in het verleden. Naast de bewegingskaarten gebruiken we ook fotometrie van de ruimtetelescoop *Spitzer* en het NACO-instrument op de VLT om anisotrope, axisymmetrische dynamische Jeans-modellen op te zetten. Hieruit leiden we de massaverdeling van de centrale sterrenhoop af en berekenen we de massa van het zwarte gat. Deze massa is de helft van wat er is berekend op basis van de waarnemingen van de omloopbanen van individuele sterren vlakbij het zwarte gat.

In **hoofdstuk 3** bestuderen we de massaverdeling en omloopbanen van de centrale sterrenhoop in de Melkweg in meer detail. We construeren triaxiale dynamische Schwarzschild-modellen op basis van de omloopbanen en passen deze toe op de spectroscopische kaarten en fotometrische data van *Spitzer* uit hoofdstuk 2. We gebruiken de modellen om de triaxiale vorm van de sterrenhoop te bepalen, alsmede de dynamische verhouding tussen massa en licht (Y) en de massa van het superzwarte zwarte gat (M_{\bullet}). Deze massa is nu wel in overeenstemming met de massa die bepaald is uit de individuele omloopbanen vlakbij het zwarte gat. Het model dat het beste overeenkomt met de data reproduceert de complexe substructuren die we zien in de snelheidskaarten.

In **hoofdstuk 4** richten we ons op de jonge sterpopulatie in de binnenste 43 vierkante lichtjaar van de centrale sterrenhoop in de Melkweg. We hebben spectra in het nabije infrarood (genomen met KMOS op de VLT) van 114 hete, jonge sterren die slechts 3–8 Myr geleden zijn ontstaan. We classificeren deze sterren in een aantal subgroepen. De jonge sterren bevinden zich vooral in het binnenste van het bestudeerde gebied, in tegenstelling tot de koudere sterren, die verspreid over het hele gebied voorkomen. Deze sterke concentratie van hete, jonge sterren geeft aan dat ze ter plekke in het centrum van de sterrenhoop zijn gevormd. In het geval van radiële verplaatsing hadden we namelijk meer jonge sterren op grotere afstanden moeten zien.

In **hoofdstuk 5** analyseren we de verdeling van metaalgehalten in de populatie van sterren met een laat spectraaltipe in de centrale sterrenhoop van de Melkweg. We gebruiken de KMOS-spectra uit hoofdstuk 4. De sterren met een laat spectraaltipe hebben sterkere lijnen van Na I dan vergelijkbare sterren in catalogi. We vergelijken de volledige spectra van meer dan 700 sterren met een collectie kunstmatige spectra. Zodoende bepalen we voor elke ster de effectieve temperatuur, het metaalgehalte, de zwaartekracht aan het oppervlak en de radiële snelheid. De meeste sterren zijn koude rode reuzen met temperaturen van 3000–5000 K. We zien een vlakke verdeling van metaalgehalten, variërend van $[M/H] < -1$ dex (tien keer lager dan de zon) tot $\gtrsim +0.3$ dex (twee keer hoger dan de zon). Slechts zo'n vijf procent van de sterren gelden als metaalarm ($[M/H] \leq -0.5$ dex, drie keer lager dan de zon). Sterren met $[M/H] \leq 0.0$ dex (gelijk aan de zon) hebben wellicht hun oorsprong in invallende bolhopen. De meeste sterren (ong. 75%) zijn meer metaalrijk dan de zon; voor deze sterren kunnen we het scenario van een invallende bolhoop uitsluiten.

Conclusies en vooruitblik

We hebben aanwijzingen gevonden voor twee verschillende ontstaansmethoden voor de centrale sterrenhoop van de Melkweg. Snelheidskaarten van de populatie van oude rode reuzen vertonen complexe structuren. Dit betekent dat de centrale sterrenhoop een aantal bolhopen heeft opgeslokt. De ontdekking van metaalarme sterren is een andere aanwijzing voor het scenario van invallende bolhopen, aangezien bolhopen uit zulke sterren bestaan. Metaalarme sterren zijn echter ook gezien in de galactische schijf en de verdikking, en kunnen daar zijn

gevormd. Gezien het kleine percentage aan metaalarme sterren kan het invallen van bolhopen niet de belangrijkste manier zijn waarop de centrale sterrenhoop van de Melkweg is ontstaan.

De meeste sterren hebben een metaalgehalte gelijk aan of hoger dan die van de zon, wat niet rijmt met een oorsprong in bolhopen. Deze sterren moeten zijn ontstaan uit verrijkt materiaal, ofwel ter plaatse in de kern van de Melkweg, ofwel elders gevolgd door migratie richting de kern. De jonge sterren zijn beslist gevormd in het binnenste lichtjaar van de Melkweg. Ze zijn sterk centraal geconcentreerd, in tegenstelling tot wat men kan verwachten in het geval van migratie.

Vergeleken met eerdere onderzoeken hebben we in een significant groter gebied de sterpopulaties bestudeerd. Niettemin omvatten onze data slechts een klein deel van de centrale sterrenhoop. We zouden meer kunnen leren over het ontstaan van de centrale sterrenhoop door de sterpopulaties in een groter gebied te analyseren en te zoeken naar gradiënten in leeftijd en metaalgehalte. We hebben aangetoond dat het binnenste deel van de centrale sterrenhoop van de Melkweg slechts enkele metaalarme sterren bevat. Mogelijk bevinden zich in de buitendelen meer van zulke sterren, in het bijzonder als deze afkomstig waren uit een invallende bolhoop. Er zouden op grotere afstanden ook nog losse jonge sterren kunnen voorkomen, die tot nu toe niet zijn ontdekt. Deze jonge sterren zouden bewijs vormen voor recente momenten van accretie.

Een verloop in de sterpopulaties betekent ook dat de verhouding tussen massa en licht niet constant is, hoewel we dat wel hebben aangenomen. Dit zou gevolgen hebben voor de massaverdeling die we voor het sterrencluster hebben berekend. Waarnemingen met hogere resolutie zijn nodig om onze metingen van het metaalgehalte te bevestigen en om de elementaire abundanties van koude sterren te bepalen. Spectra met hogere resolutie zijn ook nodig om het spectraaltypen en de leeftijd van de ontdekte jonge sterren vast te stellen. In dit proefschrift hebben we aangenomen dat ze even oud zijn als al bekende jonge sterren, maar dat moet gecontroleerd worden.

Er is ook ruimte voor verbetering in de analyse van de bewegingen in de centrale sterrenhoop. Onze bewegingskaart beslaat niet de hele sterrenhoop. De rotatiekromme van het binnenste deel van de Melkweg en de galactische potentiaal aldaar zijn nog steeds grotendeels onbekend. Om dit soort tekortkomingen op te lossen hebben we meer waarnemingen verricht met KMOS (VLT) en FLAMINGOS-2 (*Gemini South Telescope*). Deze twee datasets kunnen worden samengevoegd en gebruikt voor dynamische modellen. De modellen kunnen worden uitgebreid door een gasschijf als extra onderdeel toe te voegen en door de eigenbewegingen van de sterren in te voeren. Het gebruik van modellen die de bewegingsdata niet hoeven te middelen zou een verdere verbetering betekenen.

De toekomst biedt vele mogelijkheden voor waarnemingen van de kernen van sterrenstelsels. Nieuwe telescopen worden momenteel gepland en gebouwd. In 2018 wordt bijvoorbeeld de *James Webb Space Telescope* (JWST) gelanceerd. Dankzij zijn hoge gevoeligheid en ruimtelijke resolutie zullen we de gelegenheid hebben om gradiënten te bestuderen in de sterpopulaties in centrale sterrenhopen in andere sterrenstelsels dan de Melkweg. Daarnaast wordt er een nieuwe generatie telescopen op aarde gebouwd. Deze extreem grote telescopen hebben spiegels met diameters van meer dan twintig meter: de *Giant Magellan Telescope*

(GMT, $d = 24.5$ m), de *Thirty Meter Telescope* (TMT, $d = 30$ m) en de *European Extremely Large Telescope* (E-ELT, $d = 39.3$ m). De instrumenten met hoge spectrale en ruimtelijke resolutie zullen van pas komen in de zoektocht naar superzware zwarte gaten in de centrale sterrenhopen van andere sterrenstelsels. In de centrale sterrenhoop van de Melkweg zullen deze gevoelige telescopen zwakkere sterren kunnen waarnemen dan momenteel mogelijk is, waaronder dwergsterren van spectraaltype A of F. Nieuwe telescopen en modellen zullen bijdragen aan een beter begrip van het ontstaan en de ontwikkeling van sterrenstelsels en in het bijzonder van hun kernen. We verwachten een heldere toekomst voor dit onderzoeksgebied.

Summary

Galaxies

On a clear, moonless night one can see a diffuse glowing band across the sky, even without a telescope. This band consists of billions of stars, and is called the Milky Way. Figure S1 shows an image of the Milky Way. In addition, there are many smaller diffuse nebulae distributed all over the sky (see also bottom right of Figure S1). In the 1920s, Edwin Hubble proved that many of these nebulae are galaxies. They are located at great distances, outside of the Milky Way. The Milky Way is only one galaxy among billion others.



Figure S1: The Milky Way galaxy (image by Serge Brunier)

Galaxies consist of stars, planets, gas, dust, and invisible mass, called dark matter. Dark matter does not interact with light, so it cannot be detected directly with a telescope. However, dark matter in the galaxy halo is necessary to explain the motions of stars and gas in galaxies. Systems of globular clusters surround the galaxies. Globular clusters are dense, spherical star clusters in the galaxy halo, which consist of mostly old, metal-poor stars. Many galaxies are so-called spirals, like the Milky Way, but there exist also featureless galaxies, called ellipticals. Figure S2 provides a schematic side view of the Milky Way. The gas and dust are mostly located in the Galactic disc and in the Galactic nucleus. Most stars are also in the disc and in the nucleus, as well as in the bulge.

Nuclear star clusters

In the 1990s, astronomers used the *Hubble Space Telescope* and 8–10 m ground-based telescopes to image the central regions of galaxies. Many galaxies are very bright at the centre,

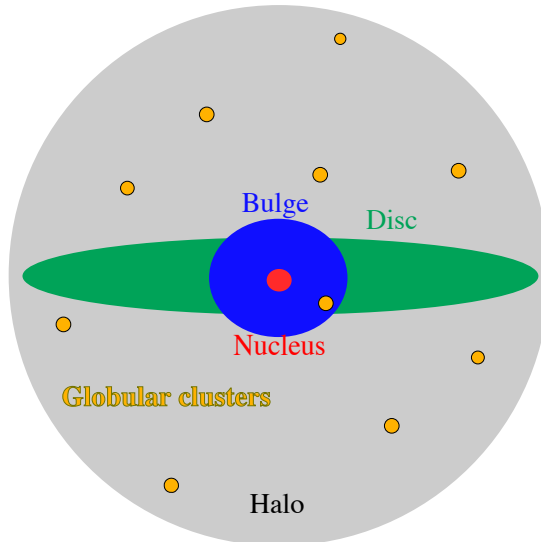


Figure S2: Schematic side view of the Milky Way galaxy. The different components are not to scale.

as there is a dense cluster of stars, called a nuclear star cluster. We show some images of galaxies with nuclear star cluster in Figure S3. Nuclear star clusters contain many millions of stars, and the total masses of the clusters range from about one million to hundred million times the mass of the sun. About 50 to 75 per cent of galaxies, including the Milky Way, contain a nuclear star cluster. The clusters are common in galaxies with low- to intermediate mass. Massive, bright galaxies do not contain nuclear star clusters. Astronomers want to find out how nuclear star clusters formed, and why they are located in some galaxies, but not in all of them.

Nuclear star clusters are more massive when the host galaxy is more massive or more luminous. Such correlations are interesting, since they can possibly tell us something about the common evolution of the galaxy and its nucleus. The clusters have radii of 3 to 30 light-years, whereas their host galaxies have radii ranging from roughly 1 000 to several 100,000 light-years. The correlations can help to understand the physical processes that shape the centres of galaxies. Astronomers suggested different formation mechanisms for nuclear star clusters, which can be divided in two main categories: (a) Gas from the galaxy accumulates in the centre, and stars form directly in the nucleus of the galaxy; and (b) stars form in dense star clusters elsewhere in the galaxy, e.g. in globular clusters. The star clusters migrate towards the centre of the galaxy and become the nuclear star cluster. It is also possible that both processes contribute to the formation of a nuclear star cluster.

The stars in a nuclear star cluster have different ages. Some of the stars are young, only a few million years old, other stars are up to 10 billion years old. This means that the clusters contain multiple “stellar populations”. Stellar populations may be distinct in age, but they can also have a different chemical composition, as the stars did not form at the same time and

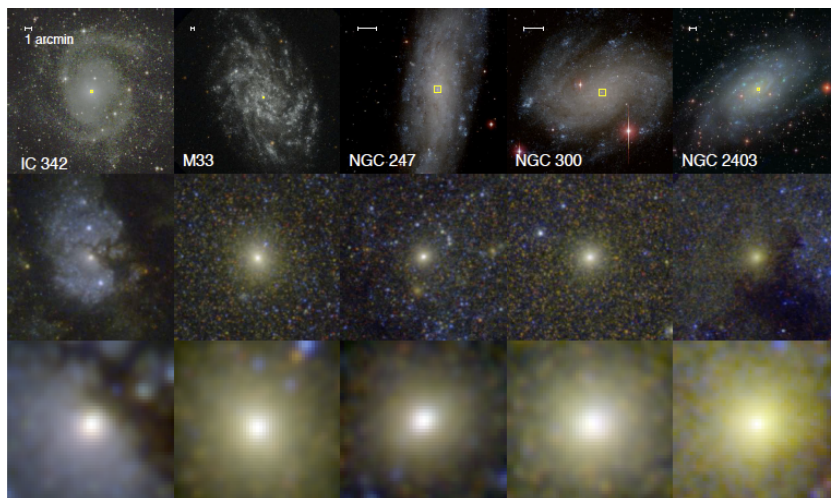


Figure S3: Images of different spiral galaxies with nuclear star cluster. The top panel shows the entire host galaxy, the middle panel is a zoom to the inner region of the galaxy (approximately $500 \text{ light-years} \times 500 \text{ light-years}$), and the bottom panel shows the central nuclear star cluster (approximately $80 \text{ light-years} \times 80 \text{ light-years}$). The scale bars on the top row denote 1 arcmin (approximately $2\,400 \text{ light-years}$, image from Carson et al. 2015).

from the same material. The stellar populations may have a characteristic spatial distribution, or move in a characteristic way. Investigating the properties of different stellar populations is useful to understand the formation and evolution of the nuclear star cluster.

Supermassive black holes

It is hard to imagine a black hole: An object that is so massive that nothing can escape from it. Black holes are not visible; particles or light that fall on a black hole can never leave it again. Due to gravity, a black hole influences the surrounding stars and gas. It is possible to infer the existence and mass of the black hole from the motions of stars in orbits around it.

Supermassive black holes are between ten thousand to ten billion times as massive as the sun. They are located in the centres of most galaxies, especially in massive galaxies. There is no consensus on the processes that formed supermassive black holes and let them grow. It was suggested that black holes either formed as the end-product of stellar evolution, or directly from a collapsing gas cloud in the early Universe. The black hole seeds must then have grown rapidly to explain the presence of supermassive black holes in the young universe, only about one billion years after the Universe formed.

Also the Milky Way contains a supermassive black hole at its centre, within the nuclear star cluster. The stars around the Milky Way black hole have been monitored over more than a decade, they move in ellipses around an invisible object. From the stellar motions, the mass

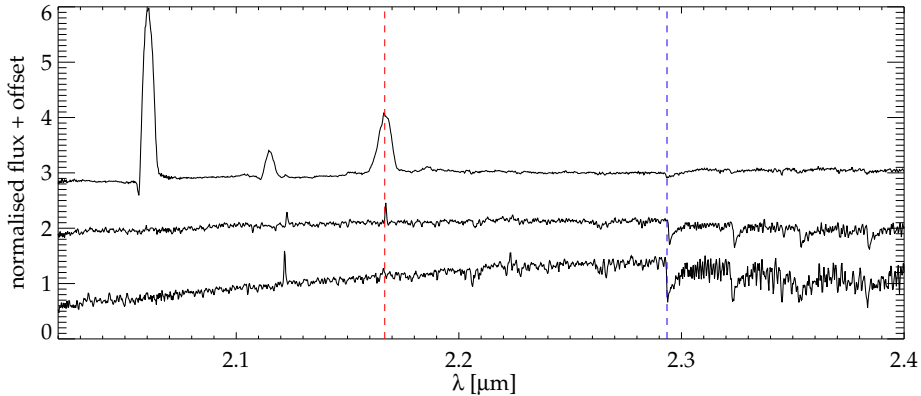


Figure S4: Spectra of three different stars, measured with the instrument KMOS at the *Very Large Telescope* in Chile. The light flux is shown as a function of wavelength (λ) in the near-infrared. The red dashed line marks one of the emission lines, the blue dashed line marks one of the absorption lines. The top spectrum is from a hotter star than the two lower spectra.

of the supermassive black hole was measured to four million solar masses. At the moment, this method to detect a supermassive black hole is only possible in the nearby Milky Way centre.

To find supermassive black holes in other galaxies, astronomers apply different methods. One of them is to construct dynamical models. Dynamical models are a useful tool to infer the entire mass distribution of a stellar system. In a dynamical model, the observed light distribution and the movements of visible stars are reconstructed. Since the stellar motions are influenced by the entire gravity of the system, the dynamical model reveals the total mass distribution of the stellar system, including the mass of invisible components such as black holes and dark matter.

Spectroscopy

A spectrograph splits light into a spectrum, this means the flux becomes a function of the wavelength. Spectra contain a wealth of information on the source of the light. There can be lines in the spectra, either bright lines on a dark background, called emission lines, or dark lines on a bright background, called absorption lines. The lines are generated by interactions of electromagnetic radiation with matter. The intensity, wavelength, and width of the lines are useful to infer properties of the spectrum's source. We show the spectra of three stars in Figure S4. The red dashed line marks one of the emission lines, the blue dashed line marks one of the absorption lines.

Each line in a spectrum is generated by a certain type of matter, e.g. an atom or a molecule. The line intensity depends on the number of atoms or molecules of the specific matter in the

star. For example, an iron line becomes stronger when there are more iron atoms in the star. But the line intensity is also influenced by the surface temperature of the star. Certain lines are only visible above or below a certain temperature. Also, the lines are weaker or stronger at different temperatures. Thus, by measuring the intensity of the lines in a stellar spectrum, we can determine the so-called metallicity and effective temperature of the star. In Figure S4, the strength of the absorption line (marked with a blue dashed line) changes for the different stars. Further, there are some emission lines in the top spectrum that are not seen in the two lower spectra, since the two bottom stars are much cooler.

When the source is moving at a certain velocity with respect to the observer, the spectral lines are shifted to a different wavelength. This is the so-called Doppler effect. By measuring the wavelength of the observed line, we can determine the velocity of a star along the line-of-sight. Also the spectra shown in Figure S4 are slightly shifted with respect to each other, as the stars are moving with different velocities.

Sometimes it is not possible to observe the spectrum of a single star, as the star is too far away and hence too faint. But we can observe the unresolved integrated spectrum of an ensemble of stars. Such a spectrum contains the light of many stars, weighted by their respective brightness. This means the measured velocity, effective temperature and metallicity will be a luminosity-weighted average of the stars that contribute to the spectrum. But as not all stars move with the same velocity, each spectral line will be broadened with respect to the line of only one star. The amount of broadening contains information about the relative motion of the stars with respect to each other. If the stars move all with roughly the same speed and in the same direction, the line broadening will be small, but if the random motion (i.e. the velocity dispersion) of the stars is large, the line broadening will increase. This velocity dispersion is important for dynamical modelling, as it depends on the underlying total (luminous and dark) mass.

This thesis

In this thesis we study the assembly history of the nuclear star cluster in the Milky Way. The cluster's size is rather typical for a nuclear star cluster, with a radius of approximately 14 light-years. The Earth's distance to the Milky Way nuclear star cluster is approximately 26,000 light-years. It is the closest nuclear star cluster, and for that reason it can be studied in much more detail than possible in other galaxies. We show an image of the Milky Way nuclear star cluster in Figure S5.

In **Chapter 2** we study the kinematics and mass distribution of the Milky Way nuclear star cluster. We use the near-infrared long-slit spectrograph ISAAC at the *Very Large Telescope* (VLT) to map a large area of 640 light-years squared of the Milky Way nuclear star cluster. In addition we observe six smaller fields out to a radius of 62 light-years along the Galactic plane. The data extend out to the radius of influence of the central supermassive black hole of approximately 9 light-years. We measure line-of-sight velocities and CO absorption line strengths from 1 375 spectra of individual stars. We derive velocity and velocity dispersion



Figure S5: Image of the central 45 light-years \times 30 light-years of the Milky Way, where the nuclear star cluster is located (image from VVV survey, Saito et al. 2012).

maps using the unresolved integrated light spectra of red giant stars. The velocity map reveals the rotation of the nuclear star cluster, and additional complex structures. In particular, we discover a misalignment of the rotation axis by 9° with respect to the photometric minor symmetry axis, and indications for a rotating substructure perpendicular to the Galactic plane at a radius of about 2.6 light-years. These structures may be the signatures of distinct accretion events. In addition to the kinematic maps, we use photometry from the *Spitzer Space Telescope* and NACO on the VLT and construct anisotropic axisymmetric Jeans dynamical models. We derive the mass distribution of the nuclear star cluster and measure the black hole mass. The resulting black hole mass is half the amount measured directly via the resolved orbits of individual stars.

In **Chapter 3** we further study the mass distribution and orbital structure of the Milky Way nuclear star cluster. We construct triaxial orbit-based Schwarzschild dynamical models of the Milky Way nuclear star cluster, and apply them to the spectroscopic maps and photometric *Spitzer* data from Chapter 2. We use these models to constrain the triaxial shape of the nuclear star cluster, the dynamical mass-to-light ratio Y , and supermassive black hole mass M_\bullet . We now obtain a black hole mass that is in agreement with the black hole mass measurement via resolved stellar orbits. Our best-fitting model recovers the complex kinematic substructures in the velocity map.

Chapter 4 presents a study of the young stellar population in the central 43 light-years squared of the Milky Way nuclear star cluster. Our near-infrared KMOS (VLT) data contain spectra of 114 hot, young stars that formed only 3–8 Myr ago. We classify the young stars in different subgroups. The young stars are very centrally concentrated, in contrast to the cool stellar population, which is distributed over the entire radial range of the data. The

strong concentration of hot, young stars indicates that they formed in-situ in the centre of the cluster, as we would expect more young stars at larger radii in the case of inward radial migration.

In **Chapter 5** we analyse the metallicity distribution of the late-type stellar population in the Milky Way nuclear star cluster. We use the late-type stellar spectra of the KMOS (VLT) data from Chapter 4. The late-type stars have stronger Na I lines than comparable stars in spectral libraries. We apply full spectral fitting on the spectra of more than 700 stars. Using a library of synthetic spectra, we fit the stellar effective temperatures, metallicities, surface gravities, and radial velocities. Most of the stars in our data set are cool red giants with temperatures in the range of 3 000 – 5 000 K. We find a smooth metallicity distribution, ranging from $[M/H] < -1$ dex (i.e. 1/10 of solar metallicity) to $\gtrsim +0.3$ dex (i.e. 2 times solar metallicity). Only approximately five per cent of the stars are metal-poor ($[M/H] \leq -0.5$ dex, i.e. 1/3 of solar metallicity). Stars with $[M/H] \leq 0.0$ dex (solar metallicity) might originate from infalling globular clusters. Most stars (about 75 per cent) have super-solar metallicities, and for those stars the globular cluster infall scenario can be ruled out.

Conclusions and outlook

We found indications for two different formation mechanisms of the Milky Way nuclear star cluster. Velocity maps of the old red giant star population reveal complex structures. This indicates that star clusters were accreted by the nuclear star cluster. The detection of metal-poor stars is another indication for the star cluster infall scenario, as globular clusters consist of such stars. However, metal-poor stars are also observed in the Galactic disc and bulge, and may also have formed there. Based on the low fraction of metal-poor stars, globular cluster infall cannot be the major formation process for the Milky Way nuclear star cluster.

Most stars have solar or super-solar metallicities, which are inconsistent with a globular cluster origin. These stars must have formed from enriched material. They either formed directly in the Galactic nucleus, or somewhere inside the Milky Way with later migration to the nucleus. The young stars, though, formed directly within the central 3 light-years of the Milky Way. They are very centrally concentrated, which is inconsistent with a migration scenario.

Although we studied the stellar populations in a significantly larger area than previous studies, our data cover only a small region of the nuclear star cluster. Studying the stellar populations over a larger area, and searching for possible gradients of age and metallicity would be useful to increase our understanding of the nuclear star cluster formation. As we showed, there are only few metal-poor stars in the centre of the Milky Way nuclear star cluster. It could be that there are more metal-poor stars further out, in particular if these stars were stripped off a globular cluster during its infall. There might also be isolated young stars at larger radii, which have not been detected yet. These young stars would trace recent accretion events.

A gradient of the stellar populations also implies that the mass-to-light ratio, which we assumed to be constant, is spatially varying. This would change our results of the cluster's stellar mass distribution. In order to verify our metallicity measurements and to measure element abundances of cool stars, observations at higher spectral resolution are needed. High-resolution spectra are also required to determine the spectral type and age of the newly discovered young stars. In this thesis we assumed that their age is consistent with the already known young stars, but this assumption should be tested.

There is also room for improvement in the kinematic studies of the nuclear star cluster. Our kinematic map does not cover the entire nuclear star cluster. The rotation curve of the inner Galaxy and the central Galactic potential are still largely unconstrained. We obtained more data with KMOS (VLT) and FLAMINGOS-2 (*Gemini South Telescope*) to address some of these issues. These two data sets can be combined and used for dynamical modelling. One can extend the models by including a gas disc component, and implementing stellar proper motions. Another improvement is using models that do not require binning of the kinematic data.

The future will open new horizons for observations of galactic nuclei. New observing facilities are presently planned and built. For example, the *James Webb Space Telescope* (JWST) will be launched in 2018. Due to its high sensitivity and spatial resolution it will be possible to study stellar population gradients in extragalactic nuclear star clusters. In addition, a new generation of ground-based telescopes is currently being constructed: Extremely large telescopes with mirror diameters $d > 20$ m: the *Giant Magellan Telescope* (GMT, $d = 24.5$ m), the *Thirty Meter Telescope* (TMT, $d = 30$ m), and the *European Extremely Large Telescope* (E-ELT, $d = 39.3$ m). The high spectral and spatial resolution instruments of these telescopes are useful to search for supermassive black holes in extragalactic nuclear star clusters. These sensitive telescopes are capable to observe fainter stars in the Milky Way nuclear star cluster than currently possible, including A- and F-type dwarfs. New telescopes and models will help to achieve a better understanding of the formation and evolution of galactic nuclei, and their host galaxies. We are looking into a bright future for the research of galactic nuclei.

Publications

Refereed Publications

1. **Feldmeier-Krause A.**, Neumayer N., Schödel R., Seth A., Hilker M., de Zeeuw P. T., Kuntschner H., Walcher, C. J., Lützgendorf N., Kissler-Patig M.: KMOS view of the Galactic Centre I. Young stars are centrally concentrated, *A&A* Volume 584 (2015)
2. Schödel, R., **Feldmeier, A.**, Neumayer, N., Meyer, L., Yelda, S.: The nuclear cluster of the Milky Way: our primary testbed for the interaction of a dense star cluster with a massive black hole. *Classical and Quantum Gravity*, Volume 31 (2014)
3. **Feldmeier A.**, Neumayer, N., Seth, A., Schödel, R., de Zeeuw, P.T., Lützgendorf, N., Kissler-Patig, M., Nishiyama, S., Walcher, C.J.: Large scale kinematics and dynamical modelling of the Milky Way nuclear star cluster, *A&A* Volume 570 (2014)
4. Schödel, R., **Feldmeier, A.**, Kunneriath, D., Stolovy, S., Neumayer, N., Amaro-Seoane, P., Nishiyama, S.: Surface Brightness Profile of the Milky Way's Nuclear Star Cluster, *A&A* Volume 566 (2014)
5. Lützgendorf, N., Kissler-Patig, M., Neumayer, N., Baumgardt, H., Noyola, E., de Zeeuw, P. T., Gebhardt, K., Jalali, B., **Feldmeier, A.**: The $M_{\bullet} - \sigma$ relation for intermediate-mass black holes in globular clusters. *A&A*, Volume 555 (2013)
6. **Feldmeier, A.**, Lützgendorf, N., Neumayer, N., Kissler-Patig, M., Gebhardt, K., Baumgardt, H., Noyola, E., de Zeeuw, P. T., Jalali, B.: Indication for an intermediate-mass black hole in the globular cluster NGC 5286 from kinematics. *A&A*, Volume 554 (2013)
7. Lützgendorf, N., Kissler-Patig, M., Gebhardt, K., Baumgardt, H., Noyola, E., de Zeeuw, T., Neumayer, N., Jalali, B., **Feldmeier, A.**: Limits on intermediate-mass black holes in six Galactic globular clusters with integral-field spectroscopy. *A&A* Volume 552 (2012)

Submitted to refereed journals

1. **Feldmeier-Krause A.**, Kerzendorf W., Neumayer N., Schödel R., Nogueras-Lara F., Do T., de Zeeuw P. T., Kuntschner H.: KMOS view of the Galactic Centre II. Metallicity distribution of Late-type stars (submitted to *MNRAS*, 2016)
2. **Feldmeier-Krause A.**, Zhu L., Neumayer N., van de Ven G., de Zeeuw P. T., Schödel R.: Triaxial orbit-based modelling of the Milky Way nuclear star cluster (submitted to *MNRAS*, 2016)

Conference Proceedings

1. **Feldmeier, A.**, Neumayer, N., Schödel, R., Seth, A., de Zeeuw, P. T., Walcher, C. J., Lützgendorf, N., Kissler-Patig, M., Hilker, M., Kuntschner, H.: The Assembly History of the Milky Way Nuclear Star Cluster. Proc. of the International Astronomical Union, Volume 316 (2015)
2. Lützgendorf, N., Kissler-Patig, M., Gebhardt, K., Baumgardt, H., Kruijssen, D., Noyola, E., Neumayer, N., de Zeeuw, T., **Feldmeier, A.**: Intermediate mass black holes in globular clusters: observations and simulations. Proceedings of the International Astronomical Union, Volume 312 (2015)
3. **Feldmeier, A.**, Neumayer, N., Seth, A., de Zeeuw, P. T., Schödel, R., Lützgendorf, N., Kissler-Patig, M., Nishiyama, S., Walcher, C. J.: The Milky Way Nuclear Star Cluster beyond 1 pc. Proc. of the International Astronomical Union, Volume 303 (2014)
4. Kunneriath, D., Schödel, R., Stolovy, S., **Feldmeier, A.**: Structure of the nuclear stellar cluster of the Milky Way. Proc. of the International Astronomical Union, Volume 303 (2014)

Curriculum Vitae

I was born on December 31st, 1985 in Landau a. d. Isar, Germany. I grew up in Mamming, a small village near Dingolfing, and started my education at the primary school in Bubach. I attended the Herzog Tassilo Realschule Dingolfing, Germany, and finished with a secondary school certificate in 2002. I started an apprenticeship as assistant tax consultant in Dingolfing, which I finished in 2005. In the three years of my apprenticeship, I read the entire astronomy and astrophysics section of the public library in Dingolfing, and it became clear to me that I wanted to be an astrophysicist. For that reason, I returned to school and attended the Upper Vocational School in Landshut, Germany for two years. I graduated in 2007 with the Abitur, which allowed me to progress to a university. Due to my excellent grades, I was permitted to the examination of highly gifted ("Begabtenprüfung") of the Max Weber Program, a subsection of the "German National Academic Foundation". I was awarded with a scholarship for the time of my university undergraduate studies.

In 2007, I enrolled in the Bachelor of Physics program of the Ludwig-Maximilians-University Munich, Germany. I chose elective courses in the field of astronomy, and wrote a theoretical bachelor thesis on "X-ray Halos of Elliptical Galaxies, Galaxy Groups, and Clusters" under the guidance of Dr. Thorsten Naab. After graduating as Bachelor of Science, I enrolled in the Master of Physics program of the Ludwig-Maximilians-University in Munich. I had much freedom to choose elective courses in astronomy and astrophysics. Among those was a practical course on observing at the Wendelstein observatory in the Bavarian Alps. I went observing in a clear spring night in 2011. That night, I felt all the excitement of observing, and anticipation to work on the data. I decided to become an observational astronomer.

For my master thesis, I worked at the *European Southern Observatory* (ESO) in Garching, Germany on data from the *Very Large Telescope* and archive data from the *Hubble Space Telescope*. I studied the question "Is there an Intermediate-Mass Black Hole in the Globular Cluster NGC 5286?" under the supervision of Dr. Markus Kissler-Patig. After obtaining my M.Sc. degree in Physics in 2012, I started to work as Ph.D. student at ESO under the guidance of Prof. Dr. Tim de Zeeuw and Dr. Nadine Neumayer. I am affiliated with the International Max Planck Research school on Astrophysics (IMPRS), and as part of this program I attended several Advanced Courses in Astronomy. In the four years of my Ph.D. studentship, I participated at national and international conferences, meetings, and workshops. I presented my work in Santa Fe (USA), University of Utah (USA), Granada (Spain), Garching (Germany), Freising (Germany), Leiden (Netherlands), Aspen (USA), Honolulu (USA), and Alájar (Spain). I carried out observations at the *Very Large Telescope* and the *Gemini South Telescope* in Chile. Further, I co-organised the ESO workshop "RASPUTIN" (Resolved And Unresolved Stellar PopUlaTIOns) and the monthly "Wine & Cheese" seminar at ESO. At my wedding in July 2015, I changed my name from Anja Feldmeier to Anja Krause, however, I publish under the name Anja Feldmeier-Krause. In October 2016, I will move to Chicago, USA to start working with Prof. Dr. Wendy Freedman at the University of Chicago.

Acknowledgements

First of all, many thanks to my co-authors and colleagues for their help and support. Thank you for discussions, advice, and inspiration. I would like to thank my colleagues at ESO: The students, fellows, postdocs and staff for many interesting talks, discussions and conversations; the assistants and secretaries Stella, Isolde, Hildegard, Pam, and Christina, the IT department (both at ESO and MPIA in Heidelberg), the librarians Uta, Silvia, and Dominic for quick response and help. Thanks to Alexandra at Leiden Observatory, who helped me to organise my graduation in Leiden. I would like to thank the people at MPIA for their kindness during my visits. There are many more people I have interacted and worked with, learnt from, and spent time with during my years at ESO, also at conferences and visits. Apologies for not mentioning all of you here explicitly, I thank you all very much.

It was a pleasure to work closely with Laura, Emin, and Siyi in organising the Wine & Cheese seminar, and with Laura, Stella, Elena, and Samantha in preparing the RASPUTIN conference. I am indebted to Claudius, Hannah, Laura, and Torsten for careful reading of the manuscript. Special thanks to Ruud Visser for the translation of my Nederlandse Samenvatting, and to Andra Stroe for sharing her L^AT_EX thesis template with me. Devaky, for her reassurance before my first conference talk. Carlo and Anna, thank you for hosting me in Leiden and helping me to distribute my thesis. I would like to thank my friends for their support and encouragement.

Schließlich möchte ich mich noch bei meiner Familie bedanken: Bei meinem Ehemann Claudius der mit mir lacht, diskutiert, geocacht, mich tröstet und immer an mich glaubt. “So close, no matter how far; Couldn’t be much more from the heart; Forever trust in who we are; And nothing else matters.” Wo du hingehst, da will ich auch hingehen; wo du bleibst, da bleibe ich auch. Wir werden bald wieder zusammen sein. Bei meinen Eltern, die mir all die Jahre geholfen haben und mich ermutigt haben, meine Träume zu verfolgen. Bei meinen Schwestern und ihren Familien, meinen Schwiegereltern. Vielen Dank für eure Unterstützung.

